

Active control of trailing vortices by means of long- and short-wavelength actuation

vorgelegt von
Dipl.-Ing., Dipl.-Volksw.
Christoph Strangfeld
geboren in Berlin

von der Fakultät V — Verkehrs- und Maschinensysteme
der Technischen Universität Berlin
zur Erlangung des akademischen Grades

Doktor der Ingenieurwissenschaften
— Dr.-Ing. —

genehmigte Dissertation

Promotionsausschuss:

Vorsitzender: Prof. Dr. rer. nat. W. H. Müller (Technische Universität Berlin)
Gutachter: Prof. Dr.-Ing. C. O. Paschereit (Technische Universität Berlin)
Prof. D. Greenblatt (Technion - Israel Institute of Technology)
Dr. R. Wosidlo (The University of Kansas)

Tag der wissenschaftlichen Aussprache: 21.04.2015

Berlin 2015

D 83

Widmung

Ich widme dieses Werk der Zukunft: Meinem Sohn Constantin Yun Strangfeld.

Danksagung

Für den erfolgreichen Abschluss meiner Doktorarbeit danke ich herzlich der Prüfungskommission in Form von Herrn Professor Wolfgang H. Müller, Herrn Professor Christian O. Paschereit, Herrn Professor David Greenblatt und Herrn Doktor Rene Woszidlo.

Ich danke Herrn Professor Christian O. Paschereit für die vielen Jahre der guten Zusammenarbeit, die administrative Verwaltung und die Unterstützung auch in schwierigen Momenten während meiner Promotion. Ich danke Herrn Professor David Greenblatt für die tollen Forschungsaufenthalte am Technion, die wunderbare und umfangreiche fachliche Betreuung und die viele Unterstützung während der Anfertigung dieser Abschlussarbeit. Freundschaftlich, fair, aber auch sehr fordernd konnte ich mit deiner Unterstützung meine wissenschaftliche Arbeit auf ein höheres Niveau heben, danke David. Du bist ein Betreuer, wie ihn sich jeder nur wünschen kann. Ich danke Herrn Doktor Rene Woszidlo für die umfangreiche Unterstützung bei der Anfertigung von Veröffentlichungen und dieser Abschlussarbeit im inhaltlichen und sprachlichen Bereich. Deine Geduld und Hingabe sind außergewöhnlich und haben mir sehr geholfen, danke Rene.

Drei weitere Personen seien hier erwähnt, ohne die diese Arbeit in dieser Form nie zustande gekommen wäre. Vielen Dank an Herrn Doktor Christian Nayeri. Du hattest immer ein offenes Ohr für mich, hast immer an mich geglaubt und mir mit viel Kraft und Mühe immer wieder eine Finanzierung verschafft. Du bist die gute Seele, die man hier immer mal braucht. Lieber Heiko Stolpe, deine Hingabe für mein Projekt ist absolut außergewöhnlich. All meine Ideen hast du dir angehört, optimiert und aufgebaut. Die ganzen Versuche, die Messtechnik und die Aktuaton hätten ohne deine Unterstützung niemals dieses hohe Maß an Perfektion erreicht. Ich danke natürlich auch Hanns Müller-Vahl für die tollen Messungen am Technion und die tolle Zeit, die wir gemeinsam hatten. Ohne deinen enormen Messeinsatz, deine Hingabe und Perfektionismus hätten wir niemals diese präzisen Messungen durchführen können. Es ist einfach geil mit dir zu arbeiten.

Für die vielen schönen Jahre am HFI danke ich all meinen Kollegen mit denen ich gearbeitet, diskutiert aber auch gelacht habe. Hier danke ich besonders: Alena Bach, Basti Blümel, Bernhard Bobusch, Stefan Born, Bernhard Cosic, Karsten Düwel, Katharina Göckeler, David Holst, Oliver Krüger, George Pechlivanoglou, Pavel Piotrowski, Körling Pölkow, Lothar Rukes, Aditya Saurabh, Marcel Scheibel, Hajo Schmidt, Moritz Sieber, vor allem mir selbst, Steffen Terhaar, Professor van der Wall, Doktor Stefan Vey, und Dirk Wieser. Dankeschön, es war eine tolle Zeit mit euch.

Natürlich danke ich herzlichst der Werkstatt, die das eine oder andere Mal die Kohlen aus dem Feuer geholt hat. Dank an: Thorsten Dessin, Martin Franke, Andy Göhrs, Horst Mettchen, Willi Postel, Manfred Ziehe. Immer wurde ich toll vom Sekretariat unterstützt und konnte alle meine Sorgen und Nöte dank eurer Hilfe bewältigen. Ein großes Dankeschön an: Kristin Halboth, Lilli Lindemann, Maria Lück, Sandy Meinke, Dagmar Pölkow. Einen riesen Dank auch an Angela Pätzold, die mich immer wieder retten konnte, wenn die IT nicht so wollte wie ich.

Ich danke der Stiftung der deutschen Wirtschaft, welche mich mit einem Stipendium volle vier Jahre gefördert hat und somit den finanziellen Grundstein für meine erfolgreiche Promotion gelegt hat. Stellvertreten für die gesamte Stiftung seien hier Frau Doreen Wagner und Frau Doktor Anne Legler gedankt. Ich danke Herrn Doktor Martin Beznoska für die vielen Diskussionen über die Durchführung und die Motivation während einer Dissertation. Das lustige Gespräch bei einem guten Fußball-Kick hat so manches Problem klein werden lassen, danke Martin.

Ich danke meiner Familie für die tolle Unterstützung während der gesamten Zeit. Heidrun Wetten, liebe Mutter, vielen Dank für alles. Ohne dich wäre ich niemals so weit gekommen. Du bist der Fels in der

Brandung, das Licht im Nebel. Clemens Strangfeld, lieber Vater, ich konnte immer auf deine Unterstützung zählen. Du hast mir immer das Vertrauen geben, dass mein Weg der Richtige ist, hast immer an meinen Erfolg geglaubt. Weiterhin danke ich für die vielen Jahre der Unterstützung Karin Strangfeld, Michael Wetten und Robert Wetten.

Mein allergrößter Dank gilt meiner Frau, Miao Hu. Du hast all die Jahre an meiner Seite gestanden, mich immer mit voller Hingabe unterstützt, mich aufgefangen und motiviert. Eine Promotion, ein Leben, ohne dich wäre nicht vorstellbar. Du bist das warme Licht, das mir die Farben zeigt, die Lustigkeit, die mich zum Lachen bringt, der Ursprung meiner Energie.

Eidesstattliche Erklärung

Hiermit erkläre ich an Eides statt, dass ich die vorliegende Dissertation mit dem Titel

"Active control of trailing vortices by means of long- and short-wavelength actuation"

selbstständig und eigenhändig sowie ohne unerlaubte fremde Hilfe und ausschließlich unter Verwendung der aufgeführten Quellen und Hilfsmittel angefertigt habe. Die Zusammenarbeit mit anderen Wissenschaftlern habe ich kenntlich gemacht.

Teile dieser Arbeit sind bereits veröffentlicht oder zur Veröffentlichung eingereicht und zwar in:

- Strangfeld, C., Müller-Vahl, H., Nayeri, C. N., Paschereit, C. O., Greenblatt, D., Unsteady aerodynamics of an airfoil in an oscillating free stream, 2014, In: *7th AIAA Theoretical Fluid Mechanics Conference*, Atlanta, Georgia, USA, 16.-20.06.2014, DOI: 10.2514/6.2014-2926
- Strangfeld, C., Rumsey, C. I., Müller-Vahl, H., Greenblatt, D., Nayeri, C. N., Paschereit, C. O., Unsteady thick airfoil aerodynamics: experiments, computation, and theory, 2015, In: *AIAA Summer Conference*, Dallas, Texas, USA, *under review*
- Strangfeld, C., Müller-Vahl, H., Greenblatt, D., Nayeri, C. N., Paschereit, C. O., Airfoil in a High Amplitude Oscillating Stream, 2015, In: *Journal of Fluid Mechanics*, *under review*

Desweiteren erkläre ich, dass mir die geltende Promotionsordnung der Technischen Universität Berlin zur Erlangung des akademischen Grades Doktor der Ingenieurwissenschaften (Dr.-Ing.) in der Fassung vom 23. Oktober 2006 bekannt ist. Eine Anmeldung der Promotionsabsicht habe ich an keiner anderen Fakultät oder Hochschule beantragt.

Berlin, den

.....
Unterschrift

Abstract

Downstream of a finite wing, the vorticity sheet emitted at the trailing edge starts to roll up and a strong streamwise vortex is generated. This vortex is known as the wing tip vortex. In this thesis, the active control of trailing vortices by means of long- and short-wavelength actuation is investigated. On the one hand, local short-wavelength forcing excites the rolling up shear layer and its instabilities. Thus, the locally modified shear layer convects into the vortex core and directly influences the trailing vortex strength at its origin. On the other hand, active control of the bound, spanwise circulation influences the strength and position of the trailing vortex as well. This global long-wavelength effect is quantified for unsteady flow regimes. Both approaches are investigated experimentally and theoretically with the objective to achieve the control of unsteady circulation distribution, and hence of the trailing vortex strength. In the end, the control authority and the interaction are quantified on a realistic finite wing under unsteady conditions by means of Betz's theory.

Downstream of a swept, semi-span, backward facing step, a streamwise vortex is generated experimentally. This setup enables the assessment of circulation control of the streamwise vortex by means of local short-wavelength forcing. By means of this approach, the trailing vortex is controlled at its origin. The forced, rolling up shear layer transports another amount of vorticity into the vortex core and the trailing vortex circulation is modified. Finally, the local forcing controls the vortex strength. Baseline measurements on this newly invented generic geometry yield a stable generation of a streamwise vortex. Flow visualisations prove the high agreement of this flow structure to trailing vortices and other vortical structures like streamwise vortices on delta wings, or at the C-pillar of an Ahmed body. Its circulation is controlled by manipulating the instabilities of the separating shear layer which rolls up into this free vortex. This highly three-dimensional flow as well as the emitted twisted shear layer and its Kelvin-Helmholtz-instabilities may be sufficiently controlled by only a transversal excitation. Thus, actuators (segmented flaps) operating at arbitrary amplitudes, frequencies and phase lags are designed, developed and tested. This innovative approach of actuation shows promising results. They show a high repeatability and reliability for the frequency, amplitude, and phase lag of each distinct flap up to a frequency of 35Hz. In almost the entire region of the vortex the actuation frequency dominates the frequency spectrum. A direct and almost linear response of the flow field dependent on different phase lags is recorded and quantified. At low Reynolds numbers, the control effects amount to approximately 8%. Stronger control effects are probably prohibited by the already fully turbulent boundary layer upstream of the trailing edge on the step at considerably sub-critical Reynolds numbers. This renders a distinct actuation of a Kelvin-Helmholtz instability in laminar flow impossible. Furthermore, an ansatz to compute the natural instability frequency of twisted shear layers is proposed with the aid of stability analysis. Comparisons to inviscid and viscous two-dimensional shear layers yield a good agreement. A validation of a 2.5-dimensional shear layer fails due to the lack of reference values in the literature. However, the three velocity components of the rolling up shear layer are experimentally determined and a temporal stability analysis of the 2.5-dimensional shear layer is conducted.

The second approach to control the trailing vortex strength is the long-wavelength actuation. In this scenario, the entire wing is facing unsteady conditions like pitching, unsteady inflow, or vertical wing motion. The wavelengths of the unsteadiness are several magnitudes larger compared to Kelvin-Helmholtz instability. Nevertheless, the spanwise circulation distribution has a direct impact on the trailing edge strength and position. Thus, a precise prediction of the circulation of bound vortices along the span under unsteady conditions is of great importance although the validated theories are, as yet, missing. Based on the steady solution of Kutta-Joukowski who considers a flat plate in potential flow, the approaches of Theodorsen, Greenberg, Isaacs, and van der Wall include unsteady conditions like pitching and plunge motions, and an oscillating free stream. Although these theories are partly more than 70 years old, an experimental validation at moderate and high free stream velocity amplitudes is still missing. Thus, a NACA 0018 airfoil is experimentally investigated during pitching and facing an unsteady free stream. The experimental results show a high agreement with the theoretical predictions of the unsteady circulation. The amplitude and the phase coincide with Isaacs' and van der Wall's theories at velocity amplitudes of 50%. Furthermore, the predicted nonlinear interaction between pitching and simultaneous unsteady free stream is reproduced in the experiments. Based on these new experimental results, the theories are

validated. Moreover, Isaacs' generalised theory proposed by van der Wall is theoretically extended in this thesis to further predict the unsteady pressure distribution along the chord. This excitation gives a more detailed insight into the vorticity distribution under highly unsteady boundary conditions, in fact the unsteady free stream, oscillating pitching and plunge motion, as well as the combined effects amongst one another. These new theoretical findings and the experimentally obtained unsteady pressure distribution coincide with each other at all phase angles. Based on this validation, the reliability of the extended theory is confirmed. This validation leads to the required unsteady, spanwise circulation distribution which influences the trailing vortex strength and position. In a final step, the interaction of the streamwise and spanwise circulation due to active flow control is quantified by means of an extension of Betz's theory. It is shown that the variation of the spanwise loading influences remarkably the streamwise vortex strength and position by more than 25% already at low and moderate reduced frequencies. This unsteady, long-wavelength interaction is probably the main reason of an accelerated trailing vortex bursting.

Zusammenfassung

Ein endlicher Flügel bildet stromab eine Wirbelschicht aus, welche sich ausrollt und einen starken Längswirbel generiert. Dieser Wirbel ist bekannt als Flügelspitzenrandwirbel. In dieser Dissertation wird die aktive Kontrolle dieser Randwirbel mittels lang- und kurzwelliger Anregung untersucht. Die kurzwellige Aktuation regt einerseits die sich aufrollende Scherschicht und deren Instabilitäten an. Somit konvektiert eine modifizierte Scherschicht in den Wirbelkern und beeinflusst somit Randwirbelstärke direkt an dessen Ursprung. Andererseits beeinflusst auch die gebundene, spannwellige Zirkulationsverteilung die Stärke und Position der Randwirbel. Dieser globale, langwellige Effekt ist quantifiziert für instationäre Strömungszustände. Beide Ansätze sind experimentell und theoretisch untersucht mit dem Ziel der Kontrolle der instationären Zirkulationsverteilung und letztendlich der Randwirbelstärke. Im letzten Schritt wird die Kontrollwirkung und deren Interaktion an einem realistischen, endlichen Flügel in instationären Bedingungen mit Hilfe der Theorie von Betz quantifiziert.

Stromab einer schrägen, halbspannwelligen Stufe wird experimentell ein freier Wirbel generiert. Dieser Aufbau ermöglicht die Beurteilung der Zirkulationskontrolle von Längswirbeln mittels lokaler, kurzwelliger Anregung. Somit wird der Randwirbel direkt am Ort dessen Entstehung kontrolliert. Die angeregte, sich aufrollende Scherschicht transportiert eine veränderte Menge und Wirbelstärke in den Wirbelkern und modifiziert somit den Längswirbel. Somit kontrolliert die lokale Anregung letztendlich die Randwirbelstärke. Messungen der Grundströmung an dieser neu entwickelten Geometrie weisen die Generierung eines Längswirbels auf. Strömungsvisualisierungen stimmen mit den Strömungsstrukturen von Flügelrandwirbel und weiteren Tütenwirbelstrukturen bekannt von Delta-Flügeln oder C-Säulen am "Ahmed body" überein. Die Zirkulation soll mit Hilfe von Anregung der Kelvin-Helmholtz Instabilität erfolgen. Die hoch drei-dimensionale Strömung und die stark gekrümmte Scherschicht und deren Instabilitäten kann nur mit transversaler Aktuation zufriedenstellend angeregt werden. Somit müssen die Aktuatoren, hier segmentierte Klappen, bei verschiedenen Amplituden, Frequenzen und Phasenwinkeln zu einander operieren. Das Design, die Entwicklung und die Tests des hier neu entwickelten Aktuationsansatzes sind in dieser Arbeit dokumentiert. Die vielversprechenden Ergebnisse zeigen eine hohe Genauigkeit und Reproduzierbarkeit verschiedener Amplituden, Frequenzen und Phasenwinkel bis zu Frequenzen von 35Hz. Fast im gesamten Messbereich der synchronisierten, zeitauflösenden Oberflächendrucksensoren dominiert die Aktuationsfrequenz das Spektrum. Ein direktes und fast lineares Antwortverhalten der Strömungsstrukturen in Abhängigkeit von der Anregungsfrequenz wird beobachtet und quantifiziert. Bei geringen Reynolds Zahlen liegt der Aktuationseffekt bei ca. 8%. Stärkere Kontrolleffekte werden vermutlich durch die schon voll-turbulent ausgebildete Grenzschicht stromauf der Hinterkante der Stufe verhindert, wenn gleich theoretisch deutlich unterkritische Reynolds Zahlen betrachtet werden. Dies macht eine exakte Anregung der Kelvin-Helmholtz Instabilität in laminarer Strömung unmöglich. Weiterhin wird ein theoretischer Ansatz basierend auf der Stabilitätstheorie vorgestellt, um die Frequenz der natürlichen Instabilität einer gekrümmten Scherschicht vorherzusagen. Vergleiche zu reibungsfreien und reibungsbehafteten zwei-dimensionalen Scherschichten zeigen eine gute Übereinstimmung. Eine Validierung mit Hilfe von 2.5-dimensionalen Scherschichten scheitert auf Grund fehlender Referenzwerte in der Literatur. Dennoch werden die drei Geschwindigkeitskomponenten der gekrümmten Scherschicht experimentell bestimmt und eine zeitliche Stabilitätsanalyse einer 2.5-dimensionalen Scherschicht wird durchgeführt.

Der zweite Ansatz um die Randwirbelstärke zu kontrollieren ist langwellige Anregung. In diesem Szenario ist der gesamte Flügel mit instationären Effekten wie Nick- und Vertikalbewegung als auch einer oszillierenden Anströmung ausgesetzt. Die Wellenlängen dieser Instationaritäten sind um mehrere Größenordnungen größer als bei Kelvin-Helmholtz Instabilitäten. Dennoch hat die spannwellige Zirkulationsverteilung einen deutlichen Einfluss auf die Randwirbelstärke und deren Position. Daher ist eine präzise Vorhersage der Zirkulation von gebundenen Wirbeln entlang der Spannweite in instationären Zuständen von großer Wichtigkeit, obwohl bislang keine validierte Theorie existiert. Basierend auf der stationären Lösung von Kutta-Joukowski, welche eine ebene Platte in Potentialströmung betrachtet, haben Theodorsen, Greenberg, Isaacs und van der Wall instationäre Randbedingungen wie z. B. Nick- und Vertikalbewegung als auch eine oszillierende Anströmung mit berücksichtigt. Auch wenn diese Theorien teilweise mehr als 70 Jahre alt sind, so existieren keine experimentellen Validierungen bei mittleren und

hohen Anströmungsamplituden. Deshalb wird ein NACA 0018 Flügelprofil experimentell untersucht, welches dynamische Nickbewegungen ausführt und einer instationären Anströmung ausgesetzt ist. Die Experimente zeigen eine hohe Übereinstimmung zu den theoretischen Vorhersagen der instationären Zirkulationsentwicklung. Die Amplitude und der Phasenwinkel stimmen mit der Theorie von Isaacs und van der Wall bei einer Anströmamplitude von 50% gut überein. Weiterhin wird die nicht-lineare Interaktion zwischen simultaner Nickbewegung und oszillierender Anströmung experimentell bestätigt. Basierend auf diesen neuen experimentellen Validierungen werden die Theorien als korrekt angesehen. Außerdem wird die verallgemeinerte Theorie von Isaacs, welche von van der Wall formuliert wurde, erweitert um zusätzlich die instationäre Wirbelstärkeverteilung entlang der Flügelsehne vorherzusagen. Diese Erweiterung gibt einen detaillierteren Einblick in die Wirbelstärkenverteilung unter instationären Randbedingungen. Diese neu gewonnenen theoretischen Ergebnisse und die experimentelle, instationäre Druckverteilung zeigen eine gute Übereinstimmung bei allen Phasenwinkeln. Basierend auf diesen Messungen wird die hier präsentierte Theorieerweiterung als validiert betrachtet. Diese Validierung ermöglicht nun die benötigte Bestimmung der instationären, spannweiten Zirkulationsverteilung, welche die Randwirbelstärke und deren Position beeinflusst. Im letzten Schritt wird die Interaktion der spannweiten und längsseitigen Zirkulation durch aktive Strömungskontrolle mit Hilfe der Erweiterung der Betz Theorie quantifiziert. Dabei wird gezeigt, dass schon bei geringen und moderaten, reduzierten Frequenzen die Variation der spannweiten Lasten einen deutlichen Einfluss von mehr als 25% auf die Randwirbelstärke und deren Position hat. Diese instationäre, langwellige Interaktion ist vermutlich der Hauptgrund für einen beschleunigten Wirbelzerfall.

Contents

List of Figures	I
List of Tables	VII
Nomenclature	IX
1. Motivation of circulation control by means of long- and short-wavelength excitation	1
1.1. Short-wavelength excitation of trailing vortices	3
1.2. Long-wavelength excitation of trailing vortices	6
1.3. Interaction of the trailing edge vorticity sheet and the wing tip vortex	8
2. Literature review and theoretical approaches	9
2.1. Free vortices and Kelvin-Helmholtz instabilities	9
2.2. Designing of the active flow control actuators for short-wavelength excitation	22
2.3. Linear stability analysis	27
2.4. Bound vortices in a historical perspective and the Kutta-Joukowski theorem	31
2.5. Prediction of unsteady lift	33
2.6. Interaction of the streamwise and spanwise vortices	40
3. Experimental setup and validation	43
3.1. Experimental setup of the swept, semi-span, backward facing step	43
3.2. Development of the oscillating flap array	47
3.3. Numerical implementation of the Orr-Sommerfeld equation	55
3.4. Derivation of the unsteady bound circulation and vorticity sheet	56
3.5. Experimental setup for validation of Isaacs' and van der Wall's theories at high inflow velocity ratios	61
3.6. Determination of the streamwise and spanwise vorticity interaction	65
4. Results	67
4.1. Flow visualisation of the baseline flow at the swept, semi-span, backward facing step	67
4.2. Pressure measurements of the baseline and forced flow	71
4.3. Investigation of the twisted boundary layer upstream of the trailing edge	80
4.4. Shear layer velocity profiles and their instabilities	84
4.5. Validation and results of the unsteady bound circulation	89
4.6. Interaction between streamwise and spanwise vortices	99
4.7. Improvement and future work	103
5. Conclusion	107
Bibliography	109
A. Appendix	127

List of Figures

1.1.	Sketch of a DeHavilland Beaver DHC-2 with the loading along the span (yellow line normal to the wing); the flow at the wing tip separates (green lines) and initiates the trailing vortex; the vorticity sheet emitted at the trailing edge rolls up into one streamwise vortex orientating in downstream direction (red lines)	2
1.2.	Six occurrences of streamwise vortices (red lines) in technical applications; the flow separation (green lines) is tilted to the free stream (blue arrow) and a rolling up shear layer is generated	3
1.3.	Left: sketch of a swept, semi-span, backward facing step surrounded by a fixed floor and fixed side wall; right: detailed sketch of an arbitrary part of the vortex	5
1.4.	Sketch of a pitching airfoil in an oscillating free stream which generates an unsteady wake vortex sheet	7
2.1.	Cross-sectional visualisation of the rolling up shear layer at the leading edge on a delta wing; photograph is taken by Payne [1987]	19
2.2.	Sketch of the magnetic field (green lines) generated by a direct current-carrying conductor	24
2.3.	Sketch of yoke and armature of an electromagnet	25
2.4.	Sketch of an oscillating armature drive with springs to achieve the passive back motion; left: linear oscillation; right: rotational oscillation	26
3.1.	Perspective front and back view of the swept, semi-span, backward facing step installed in the wind tunnel	43
3.2.	Sketch and dimension of the swept, semi-span, backward facing step including the two global vortices in the wake	44
3.3.	Coordinate system of the step	45
3.4.	Illustration of the 122 pressure tap positions	45
3.5.	Sectional view of the large wind tunnel at the HFI	46
3.6.	Construction of one single oscillating flap with a total frame size of 114x48x32mm	48
3.7.	Circuit layout of the supply voltage (grey dashed box) and the amplified control voltage	49
3.8.	Construction of the array including 16 oscillating flaps; the frequency and the phase are software-controlled, the amplitude is proportional to the RMS value of the AC supply voltage	49
3.9.	Photo of the flap array; cables on the left hand side deliver the supply voltage	50
3.10.	Presentation of the measured amplitude of flap 10 for 10, 25 and 60Hz (via LDV). At each frequency, three arbitrary periods are depicted with the corresponding ideal sinusoidal motion curve. At 10Hz, only every third measurement sample is marked by a red point.	51
3.11.	Amplitude spectrum of flap 10 at 60Hz and $10V_{pp}$	52
3.12.	Power spectral density of flap 10 at 60Hz and $10V_{pp}$	52
3.13.	Peak-to-peak motion amplitude of flap 10 at 5 to 60Hz and variable control voltages from 1 to $10V_{pp}$	53
3.14.	Peak-to-peak motion amplitude of flap 10 at 4, 6, 8, and $10V_{pp}$ and variable frequencies from 5 to 150Hz	53
3.15.	Analogue output voltage determined by the in-situ calibration at a frequency of 30Hz and at a desired peak-to-peak amplitude of 4mm	54
3.16.	Sketch of the wind tunnel setup: The louver mechanism is placed at the end of the wind tunnel. The wing is rotatable and the unsteady free stream velocity is recorded upstream of the wing via two hotwires.	61

3.17. Schematic sketch of the used NACA 0018 airfoil including the two AFC slots	62
3.18. Illustration of the symmetrically distributed pressure taps	63
3.19. Chordwise position of the 40 pressure sensors	63
3.20. Photograph of the 13 louver vanes at the end of the test section in open and closed position	63
3.21. Comparison of the measured free stream velocity $u(\phi)$ and the ideal sinusoidal free stream velocity $u_s(1 + 0.5 \sin(\phi))$ at a frequency of $f = 1.2Hz$ and $Re = 300000$	64
3.22. (a): a static wing encounters an oscillating free stream (blue arrows); (b) a fore-aft moving wing (blue arrows) in a constant free stream; the diagrams show the free stream velocity profile $u(\phi)$ and the induced normal velocity along the chord v_n (red line)	65
4.1. Photographs perpendicular to the back panel of the rolling up shear layer downstream of the swept, semi-span, backward facing step at three different Reynolds numbers	68
4.2. Photographs perpendicular to the inflow of the rolling up shear layer downstream of the swept, semi-span, backward facing step at $Re_H = 29000$	68
4.3. Photograph of the surface oil flow visualisation perpendicular to the slanted back panel .	70
4.4. Photograph of the surface oil flow visualisation of the step top	70
4.5. Contour plot of the pressure coefficient C_p for four different Reynolds numbers	71
4.6. Crosswise pressure coefficients at $x^* = 275mm$ with a downstream diffuser angle of 14°	73
4.7. Crosswise pressure coefficients at $x^* = 275mm$ with a downstream diffuser angle of 6° .	73
4.8. Crosswise AFC measurements at $x^* = 275mm$ and at $Re_H = 133000$ with various frequencies and amplitudes	74
4.9. Crosswise pressure coefficients at $x^* = 275mm$ with a downstream diffuser angle of 6° and a polyethylene layer on the step top	75
4.10. Crosswise AFC measurements at $x^* = 275mm$ and at $Re_H = 153000$ with various frequencies and amplitudes	76
4.11. Crosswise AFC measurements at $x^* = 275mm$ and at $Re_H = 153000$ for the baseline and for 5Hz and 20Hz	77
4.12. Frequency spectrum of the pressure tap position $x^* = 275mm, y^* = 14mm$ at $Re_H = 153000, f = 20Hz, MA_{pp} = 1.5mm$	78
4.13. Frequency spectrum of the pressure tap position $x^* = 275mm, y^* = 58mm$ at $Re_H = 153000, f = 20Hz, MA_{pp} = 1.5mm$	78
4.14. Measured net phase angle at $Re = 151000, f = 15Hz,$ and $MA_{pp} = 1.5mm$ as a function of the controlled flap phase angle	79
4.15. Boundary layer velocity profiles at different streamwise and spanwise positions on the step top	81
4.16. Boundary layer yaw angle θ_{yaw} at different streamwise and spanwise positions on the step top	83
4.17. Qualitative illustrations as streamlines of the v^*, w^* velocity component at $Re_H = 176000$ ($u_0 = 5m/s$)	84
4.18. Velocity components of the free rolling up shear layer at $x = 11mm, z = 100mm,$ and $Re_H = 269000$ ($u_0 = 8m/s$)	85
4.19. u z Plot of the computed shear layer velocity profile $u_0(z) = 0.5(1 + \tanh(z))$	87
4.20. Eigenvalue spectrum of the velocity function $u_0(z) = 0.5 * (1 + \tanh(z))$ at $Re = 40$ and $a = 0.4$; comparison to Betchov and Szewczyk [1963]	88
4.21. Maximum imaginary eigenvalue for the two wave numbers a and b at $Re = 100; \omega_{i,max} = 0.0913$ at $a = 0.44$ and $b = 0.34$	89
4.22. Static lift coefficient C_l of the NACA 0018 airfoil at different Reynolds numbers	90
4.23. Static moment coefficient C_m of the NACA 0018 airfoil at different Reynolds numbers .	91
4.24. Pure pitching motion at $Re = 350000$ and $k = 0.068$	92
4.25. Pure pitching motion at $Re = 500000$ and $k = 0.158$	92
4.26. Pure pitching motion at $Re = 350000$ and $k = 0.263$	92
4.27. Prediction of the unsteady lift coefficient at low, moderate, and high reduced frequencies	93
4.28. Comparison of the measured and theoretical lift ratio over the phase angle	94

4.29. Unsteady lift coefficient at a free stream velocity oscillation and at a constant angle of attack	95
4.30. Unsteady leading edge moment coefficient at a free stream velocity oscillation and at a constant angle of attack	95
4.31. Measured unsteady pressure distribution at three different phase angles	96
4.32. Comparison of the measured and theoretical bound vorticity sheet at $\phi = 250^\circ$	97
4.33. Depiction of the unsteady lift ratio during synchronized, simultaneous pitching $\alpha(t) = 2^\circ + 2^\circ \sin(\phi)$ and oscillating free stream $u(t) = u_0(1 + 0.5 \sin(\phi))$	98
4.34. Distribution of the spanwise circulation Γ_{sp} , the streamwise circulation $\Gamma_{st}(z = 0)$ and the tangential velocities $v_\theta(z = 0)$ of the fully developed trailing vortex for a periodic pitch motion at $\alpha(\phi) = 6^\circ + 2^\circ \sin(\phi)$, $u_0 = 40\text{m/s}$ and $f = 0.5\text{Hz}$	101
4.35. Normalised axial velocity in the trailing vortex centre for a periodic pitch motion at $\alpha(\phi) = 6^\circ + 2^\circ \sin(\phi)$, $u_0 = 40\text{m/s}$ and $f = 0.5\text{Hz}$	102
4.36. Normalised centroid meandering of the wing tip vortex due to sinusoidal pitching	103
4.37. Construction of a new actuator with a separated shaft	104
A.1. Photo of the electrical supply and control circuit	129
A.2. General assembly drawing of the three-hole probe	131
A.3. Average probe pressure of the left and right tube; normalised by its maximum value . . .	132
A.4. Calibrated angle coefficient	132
A.5. Photo of the swept, semi-span, backward facing step in the large wind tunnel at the HFI .	135

List of Tables

4.1. Overview of the measurement positions and the corresponding boundary layer parameters	82
4.2. Comparison of the computed phase velocity c with the reference values from Michalke [1964]	86

Nomenclature

latin symbols

symbol	units	denotation
a	[-]	normalised distance from the pitching axis to the mid chord
$a = a_r + ia_i$	[-]	complex wave numbers
a_m	[-]	coefficient of van der Wall's theory
a_ϕ	[-]	wave numbers
$b = b_r + ib_i$	[-]	complex wave numbers in second spatial direction
b	[-]	local shear layer width
b_n	[-]	Fourier coefficients of the wake induced velocities
c	[m]	wing chord
c_n	[-]	linear combination of Fourier coefficients
c_s	[-]	transformation constant
$c = c_r + ic_i$	[-]	complex phase velocity
c	[m]	airfoil/ wing chord length
d_n	[-]	Fourier coefficients of the self induced velocities
e_1	[-]	shear layer velocity profile constant
e_2	[-]	shear layer velocity profile constant
f	[1/s]	frequency
h	[-]	vertical airfoil motion
i	[-]	imaginary unit
k	[-]	reduced frequency
l	[m]	geometric length
l_m	[-]	coefficient of Isaacs' theory
m	[-]	wave number
n	[-]	arbitrary counter
p	[Pa]	static pressure
q	[Pa]	dynamic pressure
r	[m]	radius
r_v	[-]	shear layer velocity ratio
s	[m]	wing span
t	[s]	time
t_m	[-]	coefficient of Isaacs' theory
u	[m/s]	scalar velocity component in x-direction
u_{axial}	[m/s]	axial velocity of the trailing vortex
u^*	[m/s]	scalar velocity component in x^* -direction
u_0	[m/s]	free stream velocity
u_δ	[m/s]	velocity at the height of a boundary layer
\underline{u}	[m/s]	velocity vector including all three components
v	[m/s]	scalar velocity component in y-direction
v_θ	[m/s]	tangential velocity of the trailing vortex
v_ϕ	[m/s]	phase velocity of the actuation in traversal direction
v^*	[m/s]	scalar velocity component in y^* -direction
v_n	[m/s]	normal velocity at the wing chord
w	[m/s]	scalar velocity component in z-direction
w^*	[m/s]	scalar velocity component in z^* -direction
x_0	[m]	distance between geometrical and virtual origin
y_c	[m]	centroid position of the streamwise vortex downstream of a finite wing

symbol	units	denotation
A_m	[-]	coefficient of van der Wall's theory
B	[T]	magnetic flux
C	[-]	Theodorsen function
C_0	[-]	matrices with arbitrary constants
C_1	[-]	matrices with arbitrary constants
C_n	[-]	amplitude function
C_p	[-]	pressure coefficient
D	[-]	derivation matrix at the Gauss-Lobatto sampling points
F	[-]	real part of the Theodorsen function
G	[-]	imaginary part of the Theodorsen function
H	[m]	step height
H_m	[-]	coefficient of van der Wall's theory
H_{mag}	[A/m]	magnetic field
H_{12}	[-]	boundary layer form parameter
I	[A]	electric current
J	[-]	Bessel function of the first kind
L	[N]	lift
N	[-]	total number of sampling points
N_w	[-]	total number of windings
M	[-]	pitching moment
$M(k, m)$	[-]	confluent hypergeometric Kummer function
M_v	[-]	number of merged vortices
Q	[m ² /s]	transformed time varying circulation
R	[m]	fringe radius of a streamwise vortex
R_m	[-]	coefficient of van der Wall's theory
Re	[-]	Reynolds number
S	[-]	bijjective mapping function
S_m	[-]	substitution coefficient
St	[-]	Strouhal number
Tu	[-]	turbulence level
T_n	[-]	Chebyshev polynomial
U	[-]	diagonal matrix containing the basic flow u_s
V	[-]	diagonal matrix containing the basic flow v_s
W	[m]	airfoil travel distance
Y	[-]	Bessel function of the second kind

greek symbols

symbol	units	denotation
α	[°]	angle of attack
γ	[1/s]	vorticity sheet
δ_1	[m]	boundary layer displacement thickness
δ_2	[m]	boundary layer momentum thickness
δ_w	[m]	shear layer thickness
ϵ	[-]	disturbance amplitude
μ	[N/A ²]	magnetic permeability
η	[kg/m/s]	dynamic viscosity
η	[m]	coordinate along the airfoil chord
η_u	[-]	coordinate of the unit interval [-1,1]
θ	[-]	cylinder coordinate along the airfoil chord
θ_{step}	[°]	swept angle of the step
θ_{yaw}	[°]	boundary layer yaw angle
κ	[-]	integral in the numerator of the solved b_n
λ	[-]	shear layer velocity ratio
λ_{osc}	[-]	wavelength of the inflow oscillation
ν	[m ² /s]	kinematic viscosity
ρ	[kg/m ³]	fluid density
σ	[-]	amplitude of the free stream velocity oscillation
τ	[s]	arbitrary time interval
ϕ	[°]	phase angle
ω	[1/s]	angular frequency
$\omega = \omega_r + i\omega_i$	[-]	complex wave frequency
Γ	[m ² /s]	circulation
Δ	[-]	derivation matrix of the mapping function S
Λ	[m]	airfoil travel distance between two instants of time
$\tilde{\Lambda}$	[-]	normalised airfoil travel distance between two instants of time
Θ_m	[A]	magnetomotive force
Θ	[-]	local width of shear layers

indexes

index	denotation
b	bound
$crit$	critical
f	forced
i	imaginary part
j	arbitrary counter
k	arbitrary counter
le	leading edge
n	arbitrary counter
pp	peak-to-peak
qs	quasi steady
ref	reference
res	response
s	steady
sp	spanwise
st	streamwise
sv	streamwise vortex
t	total
r	real part
w	wake
C	cosine part of an oscillation
H	step height
S	closed loop curve line
S	sine part of an oscillation

superscript

index	denotation
\sim	disturbed quantity
$-$	time averaged quantity

operators

index	denotation
\cdot	scalar product
$(\dot{\quad})$	time derivation
$ \dots $	absolute value
Δ	difference
∇	nabla operator
\Im	imaginary part of a complex number
\Re	real part of a complex number

abbreviation

abbreviation	denotation
AC	alternating current
AFC	active flow control
DC	direct current
DNS	direct numerical simulation
HFI	Hermann-Föttinger Institut
ISO	international organisation for standardisation
ISTA	Institut für Strömungsmechanik und Technische Akustik
K-H	Kelvin-Helmholtz
LDV	laser Doppler vibrometer (measuring structural vibrations)
MA	motion amplitude
MAV	micro air vehicle
NACA	National Advisory Committee for Aeronautics
OPV	operational amplifier
PDS	power density spectrum
R	resistor
RMS	root mean square
tanh	hyperbolic tangent
TU	Technische Universität

1. Motivation of circulation control by means of long- and short-wavelength excitation

The total number of passenger airplanes will increase by 107% in the next 20 years [AIRBUS, 2014]. This significant increase in air traffic demands high standards of airplanes in the future. Beside safety requirements, more efficient operation is crucial for airline companies. Already today, hub airports limit the capacity of air traffic. In particular, the waiting time on the runway is the main factor which confines a higher air traffic efficiency [Holzäpfel, 2006]. The occurrence of strong vortices in the wake of airplanes constitutes a hazardous stream for the following plane. A reduction of these hazardous vortices is a research focus to increase hub airport efficiency as well as strengthen the safety in air traffic in the future. Hence, an accurate prediction of the wake flow structures is required.

By 2050, the portion of renewable energy has been forecasted to 60% [Deutscher Bund et al., 2012] in Germany and up to approximately 25% worldwide [Shell, 2008]. In Germany, wind energy will be the main source of renewable energy. The expansion of wind energy parks and the current idea of urban energy production provoke resistance from local residents who are disturbed by this form of energy production. The emission of noise is the main reason. On the one hand, measurements show that almost all broadband noise is emitted at the 10 to 20% outer part of the wings [Wagner et al., 1996]. On the other hand, the physics of sound generation under unsteady conditions is not fully understood. This limitation makes noise control difficult. It is generally known that wing tip vortices and their interactions with the wake are the main sources of noise. Thus, to make wind energy more silent and efficient, a deeper understanding of the spanwise loading and the trailing vortex is required.

In helicopter aerodynamics, accurate prediction and control of unsteady blade loads, blade vibrations, and obtrusive rotor noise is still the main focus of research. The main source for these undesirable aspects is the presence of strong vortices emitted at the tip of each blade and their interaction with the wake. Although all aspects are investigated and understood individually, in detail, the strong interaction among the several aspects renders an exact prediction impossible [Leishman and Bagai, 1998]. Therefore, the prediction of the effect of the tip vortex on the wings is crucial for increasing safety, especially under unsteady flight conditions.

All mentioned applications possess the same basic flow characteristics as shown in figure 1.1. Here, a DeHavilland Beaver DHC-2 is shown (black lines). The wing generates the required lift and the corresponding spanwise circulation distribution is illustrated in yellow. At the wing tip, the circulation is zero because no pressure difference exists at this point. Around the mid-span, the circulation reaches its maximum. Although the wing is rectangular, the circulation distribution is nonlinear due to the pressure equalisation at the wing tip. This pressure equalisation has two consequences. The first one is that the fluid tries to flow from the pressure side to the suction side in form of a local crossflow. At the wing tip, the fluid is not able to follow the geometry anymore and separates (green arrows). The spatial direction of the separation does not coincide with the free stream (blue arrows) and a rolling up shear layer is generated. Thus, the wing tip region and the rolling up shear layer is the origin of a streamwise vortex. At this point, short-wavelength actuation forces instabilities in the shear layer and controls the amount of vorticity which convects into the vortex core. The accumulated vorticity feeds the circulation and finally influences the vortex strength. Furthermore, this streamwise vortex produces an up-wind out of the wing. The second consequence is that the lift generation causes a down-wind in the wake of the wing. Directly downstream of the wing, this unequal distributed velocity field induces velocities on each other and the roll up process which is initiated at the wing tip continues and strengthens (red lines). As the downstream distance increases, the vorticity sheet and the streamwise vortex at the wing tip is becoming increasingly compact and finally, one strong trailing vortex evolves. This interaction of the spanwise loading on a finite wing with the resulting circulation of the trailing vortex is quantified by Betz's theory for steady

1. Motivation of circulation control by means of long- and short-wavelength excitation

conditions [Betz, 1932]. This theory determines the trailing vortex strength and position based on the spanwise circulation distribution. The relation enables the opportunity of long-wavelength actuation. A time varying spanwise circulation distribution produces variable trailing vortex strengths and positions which promote a faster trailing vortex bursting. The long-wavelength actuation itself is produced, for example, by means of pitching motions, an unsteady free stream, or vertical wing motions.

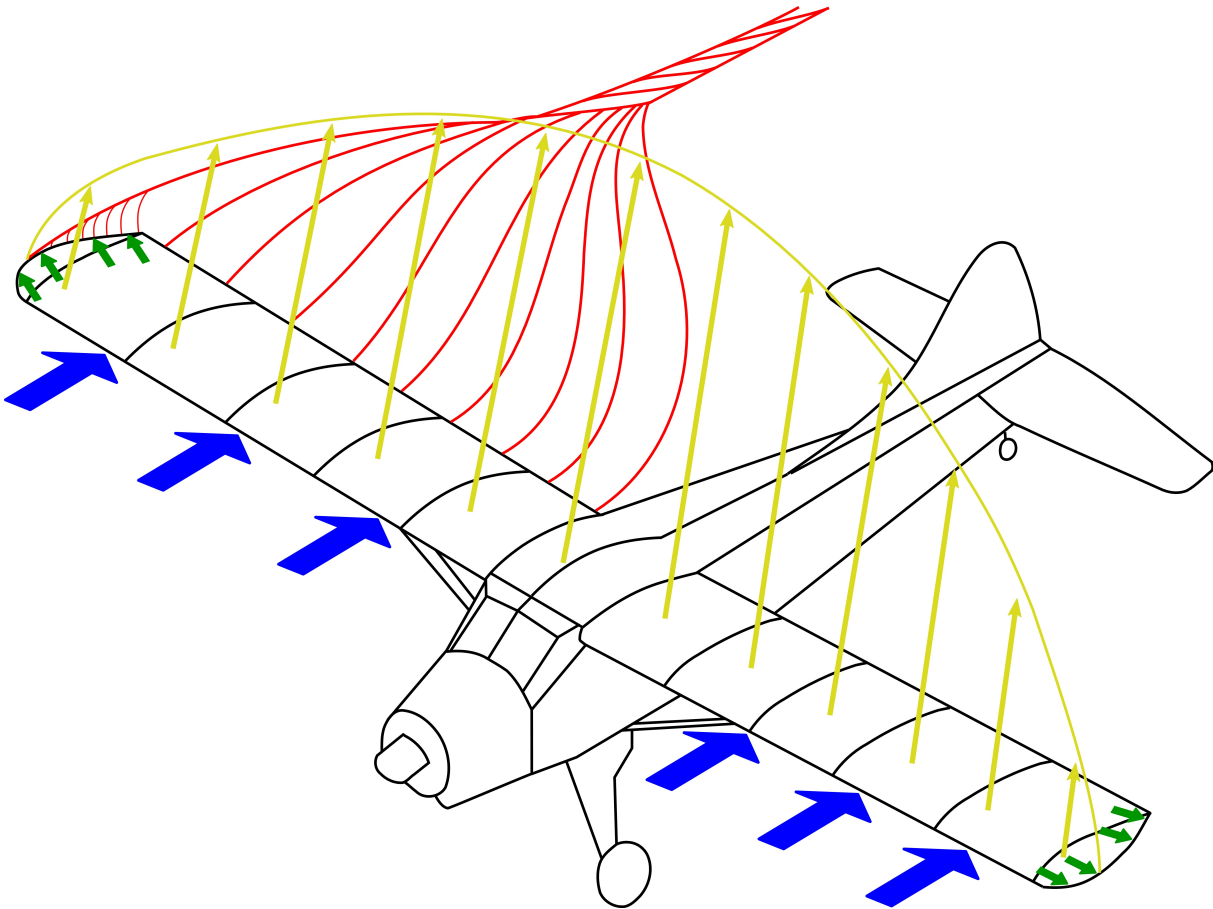


Figure 1.1.: Sketch of a DeHavilland Beaver DHC-2 with the loading along the span (yellow line normal to the wing); the flow at the wing tip separates (green lines) and initiates the trailing vortex; the vorticity sheet emitted at the trailing edge rolls up into one streamwise vortex orientating in downstream direction (red lines)

The flow topology depicted by an airplane is similar to that of the finite wings of helicopter rotor blades and of horizontal and vertical wind turbines. Horizontal wind turbines operate in the earth boundary layer, thus the inflow velocity oscillates due to the vertical position of the blade. Accordingly, the effective total velocity at the leading edge oscillates as well and an unsteady lift is produced. Furthermore, the pitching mechanism tries to compensate the various inflow via an oscillating angle of attack. Gusts, tower passing, or yaw misalignment significantly increase the unsteady effects. Vertical axis wind turbines face much larger free stream velocities and angle of attack oscillations. Thus, the flow is highly unsteady during one revolution. Helicopter blades in fast forward flight encounter strong free stream velocity variations as well. To understand the resulting forces and the nonlinear lift response better, the predictions have to take into account all these unsteady phenomena and the interactions between the rolling up shear layer at the wing tip, the spanwise circulation distribution, and the trailing vortex.

Holzäpfel [2014] investigates the influence of several meteorological and aircraft parameters on the wake vortex behaviour. He summarises that only six of them are important: wind, thermal stratification, turbulence, position, mass, and spanwise load factor. Considering an already existing aircraft flying on a predefined flight path, only the latter parameter may be influenced. Consequently, long- and short-wavelength excitations are important for active wake and trailing vortex control. This thesis follows the

distinction of Williamson et al. [1998]. They find short-wavelength instabilities as well as long-wavelength instabilities in the wake of finite wings and downstream of delta wings. Short-wavelength actuation directly controls the streamwise vortex at its origin and thus modifies the initial vortex strength and position at the wing tip. The long-wavelength actuation has a more global effect on the trailing vortex. It influences the strength and position and promotes a fast trailing vortex bursting.

1.1. Short-wavelength excitation of trailing vortices

Free streamwise vortices represent highly rotational flows. They possess a distinct starting point where the vortex starts to form. These vortices do not require any boundary. In some applications, they evolve as free trailing vortices while in other applications they are surrounded by at least one solid wall. They possess high tangential and axial velocity components. The vortex radius increases along the vortex axis due to vortex diffusion. The vortex centre behaves like a solid body caused by the dominance of viscous forces. In the far field, the velocity profile may be approximated by potential vortices. Streamwise vortices disappear in time due to diffusion and dissipation. Some free vortex cases are discussed in the following paragraphs and illustrated in figure 1.2. It is worth to mention that the flow structures are very similar to each other although the corresponding geometries vary considerably. This similarity yields an analogy of all the discussed free vortices. This leads to one general, generic geometry introduced as a swept, semi-span, backward facing step to model streamwise vortices.

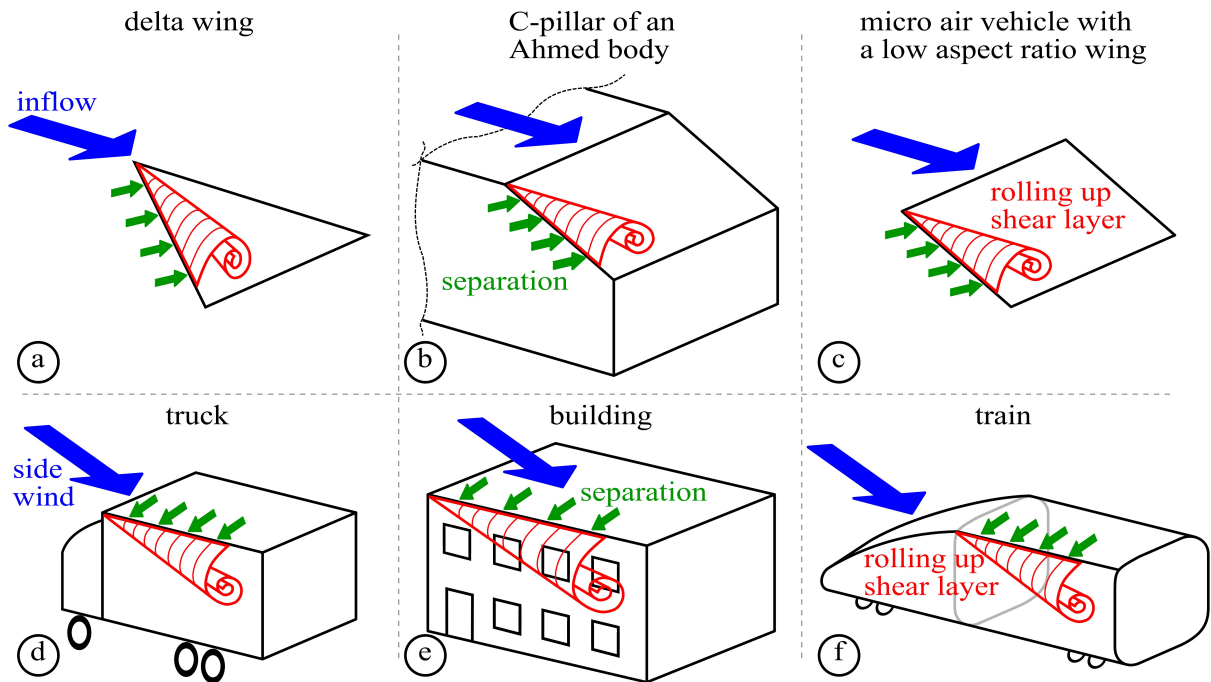


Figure 1.2.: Six occurrences of streamwise vortices (red lines) in technical applications; the flow separation (green lines) is tilted to the free stream (blue arrow) and a rolling up shear layer is generated

Figures 1.2a-f depict six examples of streamwise vortices which are discussed consecutively. Delta wings (figure 1.2a), also known as vortex generators, produce two strong vortices on the suction side. These vortices possess a high circulation and cause a strong low pressure region. This phenomenon is called the vortex extra lift and is known since at least 1867 when Butler and Edwards [1867] submit a patent for a flying machine based on the delta wing geometry. Today, small scale delta wings are commonly used as vortex generators for passive flow control to prevent flow separation and large scale delta wings are directly used as wing profiles (e.g. the *Concorde*). The analogy between trailing vortex pairs of finite wings and leading edge vortices on delta wings is experimentally proven by Williamson et al. [1998]. Furthermore, they show that both flow structures possess the same long- and short-wavelength instabilities. At the Ahmed body (figure 1.2b), strong vortices arise at the C-pillar and increase the drag significantly by

1. Motivation of circulation control by means of long- and short-wavelength excitation

up to 25% [Hucho, 2005]. The automotive manufacturers are concerned about these strong flow structures and try to minimise their negative influences during the design process. According to the prediction by Shell Deutschland Oil GmbH [2009], the total number of cars on earth will double (compared to 2010) to more than two billion by 2030. A better understanding of these vortices and the possibility to control them on realistic cars will save petrol consumption and carbon dioxide emissions [Cheng et al., 2011]. Micro air vehicles have gained focus in recent years. Figure 1.2c illustrates one of the simplest geometries. A flat plate with a low aspect ratio is used as a wing. It is a hybrid of the delta wing and the slant of an Ahmed body. The manipulation of the streamwise vortices at the wing tip enables the lift and roll moment control without additional flaps [Taira and Colonius, 2009b]. The development of civil micro air vehicles is actually being pushed by companies like *Amazon*, *Google*, *Deutsche Post*, etc., which opens up commercial opportunities for a profitable market [Frankfurter Allgemeine Tageszeitung, 2014.08.29]. A stable and reliable flight is a key parameter for certification.

Today's logistics also runs on trucks which are again affected by side wind, as shown in figure 1.2d. A streamwise vortex on the leeward side causes strong low pressure on the side. This phenomenon affects the side force and the roll moment dramatically. In the worst case, the truck loses stability and this may result in a fatal accident. In the more than 3000 accidents in Germany in 2013 with the involvement of heavy trucks, environmental influences are noted to be involved [Statistisches Bundesamt, 2013]. Improved control authority on these vortices will save lives and costs. Lightweight automobiles (i.e. less than 400kg) with futuristic powertrains face the same problem. During fast cornering or side wind, streamwise vortices occur at the fenders, the A- and C-pillar and compromise the stability [Wojciak et al., 2011], [Tsubokura et al., 2012]. Large containerships, or more precisely their loads, are affected by strong forces due to vortices in their vicinity. In 2000, more than 2400 containers are lost and more than 3400 are damaged on open sea due to storms and rough sea conditions [Gabrysch, 2006].

Wind loads are also one of the main challenges for buildings [Cook, 1985], [Simiu and Scanlan, 1996]. In side wind situations, the leeward vortex generates a strong upwind flow close to the roof as illustrated in figure 1.2e. It may locally damage the building facade. For instance, in Germany in 2007, a steel beam weighing two tons rips out from the facade of the newly opened *Berliner Hauptbahnhof* during a hurricane [Nassoufis and Rabenstein, 2007.01.19]. The last example illustrated is a train in side wind situation in figure 1.2f. The strong side force and roll moment lead to a tilt of the train around the leeward wheel. In the worst case, the entire train rolls over. During a hurricane in Switzerland in 2007, two wagons of a passenger train turn over completely and land approximately 8 meters away from the rails on a public road [Feuerwehr-Schweiz, 2007.01.25]. High speed and double-decker trains are especially endangered and side wind stability is for long one of the main parameters in the certification tests [TSI HS RST, 2008], [EN 14067-6, 2010].

The finite wing in figure 1.1 generates a strong streamwise vortex as well. The origin of this flow structure is the wing tip due to the misalignment between the separation line and the inflow direction. In the case of a finite wing, the rolling up shear layer at the wing tip interacts with the trailing edge vorticity sheet. This interaction may increase loads especially under unsteady conditions on wind turbines and helicopter blades. Furthermore, this interaction is the main cause of broadband noise.

Streamwise vortices appear in all these different applications and are based on the same mechanism. Firstly, the flow is attached on the object or the object is subjected to a parallel inflow. The flow tries to follow the object shape until a geometry or pressure induced separation occurs. The flow separates and a free shear layer emerges. This shear layer does not convect straight as it does in the case of a two-dimensional flow. Instead, it is tilted downstream of the separation line and a roll up process starts due to a parallel pressure gradient or entrainment from the other side. Based on the mass balance, the flow has to tilt in the direction of the free stream and thereby convects downstream. In Hammas' words: "*The reason that the vortices are conical has to do with the edges having an angle against the direction of the flow, i.e. the separation does not occur in the same direction as the flow travels, which gives the conical shape*" [Hammas et al., 2010]. In fact, this misalignment between the flow direction and the separation line leads to the occurrence of streamwise vortices in the cases discussed here.

Although the mechanism of rolling up shear layer is essential in many applications, only a few studies look into the details of it. Only in the field of delta wings [Margalit et al., 2005] and micro air vehicles

[Taira and Colonius, 2009a], [Vey, 2014] is the tilted rolling up shear layer considered and investigated as the key to controlling the generated vortices. The lack of knowledge probably exists because streamwise vortices are considered as stable. A modification of their strength is possible, but a complete elimination is not realistic. Thus, the benefit may be regarded as minor because the global flow topology will not change. A second reason is that other effects dominate the global flow field. At realistic cars for instance, the flow separates at the roof and also at the base. All separated flows merge into one wake. Depending on the geometrical dimensions, the streamwise vortices are less important regarding the overall drag. A third reason is the interaction with other parameters. Ground clearance, side flows, two-dimensional separation bubbles in the vicinity, and Reynolds number effects on convex shapes (e.g. the train head) render an isolated investigation of streamwise vortices impossible.

In order to reduce the lack of investigations mentioned, a generic model design in analogy to the cases shown in the figures 1.1 and 1.2 is proposed. Its shape should perform a geometry induced separation to reduce Reynolds number effects. This request excludes concave geometries like trains or round notch backs. Other influences like underflow, side flow, or a high sensitivity to free stream misalignment have to be avoided as well, as in the case for trucks and the Ahmed body. The last requirement is to provide enough space inside the model to install measurement techniques and a sufficient active flow control system. This renders the use of a delta wing, a flat plate, or a thin finite wing unsuitable. Hence, a swept, semi-span, backward facing step is examined in this thesis and illustrated in figure 1.3. This generic model can be regarded as a half Ahmed body without a base and is directly mounted on the floor or as a flat plate elongated in the direction of the free stream. The separation line is fixed by the geometry and all edges are sharp to avoid any kind of Reynolds number effects. No underflow or side flow interacts with the wake due to the solid boundaries. This step contains enough space for different AFC systems. The tilting of the separated flow to the inflow is obvious and a streamwise vortex emitted by a rolling up shear layer is clearly observable.

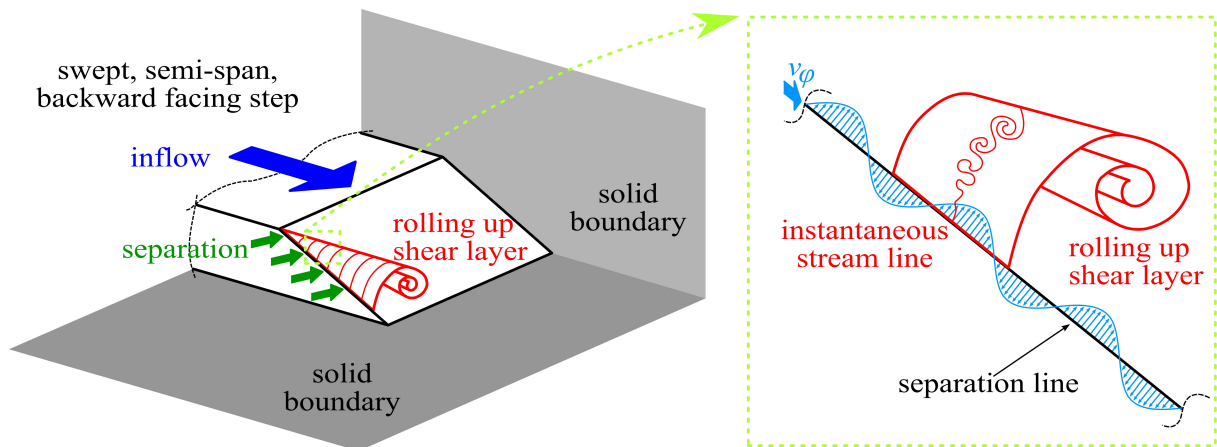


Figure 1.3.: Left: sketch of a swept, semi-span, backward facing step surrounded by a fixed floor and fixed side wall; right: detailed sketch of an arbitrary part of the vortex; one instantaneous stream line is added (thin red line); active flow control along the separation line is indicated by a sinusoidal signal (light blue lines) including a phase velocity v_φ

On the right hand side of figure 1.3, an arbitrary part of the vortex is highlighted. A piece of the stable, time averaged streamwise vortex is drawn. For the flow physics, described in the following, it is of minor interest whether this streamwise vortex is a free trailing vortex, or in the vicinity of a solid wall. However, one instantaneous stream line is added. This stream line separates directly at the trailing edge and convects straight into the tilted shear layer. Due to small disturbances, this stream line does not remain straight and starts to oscillate. The resulting instability increases its amplitude and the fluctuations become larger. This so called Kelvin-Helmholtz instability causes a vortex sheet. The vorticity produced during this process convects inside the vortex core and feeds the circulation. This circulation feeding occurs along the entire trailing edge. Thus, the vortex becomes increasingly stronger along its axis.

The main focus of the experimental part is circulation control. By means of manipulating the K-H

1. Motivation of circulation control by means of long- and short-wavelength excitation

instabilities directly at the trailing edge, the vorticity produced by the emitted vortex sheet is modified. This modified vorticity still convects into the vortex core and, finally, affects the entire circulation of this streamwise vortex. The amplification or damping of the K-H instabilities is achieved by small external disturbances at the trailing edge (marked in light blue in figure 1.3). Jürgens [2006] already shows at a swept, infinite, backward facing step that the most efficient direction of actuation is not necessarily the direction of the inflow or that of the trailing edge. Rather, the optimal direction is estimated between the inflow and the trailing edge. To take this finding into account, the external perturbation signal possesses a phase velocity v_φ and allows an actuation in all downstream directions. This experimental approach is supported by temporal and spatial stability analysis based on measured velocity profiles. This theory predicts the desired frequencies and directions of actuation for an optimal circulation control of streamwise vortices.

1.2. Long-wavelength excitation of trailing vortices

Bound vortices are not directly observable. They are more of a theoretical construct in the field of potential flow. Hence, no diffusion or dissipation exist and the vortices persist forever. Bound vortices have fixed positions and do not possess any convection velocity. They represent a closed-curve or an infinite long vortex tube. An arbitrary geometry may be modulated in potential flow by means of a sheet of bound vortices. The strength of each bound vortex is adjusted to fulfil the constraint that no flow normal to the geometry exists. The concept of bound vortices shows a high accuracy in several applications. Thus, this theory is widely used for more than a century and remains as a powerful tool for many problems in fluid mechanics until today.

In 1906, Kutta [1902] and Joukowski [1906] reveal the proportionality between the circulation generated by an airfoil and the lift it achieves. The relation is expressed by means of the Kutta-Joukowski equation. This theory predicts the lift and the pitching moment produced by the circulation of the bound vortex which imitates the airfoil shape. Under steady conditions, the circulation may be varied only via a modification of the geometry. Under unsteady conditions due to pitching, unsteady free stream, or vertical airfoil motion, the circulation varies significantly in time. At medium oscillating free stream amplitudes or at high reduced frequencies, the circulation variation reaches 50% and more. In the 1930s and 40s, Theodorsen, Isaacs and Greenberg develop theoretical models to predict these unsteady variations.

Today, wind turbines operate in highly unsteady flow regimes. Horizontal axis wind turbines face several unsteady effects during one rotor rotation. Tower passing, yaw misalignment, variable free stream velocity due to the earth boundary layer, all occur during each rotation and increase the fatigue loads and reduce the life time. Vertical axis wind turbines are subjected to high free stream oscillations and angle of attack variations. These unsteady effects drastically increase the fatigue loads and, therefore, the cost of energy production. Helicopter blades in fast forward flight also experience an oscillating free stream during one rotation. The increased lift on one side and the decreased lift on the other side lead to an imbalance which is compensated by a complex and expensive pitching mechanism. All applications mentioned above encounter high unsteadiness, although the flow stays attached during the entire revolution.

All these phenomena are widely known. Surprisingly, almost nobody is taking them into account although the theories exist for more than 75 years. In the field of horizontal axis wind turbines, these effects are generally neglected. The focus lies more on aperiodic events like inflow turbulence and small scale gusts. In these cases, the wavelength of the disturbance is in the order of the chord length [Pechlivanoglou, 2013]. These effects certainly produce strong local, undesired forces and vibrations. Nevertheless, large scale oscillations with wavelengths of one or two magnitudes longer than the chord length arise from yaw misalignment and the sheared inflow. This large scale unsteadiness also induces fatigue loads, vibrations and reduce the lift time [Leishman, 2002]. Further continued neglect of these large scale phenomena will provoke additional costs in the future, especially for Germany. The German "Energiewende" is based mainly on wind energy. In 2011, already up to 8% of the energy produced is wind energy [Pfaffel et al., 2012]. It will increase up to 18% by 2020 and to 60% by 2050 [Deutscher Bund et al., 2012]. Hence, this tiny detail of an improved circulation prediction caused by large scale unsteadiness may yield a national economic benefit.

Vertical axis wind turbines represent a fairly small part of the global energy mix. However, they are gaining focus during the last decade for urban and local energy production. These wind turbines are exposed to even higher unsteady effects although they operate under optimal conditions. At low wing tip speed ratios, the velocity amplitude exceeds 50% and the angle of attack variation amounts to more than $\pm 30^\circ$. Thus, the unsteady effects occupy a crucial role on the fatigue loads and the total energy costs. Manufacturers take into account the load oscillations by means of increased safety factors but an appropriate circulation control has not yet been considered. Only few academic feasibility studies exist [Müller-Vahl et al., 2014a], [Müller-Vahl et al., 2014b].

Helicopter blades in forward flight also encounter an oscillating inflow during one revolution. Besides unsteady inflow and blade pitching, a fast vertical airfoil motion is the third source of large scale unsteadiness. Only in the helicopter research field efforts are seriously undertaken to develop a better circulation prediction. In the early 90s, van der Wall and Leishman extend Isaacs theory and perform several theoretical parameter studies [van der Wall and Leishman, 1992]. They state that no experiments exist which are able to confirm the theoretical findings and claim more research in this field. Although van der Wall highly contributes to a better understanding of unsteady airfoil circulation, his extended theory allows only the prediction of global quantities like lift and pitching moment. The prediction of the pressure distribution along the chord is crucial for a more detailed understanding and for efficient control strategies. Most recently, a new wind tunnel is built which is designed as an unsteady wind tunnel from the beginning [Furman et al., 2013]. This wind tunnel allows for the first time a validation of the 75 year-old theories at medium and high reduced frequencies and velocity amplitudes [Müller-Vahl et al., 2015]. In combination with the experimental validation, van der Wall's general theory is extended to predict the unsteady pressure distribution during an oscillating inflow [Strangfeld et al., 2014].

The theory from Theodorsen, Isaacs and Greenberg exist for more than 75 years. As mentioned earlier, almost no research is conducted in the field of airfoils including unsteady attached flow. On the one hand, the lack of experiments is probably due to the lack of appropriate wind tunnels. Most unsteady wind tunnels are originally designed as steady wind tunnels and are modified later to enable unsteady investigations. In most cases, this inadequate design facilitates only weak unsteady effects. On the other hand, existing appropriate test facilities investigate mostly separation and detached phenomena like dynamic stall in unsteady flow regimes [Favier et al., 1988]. Measurement techniques like time resolved pressure sensors or balances are developed in the recent decades. Thus, techniques to quantify the unsteadiness are much newer compared to the original theory. Numerical simulations are very complex and require a lot of resources. Due to the pitching motion, the grid is adjusted at each time step. The setup of the boundary conditions is tricky considering the unsteady inflow. Additionally, the grid has to be very fine in the wake of the wing to capture the unsteady wake vortex sheet without smearing effects. These requirements demand high numerical effort even for just one parameter combination. Another possible reason for the lack of investigations is that these old theories may be simply forgotten in the field of modern research. The generation of computer-based semi-empirical results (e.g. panel codes) is more comfortable than the derivation of analytical solutions. However, due to its significantly increased importance especially in the field of wind turbines, a better understanding of unsteady circulation behaviour is essential. An exact and reliable prediction is the first step towards proper circulation control. Hence, pitching airfoils facing unsteady inflow are investigated experimentally and theoretically in this thesis.

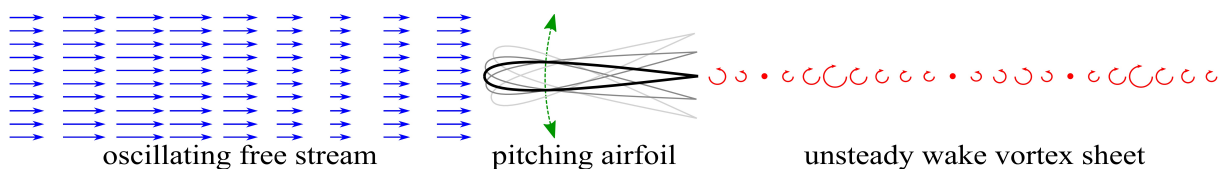


Figure 1.4.: Sketch of a pitching airfoil in an oscillating free stream which generates an unsteady wake vortex sheet

Figure 1.4 depicts a sketch of the chosen setup. A symmetrical airfoil, a NACA 0018 (black line), is pitching periodically around the quarter chord position (green arrow). The airfoil may move to all positive

1. Motivation of circulation control by means of long- and short-wavelength excitation

and negative pre-stall angles of attack. Moreover, the airfoil is treated by an unsteady free stream. The length of the blue arrows outlines the time varying velocity amplitude. The frequencies of these two oscillations are identical and the phase shifts are arbitrary. Caused by these two unsteady effects (unsteady inflow, wing motion), the lift and the proportional circulation of the bound vortex vary in time. The entire circulation in the global system has to remain constant. Thus, a circulation change of arbitrary strength at one time step requires the shedding of a vortex into the wake with opposite strength at this time step (red arrows in the wake). This mechanism ensures a constant circulation. The shed wake vorticity induces normal velocities on the airfoil which are adapted by a further circulation change. Thus, the wake contributes to the lift generated. The higher the velocity amplitudes or the reduced frequencies, the larger the influence of the wake vorticity. This setup is investigated experimentally, including measurements of the lift and pressure distributions. van der Wall's theory is extended for periodical pitching motion and unsteady inflow to confirm the experimental findings. A closed-form analytical solution of the unsteady lift and unsteady pressure distribution is derived in this thesis. This gives an exact prediction of the oscillating circulation. Based on these new findings, a proper circulation control will reduce the fatigue loads, increase the lifetime and contribute to a cheaper sustainable energy production.

1.3. Interaction of the trailing edge vorticity sheet and the wing tip vortex

As shown for a finite wing in figure 1.1, the trailing vortex is influenced by the initial conditions of the streamwise vortex at the wing tip and the spanwise circulation distribution. Therefore, both aspects have to be considered for an optimal actuation [Williamson et al., 1998]. The short-wavelength actuation excites the rolling up shear layer and the streamwise vortex at its origin. It controls the vortex strength and position and thus changes the pressure field. On the one hand, the local actuation possesses an impact on the local pressure field. The interaction of the wing tip vortex and the spanwise circulation at the outer part of the wing is the main source of broadband noise. Thus, active noise reduction requires a deeper understanding of the pressure field interaction of these two vortical structures. On the other hand, the short-wavelength actuation forces the rolling up shear layer and controls the initial conditions of the trailing vortex.

Betz's theory is used for determining the long-wavelength actuation. It reveals for the steady case that the streamwise circulation of the wing tip vortex is equal to the spanwise circulation at mid-span. This theory predicts the centroid position of spanwise vorticity sheet as well. The centroid position of the wake is identical to the vortex centre of the streamwise vortex tube. In the field of wind turbines and helicopters, the spanwise circulation distribution becomes unsteady due to an oscillating inflow and the angle of attack variations. Thus, the interaction between the two flow structures has to be modulated unsteady as well. Therefore, Betz's theory is extended to time varying circulation distributions. The corresponding streamwise circulation distribution and the vortex centre position are calculated. The trailing vortex reacts sensitively to these changes and the centroid position of the wake is not fixed, as is the case under steady conditions. The resultant meandering vortex centre produces a spiral vortex tube instead of a straight one. This probably promotes a fast trailing vortex bursting in the wake of a finite wing.

The inverse Betz's method enables the computation of the spanwise circulation distribution due to a modified wing tip vortex. Following this approach, the short-wavelength actuation controls the spanwise loads as well because the streamwise and spanwise circulations have to be balanced. Thus, this local device may be used as spanwise load control to reduce the effects of gusts. The modified wing tip vortex and the gust affect the spanwise circulation distribution. This again manipulates the resulting trailing vortex in the wake. Consequently, the initial conditions of the streamwise vortex have to be readjusted by means of the mentioned transversal actuation. Therefore, the idea of a highly dynamic system between short- and long-wavelength control arises which is linked by streamwise and spanwise circulations. This concept may be used to control the loads and the resulting bending moment on wind turbines. An excitation of the shear will also change the acoustic field and may reduce noise emissions. In addition, a reduction of structural vibration [Wong et al., 2000] or an increase in the aeroelastic damping are additional parameters which are controllable. Coming back to figure 1.1, a sensible combination of short- and long-wavelength actuation reduces the adverse effects of trailing vortices and increases the air traffic security significantly.

2. Literature review and theoretical approaches

In the first section of this literature review, streamwise vortices and K-H instabilities in shear layers are discussed. The short-wavelength actuation focuses on these K-H instabilities and the forced rolling up shear layer sets the initial condition of the trailing vortex. Thus, the analogy between simple plain two-dimensional shear layers and rolling up shear layer is explained in detail. It begins with the two-dimensional shear layer and the corresponding flow mechanics. The essential findings regarding the AFC of two-dimensional shear layers are transferred to 2.5-dimensional and three-dimensional shear layers. The resulting effects and the connection to the circulation control of streamwise vortices is considered at the end of the first section. The second section outlines a brief introduction into the theoretical operation principles of the actuators. The proposed new concept with segmented actuation, including the control of frequency and phase, is an essential part of this thesis. This developed AFC system manipulates the streamwise vortex at its origin directly. The third section motivates the theoretical prediction of instabilities in skewed shear layers by means of linear stability analysis. The fourth section considers the theoretical concept of bound vortices in a historical perspective. The steady solutions provide the basis of circulation control in unsteady flow. The fifth section depicts the existing approaches of Theodorsen, Isaacs, Greenberg and van der Wall to predict the unsteady bound circulation. The governing equations are presented and explained to perform the required theoretical fundamentals to extend these theories. Based on these equations, one is able to calculate the spanwise circulation distribution on a finite wing under unsteady conditions. This is the key to use Betz's theory for computing the strength and position of the unsteady streamwise wing tip vortex. Thus, the theory of Betz and further approaches which consider wing tip vortices are briefly summarised in the final section.

2.1. Free vortices and Kelvin-Helmholtz instabilities

Intermediate conclusion: K-H instabilities are a crucial feature of rolling up shear layers. As a first step, several definitions of simple two-dimensional shear layers and the origin of these instabilities are described. In a second step, reattaching shear layers downstream of a straight, backward facing step are discussed. The existence of a connected recirculation zone and the gentle curvature of the shear layer yield a more realistic comparison to rolling up shear layers. Next, 2.5-dimensional shear layers downstream of a swept, infinite, backward facing step are reviewed. This geometry generates a tilt of the shear layer which is a further feature of rolling up shear layers. In a final step, complete three-dimensional rolling up shear layers are discussed. In particular, the flow structures on delta wings are similar to the observed flow field in this thesis. For different kind of shear layers, the control strategies of K-H instabilities and the existing techniques of active flow control are summarised.

In the field of fluid mechanics, it is hard to find applications without any kind of shear layer. In general, shear layers describe the transition region of a parameter which is globally unequally distributed in a continuum. These are, for example, temperature gradients, density stratifications, concentration differences, multi-phase flow, velocity variations, etc. All these phenomenons automatically yield shear layers in the fluid. This thesis considers only velocity gradients in an incompressible single fluid at low Mach numbers. All other material parameters are assumed to stay constant and homogeneously distributed. The simple case is a free two-dimensional shear layer. A main feature of these shear layers is the occurrence of K-H instabilities. This phenomenon and its control are discussed in detail initially. Based on this, two-dimensional reattaching shear layers downstream of a backward facing step are considered. They possess a steady vortex in the recirculation zone. The interaction between K-H instabilities and the wake is described. Then, 2.5-dimensional shear layers downstream of a swept, backward facing step and

2. Literature review and theoretical approaches

their control are considered. The focus lies especially on the work of Spieweg, Kaltenbach and Jürgens. In a final step, three-dimensional shear layer and the generated streamwise vortices are outlined. Several applications like delta wings or the Ahmed body are facing this kind of flow structure. The corresponding investigations provide the basis for comparison with the flow field generated by the new introduced swept, semi-span, backward facing step. The tip of a finite wing tends towards zero, thus the implementation of AFC devices is complex or impossible. The step model is considered to be the best alternative. It avoids the influence of several ambient parameters and the generated flow structure is similar to the streamwise vortices downstream of a wing.

2.1.1. Two-dimensional free shear layers, their definitions and the inherent Kelvin-Helmholtz instability

Already in the 1850s, it is known that acoustic actuation of shear layer yields wavelike perturbations. Hence, the concept of AFC on shear layer is known for more than 150 years [Leconte, 1858], [Tyndall, 1867]. Around the 1870s, von Helmholtz [1868] and Kelvin [1871] investigate experimentally two streaming fluids of different densities. They observe instabilities at arbitrary speed and density ratio. This discovered instability is called the Kelvin-Helmholtz instability. It also occurs in a single fluid which is facing velocity shear. In the early 1900s, Prandtl uses his newly designed water tunnel to visualise and investigate free shear layers. This gives the first qualitative impressions of the flow structures in a free shear layer [Prandtl, 1904]. In 1947, Liepmann and Laufer [1947] are one of the first who investigate experimentally laminar and turbulent shear layers by means of quantitative methods, in this case using a hotwire. Their work is the most holistic one for almost two decades. They prove that the flow in a laminar and turbulent mixing layer is self-preserving. Furthermore, by measuring the fluctuations in a turbulent shear layer, they show that the mixing length and the exchange coefficient vary across the mixing region. Hence, they disprove Tollmien's and Prandtl-Görtler's theories which assume a constant mixing length [Tollmien, 1945]. In their conclusion, they claim that theories which consider only time averaged quantities are inaccurate for describing the physics of turbulent flow. Rather, time dependent fluctuations and terms of higher order like the Reynolds stresses are an inherent part of turbulence and play a crucial roll in mixing. One year later, Schubauer and Skramstad [1948] investigate a free shear layer by means of a hotwire. They observe oscillating velocity profiles at different downstream positions. They relate mistakenly this phenomenon to vibrating ribbons in the boundary layer or vibrations emitted by the wind tunnel. However, it is probably the first experimental confirmation of K-H instabilities.

Chapman et al. [1958] are probably the first who classify the three types of shear layers: laminar, transitional, and turbulent shear layers. In the first case, the inflow and the boundary layer are laminar. The shear layer is laminar itself and remains laminar until it disappears due to diffusion or reattachment. The turbulent case is the opposite. Here, the upstream boundary layer is already turbulent and the emitted shear layer as well. In the transitional case, the boundary layer and the beginning of the emitted shear layer are laminar. Further downstream, the instabilities in the shear layer get amplified and transition to turbulence occurs. This classification is used for free, reattaching and 2.5-dimensional shear layers. In the case of streamwise vortices generated by a three-dimensional rolling-up shear layer, this concept is sometimes used as well.

In the mid 1960s, Michalke [1964] starts to investigate shear layers from an instability analysis point of view. He assumes a hyperbolic-tangent velocity profile and computes a temporal stability analysis. Furthermore, he investigates an excited shear flow as well. He finds two concentrations of vorticity in the amplified shear layer. This is the first theoretical description of the vortex pairing process although he does not use this term at that point. Michalke [1965] performs a spatial stability analysis of the natural and excited flow as well. He finds discrete vorticity amalgamations and relates these phenomena to regions of high dye or smoke concentrations in experimental flow visualisations. In 1966, Browand [1966] finds the occurrence of subharmonics in free shear layers. He relates these frequencies erroneously to a transition process of the laminar shear layer. At that time, no thoughts about coherent structures or harmonic behaviour of turbulent flow exist. However, he is probably the first who records frequencies and subharmonics which are directly linked to the vortex pairing process. Based on Liepmann's work, Wagnanski and Fiedler [1970] repeat the experiments performed and try to quantify fluctuations to the

fourth order. Furthermore, by means of lateral and longitudinal correlations of different simultaneously recorded hotwire signals in a turbulent shear layer, they present intermittency measurements. They show self-preservation of the mixing layer in the entire considered downstream region which is consistent with Liepmann's measurements, although the growth rate itself differs by about 30%. Moreover, they find first indications for oscillations in the mixing layer because the turbulence does not generate constant mean shear. However, thoughts about coherent structures in turbulent flows still remain unnoticed. Miksad [1972] separates the transition process in five different stages which are consistent with linear stability theory. Furthermore, he excites a laminar shear layer by means of sound. The acoustic waves amplify the K-H instabilities and accelerate flow transition. In 1974, Winant and Browand [1974] visualise laminar and turbulent shear layers at moderate Reynolds numbers in a water tunnel. Large scale structures in the shear layer are evident and they relate the mixing layer growth to the vortex pairing process. They speculate that these large scale coherent structures exist at higher Reynolds number as well. In the same year, Brown and Roshko [1974] investigate fluids of different densities. They define the spread rate as a quantity to describe the shear layer growing. It is the derivation of the maximum velocity profile thickness δ_w in streamwise direction and is depicted in equation 2.7. They find that each mixing layer spreads linearly and independent of the density or velocity ratio, see equation 2.2. The even more important result bases on flow visualisations of a turbulent shear layer. Large regular coherent structures are evident and they use the word "astonishing" to describe this new finding. The existence of coherent structures in turbulent flow is a big surprise for the fluid dynamics community at that time. Based on these observations they compute the trajectory of the vortices and prove that the so called amalgamation events are caused by the vortex pairing process. The work of Brown and Roshko [1974] is a milestone in the field of turbulent flow. Before this work, turbulent flow is seen as totally chaotic and random and only pure stochastic approaches are able to capture the flow. These highly regular structures are completely unexpected and change the view of turbulence holistically.

Batt [1975] reproduces the experiments of Liepmann and Wygnanski. He is able to match both experiments via boundary layer manipulation. In the case of a laminar boundary layer, his experiments coincide with Liepmann measurements and in the case of a tripped boundary layer, he reproduces Wygnanski's results. Thus, he is able to explain the deviations in the growth rate of mixing layers. According to this, Dimotakis and Brown [1976] investigate shear layers via LDA. They emphasise that the initial conditions upstream of the separation edge possess a high and important influence on the mixing layer. Furthermore, their measurements suggest a feed-back mechanism which synchronises the initial instabilities of the upstream boundary layer with the downstream coherent structures in the free shear layer. Roshko [1976] visualises well organised coherent structures in a turbulent shear layer at high Reynolds number. He states that turbulence is not purely chaotic. Rather, it is dominated by these large scale structures even at high turbulence levels. Further, the vortex pairing and the entrainment are almost independent of the Reynolds number. Consequently, these K-H instabilities are an inviscid phenomenon which is in agreement with Rayleigh's statement almost 100 years ago [Rayleigh, 1879].

Motivated by this new perspective of turbulent flow, the idea of flow control comes more into focus. The existence of coherent structures and their excitation open up new approaches to turbulent flow control. In 1978, Oster et al. [1978] perform shear layer investigations with actuation at the trailing edge of the splitter plate. 20Hz is the most effective excitation frequency at a velocity ratio of $r_v = 6\text{ms}/15\text{ms} = 0.4$ (see equation 2.1) and almost doubles up the shear layer width. This frequency is associated to the far wake (500mm downstream of the splitter plate) and the corresponding dominant eddies in this region. Wygnanski et al. [1979] quantify how far downstream a disturbed shear layer stays two-dimensional. They yield higher correlations in the case of turbulent boundary layers compared to laminar ones. Further, their measurements confirm Roshko's flow visualisations and conclusions. Coherent structures persevere for a long time and are a common and inherent feature of laminar and turbulent shear layers. They show that this statement holds even for higher turbulence levels up to $Tu > 3\%$. A good overview of the role of coherent structures in turbulent flow at this time is given by Jimenez [1981].

In the mid 1980s, Bechert [1983] starts to investigate the sensibility of shear layers due to acoustic actuation. In his theory, he assumes an acoustic source which generates a pulsating force [Bechert, 1988]. The effect of placing this source downstream of the splitter plate is very weak. Significant effects are achieved

2. Literature review and theoretical approaches

if the source is placed upstream of the splitter plate close to the plate surface. The predictions agree with the experiments [Bechert and Stahl, 1988]. They state that the excitation generates an antisymmetric pressure field directly downstream of the splitter plate. The pressure difference between the two sides of the splitter plate represents the relevant quantity for acoustic actuation. In 1982, Oster and Wygnanski [1982] show that the growth rate of the local width b in equation 2.3 and the momentum thickness Θ in equation 2.9 increase linearly with the magnitude of the velocity difference λ in equation 2.2. They interpret this as evidence for large coherent structures in shear layers. Furthermore, they use a flat plate at the trailing edge (10mm long) to actuate the flow. In this case, b and Θ do not increase linearly any more. At amplitudes of more than 1mm, saturation is reached at some downstream positions and at 2mm the momentum thickness partly decreases. In the forced cases, the total turbulent energy and the Reynolds stresses change significantly and are increased by almost one order of magnitude at some downstream positions. Hence, shear layers are very susceptible to small periodic amplifications at the trailing edge where they originate. In the same year, Ho and Huang [1982] investigate natural and forced shear layers. The wake downstream of the splitter plate gradually evolves into an approximated tanh-velocity profile. If vortex merging occurs, the velocity profiles show deviations from the assumed tanh-form. When the merging ends, the velocity profile yields again a tanh-form. However, vortex merging in the natural flow is a random event in space and time. Furthermore, in the amplified cases they observe a kind of lock-in frequency and the dominant shear layer frequency is not necessarily the forcing frequency. Depending on the forcing frequency, they are able to merge several vortices together. They state a linear connection between the response frequency f_{res} and the forcing frequency f_f multiplied by the number of merged vortices M_v ($f_{res} = M_v \cdot f_f$). The explanation is that the response frequency tries to be close to the most amplified frequency. Thus, M_v switches to a higher value if the forcing frequency is reduced. If $M_v = 1$, the subharmonic is suppressed and merging is remarkably delayed. Hence, the subharmonic is required for vortex pairing as well as to achieve a higher entrainment. Weisbrot et al. [1982] investigate the spread rate of the shear layer (see equation 2.7) at a constant velocity ratio λ for different absolute velocities. In contrast to Brown and Roshko [1974], they determine a spread rate dependency of the velocity ratio and relate this phenomenon to an instability in the flow field. Fiedler and Mensing [1985] show by means of mono-frequent excitation that vortex pairing is suppressed or achieved. Furthermore, in contrast to the natural shear layer, the spread rate of the excited shear layer is nonlinear. In the region of vortex formation, a step-like shear layer width increase is observed. Above this point, the spread rate reduces to values below the unforced mixing layer.

After these comprehensive and holistic experimental studies in the mid 1980s, theoretical models come more into focus to describe these effects. Especially linear stability analysis is considered as a powerful tool to predict instabilities in natural and excited flows. A detailed review is given in chapter 2.3.2. The group of Wygnanski further investigates experimentally free shear layers excited by active flow control [Gaster et al., 1985], [Wygnanski and Petersen, 1987], [Weisbrot and Wygnanski, 1988], [Wygnanski and Weisbrot, 1988]. Until today, the focus continues to be the comparison to stability analysis. The view of the fundamental flow physics driven by the K-H instability does not change and persists. Dimotakis [1986] focuses on the entrainment of a shear layer. He discovers an unequal entrainment from the two corresponding free streams which favours the high-speed side. This unequal volume flux causes the higher spreading of the shear layer to the low speed side. Bernal and Roshko [1986] study the development of three-dimensional motion in a plain mixing layer experimentally. Besides the global dominating primary K-H instability, they find a superimposed secondary instability. It is orientated streamwise and causes a spanwise entrainment pattern. According to the primary one, the secondary instability increases with downstream distance as well. Fiedler [1988] states that between 10% to 25% of the entire turbulent energy is generated by coherent structures. This emphasises the important roll of coherent structures in turbulent flow analysis. Lasheras and Choi [1988] excite the plane shear layer along the span. They find that the primary K-H instability develops first and generates an almost two-dimensional array of spanwise oriented vortices. These vortices experience axial stretching and additional streamwise vortices are formed. Nevertheless, the spanwise vortices remain two-dimensional and hence, they conclude that the two-dimensional K-H instability and the three-dimensional instability are almost uncoupled. Fiedler and Fernholz [1990] elaborate a holistic and detailed review to turbulence control. They discuss experiments

and stability analysis of several flow configurations and strategies of passive and active flow control.

In the early 1990s, numerical simulations based on DNS codes become affordable. Moser and Rogers [1993] investigate laminar shear layers via DNS. They focus on the vortex pairing process in perturbed laminar shear layers. In the case of a two-dimensional shear layer with small three-dimensional disturbances the flow is still highly governed by K-H instabilities. If the two-dimensional shear layer is excited by strong three-dimensional disturbances, the flow field is very complex and highly three-dimensional. In some cases, the shear layer becomes turbulent.

In 2001, De Zhou and Wygnanski [2001] use a small flap at the trailing edge in their experimental setup to actuate the flow at the fundamental and subharmonic frequencies. Excitation with the fundamental and the first subharmonic show the best effect and the shear layer thickness is twice as large. They state that when the fundamental frequency reaches its saturation downstream of the plate, the subharmonic increases further. Hence, the subharmonic reaches saturation further downstream. In the interstice between the two points of saturation, the entrainment increases significantly due to the subharmonic and a higher mixing is reached. In 2012, Zhou et al. [2012] investigate numerically a compressible, forced shear layer via DNS. He finds λ -structures and hairpin vortices in the mixing layer which significantly influence the Reynolds stresses. These findings may hold for incompressible shear layers as well. D'Ovidio and Coats [2013] compute an incompressible transitional shear layer via DNS. They find clear differences between the pre- and post-transitional flow. The laminar shear layer behaves completely two-dimensional and the growth rate is driven by vortex amalgamation. In contrast, the turbulent shear layer shows three-dimensional effects to a certain extent and the entire three-dimensional turbulent Reynolds stress tensor has to be taken into account for a valid simulation. In this region, the turbulent shear layer tries to maintain a constant ratio between the structure spacing of the vortices and the local shear layer thickness.

Curved shear layers are a more general description of shear layers. Due to the additional curvature, a radial pressure and more complex flow structures appear. In experiments, curved shear layers are emitted in the same way as straight plain shear layers downstream of a splitter plate. Then, in downstream direction, the entire wind tunnel duct is bent to provoke curvature. However, curved shear layers represents an interesting approach to rolling-up shear layers. They capture the dominant K-H instabilities and possess a bent trajectory in the absence of three-dimensional effects. Curved mixing layers are investigated, for example, by Margolis and Lumley [1965] and Wyngaard et al. [1968]. They determine several quantities for stable and unstable flows. Unstable shear layers occur if the radial gradient of the angular momentum becomes negative [Eskinazi and Yeh, 1956]. This happens if the higher velocity of the shear layer streams along the inner part of the curvature [Gibson and Younis, 1983]. Nevertheless, rolling up shear layers are facing the opposite scenario. Hence, only stable curved mixing layers are of interest in the current study. Castro and Bradshaw [1976] perform a comprehensive study of plain and curved shear layers. Their measurements show for several parameters like the Reynolds stresses, the dissipation length, etc., a decrease in the region of maximum curvature. Downstream of this point, all these parameters reveal an overshoot until they converge asymptotically to the plain mixing layer values. Corresponding to the measurements of Castro, Gibson and Rodi [1981] show by means of theoretical models that the shear-layer thickness evolves nonlinearly in the region of curvature. Hence, highly curved shear layers lose their self-preservation. This phenomenon makes it more complex to define the adequate forcing frequency. Holloway and Tavoularis [1992] define a non-dimensional parameter to describe the ratio of the curvature magnitude with respect to the mean shear. Depending on this ratio, an increase or a decrease of the Reynolds stresses is observed in their experiments. Finally they conclude that the effect of curvature on shear layers is qualitatively similar to curved boundary layers. Lim et al. [1995] demonstrate by means of their experiments that the length scales change significantly due to the curvature. Nevertheless, the Taylor-micro-length and the Kolmogoroff scale remain almost unaffected. This observation suggests that the large scale coherent structures, the K-H instabilities, are more strongly affected than the random small scale turbulence. To the best knowledge of the author, no further relevant publications regarding curved mixing layer are published. It is even more surprising that no CFD simulations consider this problem although the plain mixing layer is still an intensively studied topic in simulations today.

Some parameters to quantify shear layers are already discussed in this short review. However, a brief summary of the most important ones is performed here. It does not claim completeness. The first

2. Literature review and theoretical approaches

parameter is the velocity ratio r_v in equation 2.1. It is the quotient of the free stream velocity u of the two involved streams.

$$r_v = \frac{u_1}{u_2} \quad u_1 < u_2 \quad (2.1)$$

The magnitude of the velocity difference λ across the shear layer is given in equation 2.2 [Monkewitz and Huerre, 1982]. In fact, it represents another approach to describe the velocity ratio.

$$\lambda = \frac{u_2 - u_1}{u_2 + u_1} \quad u_1 < u_2 \quad (2.2)$$

The definition of the local width b of a shear layer is defined in equation 2.3 [Oster and Wygnanski, 1982].

$$b = u_{y=0.1} - u_{y=0.95} \quad (2.3)$$

$$u_{y=0.1} = u_1 + 0.1(u_2 - u_1) \quad (2.4)$$

$$u_{y=0.95} = u_1 + 0.95(u_2 - u_1) \quad (2.5)$$

Another definition of the shear layer thickness δ_w is given in equation 2.6 [Brown and Roshko, 1974].

$$\delta_w = \frac{u_1 - u_2}{\left(\frac{\partial u}{\partial y}\right)_{max}} \quad (2.6)$$

Related to this parameter is the local spread rate of the shear layer which is the deviation of the shear layer thickness in streamwise direction. Equation 2.7 depicts this relation [Brown and Roshko, 1974].

$$\frac{\partial \delta_w}{\partial x} = \frac{\delta_w}{x - x_0} \quad (2.7)$$

Based on the local width b another definition of the growth rate is given in equation 2.8. x_0 is the distance between the geometrical origin at the trailing edge of the splitter plate and the virtual origin of the shear layer [Oster and Wygnanski, 1982].

$$\frac{db}{dx} = \frac{u_{y=0.1} - u_{y=0.95}}{x - x_0} \quad (2.8)$$

Another parameter for the local width of the mixing layer is the momentum thickness Θ . It is independent of the self-similarity of the velocity profiles across the shear layer at various downstream positions [Oster and Wygnanski, 1982].

$$\Theta = \int_{-\infty}^{\infty} \frac{u(y) - u_1}{u_2 - u_1} \left[1 - \frac{u(y) - u_1}{u_2 - u_1} \right] dy \quad (2.9)$$

2.1.2. Reattaching shear layers downstream of a backward facing step

Two-dimensional free shear layers are a very common approach to investigating the evolution of these flow structures in their most natural and undisturbed form. A two-dimensional backward facing step is considered to get closer to three-dimensional skewed shear layers. The flow separates geometry-induced at the trailing edge of the backward facing step. Downstream of the step, a recirculation bubble is formed. The shear layer surrounds this bubble and reattaches at the floor after a distance of approximately 5-7 step heights. Although the entire setup is two-dimensional and boundary effects in the third dimension are neglected, the shear layer is already slightly curved due to the reattachment and interacts with a vortical structure in the close vicinity. Thus, a short overview regarding two-dimensional backward facing steps and the opportunities of flow control are given here.

In the late 1960s and early 1970s, Bradshaw investigates experimentally the flow downstream of a backward facing step. He states that the mass flow transported by the shear layer splits at the reattachment

point. One part is deflected upstream to supply the entrainment of the shear layer. The initial condition of the boundary layer significantly influences the entrainment produced by the shear layer and this is directly linked to the portion of the mass flow which deflects upstream [Bradshaw and Wong, 1972].

In 1980, Kuehn [1980] investigates a backward facing step flow affected by a streamwise pressure gradient. He finds out that this pressure gradient has a stronger effect compared to other initial conditions like the upstream boundary layer type or the expansion ratio. Eaton and Johnston [1981] give a review regarding a backward facing step in laminar, transitional and turbulent state. Furthermore, they analyse the reattaching shear layer in detail. They state that it is very similar to a free plane shear layer. The growth rate and the mean velocity profiles are almost identical upstream of the reattachment point. The velocity ratio varies from $r_v = 1$ at the separation point to 1.2 (due to the reverse flow) at around the half of the recirculation zone. Due to these variations, the shear layer will never reach a fully developed state. In the same year, Chandrusuda and Bradshaw [1981] confirm the similarity between a mixing layer bounding the recirculation bubble and a free plain shear layer.

Besides the Reynolds number and the initial boundary layer, the expansion ratio also has a strong influence on the reattachment length. This ratio is the quotient of the duct height upstream and downstream of the step. The higher the expansion ratio, the longer the recirculation bubble which is shown, for example, by Durst and Tropea [1981]. Kottke [1982] illustrates the flow field for a broad range of Reynolds numbers between $Re_H = 50$ and 28600. At $Re_H = 50$ and 100, no separation is observable. At $Re_H = 28600$, the entire flow field is fully turbulent. He states that turbulent separation starts at around $Re_H = 6000$ which is consistent with Durst and Tropea [1981]. The higher the turbulence intensity, the shorter the recirculation bubble due to an increased entrainment. Further, the aspect ratio of the step has an influence on the reattachment length as well and should be larger than 10 for two-dimensional investigations [Kottke, 1982].

The backward facing step includes several aspects of fluid dynamics although the geometry is very simple. Boundary layers, vortical structures, reattachment and the complex interaction of these parameters exist. Thus, this setup represents a good test case for numerical studies and is broadly used. One of the first numerical validations with this geometry are performed by Armaly et al. [1983]. They investigate laminar, transitional and turbulent flows experimentally and numerically. The simulations yield a precise prediction of the experiments. Besides the beginning of numerical studies, more experiments are carried out. Adams [1984] investigates transitional and turbulent shear layers experimentally. He states that the reattachment length increases by 30% and the skin friction in the recirculation zone decreases by 50% if the flow is turbulent comparing to the transitional case. Driver and Seegmiller [1985] measure the recirculation bubble in a parallel-wall setup and in a deflected top-wall of 6° downstream of the step. The negative pressure gradient achieved leads to an increase of the recirculation bubble of 30%. Hence, besides the pressure drop at the step due to the sudden expansion, the pressure gradient in streamwise direction is the governing influence factor. These results are in agreement with the findings of Kuehn [1980]. Nagib et al. [1985] find two distinct frequencies downstream of the step. One scales with the step height, the other one corresponds to a periodic shedding of the separation bubble.

In 1986, Roos and Kegelmann [1986] are one of the first who apply AFC to the separated flow downstream of a backward facing step. This holistic study yields several observations. The scale of the coherent structures in the reattaching shear layer scales with the shear layer thickness itself, which is consistent with the findings of Eaton and Johnston [1981]. These coherent structures dominate the entire flow field. The natural frequency of a laminar shear layer amounts to $St_H = 0.41$. In the turbulent case, no distinct peaks are measured. They state that slight excitation by means of flaps at the step edge has a strong influence. A stronger effect is determined for turbulent boundary layers. However, during excitation of laminar flow at $St_H = 0.29$ most of the energy is concentrated at the frequency whose wavelength is two times the step height. At $St_H = 0.22$, the energy concentrates at the first harmonic. In the turbulent case, the reattachment length was reduced by two step heights at a forcing frequency of $St_H = 0.29$. Thus, they state that laminar and turbulent shear layers require different excitation frequencies. This implies that in the transitional case, excitation via a single frequency is suboptimal. Modulated excitation which includes the subharmonic may yield high control effects. Furthermore, they observe almost no effects of the AFC on the mean flow velocity profiles. Rather, the Reynolds stresses are increased significantly in the laminar

2. Literature review and theoretical approaches

and turbulent cases. Ötügen [1991] focuses on the influence of the expansion ratio. He states that larger expansion ratios generate a higher turbulence intensity in the free shear layer. This promotes a higher turbulent diffusion which leads to an increased shear layer growth rate. This shortens the reattachment length of the recirculation zone. In 1992, Hasan observes two kinds of instability modes. The step mode which scales with the step height and a shear layer mode which scales with the momentum thickness δ_2 of the laminar boundary layer. After few stages of vortex pairing, the shear layer mode reduces to the step mode [Hasan, 1992], [Hasan and Khan, 1992]. Fernholz [1994] investigates the recirculation bubble of a two-dimensional step. He counts this flow to the category of recirculation with strong reverse flow. The maximum observed reverse flow amounts to approximately 20% of the free stream velocity. He speculates that the feedback of disturbances through the recirculation bubble may change the shear layer from convectively unstable to globally unstable. Nevertheless, Castro [1991] originally has the idea of feedback. In 1995, Michalke et al. [1995] compute a linear stability analysis of the shear layer downstream of a backward facing step. They assume a tanh-velocity profile (equal to a free shear layer) and include a curvature factor. Depending on the frequency, the curvature may increase or decrease the instability. Dovgal et al. [1995] confirm these results experimentally. Huppertz excites the shear layer downstream of a backward facing step by means of five loudspeakers. This setup permits an actuation with a phase angle between adjacent cavities. In the case of two-dimensional excitation, the reattachment length is reduced by 32% at a frequency of $St_{\delta_2} = 0.12$. He states that the K-H instabilities are sensitive to phase shifted excitation along the trailing edge for a broad range of phase shift angles. This broadband receptivity is consistent with the stability analysis prediction of Pierrehumbert and Widnall [1982]. If the wavelength of the phase shifted signal is similar to the wavelength of the K-H instability, the reattachment length is further reduced. In this configuration, large three-dimensional structures arise. In this experiment, the wavelength of the K-H instability is similar to the step height, hence they are unable to determine which quantity scales the transverse waves [Huppertz, 1994], [Huppertz and Janke, 1996].

Chun and Sung [1996] excite the turbulent boundary layer upstream of the step experimentally via loudspeakers. They use the momentum thickness to achieve similarity. They find two distinct frequencies and state the lower one is related to the vortex shedding of the emitted shear layer and is related to the modulation induced momentum exchange [Nagib et al., 1985]. The higher frequency is associated with initial boundary layer instability of the unforced case. However, they state that the most efficient forcing frequency is approximately the vortex shedding frequency $St_{\delta_2} = 0.01$. In a second study at a moderate Reynolds numbers of $Re_H = 1200$, Chun and Sung [1998] analyse the effect of actuation by means of snapshot flow visualisations. At frequencies above $St_H = 0.822$ the actuation does not penetrate the shear layer anymore. They conclude that vortex pairing yields the most entrainment and cause the shortest reattachment length at $St_H = 0.477$. The DNS computed by Le et al. [1997] shows that the three-dimensional Navier-Stokes equations have to be considered to capture the correct turbulence distribution. Merely in the viscous dominated sublayer of the turbulent boundary layer a two-dimensional simplification is legitimate. Hence, a pure two-dimensional computation of the simple backward facing step geometry is not applicable for transitional and turbulent shear layers. Based on all the studies regarding a backward facing step, Nishri and Wygnanski [1998] apply the findings on a flap in leading edge stall configuration. By means of acoustic excitation, they are able to increase the static stall angle by additionally 5° . This realistic experiment fairly shows that AFC is able to increase the performance in modern aviation. Nayeri [2000] investigates experimentally two coaxial jets which rotate against each other. The emitted shear layer is twisted as well and a significant increase in the turbulent kinetic energy is measured. The complexity of the flow structures is increased because the shear layer interacts with the wake, and helical modes are observed. Hence, a discrete, separated investigation of the K-H instability is not possible. Huppertz [2001] excites a transitional shear layer downstream of a backward facing step. He tests mono-frequent and subharmonic actuation as well. If vortex pairing is forced by a distinct frequency, a subharmonic further decreases the reattachment length. Although a bimodal excitation shows significant effects, mono-frequent actuation at the optimal frequency performs better at all frequencies and flow states. Hence, Huppertz claims that it is irrelevant if the shear layer structure arises via vortex pairing or via a direct roll up. All these experimental results are reproduced by the numerical simulations of Wengle et al. [2001]. Yoshioka et al. [2001a,b] reduce the reattachment length by more than 30% at $St_H = 0.19$ in

their experiments. Via phase averaging of the velocity field, they separate the generated turbulence caused by coherent structures from the random turbulence. By means of this triple decomposition [Hussain and Reynolds, 1970] of the unsteady velocity field, they conclude that optimal actuation maximises the Reynolds stresses in the region around the reattachment point.

During the last decade, numerical studies on backward facing step become more dominant. Only a few publications are mentioned here. Weinkauff et al. [2003] illustrate a transitional flow field based on their computations. The two-dimensional character is dominant although small streamwise vortices exist. Wee et al. [2004] investigate the flow on a two-dimensional grid and perform linear stability analysis based on the computed velocity profiles. They state that the flow is absolutely unstable and the vortex shedding frequency is $St_H = 0.07$. Biswas et al. [2004] run a two-dimensional simulation of laminar step flow at Reynolds numbers between $0.01 < Re_H < 800$. The results agree well with the computations of Armaly et al. [1983]. Šarić et al. [2005] include in their simulations periodic perturbations at the trailing edge. They use these cases with excited flows for a comparison of different CFD models. The baselines are taken from Yoshioka et al. [2001a,b]. Dandois et al. [2007] investigate numerically a smooth ramp and the influence of synthetic jets. They document a shortening of the recirculation bubble of 54%. Erturk [2008] performs a comprehensive two-dimensional CFD study. He elaborates some geometrical quantities for the computation domain to yield precise results. Creusé et al. [2009] implement open and closed-loop control at a backward facing step based on numerical simulations. They consider unsteady inflow and AFC via two blowing jets. One is placed at the trailing edge and the other at the step foot. The closed-loop control reduces the reattachment length by 50% even though an experimental validation is missing. As shown in this review, the two-dimensional step is regarded as reference case for CFD code validation.

In 2010, Tihon et al. [2010] investigate experimentally a backward facing step at $30 < Re_H < 1800$ facing unsteady inflow at the inlet. They achieve a reduction of the reattachment length up to 80%. Furthermore, they find two instability modes. The step mode ($St_H = 0.15$) dominates the laminar flow regime and the shear layer mode affects the transitional flow. In some operating conditions, both frequencies reveal the same shortening effects but the near-wall flow characteristics differ significantly. Leyh [2014] clearly shows in his experiments that the natural frequency in laminar and transitional flow ($Re_H < 1500$) regimes scales with the momentum thickness δ_2 and not with the step height. Kapiris and Mathioulakis [2014] use zero mass flux actuation installed in the back panel of the backward facing step. They state that the optimum Strouhal number for shear layer excitation is $St_H = 0.16$ or $St_{\delta_2} = 0.01$ at $Re_H = 6940$. They achieve a recirculation bubble length reduction of 20%.

2.1.3. 2.5-dimensional shear layer

Plain shear layers are assumed to be homogenous in y - z -direction. The more general treatment are 2.5-dimensional shear layers. In this case, the two flows above and beneath the splitter plate are not parallel to each other, or the trailing edge of the splitter plate is not perpendicularly oriented to the inflow. Hence, the flow is inhomogeneous in one additional direction. Although most authors call this kind of shear layer already three-dimensional, the description 2.5-dimensional shear layer is more appropriate. Although the resulting mixing layer is highly three-dimensional, the initial conditions still assume homogeneity in at least one of the spatial directions, mostly in spanwise direction.

Hackett and Cox [1970] are probably the first who investigate 2.5-dimensional shear layers. Their experiments enable two different setups. In the first setup the flow above the splitter plate has an angle of 45° to the trailing edge and the flow below of -45° . In the second one, both flows are parallel to each other but encounter the trailing edge at a 45° angle. They determine an increase of the maximum shear stress normalised by the square of the shear velocity difference of about 50%.

In the mid 1990s, the group of Fiedler starts to investigate 2.5-dimensional shear layer intensely. Similar to Hackett, they investigate two setups. Two non-parallel flows pass the trailing edge perpendicularly or two parallel streams encounter the trailing edge under an arbitrary angle. Gründel and Fiedler [1993] investigate experimentally the case of two non-parallel streams crossing a perpendicular trailing edge with a maximum angle of $\pm 15^\circ$ of the two streams to the x -axis. Impressive flow visualisations show highly three-dimensional structures clearly. The streamwise vortices start to form directly downstream of the trailing edge and are oriented in mean free stream direction. Moreover, these streamwise vortices tend

2. Literature review and theoretical approaches

to merge in several stages. The topology is similar to the vortex pairing process of spanwise oriented vortices due to K-H instabilities. They also investigate the effect of passive flow control via small vortex generators upstream of the trailing edge. This passive method yields an equidistant distribution of the streamwise vortices. Based on experiments and simulations, Fiedler et al. [1995] show that these high ordered streamwise vortices occur only if the wave vector of the most amplified instability is perpendicular to the mean vorticity vector. Only symmetrical configurations provide this ordered pattern. Furthermore, they demonstrate that a plain two-dimensional shear layer forced in slanted direction evolves similar to unforced streams passing a slanted trailing edge. This result is further confirmed by the work of Spieweg and Gründel [1995] and Gründel et al. [1995]. Kruscha and Fiedler [1994] compute some linear stability analysis based on these experiments. The results are discussed in detail in the next section.

Kaltenbach and Janke [2000] analyse an infinite, swept, backward facing step by means of DNS in transitional condition. Kaltenbach states that the sweep independence principle holds till sweep-angles of $\leq 40^\circ$. The simulations agree with the experiments of Selby [1982] with a maximum angle of 38° . This principle is discovered by Reynolds, who states that such a flow is decomposed in two velocity components, a velocity parallel and one normal to the trailing edge. The latter component is independent of the sweep angle. Furthermore, they state that the free shear layer is dominated by a K-H instability and the skewing effects on the growth rate of instabilities is weak. Jürgens and Kaltenbach [2003] investigate the same setup via DNS. They compute an eigenmode decomposition of the flow field and resolve the dominant coherent structures. The most energetic eigenmode occurs directly downstream of the trailing edge. It contains at least 10% of the local kinetic energy for all sweep angles between 0° and 60° . Furthermore, the vortex axis of this dominant coherent structure is roughly normal to the inflow direction. A stability analysis at a swept angle of 40° confirms this statement. Finally, they state that the shear layer dynamics are dominated by the spanwise vorticity because the axial vorticity is significantly smaller (with respect to the coordinate system of the inflow). Based on the finding of Kaltenbach that the twisted shear layer is still dominated by a K-H-instability, and also based on the finding of Jürgens that the vorticity normal to the inflow dominates the flow, one might speculate that AFC normal to the inflow at the trailing edge is the most efficient approach. Kaltenbach [2004] investigates this geometry in turbulent conditions. In this scenario, the independence principle does not hold. All parameters change scaling and the scaling factor varies as well. Only the u and v velocity profiles behave independently.

Based on the baseline investigations of Kaltenbach and Jürgens, Jürgens [2006] studies the flow field in forced cases. He uses a sinusoidal excitation directly at the trailing edge of the step. This is the most efficient position because instabilities are exponentially amplified in laminar flow regimes. He simulates all three flow cases, laminar, transitional, and turbulent flow. On closer consideration, the pure sweep independence principle holds only for the laminar case. The DNS simulations show that also in transitional and turbulent flows, sweep independency in a weaker form exists for swept angles $\leq 40^\circ$. His simulations for all cases and stability analyses for the laminar and transitional case yield the same observation. AFC approximately in the direction of the inflow is significantly more efficient compared to the actuation in step normal direction. The consequence is that the excitation wave of the AFC requires a phase velocity along the trailing edge. The difference between laminar and turbulent flows is the amplitude. In the laminar and transitional case, amplitudes of 1% of the free stream velocity are sufficient but in the turbulent flow regime amplitudes of 25% are required. A compact summary of these results is also given by Jürgens and Kaltenbach [2012].

2.1.4. Three-dimensional shear layers and streamwise vortices

Streamwise vortices generated by rolling up mixing layers occur in several applications as discussed in chapter 1. Hence, an exhaustive number of publications exists. In this thesis, the proposed geometry of a swept, semi-span, backward facing step is a design-hybrid of a vortex generator and an Ahmed body. In this section, a brief overview of delta wings and MAV's, the Ahmed body, and technical applications like trains and realistic car models is given.

Figure 2.1 depicts a flow visualisation on a delta wing with a swept angle of 85° made by Payne [1987]. The flow comes from the left and the delta wing tip is outside of this photograph's range. Nevertheless, the five cross-sectional smoke visualisations clearly show the spatial evolution of the two leading edge vortices.

The fascinating detail of this photograph is the rolling up process. Already in the third cross-section, K-H instabilities are evident in the curved shear layer emitted at the leading edge. The trajectory shows the same pattern as plain two-dimensional shear layers. The wavy form increases its amplitude during the rolling up. The shear layer itself is twisted and highly curved and possesses a spanwise velocity component which, in general, is not constant. Thus, this mixing layer is regarded as completely three-dimensional because no homogenous spatial direction exists. A good distinction of the different classifications of shear layer is given by Fiedler et al. [1998]



Figure 2.1.: Cross-sectional visualisation of the rolling up shear layer at the leading edge on a delta wing; photograph is taken by Payne [1987]

In the late 1950s, vortex generators and delta wings become the focus of attention. Werlé [1960] is probably the first who uses active flow control to influence vortex breakdown. Through an external (manually traversed) probe, suction and blowing are possible. With this setup, he is able to shift the vortex breakdown position upstream to the wing tip or downstream to the probe inlet. The effects are quantified by means of flow visualisations. Lambourne and Bryer [1962] also visualise the flow and try to find an analytical model to describe the flow field. In 1985, Gad-el Hak and Blackwelder [1985] confirm the phenomenon of vortex pairing inside the curved rolling up shear layer in spanwise direction on a delta wing via flow visualisations. This is a further hint that these highly three-dimensional shear layers behave similar to the plain two-dimensional ones. Gordnier and Visbal [1994] carry out a numerical simulation of the delta wing flow. They state that the shear layer is highly subjected to K-H instabilities. Further, they show that the shedding frequency depends on the axial location. This spatial dependency would yield an inefficient actuation by means of a mono-frequent excitation. Based on their computations, Visbal and Gordnier [1995] state that the curved, rolling up shear layer is convectively unstable. This finding implies the consequence that continuous forcing is required to provoke any kind of control authority. Menke et al. [1999] investigate experimentally the unsteady flow on a delta wing. They determine the reduced frequencies for the many unsteady phenomena such as vortex shedding, helical mode instabilities, K-H instabilities, etc. Visbal and Gordnier [2003] compute simulations with spatial discretisation to investigate

2. Literature review and theoretical approaches

the rolling up shear layer in more details. They find several coherent substructures in the three-dimensional shear layer under transient conditions. Furthermore, they show complex vortical structures in streamwise and spanwise direction. It looks like instabilities co-exist in different spatial directions. In the review by Gursul [2004], several instabilities are discussed. He states that K-H instabilities in the three-dimensional shear layer on delta wings are an inherent and dominant part of the flow as much as in two-dimensional mixing layer. Parallel to all these baseline measurements, several experiments use constant blowing or suction along the leading edge as AFC [Gad-el Hak and Blackwelder, 1987], [Visser et al., 1989], [Guy et al., 1999b], [Morton et al., 1999], [Siegel et al., 2002]. Although at high momentum coefficients of the AFC system, impressive extra lift is produced, this type of actuation does not focus on K-H instabilities. In contrast to constant blowing, Margalit et al. [2002, 2005] work with cavity-installed piezoelectric actuators for periodic zero mass flux actuation. Along the leading edge, five separated cavities exist for a segmented actuation. They find an optimal reduced frequency for flow excitation of one. The largest effects of more than 25% are observed during an in-phase excitation. The smallest effects are measured at a phase angle of 180° between neighbouring cavities. Hence, they claim that the more three-dimensional the actuation, the less the control effects. Greenblatt [2007] uses plasma actuators along the leading edge which actuate at arbitrary frequencies. Furthermore, by varying the duty cycle, a kind of rectangular actuation signal is achieved. Actuation at a reduced frequency of one yields an increase in the normal force of more than 20%. During the last decade, MAVs come into the focus of interest due to applications in industry and logistic. Mueller [2007] investigates rectangular wings. At low aspect ratio less than 2, the influence of the wing tip vortices becomes dominant and comparable to delta wings. Furthermore, the dominant streamwise vortices increase significantly the maximum angle of attack before deep stall occurs. MAVs in general operate only at low and medium Reynolds numbers. Hence, AFC especially in the laminar and transitional case may produce a remarkable extra lift. Taira and Colonius [2009a] present detailed flow visualisations based on their numerical computations for low aspect ratio wing. Furthermore, even at an aspect ratio of four, no two-dimensional von Kármán vortex shedding is observed. Hence, the flow is still highly three-dimensional and is influenced by the tip vortices. Taira and Colonius [2009b] state that in the past, the research is focused on increasing the spanwise circulation to enhance the lift. But the tip vortices also contribute remarkably to the lift generation in post-stall flow. Via blowing at the trailing edge, he provokes an interaction between the leading edge and trailing edge vortices. Thus, the wake of the trailing edge merges with the tip vortices and strengthens the downwash effect of these two vortices. This presses the streamwise leading edge vortex closer to the wing surface and increases the lift. Finally, they consider the control of tip vortices as highly beneficial for lift enhancement. Vey et al. [2010] find in their experiments that the lower the aspect ratio, the less efficient the leading edge excitation because of the increased influence of the tip vortices. At an aspect ratio of 0.75, actuation of the streamwise tip vortices generates a remarkable increase in lift at post-stall angles of attack although leading edge actuation still has an higher control effect [Vey, 2014].

Particularly in the range of delta wings and swirling jets, vortex breakdown is an intensively discussed topic. This phenomenon occurs at swirl numbers larger than approximately 1.3 [Billant et al., 1998]. These high swirl ratios are not reached in the wake of the swept, semi-span, backward facing step. Hence, vortex breakdown is not considered in this thesis. Nevertheless, excitation of K-H instabilities may not only control the circulation, but also the vortex breakdown position. Comprehensive reviews regarding vortex breakdown and its control are given by Leibovich [1978], Escudier [1988], Sarpkaya [1995], Mitchell and Délery [2001] and Oberleithner et al. [2011].

Another interesting object to control streamwise vortices generated by a rolling up shear layer is the slanted back of an Ahmed body. This generic car model is propagated for the first time by Ahmed et al. [1984]. Depending on the angle of the slant, the streamwise vortices may generate up to 20% of the entire car drag. Hence, a lot of research focuses on weakening these vortices via AFC. However, almost all authors are searching further for circulation control methods to increase the entrainment in the body's wake. Surprisingly, nobody is trying to excite explicitly the K-H instabilities in the free shear layer. Nevertheless, the geometry of the Ahmed body is close to the swept, semi-span, backward facing step. Thus, a very brief overview to AFC on the Ahmed body is given here.

Beaudoin et al. [2004] visualise the C-pillar vortex on the slanted back in a water tunnel by means of

cavitation. Besides the visualisation, the occurrence of cavitation clearly depicts the strong low pressure which is generated by the streamwise vortex. Lehugeur and Gilliéron [2006] show numerically that AFC at the separation edge with blowing rates of 100% and 150% of the free stream velocity provokes vortex breakdown. Breakdown changes the wall pressure distribution drastically and a gross drag reduction of almost 6% is achieved. At a blowing rate of 50%, breakdown does not occur, rather the vortex gets stronger and the drag increases [Lehuguer, 2007], [Kourta and Gilliéron, 2009]. According to this, the computations of Wassen and Thiele [2007] yield a gross drag reduction of 6.4% with blowing at all edges of the slant. Nevertheless, the remaining net effect amounts to only 0.8%. An experimental validation of these simulations is performed by Brunn et al. [2007]. Although the blowing weakens the vortex strength drastically, the effect on the total drag of the Ahmed body remains insignificant. Based on these findings, Wassen uses fluid actuators instead of constant blowing to decrease the required external energy supply. These improvements reduce the total drag by 9.4% with AFC at the slant and by 14% with AFC at the slant and at the base [Wassen and Thiele, 2008, 2009]. The required energy for the AFC is reduced to 0.6% of the propulsion energy. In total, this is a remarkable net effect. In the experiments by Ivanov [2011], a similar AFC system is installed. In contrast to Wassen, the use of fluid actuators yields a negative net effect although the gross drag reduction is 7.1%. Ivanov achieves the strongest effect by constant suction along the spanwise edge of the roof and the slanted back. This way, the flow remains attached in the plain of symmetry and the C-pillar vortices are suppressed. The net effect is a total drag reduction of 11.1%. Hammas et al. [2010] actuate along the C-pillar of the Ahmed body. At a suction rate of 150% of the free stream velocity, the drag is increased by 8.2%. Blowing with 60% increases the drag by 0.8% as well. All these discussed results show that no general strategy exists to reduce the total drag of an Ahmed body. The partly conflicting findings are caused by the strong interaction of the wake structures. If the spanwise oriented recirculation bubble is decreased, the streamwise vortices may increase and the total effect is undesirable. Otherwise, an elimination of the streamwise vortices will increase the pressure at the C-pillar. The total effect may still be negative because the downwash effect of the two vortices is missing and the entire wake is increased. Due to this complex interaction and the sensitivity to other parameters like the slant angle, the ground clearance, etc., K-H instabilities are probably of minor interest in this setup. Streamwise vortices play an important role in the vicinity of realistic car models as well. A comprehensive overview is given by Hucho [2005]. The automotive industry is already concerned about strong streamwise vortices at the C-pillar during the design process and reduces their negative effect through large radii instead of sharp edges. However, Okada et al. [2009] investigate numerically a realistic car model. They show that a modern automotive is highly affected by streamwise vortices. These structures occur at the door mirrors, around the wheels, at the car's fender, in the underfloor flow, at the A-pillar, etc. In short, the entire vehicle is fairly surrounded by streamwise vortices. This statement is confirmed by Heft et al. [2011]. Their simulations with different turbulence models depict the high density of vortical structures around the entire DrivAer car model. The numerical simulation of Cheng et al. [2012, 2011] investigate the interaction of the A-pillar and C-pillar vortices in a notch back configuration. Already small geometrical changes of the radii at the pillars change the entire flow field in upstream and downstream direction. This tiny selection of publications illustrates explicitly the importance of a better understanding of rolling up shear layers and the corresponding streamwise vortices for the purpose of drag reduction. Furthermore, Wojciak et al. [2011] prove via simulations and experiments that the entire vehicle stability is reduced due to the time lag between the occurrence of streamwise vortices at the car's wing, A-pillar and C-pillar. This phenomenon becomes a safety issue especially for lightweight cars during fast cornering. Wieser et al. [2014] perform flow visualisations during wind tunnel tests on the DrivAer model in fast and notch back configuration. In the baseline case, the shape optimised geometry of the DrivAer model does not yield any streamwise vortices in its wake. Once crosswind of 5° or 10° occurs, strong streamwise vortices are emitted at the C-pillar. The corresponding drag is increased remarkably by 9.7%. The computations of Gaylard [2012] for a similar case reveals an increase of almost 20%. Although streamwise vortices are still a big issue for the automotive industry, AFC of these vortical structures is not yet considered. A theoretical large net benefit of 10% drag reduction will probably not cover the costs of development, certification, installation and maintenance. Thus, AFC remains as a topic in the academic world. This stance may change due to the higher interest in electric cars. In this case, drag does not affect the costs of

2. Literature review and theoretical approaches

fuel alone. It will also decrease the maximum driving range and this is a customer need with high priority. In the field of commercial passenger trains, lightweight construction is becoming more and more common. Due to the lower mass, the trains are more affected by aerodynamic loads. Thus during the last decade, crosswind stability comes more into focus already during the design phase. The proof of crosswind stability is a requirement during the certification [TSI HS RST, 2008], [EN 14067-6, 2010] and is of high importance for high speed and double-deck trains. Krajnović [2009] investigates numerically the geometry on a general train model to achieve higher crosswind stability. The main source of optimisation is the geometry of the train head. Tanneberger [2012] computes the influence of several geometry variations of a *Do2010* train head. In the optimal setup, the roll moment due to crosswind is decreased by 7.5%. In an experimental study, Neumann [2014] investigates the influence of several geometrical devices like flaps or vortex generators at different positions on the train head of an *ICE3* model. The roll moment is reduced by up to 30% although it is questionable if these devices are installable on a real train. However, active flow control is actually not in the scope of interest in commercial train construction and, consequently, no publication discusses K-H instabilities as a fundamental part of rolling up shear layers.

At the end of this literature section, some new approaches regarding rolling up shear layers are mentioned briefly. Gursul and Xie [2000] study the vortex wandering of the primary vortex on a delta wing analytically. They assume small vortices in the curved rolling up shear layer due to K-H instabilities. Then, they calculate the velocities induced by these small vortices according to Biot-Savart law. They confirm a nonlinear interaction as the origin of the vortex wandering. According to this, in laminar flow the vortex centre position is almost steady. Hence, beyond the fully laminar case, K-H instabilities arise and have the power to displace the vortex. Shan et al. [2000] present another form of interaction on delta wings. The secondary vortex and the K-H instability in the shear layer interact. Based on their numerical simulations, they show that the secondary vortex is lifted by the K-H instability and convects into the shear layer. The resulting free space is filled by a counter-rotating vortex emitted by the shear layer. This vortex grows until a new generated secondary vortex is strong enough to push this vortex away into the shear layer. Hence, a highly dynamic and periodical behaviour between the secondary vortex and the K-H instabilities in the shear layer is documented. Krajnović and Davidson [2005b] use a topological approach to describe the flow field in the wake of an Ahmed body. By arranging some simple nodes, they try to reproduce the original flow field. They confirm that this approach is complex, especially because the time average and the instantaneous flow field differ completely. Rütten [2007] uses a similar ansatz to describe the leading edge vortex on a delta wing. Based on the three invariants of the gradient tensor of the velocity vector, he predicts different flow states.

Wynanski et al. [2011, 2014] speculate that a skewed three-dimensional mixing layer may be divided into two shear layers, one normal and one parallel to the trailing edge. They state that this ansatz holds for turbulent mixing layers as well. They find in their experiments that the mean velocity profile normal to the edge is proportional to the mean velocity profiles parallel to the edge. Another huge field of research is mixing layers in reacting flows. In combustion chambers, highly curved mixing layers experience K-H instabilities as well. A sufficient control of the mixing layer is important because they govern the flow field in a combustion chamber. This has a direct impact on the mixing and thus on the efficiency and the resulting emissions [Corrsin, 1958], [Hill, 1976], [Paschereit et al., 2014].

2.2. Designing of the active flow control actuators for short-wavelength excitation

Intermediate conclusion: Based on the literature considering active flow control and the given framework conditions of this project, a setup with active flaps based on electromagnets is the most promising approach. After a short introduction to electromagnetism, oscillating armature drives are discussed in detail. The motion path and the bearing are the two crucial points for the designing and the construction to achieve a desired motion amplitude of $\pm 2\text{mm}$.

Two general approaches of flow control are commonly used; passive and active flow control. Passive flow control does not need external energy. These fixed mounted devices use the energy of the free stream

to perform the desired effects. In contrast, AFC requires additional external energy from an additional device which is, for example, mechanical, electrical or pneumatic. The advantage of AFC is a possible broad range of available amplitudes, frequencies, phase velocities, low response time, etc. Furthermore, in technical applications, AFC is switched off if the effect is not required. In contrast, passive flow control devices always generate distinct effects although they are not required in many situations. They still generate the corresponding unintended effects like total pressure losses or an increased drag. General reviews considering the several types and mechanisms of flow control are discussed by Fiedler and Fernholz [1990], Gad-el Hak et al. [1998], and Greenblatt and Wagnanski [2000].

In this thesis, the development of a sufficient AFC system is the foundation for the experiments. Based on the previous studies, the specifications of the AFC system are estimated here. A first step is experiments considering two-dimensional excitation of shear layers. Oster et al. [1978] use a single flap with an amplitude of 0.3 to 2.5mm. The most efficient frequency is 20Hz at a velocity ratio of $r_v = 6\text{ms}/15\text{ms} = 0.4$. Fiedler and Mensing [1985] actuate with loudspeakers at 30Hz at a free stream velocity of 11m/s. Gaster et al. [1985] use a flap in the experiments to validate stability analysis results. The amplitudes are 0.5 and 1mm, the frequency is 20Hz at free stream velocities of 2 to 19m/s and velocity ratios of $r_v = 0.25$ and 0.43. Roos and Kegelmann [1986] state that a flap displacement of less than 1% of the boundary layer thickness is sufficient. Weisbrodt and Wagnanski [1988] show frequency spectra between 1 and 20Hz for free stream velocities between 2.5 and 13.5m/s at a velocity ratio of 0.6. Although Menke et al. [1999] state that the reduced frequency of K-H instabilities on delta wing is around $St_c = 10$, Margalit et al. [2005] find the most efficient frequency at around $St_c = 1$. This would lead to frequencies of up to 20Hz (with a characteristic length of 0.5m). Jürgens [2006] states a frequency of $St_H = 0.45$ at the 2.5-dimensional backward facing which delivers frequencies of the same order. Based on all these findings, the AFC system has to cover amplitudes up to 2.5mm. At free stream velocities in the large wind tunnel at the HFI between 4 and 20m/s, a frequency range from 1 to 60Hz is considered as sufficient to cover all required frequencies. Gordnier and Visbal [1994] find that the optimal excitation frequency varies along the leading edge on delta wings. Hence, mono-frequent actuation along the entire edge will never be efficient at all positions. Thus, segmented actuation is required to perform an optimal actuation frequency at all positions. Jürgens [2006] states that the direction of the highest amplification downstream of a swept, infinite, backward facing step lies between the free stream direction and the trailing edge direction. Actuation normal to the edge is less efficient. In fact, the actuation has to perform a transversal phase velocity along the trailing edge.

In conclusion, an actuation segmented and phase controlled with frequencies between 1 and 60Hz has to be developed. Possible settings are segmented flaps or tabs, segmented zero mass flux actuators, segmented and time controlled blowing, or segmented plasma-actuators [Cattafesta and Sheplak, 2011]. The entire system has to be compact to fit into the swept step. Mechanical vibrations or electromagnetic noise has to be minimised to ensure high accurate measurements. The financial framework is limited to €1000.

The advantages and disadvantages of different actuation methods are reviewed by Cattafesta et al. [2003]. However, a selection of the most promising actuator type is required in this individual case of a swept, semi-span, backward facing step. Preliminary tests at the HFI with plasma actuators yield huge noise levels on the piezo-electrical pressure sensors due to the high-voltage, high-frequency power supply. Although plasma actuators might work, the electromagnetic noise renders any quantification impossible. Zero mass flux actuators based on piezo elements are also driven by high-voltage energy supply [Gallas et al., 2003]. Furthermore, the surrounding cavity is optimised for the desired frequency [Holman et al., 2005]. In the current experiments, a wide range of frequencies has to be covered. These facts exclude piezo driven actuators. Time regulated blowing by means of fast switching valves is another option. Each valve including tubing, adapters, etc., costs around €100. Furthermore, a central valve terminal is needed and costs around €1800. Thus, this promising approach exceeds the financial limit. Actuation with loudspeakers is another ansatz. Due to the low frequencies down to 5Hz, the loudspeakers need a large membrane to perform an acoustic wave with a sufficient amplitude. These kind of speakers are too large to fit into the wind tunnel model in higher quantities. Thus, segmented flaps or tabs remain the only option. In this case, amplitudes up to 2mm have to be realised.

Each flap needs its own drive unit to perform the desired motion. Electric or servo motors require further

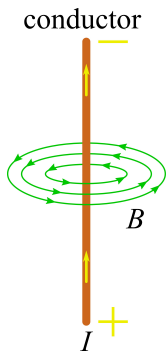
2. Literature review and theoretical approaches

devices like an encoder and a controller [Kremser, 2007]. Low-cost devices are available but their reacting time is too slow and they are not designed for long-term motions. Better commercial devices which fulfil the requirements exist but cost at least €200 each. Simple electrical motors with a connected redirecting gear probably overheat during long-term tests and are excluded as well. Preliminary tests with linear motors yield an inertia which is too high for frequencies above 10Hz. Other preliminary tests with voice coils show very promising dynamic motion. Nevertheless, the initial position is unknown after deactivation and a very high sensitivity to position changes makes any kind of pre-calibration impossible. Besides, voice coils are also too expensive. At the end of this intensive feasibility analysis and several prototype tests, electromagnet drive units, especially the oscillating armature drives, remain the last option. These devices fulfil all requirements and are realisable within the financial scope of €1000.

In the next subsection a short introduction into electromagnetism, electromagnets and oscillating armature drives is given. These discussed fundamental principles have a direct impact on the design and construction of the AFC system.

2.2.1. Fundamental equations of electromagnetism

In the given framework of requirements of the AFC actuators and the provided financial resources of €1000 for the entire actuation system, electromagnets are used as actuators. To the best knowledge of the author, this chosen approach is new and moreover essential for this thesis. Therefore, a brief introduction to the physics of electromagnets is given. Furthermore, the modifications needed for its use as an actuator in the field of fluid dynamics is specified.



A magnetic field is generated if electricity runs through a straight infinite conductor. This effect is illustrated in figure 2.2. The conductor carries in this case the direct current I and thereby generates the magnetic flux B . The green lines are formed concentric to the conductor and represent equipotential lines of the counter-clockwise oriented magnetic flux. There are two variables to express the strength of this magnetic field, the magnetic flux B and the magnetic field H_{mag} . The linear dependence of these two quantities is given in equation 2.10. The slope of this proportionality is the magnetic susceptibility or magnetic permeability μ [Küpfmüller et al., 2008].

$$B = \mu H_{mag} \quad (2.10)$$

Figure 2.2.: Sketch of the magnetic field (green lines) generated by a direct current-carrying conductor

Ampère's circuit law relates the close-loop integral S of the magnetic field H_{mag} to the current I of the conductor enclosed by the space curve s and is presented in equation 2.11 [Springer et al., 1997].

$$\oint_S H_{mag} \cdot d\vec{s} = I \quad (2.11)$$

This general formulation applied to one arbitrary equipotential line with the radius r in figure 2.2 yields equation 2.12. Θ_m is the magnetomotive force which is of interest in the case of an electromagnet.

$$\Theta_m = \oint_S H_{mag} \cdot d\vec{s} = 2\pi r H_{mag} \quad (2.12)$$

Instead of just a single conductor, the strength of the generated magnetomotive force Θ_m is fairly increased by means of a lean inductor with the length l and a total number of windings N_w . The amplification is approximated in equation 2.13 [Küpfmüller et al., 2008].

$$\Theta_m = N_w I = H_{mag} l \quad (2.13)$$

2.2.2. Electromagnets

A classic magnetic coil is constructed by winding an inductor around a soft iron yoke. If the yoke has a horseshoe-shape, a magnetic field B is achieved which is comparable with figure 2.3. A homogenous magnetic field is formed between the magnetic north pole **N** and the magnetic south pole **S** inside the yoke. If a free current-carrying conductor is placed inside the "U"-form, a force, known as the Lorentz force, results.

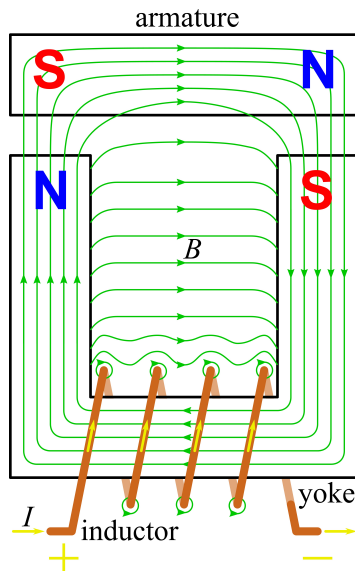


Figure 2.3.: Sketch of yoke and armature of an electromagnet

However, to yield an electromagnet, an armature is required. The armature itself is ferromagnetic or a permanent magnet, movable or at a fixed position and maintains an air-gap to the yoke. In contrast to electrical transformers, electromagnets do not possess a closed yoke. Figure 2.3 illustrates a schematic sketch of a common electromagnet. The current-carrying (yellow arrows) brown wire surrounds the yoke and induces a magnetic field, illustrated by green lines. In the case of direct current, a steady polarity is yielded, which is marked with **N** and **S**. Inside the inductor, a strong and homogenous magnetic field is generated. Outside, the magnetic field lines follow the lowest magnetic resistance. In the case of a yoke made of soft iron, the magnetic resistance is distinctly lower compared to the ambient air, thus almost the entire magnet flux is canalised through the yoke and the armature. Any kind of undesired magnetic flux eddies are neglected in this sketch. If a ferromagnetic armature is installed, the opposite polarity occurs (pole changing) to minimise the magnetic resistance. Thus, independent of the polarity of the yoke, the armature strive to close the air gap to the yoke. This behaviour is known as the Lenz's law [Lenz, 1834]. If a permanent magnet is installed as armature, the polarity is steady

and independent of the yoke. The variation in this case is the direction of motion. The assumed polarity in figure 2.3 forces the armature towards the yoke although a permanent magnet is used. If the direction of the direct current changes, the polarity of the yoke changes as well. Now, two south poles persist on the left hand side and two north poles on the right hand side. The armature is forced away from the yoke to minimise the magnetic resistance. In this setup, the armature is moved in both directions depending on the polarity of the yoke. The back motion of the armature is achieved via weight forces, other external forces, reversal polarity, mechanical actuator, etc.

Electromagnets are compact, very robust and cheap, and therefore repress the use of electromotors, hydraulic or pneumatic actuators in several conventional applications. The advantage is that no further moving parts or any kind of gearing is needed. Depending on the requirements and size, motion ranges from 0.1mm to 100mm and folding squares of 0.1° to 90° are realised [Stölting, 2006]. The fast response time and the potentially high generated forces enables a broad field of applications in control loops. Thus, several types of eletromagnetic actuators exist (e.g. alternating/ direct current voltage, lifting/ holding/ moving magnet, etc.). A classification is given by Kallenbach et al. [2008] and Weißgerber [2008].

2.2.3. Oscillating armature drive

The function of oscillating armature drives is based on electromagnets. Magnetic attractivity induces the active motion. In general, oscillating armature drives possess a passive back motion by means of springs to regain the initial position. Thus, the bearing and the mass of the armature construct a dynamic mass-spring oscillator possessing a distinct eigen frequency. Linear or rotational oscillations are empowered according to the bearing of the armature. Figure 2.4 depicts the two different types of oscillators. On the left hand side, the cyan arrows mark the linear motion. To perform a rotational motion, a kind of antisymmetry is required. In the case presented on the right hand side, the armature is placed above one end of the yoke. Another solution is the design of an antisymmetric yoke. Rotational motion always requires a fixed centre of rotation which has to be considered during the construction process.

2. Literature review and theoretical approaches

Oscillating armature drives are designed to operate at higher frequencies. Direct current may need an additional switchgear assembly because the return of the armature is implemented by a simple switch of the inductor. Therefore, only alternating current is considered. In this case, the armature follows the change of the magnetic polarisation and precise motions at higher frequencies are realised. The oscillation frequency depends directly on the frequency of the alternating current of the inductor. In the case of a ferromagnetic material, the armature strive tends to close the air gap, although the positive or the negative phase of the current is present. During the phase change, the polarity of the armature changes as well and for a short while, no magnetic flux exists and the back motion follows. Thus, the frequency of the actuator is twice that of the power supply frequency. The implementation of a precise sinusoidal motion is complex and needs further control devices.

Figure 2.4 represents the use of a permanent magnet as an armature. The oscillation moves in positive and negative direction and is in phase with the alternating current. Thus, the frequency of the actuator is equal to the power supply frequency. Moreover, the motion is much more efficient and precise [Janocha, 1992]. Theoretically the shape of motion is already sinusoidal. The highest motion amplitudes are reached in the range of the eigen frequency. It depends mainly on the mass of the armature and the stiffness of the springs. In most applications, the eigen frequency of the system is adapted to the commercial power frequency (50Hz).

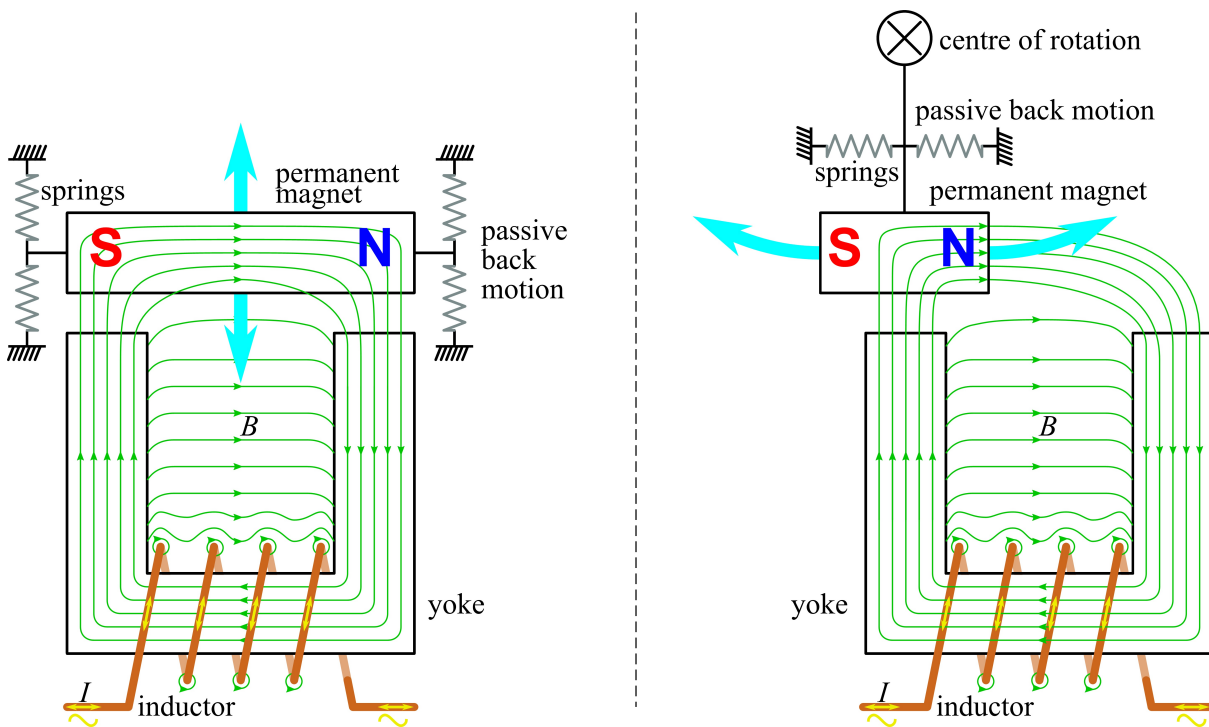


Figure 2.4.: Sketch of an oscillating armature drive with springs to achieve the passive back motion; left: linear oscillation; right: rotational oscillation

These actuators are very robust because the entire driving unit is insensitive to overload, overuse, and blocking. The lifespan only depends on the durability of the armature mounting and the fatigue of the retaining springs [Häberle and Häberle, 1990]. Thus, they are utilised in many commercial products. Famous applications are razors, hair clippers, aquarium pumps, impact screens, piston and membrane pumps, etc. [Janocha, 1992], [Häberle and Häberle, 1990]. One disadvantage of this type of driving unit is that dynamic imbalances cannot be compensated. Thus, the entire casing may vibrate during operation. Several options exist to increase the amplitude and/or the force of these actuators. The mechanism of action is the magnetic field induction, thus the usage of materials with low or no electromagnetic conductivity avoids undesired disturbances or distortions of the magnet field in the vicinity of the electromagnet. Furthermore, the magnetic field is highly time dependent. Thin lamellated iron plates reduce magnetic eddy currents (also known as Foucault currents [Fink and Christiansen, 1989]) compared to an iron block.

Often materials with higher specific electric resistance like silicon alloyed steel are applied [Janocha, 1992]. A permanent magnet with a stronger polarity also increases the effects until magnetic saturation occurs. Equation 2.13 constitutes that a higher current, more windings, and a longer inductor also strengthen the magnetic flux. The last mentioned influence is the air gap between yoke and armature. The smaller the gap, the less the losses of the magnetic flux.

2.3. Linear stability analysis

Intermediate conclusion: The approach of stability analysis is used to predict the dominant frequency of the natural flow due to K-H instabilities in rolling up shear layers. After a short literature review, the modified Orr-Sommerfeld equation is derived. In the presented case, the tilted shear layer possesses two velocity components in the mean flow field. Thus, the disturbance ansatz and the derived Orr-Sommerfeld equation take this modification into account.

The linear stability analysis predicts the evolution of waveshaped disturbances with infinite amplitude. It assumes parallel, laminar stream at a given steady flow field. This theory computes the amplification or damping of linear disturbances depending on the frequency and the wave number. Thus, the boundary layer upstream and the free shear layer downstream of the trailing edge of the swept, backward facing step are examined based on experimental data. The results yield the most amplified frequencies which are used afterwards for the oscillating flaps. However, linear stability analysis is a broad field and here, only a very short overview is given. The focus is on K-H instabilities in subsonic and incompressible flow.

2.3.1. A historical perspective

Although laminar and turbulent flows are already known, the mechanism why transition occurs is still unknown. Around 1878, Strutt and Rayleigh [1878] and Rayleigh [1879] consider analytically the instabilities of inviscid flow. They show that inviscid velocity profiles with an inflection point are unstable in all conditions and at all time. Thus, the instabilities of free jets and free shear-layers are explained. These instabilities are also entitled as inflection point instabilities. However, the reasons for occurrence of instabilities in viscous flow, especially the laminar-turbulent transition of boundary layer, remains unknown for several decades. Around 1907, the two mathematicians Orr [Orr, 1907a,b] and Sommerfeld [1908] develop an eigenvalue equation for viscous, incompressible flow based on the Navier-Stokes equations. It is a fourth-order differential equation and constitutes the origin of computing instabilities of laminar, parallel flow. This famous equation is named Orr-Sommerfeld equation. In 1921, the group of Prandtl focuses on stability analysis of viscous fluids [Prandtl, 1921]. Based on the first approaches of Heisenberg to solve the Orr-Sommerfeld equation [Heisenberg, 1924], Tollmien finds a solution for viscous instabilities [Tollmien, 1928]. One of the first applications of Tollmien's results is the prediction of the laminar-turbulent transition of boundary layer. This is performed by Schlichting and the transition process is named the Tollmien-Schlichting instability [Schlichting, 1933]. At that time, it is still questionable if the use of a linear ansatz is able to capture highly three-dimensional processes like transition. In 1947, Schubacher is the first who measures experimentally the existence of instability waves in boundary layers and thus validates the linear stability theory [Schubauer and Skramstad, 1947].

2.3.2. A brief literature review of shear-layer instabilities

In the early 1960s, the development of computers permits the investigation of several stability problems. Serrin [1959] uses an energy method instead of the linearised perturbation theory to compute different duct geometries and other bounded streams. Based on this viscous stability analysis he states that all bounded flows are stable for Reynolds numbers below 5.71. Betchov and Michalke are the first who investigate shear layer stability. Both approximate the shear layer velocity profile via a tanh-function. Betchov proves for the inviscid case that instabilities emerge at all Reynolds numbers [Betchov and Szewczyk, 1963]. These results are consistent with Rayleigh's findings. Furthermore, Betchov states that the laminar-turbulent transition arises at a Reynolds number of 150. Michalke examines the natural and

2. Literature review and theoretical approaches

amplified inviscid shear layer. He considers the vorticity distribution and he is able to find topological differences between the natural and forced case. He is the first who predicts the onset and control of vortex pairing by means of AFC [Michalke, 1964]. Furthermore, Michalke extends the theory also for viscous shear layers. Michalke's results are confirmed experimentally by Freymuth [1966] for laminar boundary layer. Nayfeh studies K-H instabilities in sub and supersonic flow. He applies linear as well as nonlinear stability theory. In the nonlinear case, the cut-off wave numbers are amplitude dependent. He considers the phase velocity of the first and second harmonic and their interactions [Nayfeh and Saric, 1971], [Nayfeh and Saric, 1972].

In 1970, Hackett is probably the first who investigates three-dimensional mixing layers experimentally and via stability analysis downstream of a 45° slanted trailing edge [Hackett and Cox, 1970]. Monkewitz and Huerre [1982] assume a tanh-function to estimate the velocity profile of a shear layer. They come to the conclusion that the maximum growth rate of a two-dimensional shear layer decreases approximately linearly with the velocity ratio λ . Furthermore, the ratio of the neutrally stable frequency and the most amplified is approximately two. Based on this statement, Ho and Huang [1982] state that the local length scale changes due to vortex merging. Based on their own stability analysis, they show that the most amplified frequency becomes stable during merging and the resulting subharmonic becomes the most amplified one. Furthermore, this newly regenerated subharmonic possesses the same growth rate as the linear amplification rate. Thus, they conclude that the linear stability analysis seems to capture some nonlinear mechanisms. Pierrehumbert and Widnall [1982] find two main instabilities in their stability analysis of a shear layer. One is a subharmonic one which corresponds to vortex pairing. This instability becomes most unstable in the two-dimensional case which means that the perturbations do not have a spanwise direction variation. The second instability is a transverse mode which requires a perturbation in spanwise direction and a cascade of vortical structures in spanwise is the consequence. This instability has a broadband receptivity to different phase shifts. In the same year, based on systematic studies of K-H instabilities in forced cases, Oster and Wygnanski [1982] validates several theoretical predictions. Furthermore, he suggests to extend the applicability of inviscid linear stability analysis to fully turbulent shear layers. Gaster et al. [1985] compare linear stability analysis with experiments of a forced shear layer. Although some parameters like the lateral phase angle distribution show a high agreement, the predicted amplifications of the forced flow exceed the observations in experiments. Based on the experiments by Wygnanski and Petersen [1987] with a forced shear layer at its fundamental and subharmonic frequency, Weisbrot and Wygnanski [1988] compute the corresponding linear stability analysis. A high agreement is observed for all measured parameters and only the prediction of the amplification rate in streamwise direction failed in case of forced flow. Lu wants to analyse rolling up shear layers which generates streamwise vortices. Due to the complexity, he isolates the skewing effect and examines skewed, inviscid mixing layers. He shows for incompressible, inviscid shear layers that the most unstable wave propagates approximately in the direction of the effective shear, especially for skew angles less than 40° [Lu and Lele, 1993].

In 1994, Kruscha and Fiedler [1994] compute stability analysis of non-parallel shear layers. They use measured velocity profile from Gründel and Fiedler [1993]. Thus, the velocity profile is given at discrete positions. They estimate the vorticity thickness and the characteristic velocity by means of a manually optimised best fit approach. Unfortunately, the estimated velocity profiles based on spline-functions are not documented, which renders a comparison impossible. Furthermore, they use a shooting method which is highly dependent on the chosen initial conditions. In 1995, Fiedler et al. [1995] states that linear stability analysis is in good agreement with experiments and he confirms that the most unstable wave vector is always normal to the mean vorticity vector. Jisheng and Fiedler [2001] use weak nonlinear approach to compute nonlinear effects as well. They conclude that three-dimensional shear layers have a higher maxing capacity due to the transverse mixing in the third spatial direction. Jürgens investigates a swept, backward facing step of infinite span. He finds that the most energetic eigenmode is dominant directly downstream of the step's trailing edge, where the shear layer emerges [Jürgens and Kaltenbach, 2003]. Based on these numerical data from Jürgens and Kaltenbach, Kelch computes the temporal and spatial stability of skewed shear layers [Kelch, 2003]. He uses the Chebyshev collocation method. This ansatz is regarded as the most promising approach to solve stability problems in this thesis. However,

Kelch still requires analytical functions and their derivations. In the presented thesis, the analysis tool is extended to capture discrete, non-equidistant sampling points as well. In 2006, Jürgens provides linear stability analysis of a skewed shear layer downstream of the swept, backward facing step. His analysis demonstrates that the spatial direction for the most effective amplification is not necessarily the direction of the ambient mean flow or the direction of the trailing edge. Rather, the optimal spatial direction lies between these two [Jürgens, 2006].

2.3.3. Derivation of the Orr-Sommerfeld equation

As stated in this very brief literature review, the Orr-Sommerfeld equation constitutes the origin of computing instabilities. Thus, the main steps to derive this fundamental equation are restated here. Equations 2.14 and 2.15 yield the mass balance and the momentum balance assuming a constant density and viscosity [Schade et al., 2007].

$$\nabla \underline{u} = 0 \quad (2.14)$$

$$\frac{\partial \underline{u}}{\partial t} + (\underline{u} \nabla) \underline{u} + \nabla p - \frac{1}{Re} \Delta \underline{u} = 0 \quad (2.15)$$

All quantities have to be normalised in the Navier-Stokes equation. The velocity is normalised by the reference velocity u_{ref} , all length scales by the reference length l_{ref} and the pressure by the reference pressure p_{ref} . The corresponding Reynolds number is $Re = \frac{\rho u_{ref} l_{ref}}{\eta}$. Besides the basic steady flow field (\underline{u}_s, p_s) , an expression for the small disturbances is required. Equations 2.16 and 2.17 approximate the disturbances with the amplitude $(0 \leq \epsilon \ll 1)$ via an infinite power series [Oertel, 1996].

$$\tilde{\underline{u}} = \epsilon \tilde{\underline{u}}_1 + \epsilon^2 \tilde{\underline{u}}_2 + \dots + \epsilon^n \tilde{\underline{u}}_n + \dots \quad (2.16)$$

$$\tilde{p} = \epsilon \tilde{p}_1 + \epsilon^2 \tilde{p}_2 + \dots + \epsilon^n \tilde{p}_n + \dots \quad (2.17)$$

The steady velocities and the disturbance velocities are superimposed and further all terms owning an amplitude of $(\geq \mathcal{O}(\epsilon^2))$ are neglected. The sole consideration of terms with the magnitude $\mathcal{O}(\epsilon)$ represents the linear character of this stability analysis. The summation of the steady and disturbed flow $\underline{u} = \underline{u}_s + \epsilon \tilde{\underline{u}}$, $p = p_s + \epsilon \tilde{p}$ contains the entire linearised flow field. They are added in Navier-Stokes equations (equation 2.14 and 2.15) and give the following equations 2.18 and 2.19.

$$\nabla(\underline{u}_s + \epsilon \tilde{\underline{u}}) = 0 \quad (2.18)$$

$$\begin{aligned} \frac{(\partial \underline{u}_s + \epsilon \tilde{\underline{u}})}{\partial t} + (\underline{u}_s \cdot \nabla) \underline{u}_s + (\epsilon \tilde{\underline{u}} \cdot \nabla) \underline{u}_s + (\underline{u}_s \cdot \nabla) \epsilon \tilde{\underline{u}} \\ + \nabla(p_s + \epsilon \tilde{p}) - \frac{1}{Re} \Delta(\underline{u}_s + \epsilon \tilde{\underline{u}}) = 0 \end{aligned} \quad (2.19)$$

This is the general formulation of the differential equations for the linearised, disturbed flow. If the assumed disturbances are zero ($\epsilon = 0$), the flow field in the equations 2.18 and 2.19 is equal to the basic steady flow. Thus this ansatz is considered to be physically consistent. However, the steady flow field fulfils the Navier-Stokes equations under any conditions and at all times, independent of the superimposed disturbances. Hence, in equations 2.20 and 2.21, the steady solution is not considered any more and, furthermore, the equations are divided by ϵ for clarity. They represent the linearised differential equations for incompressible, disturbed flow.

$$\nabla(\tilde{\underline{u}}) = 0 \quad (2.20)$$

$$\frac{\partial \tilde{\underline{u}}}{\partial t} + (\underline{u}_0 \nabla) \tilde{\underline{u}} + (\tilde{\underline{u}} \nabla) \underline{u}_0 + \nabla(\tilde{p}) - \frac{1}{Re} \Delta(\tilde{\underline{u}}) = 0 \quad (2.21)$$

A direct solving of these equations creates enormous computational effort. Thus, further assumptions are necessary to reduce the scope of this problem. The physical application of this stability analysis is the rolling up shear layer downstream of a swept, semi-span, backward facing step. The developing shear layer is skewed and curved. In the case of an infinite step, Kelch [2003] as well as Jürgens [2006] neglect

2. Literature review and theoretical approaches

the curvature of the shear layer, because it possesses no significant influence on the stability results. In the case of a finite step, the rolling up shear layer is much more curved. Thus, the region of interest is reduced to flow directly downstream of the trailing edge where the curvature is small compared to the skewness. Furthermore, by means of the parallel flow assumption, all velocity components of the steady flow depend only on the spatial direction z . This simplification holds only for high Reynolds numbers. Jürgens provides already good agreement at Reynolds numbers of $Re_h = 3000$ (based on the step height) [Jürgens, 2006]. The Reynolds numbers in this presented thesis are significantly higher, thus the parallel flow assumption is considered as valid. These reductions simplify the steady velocity vector as shown in equation 2.22. The disturbance velocities still depend on all spatial directions.

$$\underline{u}_0 = \begin{pmatrix} u_0(z, t) \\ v_0(z, t) \\ 0 \end{pmatrix}, \quad \underline{\tilde{u}} = \begin{pmatrix} \tilde{u}(x, y, z, t) \\ \tilde{v}(x, y, z, t) \\ \tilde{w}(x, y, z, t) \end{pmatrix}, \quad \tilde{p} = \tilde{p}(x, y, z, t) \quad (2.22)$$

The considered basic flow and the boundary conditions are steady and the starting process is neglected. Thus, the entire flow field is homogenous in time and the separation of variables ansatz is applied to the three-dimensional disturbances. The disturbances themselves are modulated by means of a complex Fourier-series. Equations 2.23 to 2.26 depict the chosen separated wave ansatz.

$$\tilde{u}(x, y, z, t) = \tilde{u}(z)e^{i(ax+by-\omega t)} \quad (2.23)$$

$$\tilde{v}(x, y, z, t) = \tilde{v}(z)e^{i(ax+by-\omega t)} \quad (2.24)$$

$$\tilde{w}(x, y, z, t) = \tilde{w}(z)e^{i(ax+by-\omega t)} \quad (2.25)$$

$$\tilde{p}(x, y, z, t) = \tilde{p}(z)e^{i(ax+by-\omega t)} \quad (2.26)$$

The complex wave numbers $a = a_r + ia_i$ and $b = b_r + ib_i$ and the complex wave frequency $\omega = \omega_r + i\omega_i$ represent disturbances which propagate parallel to the x-y plain and vary in time. $\tilde{u}(z), \tilde{v}(z), \tilde{w}(z), \tilde{p}(z)$ are the corresponding spatial amplitude functions. This leads to equation 2.27, which exhibits the physically sensible real part of the disturbances.

$$\Re(\underline{\tilde{u}}) = e^{\omega_i t} \underline{\tilde{u}} \cos(-a_i x - b_i y + \omega_r t) \quad (2.27)$$

The sign of ω_i determines the sign of the exponent. Hence, a positive ω_i lets the exponential function and the represented disturbances grow to infinity and amplification is present. In the opposite case of a negative ω_i , damping happens and the disturbances decrease asymptotically to zero. However, the wave ansatz is added in the two equations 2.20 and 2.21. For clarity, the resulting ordinary differential equation system in equations 2.28 to 2.31 is divided by $e^{i(ax+by-\omega t)}$.

$$a\tilde{u} + b\tilde{v} - i\tilde{w}_z = 0 \quad (2.28)$$

$$\left[au^{(0)} + bv^{(0)} - \omega \right] \tilde{u} - iu_z^{(0)}\tilde{\omega} + a\tilde{p} - \frac{i}{Re} \left(a^2 + b^2 - \frac{d^2}{dz^2} \right) \tilde{u} = 0 \quad (2.29)$$

$$\left[au^{(0)} + bv^{(0)} - \omega \right] \tilde{v} - iv_z^{(0)}\tilde{\omega} + b\tilde{p} - \frac{i}{Re} \left(a^2 + b^2 - \frac{d^2}{dz^2} \right) \tilde{v} = 0 \quad (2.30)$$

$$\left[au^{(0)} + bv^{(0)} - \omega \right] \tilde{w} - i\tilde{p}_z - \frac{i}{Re} \left(a^2 + b^2 - \frac{d^2}{dz^2} \right) \tilde{w} = 0. \quad (2.31)$$

This linear and homogenous system of ordinary differential equations includes derivations only in one spatial direction (here z -direction). These four equations are transformed into one single equation 2.32 by

simple line operations and the elimination of the pressure.

$$\left\{ [au_0 + bv_0] \left[\frac{d^2}{dz^2} - (a^2 + b^2) \right] - \left(a \frac{d^2 u_0}{dz^2} + b \frac{d^2 v_0}{dz^2} \right) + \frac{i}{Re} \left[\frac{d^2}{dz^2} - (a^2 + b^2) \right]^2 - \omega \left[\frac{d^2}{dz^2} - (a^2 + b^2) \right] \right\} \tilde{w} = 0. \quad (2.32)$$

This equation is widely known as the Orr-Sommerfeld equation. This result may also be derived by means of the multiple scale analysis [Oertel, 1996]. However, boundary conditions have to be implemented to derive a closed solution. In both cases, either a solid wall or an undisturbed free stream in the far field, the disturbances reduce asymptotically to zero. Hence, the amplitude itself and its gradient become zero. The boundary conditions of a free shear layer are depicted in equation 2.33.

$$\tilde{w} = \frac{d\tilde{w}}{dz} = 0, \quad z \rightarrow \pm\infty \quad (2.33)$$

Besides the trivial solution, only distinct combinations of a, b, ω solve the Orr-Sommerfeld equation at a given basic flow field. Thereby, a temporal stability analysis predetermines the wave numbers a, b and predicts the dominant (mostly amplified) frequency $\omega = \omega(a, b)$. A spatial analysis predicts $a = a(\omega), b = b(\omega)$ at a predetermined frequency ω . In the case of convective unstable flow, an amplification in one arbitrary spatial direction equals a damping in the opposite direction. Thus, a spatial analysis requires a distinguished spatial direction. A detailed discussion of local and global instabilities in temporal and spatial analysis is given by Huerre and Monkewitz [1990].

2.4. Bound vortices in a historical perspective and the Kutta-Joukowski theorem

Intermediate conclusion: The concept of bound vortices in potential flow to predict the generated lift is discussed. Under steady conditions, the famous Kutta-Joukowski equation yields the relationship between the generated circulation and the resulted lift. The approaches of Theodorsen, Isaacs, Greenberg and van der Wall which take unsteady conditions into consideration are summarised. The, as yet, missing validation of these theories is evident. A deep understanding and a validation of these approaches are essential for a long-wavelength actuation of trailing edge vortices. Only a precise prediction of the bound vorticity along the span under unsteady conditions yields the required input parameters for applying Betz's theory. Hence, the bound vortices are the link between an airplane motion and the generated streamwise vortex.

¹ The concept of bound vortices links the generated circulation of an object to its lift. All calculations are based on the potential flow assumption. Hence, flow separation, boundary layers, or friction do not occur in the scope of the theory. Although this assumption appears quite radical and unphysical, the lift prediction of this theory strongly agrees with airfoil measurements in pre-stall conditions. Unsteady effects like an unsteady inflow, fast pitching or plunge motion, or flap movement are included in this theory for several applications. Hence, a short introduction into the concept of bound vortices is given here.

Benjamin Robins is a military engineer and scientist, who studies the shooting range of artillery and other guns. He observes some unexplained variations in the shooting ranges and speculates that this is caused by the rotation of the bullets [Robins et al., 1805] (reprinted version from 1742). Thus, in 1742, he is probably the first who links rotation and lift. However, bullet aerodynamics is of such

¹The work presented in this section is partly based on Strangfeld et al. [2014]. Hans Müller-Vahl prepared the experimental setup at the Technion, Haifa, Israel. Christian Navid Nayeri and Christian Oliver Paschereit were responsible for the administrative frame work during this international cooperation. David Greenblatt mainly contributed to the idea to validate Isaacs' and Greenberg's theory based on the performed unsteady measurements. He also had the idea to predict the unsteady pressure distribution. However, all excerpts are written by myself.

2. Literature review and theoretical approaches

minor matter that no theoretical approaches are calculated. 150 years later, another research discipline is established which requires precise lift predictions. Near Berlin, in Derwitz, the pioneer Otto Lilienthal starts the first controlled glider flight in world history in 1891. His glider is based on the first systematic developments and tests of several different wing profiles. Otto Lilientahl performs more than 2500 flight tests, constructed more than 21 glider prototypes and continuously improves the glider, especially the wing profiles, to reach flight distances of up to 350 meters [Anderson, 1998]. In August 1896, he dies in a fatal accident while conducting another flight test. In spite of this dramatic accident, the young mathematician, Martin Wilhelm Kutta, is inspired by Lilienthal's glider flights and attempted to calculate theoretically the lift of different wing profiles. He finds that the flow leaves the trailing edge of airfoils smoothly; today this is known as the Kutta condition. Furthermore, in 1902, he is the first to publish the concept that the lift of an airfoil and the generated circulation are connected to each other [Kutta, 1902]. Just one year later, the Wright brothers start the first successful motorised flight test in world history. Independent of these events, the Russian mathematician Nikolai E. Joukowski (Zuhkouski) is the first in history who quantified the relation between the generated lift and circulation of an airfoil in 1906 [Joukowski, 1906]. Today, equation 2.34 is known as the Kutta-Joukowski theorem [Anderson, 2011].

$$L = s\rho u_0\Gamma \quad (2.34)$$

The generated lift L of an infinite two-dimensional airfoil is proportional to the span s , the fluid density ρ , the free stream velocity u_0 and the generated circulation Γ . In the steady case, the circulation is determined by the angle of attack and the cambered airfoil centre line. Once the circulation of the airfoil is known, the lift prediction is directly inferable. Thus, people are able to design appropriate airfoils by means of complex functions and conformal mapping, which is a mathematical tools to calculate the circulation. From 1911 to 1918, Ludwig Prandtl and his team develop the lifting line theory, also known as the Lanchester-Prandtl wing theory. By means of this theory, the lift of finite wing with three-dimensional vortex structures are predictable as well.

During this period and based on new mathematical approaches, new aircraft become much faster and more agile. Hence, in the twenties, the understanding of unsteady aerodynamics becomes more interesting and several aerodynamicists in the whole world worked on these problems. After two decades of Kutta and Joukowski's work, Wagner [1925] publishes calculations of forces acting on a flat plate in unsteady plunge motion. He also provides a first approach to calculate the lift of airfoils in pitching motion, which inspires Glauert [1930] to develop a complete theory for pitching motion. Challenged by the problem of wing flutter, in 1935, Theodorsen [1935] comes up with a landmark innovation by developing a general analytical solution for airfoils encountering oscillating angle of attack variations and oscillating plunge motion. Assuming a potential flow in a steady stream, he calculates all velocity potentials and determines the unsteady circulation, where the wake vorticity is determined by the Kutta condition. Today we refer to the Theodorsen function which includes multiples of the reduced frequency as its argument. In 1940, Jones [1940] uses an approximation of the Wagner function for predicting the lift overshoot of a finite wing with different aspect ratios due to a unit sharp-edge gust.

The need for more accurate estimations of helicopter blade loads motivates Isaacs [1945] to extend Theodorsen's work to include an oscillating free stream with no phase lag between the leading and trailing edges. A year later, he extends his unsteady inflow theory to include angle of attack oscillating with the same frequency [Isaacs, 1946]. Based on Theodorsen's and Isaacs' approaches, Greenberg [1947] develops a solution for the dynamic lift and moment of a flat plate in an oscillating free stream including an oscillating angle of attack and oscillating plunge motion. Furthermore, his approach includes an arbitrary phase lag between the oscillating free stream and the periodically pitching wing. However, Greenberg's modulation of the unsteady free stream also implies a fore-aft wing motion. More than 30 years later, Kottapalli develops a new theory directly motivated by helicopter aerodynamics. Its focus is the prediction of the dynamic drag behaviour under unsteady free stream. His derivation is based on an order of magnitude approximation to the in-plane perturbation velocity [Kottapalli, 1985]. Kottapalli asserts that this assumption is more plausible than Greenberg's high frequency assumption. However, Kottapalli's theory is limited to small free stream fluctuations. In 1991, van der Wall provides an extensive review of existing theoretical approaches in detail and extends Isaacs' theory to harmonic plunge motion

and unsteady angle of attack variations including arbitrary multiples of the free stream harmonic [van der Wall, 1991], [van der Wall and Leishman, 1992], [van der Wall, 1992], [van der Wall and Leishman, 1994]. He concludes that Isaacs' theory is the only "exact theory" without additional simplifications. Furthermore, he determines significant deviations of Greenberg's theory to Isaacs' theory for amplitudes higher than 0.4. Based on Theodorsen's theory, Gaunaa develops an analytical approach for variable geometry airfoils including camberline elasticity in arbitrary motion. However, he does not consider any unsteady free stream in his calculations [Gaunaa, 2006].

In light of the advances described above, in particular those of Greenberg and Isaacs, it is surprising that many of these theories have not been fully validated experimentally, especially for large free stream oscillation amplitudes [Leishman, 2002]. Favier et al. investigate a pitching NACA 0012 airfoil in unsteady free stream [Favier et al., 1979], [Favier et al., 1988]. The wind tunnel generates high reduced frequencies up to 1.6 and velocity amplitudes of more than 35%. Although the airfoil lift shows significant dynamic effects, a comparison to Isaacs' theory is not evaluated.

More recently, Granlund et al. [2014] investigate a NACA 0009 experimentally over a broad range of reduced frequencies at relatively small amplitudes of 0.1. It is not clear why this lack of validation exists, but it seems that the existing experimental facilities lack the large, unsteady amplitudes. Various wind tunnel challenges include fan stall, and large lag effects due to inertia and acoustic resonance. Indeed, a review of facilities reveals that the vast majority of them simulate only changes in airfoil angle of attack, namely pitching or plunging [Martin et al., 1974], [McCroskey and Philippe, 1975], [McCroskey et al., 1976]. Tunnels that produce an unsteady free stream are rare. The most common approach is to modify a standard steady wind tunnel to produce unsteady flows [Ham et al., 1974], [Pierce et al., 1978], [Retelle et al., 1981], [Szumowski and Meier, 1996], typically using rotating vanes, louvers or some variation of this idea. Another approach is the gust generation by a system of individually rotatable airfoils upstream of the investigated object. The upstream airfoils rotate and generate vortices in their wake which induce horizontal and vertical gusts. Nevertheless, the occurrence of three-dimensional flow structures in the measurement section make this system unattractive [Tang et al., 1996]. Some tunnels combine the independent capabilities of angle of attack and wind speed variation [Favier et al., 1979], [Goodrich and Gorham, 2008], [Gompertz et al., 2011]. An exception is the approach of Favier et al. [1988] that employs a two degrees of freedom construction to pitch and translate the airfoil. Recently, an unsteady wind tunnel is developed to produce large amplitude oscillations of the free stream [Furman et al., 2013]. Problems of fan stall, large inertial effects, and acoustic resonance are overcome during the initial design and testing phases. The tunnel proves to be ideally suited to validate large amplitude unsteady effects and, in particular, to assess the validity of theoretical approaches.

During the first half of the 20th century, the study of unsteady aerodynamics is motivated by problems associated with wing flutter, the estimation of helicopter blade loads, and the effect of wing gusts on aircraft. Many of these problems remain relevant today. In recent years, the stability and survivability of small low-flying air vehicles that are exposed to highly unsteady winds have produced renewed interest in the topic. Furthermore, the desire for robust design of wind turbines - whose blades are exposed to highly unsteady flows produced by, inter alia, yaw misalignments, blade tip plunge motion, tower passing, and atmospheric turbulence - requires an urgent need for the accurate prediction of unsteady maximum fatigue loads [Barlas and Van Kuik, 2010].

2.5. Prediction of unsteady lift

Intermediate conclusion: As a basis, the derivation of the Kutta-Joukowski equation is shortly summarised and the required modifications considering unsteady conditions are emphasised. The solution of the resulting integrals includes the Theodorsen-functions. Then, the final equations from Greenberg's, Isaacs', and van der Wall's theories considering the unsteady lift and pitching moment are presented and discussed. These equations represent the basis to predict the unsteady spanwise circulation which is crucial in determining the long-wavelength excitation of the wing tip vortices.

2. Literature review and theoretical approaches

¹ The complete derivation of unsteady lift for plunge motion, pitching, and unsteady free stream is beyond the scope of this thesis. Nevertheless, a deeper understanding of the Kutta-Joukowski theorem is necessary for the derivation of the unsteady pressure distribution in the next chapter. Thus, the derivation of the static case is recapitulated briefly to introduce the general procedure. Then, the modifications of this approach for the unsteady case are discussed. At the end, the final results from Isaacs, Greenberg and van der Wall are presented. Although these equations consider only a two-dimensional wing, they represent the basis of Betz's theory under unsteady conditions. By means of the mentioned theories, the unsteady bound vorticity is predicted at each spanwise position on a finite wing. This is crucial for computing the wing tip vortex strength and the centroid position in the end.

By means of the thin airfoil theory, the airfoil is reproduced by its centre line [Münk, 1922]. This line is replaced by a vorticity sheet. Its strength is adjusted that this geometrical line corresponds to a stream line in the potential field with a stagnation point at the leading and trailing edge. In this study, only symmetrical airfoils are considered. Thus, the centre line is straight and the airfoil reduces to a flat plate. The flat plate is modulated as an infinite number of vortices which form a continuous contour line. The superposition of the induced velocities of the vorticity sheet and the free stream result in a velocity jump above and below the plate. This velocity jump is identical to a pressure jump and the cumulated static pressure variation along the chord represents the generated lift. Hence, the lift of the wing, which is replaced by a flat plate which is modulated as a vorticity sheet, depends on the strength of the infinite number of vortices.

Two constraints have to be fulfilled to determine this strength and to predict the entire circulation which is proportional to the lift. The first constraint is equation 2.35. It takes into account that, when considering a solid plate, no fluid runs through. Hence, the normal velocity v_n has to be zero along the entire chord at all times. This constraint alone yields an infinite number of solutions. Thus, a second constraint is required to include the flow physics and to select the solution which occurs in nature. This constraint is the well known Kutta condition. Kutta states that the flow of the upper and lower side of the plate has to be aligned. If they do not, the mass balance is violated and the solution space is not convex anymore. This request finally results in the consequence that the flow at the trailing edge achieves a stagnation point. Hence, the bound vorticity sheet strength at the trailing edge becomes zero at all times, compare equation 2.36.

$$v_n(x, t) \equiv 0 \quad (2.35)$$

$$\gamma_b(x = \frac{c}{2}, t) \equiv 0 \quad (2.36)$$

In the static case, two induced velocities influence the normal velocity along the chord v_n . The first one is the free stream with $\sin(\alpha)u_0$. Here and in all further derivations, the small angle assumption is used, thus the normal velocity component of the free stream reduces to αu_0 . The second induced velocity is generated by the vorticity sheet itself. Each vortex of the bound vorticity sheet induces normal velocities $v_{n,b}$ along the chord on all neighbouring vortices. The summation of all normal velocities has to be zero as expressed in equation 2.37.

$$v_n(x) \equiv 0 = \alpha u_0 - v_{n,b}(x) \quad (2.37)$$

$$\gamma_b(x = \frac{c}{2}) \equiv 0 \quad (2.38)$$

Now a relation between the induced normal velocities and the bound vorticity sheet is required. In a potential field, Biot-Savart's law is applied. The induced velocities on an arbitrary point in space is the strength of the considered potential vortex divided by the distance to the potential vortex and 2π [Schade et al., 2007]. In our case, the flat plate is not reproduced by just one single vortex, hence the entire continuous vorticity sheet is integrated to determine the normal velocity at one fixed position x as shown

¹The work presented in this section is partly based on Strangfeld et al. [2014]. Hans Müller-Vahl prepared the experimental setup at the Technion, Haifa, Israel. Christian Navid Nayeri and Christian Oliver Paschereit were responsible for the administrative frame work during this international cooperation. David Greenblatt mainly contributed to the idea to validate Isaacs' and Greenberg's theory based on the performed unsteady measurements. He also had the idea to predict the unsteady pressure distribution. However, all excerpts are written by myself.

in equation 2.39 [Anderson, 2011].

$$v_{n,b}(x) = \frac{1}{2\pi} \int_0^c \frac{\gamma_b(\eta)}{x - \eta} d\eta \quad (2.39)$$

This expression is transformed into cylinder coordinates in equation 2.40 with $\eta = 0.5c(1 - \cos(\theta))$ to derive a closed analytical solution.

$$v_{n,\theta}(x) = \frac{1}{2\pi} \int_0^\pi \frac{\gamma_b(\theta) \sin(\theta)}{\cos(\theta) - \cos(\theta_0)} d\theta \quad (2.40)$$

The solution of this integral is given in equation 2.41 [Anderson, 2011].

$$\gamma_b(\theta) = 2\alpha u_0 \frac{1 + \cos(\theta)}{\sin(\theta)} \quad (2.41)$$

This is a fascinating result. The solution for $\gamma(\theta)$ is independent of the considered arbitrary but fixed position θ_0 . Thus, one might state that this system is kind of "self-adjusting". The integration of the bound vorticity sheet along the entire chord achieves the generated circulation of airfoil, see equation 2.42.

$$\Gamma = \int_{-0.5c}^{0.5c} \gamma_b(x) dx \quad (2.42)$$

Γ is transformed into cylinder coordinates as well and the bound vorticity sheet from equation 2.41 is added. The integral is solved and a simple expression for the circulation is found in equation 2.43.

$$\Gamma = \pi \alpha c u_0 \quad (2.43)$$

For completeness, the circulation is added into the Kutta-Joukowski equation, see 2.44.

$$L_s = s\rho u \Gamma = s\pi \alpha c \rho u_0^2 \quad (2.44)$$

Thus, in the static case a simple expression for the generated lift is found via the integration of the bound vorticity sheet. In the unsteady case, the procedure to determine the lift is the same. Nevertheless, the equations are much more complex due to the time dependence. The unsteady cases considered here assume a fixed geometry and incompressible flow. Thus, two potential sources of unsteadiness exist. The free stream velocity itself may be unsteady. This definitely leads to a time dependent circulation as well. In the case of pure pitching or plunge motion, the free stream is constant but the lift and hence the circulation vary in time as well. Although the free stream is not necessarily unsteady, the ansatz for the unsteady lift is given in equation 2.45.

$$L(t) = s\rho u(t)\Gamma(t) \quad (2.45)$$

The two constraints stay the same. The bound vorticity sheet has to be zero at the trailing edge at all times and no fluid runs through the flat plate. In the unsteady case, a third source of induced normal velocities arises. Due to the unsteady effects, the wake of the airfoil is not constant anymore. In the steady case, a starting vortex exists but after that, the emitted net vorticity is zero. In the unsteady case, the lift varies and hence the generated circulation of the airfoil. To keep the entire circulation in the system constant due to Kelvin's circulation theorem, the circulation increase has to be compensated. This is the main idea of the unsteady lift theory. If the bound circulation changes by the amount of $\Delta\Gamma$, a vortex at the trailing edge is shed into the wake with the same absolute strength and inverted rotational sense resulting in $-\Delta\Gamma$. Hence, the wake yields a time varying net vorticity distribution γ_w which induces normal velocities as well. The wake itself is assumed to stay planar. The normal velocities emitted by the wake $v_{n,w}(x, t)$ have

2. Literature review and theoretical approaches

to be taken into account in equation 2.46.

$$v_n(x, t) \equiv 0 = \alpha(t)u_0(t) + v_{n,w}(x, t) - v_{n,b}(x, t) \quad (2.46)$$

$$\gamma_b(x = \frac{c}{2}, t) \equiv 0 \quad (2.47)$$

A detailed explanation of the unsteady lift is not outlined here. The complete derivation is given by Theodorsen [1935]. However, during the derivation one obtains the following expression $C(k)$ in equation 2.48 [Theodorsen, 1935].

$$C(k) = \frac{\int_1^\infty \frac{x_0}{\sqrt{x_0^2-1}} e^{-ikx_0} dx_0}{\int_1^\infty \frac{x_0+1}{\sqrt{x_0^2-1}} e^{-ikx_0} dx_0} \quad (2.48)$$

This is the so called Theodorsen function. For a more general understanding, a short interpretation is discussed. The denominator takes into account the induced normal velocities due to the wake vorticity. The numerator stands for the induced normal velocities of the bound vorticity. Thus, the Theodorsen function incorporates both effects and expresses the dynamics of the system. This function solves all different velocity potentials for pitching, plunge motion, and flap deflection at constant free stream. Equation 2.49 illustrates the closed solution of these integrals [Theodorsen, 1935].

$$C(k) = F(k) + iG(k) = \frac{J_1(J_1 + Y_0) + Y_1(Y_1 - J_0)}{(J_1 + Y_0)^2 + (Y_1 - J_0)^2} - i \frac{Y_1(J_1 + Y_0) - J_1(Y_1 - J_0)}{(J_1 + Y_0)^2 + (Y_1 - J_0)^2} \quad (2.49)$$

The Theodorsen function is a linear combination of Bessel functions of the first kind J and the second kind Y . All Bessel functions are subjected to the argument k which is displaced for clarity. The parameter k is the reduced frequency which is nondimensionalised with respect to the free stream velocity, the airfoil chord and the angular frequency ω of the unsteady action as shown in equation 2.50.

$$k = \frac{\omega c}{2u_0} \quad (2.50)$$

Based on the results regarding the unsteady lift and moment in constant free stream, Isaacs and Greenberg extended this theory to an unsteady free stream. Their solutions are valuable results for comparison and the basis for further theoretical studies. Thus, their solutions are repeated here briefly. Both authors assume an unsteady free stream in a sinusoidal form as expressed in equation 2.51.

$$u(t) = u_0(1 + \sigma \sin(\omega t)) \quad (2.51)$$

The free stream is a superposition of the steady velocity u_0 and a time varying part with the amplitude σ . The absolute value of σ is less than one to avoid any conditions with back flow. Furthermore, the wavelength of the velocity variation is considerably larger than the airfoil chord. The equations 2.52 and 2.53 depict the results of Isaacs' theory [Isaacs, 1945, 1946]. Isaacs does not imply any additional assumptions regarding the wake. Thus, his results are considered to be mathematically exact [van der Wall, 1992]. Regarding the lift coefficient at constant angle of attack and unsteady inflow in equation 2.52, the term $0.5\sigma k \cos(\omega t)$ represents the noncirculatory solution. The rest represents the circulatory solution which contains the quasi steady lift and the unsteady wake (depicted by l_m). Isaacs' results include two

nested summations. The coefficients of the first summation are the real part \Re and imaginary part \Im of l_m .

$$\frac{C_l(t)}{C_{l,qs}} = \frac{1}{(1 + \sigma \sin(\omega t))^2} [1 + 0.5\sigma^2 + \sigma(1 + \Im(l_1) + 0.5\sigma^2) \sin(\omega t) + \sigma(\Re(l_1) + 0.5k) \cos(\omega t) + \sigma \sum_{m=2}^{\infty} (\Re(l_m) \cos(m\omega t) + \Im(l_m) \sin(m\omega t))] \quad (2.52)$$

$$\frac{C_{m,le}(t)}{C_{m,qs,le}} = \frac{1}{(1 + \sigma \sin(\omega t))^2} [1 + 0.5\sigma^2 + 2\sigma \sin(\omega t) - 0.5\sigma^2 \cos(2\omega t) + \sigma \sum_{m=1}^{\infty} (\Re(t_m) \cos(m\omega t) + \Im(t_m) \sin(m\omega t))] \quad (2.53)$$

l_m in equation 2.54 includes the second summation.

$$l_m = -m(-i)^m \sum_{n=1}^{\infty} [F_n(J_{n+m}(n\sigma) - J_{n-m}(n\sigma)) + iG_n(J_{n+m}(n\sigma) + J_{n-m}(n\sigma))] \quad (2.54)$$

$$\left. \begin{matrix} F_n \\ G_n \end{matrix} \right\} = \frac{J_{n+1}(n\sigma) - J_{n-1}(n\sigma)}{n^2} \left\{ \begin{matrix} F(nk) \\ G(nk) \end{matrix} \right. \quad (2.55)$$

The two functions $F(nk)$ and $G(nk)$ are real and imaginary parts of the Theodorsen function $C(k)$ given in equation 2.49. For very low reduced frequencies $k \rightarrow 0$, the limits are $F(nk) \rightarrow 1$ and $G(nk) \rightarrow 0$. If σ becomes zero as well, Isaacs' unsteady lift converges to the steady lift L_s in equation 2.44.

Although Isaacs and Greenberg directly calculate the unsteady lift and moment, in this thesis the lift and moment coefficient are considered. This formulation is regarded as more meaningful because the unsteady effects are clearly separated from the quasi steady effects mainly dominated by the variation of the dynamic pressure of the free stream [Strangfeld et al., 2014]. Thus, just for completeness, the normalisation of the unsteady lift is recapitulated here. The two equations 2.56 and 2.57 illustrate the normalisation by means of the time varying dynamic pressure $q = (1 + \sigma \sin(\omega t))^2$.

$$\frac{C_l(t)}{C_{l,qs}} = \frac{L(t)}{L_s} \frac{1}{(1 + \sigma \sin(\omega t))^2} \quad (2.56)$$

$$\frac{C_{m,le}(t)}{C_{m,le,qs}} = \frac{M_{le}(t)}{M_{s,le}} \frac{1}{(1 + \sigma \sin(\omega t))^2} \quad (2.57)$$

The two steady quantities are given in equation 2.58 and 2.59. The leading edge moment coefficient is considered here because the quarter-chord moment is zero for symmetrical airfoils in potential flow [Anderson, 2011].

$$L_s = \pi \rho c u_s^2 \alpha \quad (2.58)$$

$$M_{s,le} = 0.5 \pi \rho c^2 u_s^2 \alpha \quad (2.59)$$

Although Greenberg's theory includes an unsteady free stream, angle of attack oscillations, and plunge motion, only the particular case of unsteady inflow encountering a static wing is discussed in the following. In contrast to Isaacs, Greenberg's theory includes additional assumptions to derive a closed form solution. He used the high frequency assumption which gives the wake vorticity a harmonic sinusoidal form. This may be questionable because it corresponds to a small σ approximation [van der Wall and Leishman, 1994]. The two equations 2.60 and 2.61 show the total force and total moment for arbitrary harmonic inflow based on Greenberg's theory [Greenberg, 1947].

$$L = -\pi \rho (0.5c)^2 \dot{u}(t) \alpha - \pi \rho u(t) c [u_s \alpha + u_s \sigma \alpha C(k) e^{i\omega u t}] \quad (2.60)$$

$$M = -\pi \rho (0.5c)^3 \dot{u}(t) a \alpha - 0.5 \pi \rho u(t) c^2 (a + 0.5) [u_s \alpha + u_s \sigma \alpha C(k) e^{i\omega u t}] \quad (2.61)$$

2. Literature review and theoretical approaches

Using the velocity profile specified in equation 2.51, Greenberg's theory leads to the two equation 2.62, and 2.63 for the normalised lift coefficient and normalised pitching moment coefficient [Greenberg, 1947].

$$\frac{C_l(t)}{C_{l,qs}} = \frac{1}{(1 + \sigma \sin(\omega t))^2} [(1 + 0.5\sigma^2 F) + \sigma(1 + F) \sin(\omega t) + \sigma(0.5k + G) \cos(\omega t) + 0.5\sigma^2 G \sin(2\omega t) - 0.5\sigma^2 F \cos(2\omega t)] \quad (2.62)$$

$$\frac{C_{m,le}(t)}{C_{m,qs,le}} = \frac{1}{(1 + \sigma \sin(\omega t))^2} [-ka\sigma \cos(\omega t) + (1 + 2a)(1 + 0.5\sigma^2 F + \sigma(1 + F) \sin(\omega t) + \sigma G \cos(\omega t) + 0.5\sigma^2 G \sin(2\omega t) - 0.5\sigma^2 F \cos(2\omega t))] \quad (2.63)$$

Regarding equation 2.62 and 2.63, it is obvious that only the first and second harmonic are modulated. For many years, Greenberg's theory is regarded as the most valid and reliable approach for rotorcraft aeroelasticity. Although Greenberg's approach is convenient by its simplicity, the high frequency assumption limits the range of application. van der Wall states that this assumption is equivalent to neglecting the flow oscillation amplitude for the induced velocities. Consequently, the reduced frequency is underestimated for the lower velocities and overpredicted for the higher velocities. Finally, van der Wall summarises that Greenberg's prediction is valid only for small and moderate amplitudes ($\sigma \leq 0.4$) [van der Wall, 1992]. van der Wall generalises Isaacs' results. He includes plunge motion into the theory and an arbitrary pitching axis. Furthermore, Isaacs considers only a linear combination of a sine and cosine functions, van der Wall includes all higher harmonics (for the plunge motion as well) to predict the unsteady lift for arbitrary motion in both degrees of freedom, see equation 2.64.

$$\begin{aligned} \frac{C_l(t)}{C_{l,qs}} = & \frac{1}{(1 + \sigma \sin(\omega t))^2} 0.5k [(\sigma \bar{\alpha}_0 + \bar{\alpha}_{1S} + k(a\bar{\alpha}_{1C} - \bar{h}_{1C}) - 0.5\sigma \bar{\alpha}_{2C}) \cos(\omega t) \\ & + (-\bar{\alpha}_{1C} + k(a\bar{\alpha}_{1S} - \bar{h}_{1S} - 0.5\sigma \bar{\alpha}_{2S})) \sin(\omega t) \\ & + \sum_{n=2}^{\infty} n(\bar{\alpha}_{nS} + nk(a\bar{\alpha}_{nC} - \bar{h}_{nC}) + 0.5\sigma(\bar{\alpha}_{(n-1)C} - \bar{\alpha}_{(n+1)C})) \cos(n\omega t) \\ & + \sum_{n=2}^{\infty} n(-\bar{\alpha}_{nC} + nk(a\bar{\alpha}_{nS} - \bar{h}_{nS}) + 0.5\sigma(\bar{\alpha}_{(n-1)S} - \bar{\alpha}_{(n+1)S})) \sin(n\omega t)] \\ & + \frac{1}{(1 + \sigma \sin(\omega t))^2} [((1 + 0.5\sigma^2)\bar{\alpha}_0 + \sigma(\bar{\alpha}_{1S} - 0.5k((0.5 - a)\bar{\alpha}_{1C} + \bar{h}_{1C}) - 0.25\sigma \bar{\alpha}_{2C})) \\ & \cdot (1 + \sigma \sin(\omega t)) + \sum_{m=1}^{\infty} (\Re(l_m) \cos(m\omega t) + \Im(l_m) \sin(m\omega t))] \end{aligned} \quad (2.64)$$

The most general formulation of the coefficients is given by van der Wall [1992] (the coefficient $imk\frac{c}{2}$ in equation B.41 in van der Wall [1992] contains a typo, the coefficient in front of the integral must be $imk\frac{2}{c}$. This typo has no consequence for the rest of van der Wall [1992]). Equations 2.65 to 2.68 determine the desired parameters.

$$l_m = -2m(i)^{-m} \sum_{n=1}^{\infty} [F_n(J_{n+m}(n\sigma) - J_{n-m}(n\sigma)) + iG_n(J_{n+m}(n\sigma) + J_{n-m}(n\sigma))] \quad (2.65)$$

$$F_n + iG_n = [F(nk) + iG(nk)]n^{-2}(H_n + iH'_n) \quad (2.66)$$

$$H_n = \frac{J_{n+1} - J_{n-1}}{2} [\sigma \bar{\alpha}_0 - \bar{\alpha}_{1s} - k((0.5 - a)\bar{\alpha}_{1c} + \bar{h}_{1c})] - \frac{2J_n}{n\sigma} \bar{\alpha}_{1s} \quad (2.67)$$

$$H'_n = \frac{J_{n+1} - J_{n-1}}{n} \bar{\alpha}_{1c} + \frac{J_n}{\sigma} [\bar{\alpha}_{1c}(1 - \sigma^2) - k((0.5 - a)\bar{\alpha}_{1s} + \bar{h}_{1s})] \quad (2.68)$$

Although van der Wall presents the most holistic approach, the outcome of the equations is still the integral forces like the lift and the moment. The purpose of this thesis is to predict the unsteady pressure

distribution as well. Thus, some more expressions from van der Wall are required and recapitulated in the equations 2.69 to 2.73 [van der Wall, 1992].

$$a_m = \frac{A_m}{R_m} \quad (2.69)$$

$$R_0 = 1 \quad (2.70)$$

$$R_m = 1 + imk \frac{2}{c} \int_0^\infty e^{-im \frac{\omega \Lambda}{u_s}} \left(\sqrt{\frac{c}{\Lambda} + 1} - 1 \right) d\Lambda \quad (2.71)$$

$$A_0 = \pi c \alpha_s u_s [(1 + 0.5\sigma^2) \bar{\alpha}_0 + \sigma(\bar{\alpha}_{1s} - 0.5k(0.5 - a)\bar{\alpha}_{1c} - 0.5k\bar{h}_{1c} - 0.25\sigma\bar{\alpha}_{2c})] \quad (2.72)$$

$$A_m = \frac{i^m}{m} \pi c \alpha_s u_s (H_m(m\sigma) + iH'_m(m\sigma)) \quad (2.73)$$

2.6. Interaction of the streamwise and spanwise vortices

Intermediate conclusion: This brief review recapitulates Betz's theory which is considered to be the most accurate approach to determine the interaction between tip vortices and the wing wake still today. Furthermore, a connection to helicopter and wind turbine aerodynamics is depicted. In these cases, the oscillating free stream and angle of attack require an unsteady formulation of Betz's theory.

Figure 1.1 considers a finite wing. The lift or the circulation of the bound vortex at an arbitrary spanwise position generates a vorticity sheet at the wing's trailing edge. The flow around the wing tip due to the pressure difference between the pressure and suction sides constitutes the origin of the streamwise vortex and the roll up process starts. Based on the mentioned theories, the unsteady bound circulation is determined at each spanwise position. With this basis, the long-wavelength excitation of the wing tip vortex may be calculated.

Albert Betz, the successor of Ludwig Prandtl as the leader of the "Aerodynamischen Versuchsanstalt" in Göttingen, Germany, is the first who investigates this roll up process in detail. In 1932, he publishes his approach which bases on the consequent compliance of Prandtl's lifting-line theory [Prandtl, 1918, 1919] and the Kutta-Joukowski theorem. The approach of Betz contains three main assumptions. First, the circulation has to be constant in the entire system. This is just another formulation of the momentum balance. In consequence, the spanwise vorticity of each half of the wing has to be transformed into a streamwise vortex downstream of the wing. This vortex yields the same amount of circulation. Due to the symmetry of the wing, the induced velocities from one vortex to another are symmetrical as well. This leads to the second assumption. The spanwise position of the emitted streamwise vortex pair is constant at each time step. They only move in normal direction. The third assumption is that the moment of inertia has to be constant in the entire system as well. Thus, the moment of inertia of the spanwise vorticity distribution directly at the trailing edge around its centroid is equal to the moment of inertia of the emitted streamwise vortex around its vortex centre. Nevertheless, this approach seems to be forgotten for almost 40 years. Still in 1951, Spreiter and Sacks [1951] state that the roll up of trailing edge vortices at high aspect ratio wings is of "little practical importance".

In the 1960s, due to larger passenger airplanes and an increased air traffic, the hazards of strong wing tip vortices come into focus. For a first estimate, Rankine or Hamel-Ossen vortices in potential flow are applied to predict the vortex strength and maximum tangential velocity. These vortex models assume a uniform vorticity distribution in the vortex core region. Eventually, the inaccurate model predictions fail by an order of one or two magnitudes close to the vortex centre. In 1971, Donaldson [1971] rediscovers Betz's vorticity theory and applies it explicitly to different finite wing geometries. A comparison to flight tests reveals a good agreement of all vortex parameters. Donaldson [1971] concludes that ordinary potential flow vortices are insufficient and only the theory of Betz describes the vorticity sheet roll up process accurately. This new or reinvented approach initiates several research investigations in the following years. Brown [1973] investigates two different wing loading distributions, an elliptical and a parabolic one. His experiments validate Betz's theory and he shows that the loading distribution has a significant influence on the circulation and the peak velocity of the emitted streamwise vortex. Mason and Marchman [1973] validate Betz's theory experimentally as well and conclude that this theory predicts all required vortex parameters "excellently". Furthermore, they state that the streamwise vortex becomes more intense as the majority of vorticity is shed near the wing tip. Chevalier [1973] performs a free field flight test with two different airplanes, a DeHavilland Beaver DHC-2 and a Beechcraft T-34B. He pitches periodically at a mean angle of attack of 6° with an amplitude of $\pm 2^\circ$. The test are conducted at 0.125, 0.25, and 0.5 Hz. At a frequency of 0.25 Hz, the time span for vortex bursting is reduced by approximately the half. He speculates that the Crow instability is amplified by the harmonic pitching and promotes the vortex bursting. In the same year, Rossow [1973] predicts analytically the circulation distribution of the trailing vortex for different spanwise lift distributions. Furthermore, he computes the generated velocity field in the wake due to different trailing vortex shapes. Two years later, Rossow [1975] develops the inverse Betz method. With this approach, the spanwise circulation distribution is derived from the circulation of the streamwise vortex in the wake. He validates his ansatz by experiments and shows significant differences between several wing geometries. In 1977, Bilanin et al. [1977] investigate

the vortex behaviour and interaction in the wake including flaps, fuselage, and engines. They conclude that the entire roll up and vortex merging process is sensitive to small changes in the spanwise loading distribution. In 1979, Saffman and Baker [1979] publish a review paper including analytical, experimental, and numerical approaches to calculate the streamwise vorticity distribution due to a vorticity sheet roll up. They further describe two- and three-dimensional interactions between vortex pairs. After this decade of intensive investigations, validations, and testings, a second period of almost 20 years occurs whilst no remarkable research initiative considers the vorticity sheet roll up downstream of a finite wing and the transformation into a streamwise vortex.

In 1997, Rossow [1997] tries to improve Betz's theory to predict complex wakes that roll up into more than one vortex pair. He uses several vortex invariants to extract additional information. However, his intention fails and he finally concludes that the existing Betz method continue to be used. In 1998, Spalart [1998] reviews the vortex dynamics in the wake of an airplane. The instability observed, for example, by Chevalier [1973] is a phenomenon which Spalart titles as vortex bursting. He emphasises that vortex breakdown is fundamentally different to vortex bursting. Nevertheless, the causes and structures of bursting remain unknown. Furthermore, he shows distinctions between the Crow instability and vortex bursting. He derives inconsistencies when this phenomenon is considered only as a Crow instability. Hence, he concludes that the causes of tip vortex bursting are not understood in detail. Leishman and Bagai [1998] focus on the wing tip vortex which interacts with the wake and the wing structure. They show different types of natural tip vortex perturbations and their interactions with the tailboom of a helicopter fuselage whereas they consider the tip vortex roll up as the initial condition for the behaviour of the wake. Furthermore, they state that the incomplete understanding of the interaction under unsteady conditions sets a barrier to an improved helicopter design.

In 2000, Leishman [2000] publishes a holistic book in helicopter aerodynamics. He considers all unsteady degrees of freedom like oscillating inflow, pitching and plunging oscillation, etc. Although he recapitulates satisfying solutions for all single problems, the interactions of the phenomena are complex and require a deeper understanding. Furthermore, he shows the connection between the unsteady effects on helicopter blades and on wind turbine blades [Leishman, 2002]. Ortega et al. [2003] observes a rapidly growing instability of a counter rotating vortex pair with unequal strength. Although this approach is partly contrary to Betz's theory, which assumes symmetry of the vortex pair, this study depicts that the vortex strength itself plays a crucial roll in developing instabilities. De Visscher et al. [2013] develop a fast-time model for studying the wake vortex behaviour including headwind and crosswind. If crosswind occurs, the strength of the two trailing vortices downstream of the aircraft is not symmetrical anymore. This may be regarded as the link between Betz's theory and the results of Ortega et al. In 2003, Fleig and Arakawa [2004] investigate a horizontal axis wind turbine numerically. They use more than 300 million grid points and analyse different wing tip geometries. They also consider the instantaneous acoustic pressure perturbation field to link the tip geometry with the noise production. In 2005, Iida et al. [2005] are the first who investigate a full wind turbine via RNS and include a direct noise simulation. They focus on the outer part of the blade and modify the wing tip geometry. Their simulations yield a broadband noise reduction of 5dB with an optimised wing tip. This study confirms the importance of wing tip vortex and wake interaction and their consequences to noise and loads. Greenblatt uses Betz's theory for a wing with a partly installed flap [Greenblatt, 2006], [Greenblatt et al., 2009]. The AFC devices are installed along the span to provoke boundary layer separation. With this approach and Betz's theory they quantify the resulting vortex strength and centroid due to the boundary layer actuation. By means of a pure spanwise actuation, they control the wake and the strength of the streamwise vortex. Vey [2007] uses the inverse Betz method on a low aspect ratio wing with installed plasma actuators. He determines the strength and the centroid of the streamwise vortex via experimentally measured velocity fields. With these parameters and Betz's inverse method, he derives the spanwise loading on the wing. Holzäpfel develops a probabilistic two-phase airplane wake vortex model [Holzäpfel, 2006], [Holzäpfel and Steen, 2007]. Although this theory is not related to Betz's theory, the experimental validation based on free field measurements reveals only moderate agreement with his theory. Nevertheless, this study demonstrates the enormous effort which is performed to determine the vortex strength and position until today. Breitsamter investigates experimentally the interaction between flaps, engine casing, and winglets on a realistic wing geometry.

2. Literature review and theoretical approaches

He uses an active winglet to control the spanwise loading and the streamwise vortices [Breitsamter and Allen, 2009], [Breitsamter, 2011].

3. Experimental setup and validation

In this chapter, the experiments and theories for short- and long-wavelength actuation of streamwise vortices are discussed in detail. As a first step, the geometry of the developed swept, semi-span, backward facing step is illustrated which generates flow structures comparable to wing tip vortices. In a second step, the actuation system is depicted. This AFC system is the basis for short-wavelength actuation to control the streamwise vortex directly at its origin. First, an optimised single actuator is presented. Then, the entire flap array (16 flaps) and its electrical supply and control circuit are shown. The motion paths of the flaps are quantified and the calibration process of the frequency and amplitude is summarised. In a third step, the numerical implementation of the temporal stability analysis is depicted. For long-wavelength actuation, the requested equations to determine the unsteady bound circulation are presented. Based on these equations, a finite wing is considered and Betz's theory is applied for predicting the wing tip vortex strength and position.

3.1. Experimental setup of the swept, semi-span, backward facing step

Intermediate conclusion: The geometry of the proposed generic model, a swept, semi-span, backward facing step is introduced and illustrated in detail. This geometry generates flow structures comparable to wing tip vortices. The flow physics and the different coordinate systems are presented. An estimation of the critical Reynolds number in this setup is discussed and finally, the GroWiKa wind tunnel at the ISTA is presented.

This section first discusses the model and its dimension and setup. Then, the coordinate system and the pressure tap positions used are motivated in detail. At the end, the used wind tunnel itself is briefly considered.

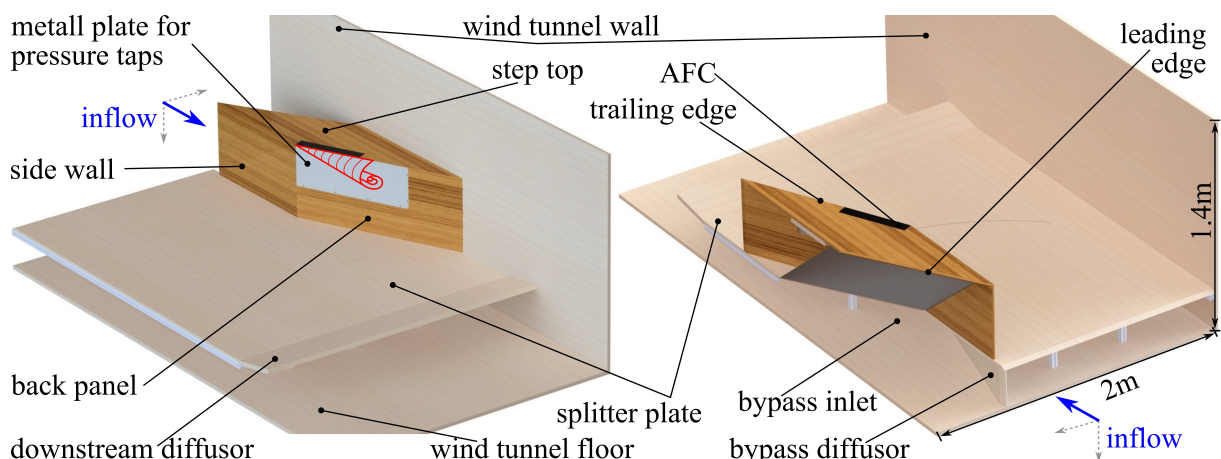


Figure 3.1.: Perspective front and back view of the swept, semi-span, backward facing step installed in the wind tunnel

The swept, semi-span, backward facing step is designed as a generic model for vortex generation in this presented study. This geometry represents the main flow structures for several technical applications and is depicted in figure 3.1. Two perspective views depict the wind tunnel setup. On the left hand side, the step is drawn from the back. The streamwise vortex at the step's trailing edge (red lines) is included for a better orientation. The nozzle of the wind tunnel is placed upstream of the step. The wind tunnel possesses

3. Experimental setup and validation

a cross section of 2m by 1.4m. The step itself is mounted on a splitter plate. The wooden splitter plate avoids distortions from the wind tunnel floor boundary layer and is the segregation of the main flow and the bypass flow. The step is made of three wooden plates (medium-density fibreboard), the side wall, the step top, and the back panel. The side wall is perpendicular to the inflow and the splitter plate. The step top is parallel to the floor. The leading and trailing edges are parallel to each other. Thus, the distance along the step top is equal at each spanwise position. This geometry avoids crossflows at the leading edge and generates a constant boundary layer thickness at the trailing edge. The leading edge of the side wall and the step top possess a radius of 9.5mm. This round edge prevents flow separation in the event of misalignment between the inflow and the step. The back panel is slanted to the free stream and the separation from the step top occurs in another direction as the free stream. A conical streamwise vortex is the consequence [Hammam et al., 2010]. An aluminium plate including more than 120 pressure taps is flush mounted inside the back panel. Directly upstream of the trailing edge, the AFC system is installed leveled in the step top.

On the right hand side of figure 3.1 is the step drawn from the front. The inlet of the bypass is placed directly beneath the step top. The distance between the splitter plate and the wind tunnel floor is 250mm. A diffuser beneath the splitter plate reduces the pressure in the bypass duct. Hence, the hazard that the ram air in front of the step's inlet separates is reduced. Furthermore, a second diffuser is mounted at the end of the splitter plate. The diffuser sets up the pressure ratio of the bypass and the main flow. This enables a further opportunity to control the ram air upstream of the step inlet. The step in this configuration yields enough internal space to install measurement techniques like pressure sensors and the required AFC system inside the box. All surfaces of the step are polished with a 400 grain to minimise roughness effects and keep the boundary layer laminar. The materials in figure 3.1 are drawn in their original appearance to illustrate the geometry more clearly. In the real setup, the splitter plate, the back panel including the metal plate, and the side walls are painted black to avoid reflections and diffuse light.

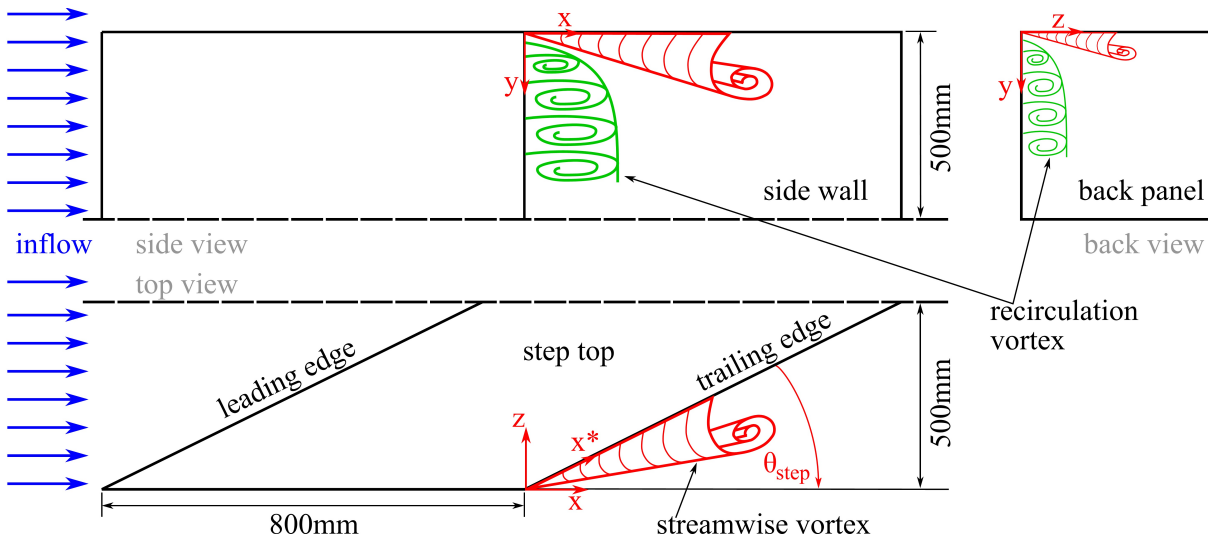


Figure 3.2.: Sketch and dimension of the swept, semi-span, backward facing step including the two global vortices in the wake; red lines illustrate the streamwise vortex emitted at the trailing edge of the slanted step top; green lines depicts the recirculation vortex coming from the side wall

Figure 3.2 illustrates a sketch of the swept, semi-span, backward facing step. Three different inclination angles are available, $\theta_{step} = 25^\circ, 30^\circ, 35^\circ$. Three corresponding back panels and step tops are manufactured. However, the red lines represent the streamwise vortex and additionally the green lines the recirculation bubble emitting from the side wall. The step is directly mounted at the side wall of the wind tunnel. The boundary layer at the nozzle exit of the wind tunnel is approximately 70mm thick [Zellmann, 2011]. Thus, in the region of the step, the assumed boundary layer thickness is approximately 100mm. To avoid cross flows on the step top and inhomogeneous flow profiles upstream of the trailing edge, a safety factor of two is applied. Thus, the first 200mm from the wall on the step top are not investigated. Furthermore, the

final flap array (discussed in detail in section 3.2.4) is 448mm long and covers, for example, 257mm of the span for $\theta_{step} = 35^\circ$. Therefore, the step span amounts to at least 457mm. The chosen step span is 500mm and the step height is equal with 500mm. The resulting displacement caused by the step model is 8.9%. The large step yields not only a lot of space inside the model, the dimension are also realistic for notch back C-pillars on commercial motorcars. At maximum wind speed of approximately 45m/s, the Reynolds number of the step scaled to a realistic car is more than four millions.

The length of the step is motivated here briefly. The purpose of this setup is circulation control by means of short-wavelength AFC. As discussed in chapter 2.1, the efficiency of shear layer actuation depends highly on the upstream boundary layer condition. The step is designed to withstand velocities up to 20m/s. The wind tunnel itself runs stable above free stream velocities of 2m/s. Therefore, the velocity of boundary layer transition should be in the range of 10m/s. The critical Reynolds number of a laminar boundary layer is defined in equation 3.1 [Schlichting and Gersten, 2006].

$$Re_{crit} = \frac{u_0 x}{\nu} \quad (3.1)$$

Hydrodynamic stability analysis yields a critical Reynolds number for a laminar boundary layer on a flat plate in the absence of a pressure gradient at $6 \cdot 10^6$ [Schade et al., 2007]. As this Reynolds number, the boundary layer gets unstable and disturbances arise. In experiments, boundary layer transition is determined at $Re_{crit} = 5 \cdot 10^5$ [White and Corfield, 1991]. This result shows that the theoretically predicted instabilities require additional time to evolve and cause transition. Furthermore, for very low turbulent inflow the critical Reynolds number increases to $3 \cdot 10^6$ [Schubauer and Klebanoff, 1955]. Nevertheless, a conservative estimation with $Re_{crit} = 5 \cdot 10^5$ and a kinematic viscosity of $\nu = 1.5 \cdot 10^{-5}$ is calculated and the chosen step length is 0.8m. This leads to a critical velocity u_{crit} of 9.375m/s as shown in equation 3.2.

$$\Leftrightarrow u_{crit} = \frac{Re_{crit} \nu}{l} = \frac{5 \cdot 10^5 \cdot 1.5 \cdot 10^{-5}}{0.8} = 9.375 \text{m/s} \quad (3.2)$$

The coordinate system is included in figure 3.2 and additionally visualised in figure 3.3 for clarity. The origin is the edge where the streamwise vortex starts to form. The first coordinate system is aligned with the inflow and the second coordinate system (marked with a star) is aligned with the trailing edge. The Pitot tube measures the static pressure of the free stream and is placed in spanwise direction in the middle of the wind tunnel ($z = -500\text{mm}$). It is positioned approximately 100m downstream of the leading edge of the side wall ($x = -700\text{mm}$) and approximately 300mm above the step top ($y = -300\text{mm}$).

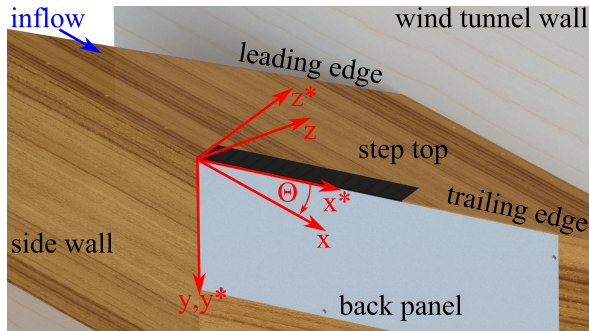


Figure 3.3.: Coordinate system of the step; x is collinear with the free stream; x^* is aligned with the trailing edge; the origin is the tip of the trailing edge

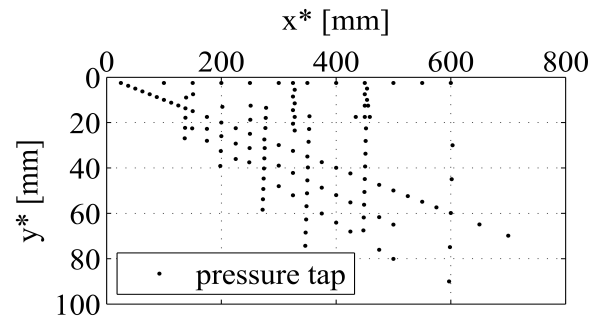


Figure 3.4.: Illustration of the 122 pressure tap positions; the two axes are not scaled equally

The pressure taps in the metal plate in the back panel enable the quantification of the AFC by means of time resolved pressure measurements. The cannula tubes possess an inner diameter of 0.7mm and an outer diameter of 1.5mm. They are approximately 12mm long and the pressure sensor is connected via an 80mm long silicon tube with an inner diameter of 1mm. All pressure sensors have the same tube length to facilitate an equivalent response and eigen frequency [Greenblatt et al., 2001]. Figure 3.4 illustrates the

3. Experimental setup and validation

positions of the 122 pressure taps (please note that the axes do not have the same scale). The pressure sensors have to be aligned with the vortex axis to quantify phase velocities of the AFC system. On a delta wing, Strangfeld et al. [2011] determine experimentally a vortex angle of 5.5° and Guy et al. [2000] observes 6.5° . Based on the experimental velocity measurements of Ivanov [2011] at the C-pillar of an Ahmed body, the angle is 6.3° . Experiments considering the swept, semi-span, backward facing step yield an angle of 9.2° via PIV, 9° via china clay and 7.5° via crosswise pressure measurements [Dash, 2012]. These results are confirmed via smoke visualisations which yield angles between 5.48° and 9.64° and additional china clay experiments reveal 6.25° [Düwel, 2012], [Strangfeld et al., 2013a]. To capture the vortex axis with certainty, three streamwise oriented pressure tap rows are installed in the final setup. Figure 3.4 represents clearly the three lines with 5.7° , 7.4° , and 9.1° which are aiming on the origin at (0,0). Furthermore, several crosswise pressure taps are installed. They are oriented perpendicular to the 5.7° pressure line. The highest spatial resolution with eleven taps are located at $x^* = 275\text{mm}$ and $x^* = 350\text{mm}$. Twelve pressure taps are placed at $y^* = 2.5\text{mm}$, directly below the AFC system. This presented pressure tap grid yields a fine spatial quantification of the pressure field in streamwise and crosswise direction.

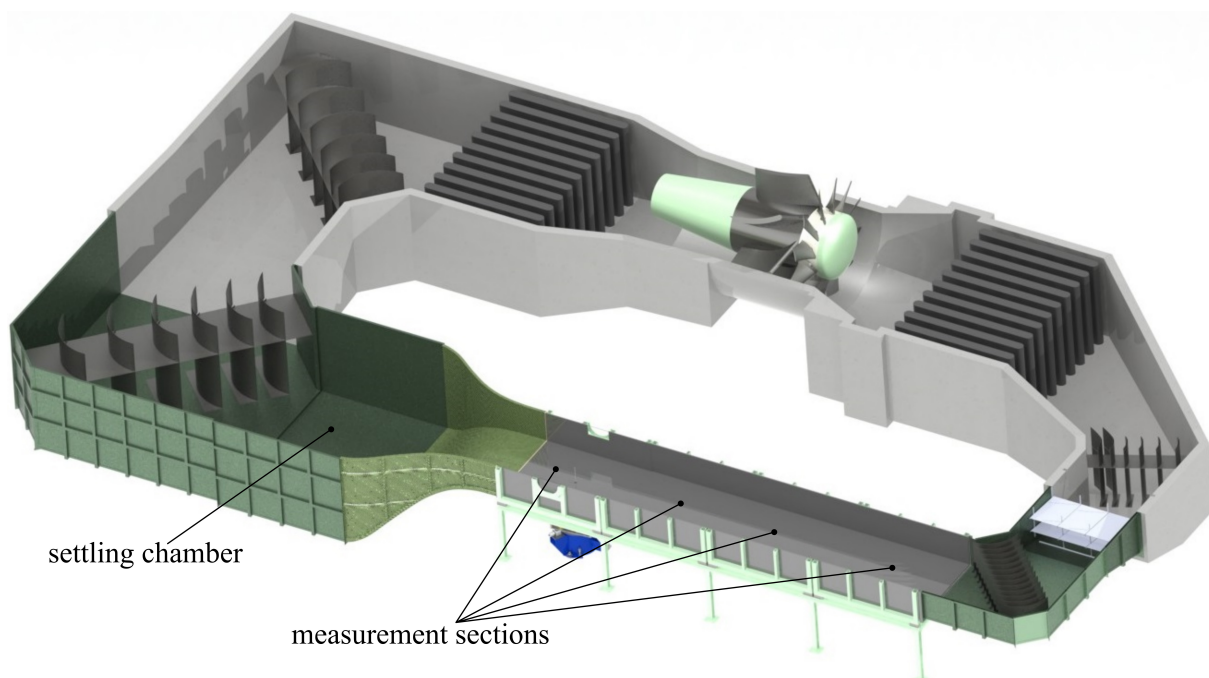


Figure 3.5.: Sectional view of the large wind tunnel at the HFI

The wind tunnel used is discussed briefly and only the parts important for the presented measurements are mentioned here. More detailed descriptions of the wind tunnel are given in Zellmann [2011], [Pechlivanoglou et al., 2011]. Figure 3.5 depicts a sectional view of the entire big wind tunnel at the HFI before the reconstruction. One loop is approximately 70m long and the measurement track consists of four sections. Each section has a cross section of 1.4 by 2m and is 2.5m long. The step is installed in the first box directly downstream of the nozzle. The maximum wind speed is approximately 45m/s and the free stream turbulence level is around 0.3% (with installed filter mat) [Institutsbericht HFI, 2008]. The cross section of the settling chamber is 4 by 4m. Parts of the measurements are performed in this configuration. Other measurements take place in the already reworked wind tunnel. During the reconstruction, one measurement section was displaced and the settling chamber was enlarged. The old analogous velocity control is exchanged by a new digital one and this yields a smoother running. Due to the new geometry and the improved velocity control, the new turbulence level is unknown so far. Furthermore, a misalignment between the nozzle axis and the measurement track axis of around 0.8° was corrected during the reconstruction. The step is fixed in the measurement section, thus the inflow conditions of the step probably vary between the two wind tunnel configurations. Moreover, this

mentioned misalignment correction causes a gap between the settling chamber and the nozzle inlet. This gap was not sealed during the final measurements (and at this time unknown by the author) although the wind tunnel was officially released for scientific measurements. The maximum opening of this triangular gap was almost 10cm. The impact on the inflow quality and the effects on the step are unknown. Other scientists observed later that the heavy flood light (>100kg) two meters above the settling chamber started shaking at a wind speed of 20m/s. Thus, the momentum loss has to be considered as significant. The generation of an angular momentum upstream of the nozzle is very likely. All these circumstances mentioned will affect the flow upstream of, around, and downstream of the model and render a comparison of the results before and after the reconstruction highly questionable.

3.2. Development of the oscillating flap array

Intermediate conclusion: The development of the AFC actuators is a complex and crucial part of this thesis. The short-wavelength actuation directly manipulates the streamwise vortex at its origin to control the vortex strength. This procedure may shift the vortex centre position as well. First, a single oscillating armature drive actuator is illustrated and explained in detail. The electromagnet, the bearing, and the leverage of the flap are the main parameters to achieve the desired motion amplitude of $\pm 2\text{mm}$. The design to control all flap units, the layout of the supply voltage and the amplified control voltage circuit is summarised. Thereafter, the entire flap array including 16 flaps is illustrated. Subsequently, the flap motion is assessed via a laser Doppler vibrometer. The presented curves of several frequencies and amplitude yield a precise and reliable sinusoidal motion and the spectra show a dominant spike at the desired frequency. This innovative actuation concept shows high accuracy and repeatability. Each single actuator acts like a simple one-mass oscillator including a distinct eigen frequency. Thus, the amplitude response is dependent on different supply voltages and actuation frequencies, which is depicted in detail. In the end, a complete calibration of the flap array for one certain operation point is documented.

After the theoretical description and the designing of oscillating armature drives, the real actuation is developed in this section. In a first step, a single flap actuator of the modular concept is depicted in detail. In a second step, the development of an array of 16 flaps including the control circuit is outlined. Eventually, time distance diagrams and corresponding parameters are presented to characterise the quality of actuation.

Although the development of the actuation is an integral part of this thesis and several types of flap geometries, bearings, string configurations, oscillating armature drives, etc., are tested and optimised, only the final configuration is discussed here in detail.

3.2.1. Design and construction of a single oscillating flap

As shown in the design, an implementation of a segmented flap array by means of an oscillating armature drive is achievable within the given financial scope of 1000Euro. Figure 3.6 illustrates the design of one single oscillating flap. The blue cube highlights the inductor (the frame size is 25x32x26mm) and is mounted on the "U"-shaped yoke which is made of thin lamellated iron plates. This completes the electromagnet (maximum power consumption of 3W) and it is held by an adapter made of aluminium through an elongated hole. This hole enables an individual adjustment of the air gap between yoke and armature of around 1mm. The entire oscillating armature drive including the permanent magnet is obtained from an aquarium pump (type: *ProSilent a50*, company: JBL). This product is a diaphragm air pump based on an alternating current electromagnet. The total costs for one aquarium pump amount to €14.

The passive back motion of the armature is realised by two springs which are directly connected to the flap. The springs (company: *Febrotec Federn*, type: *0D11140*) are 17.5mm long and 2.21N/mm stiff. The inner diameter is 2mm and they are held by appropriate pins. Each spring is individually adjustable in all three spatial directions via three elongated holes. This is important for the set up of the spring preload and for adjusting the azimuthal offset of the flap. The flap is manufactured by a 3D-rapid prototype printer

3. Experimental setup and validation

and is made of polymer plastic (material: *Photopolymers Rigid Opaque*). The total weight is less than 10g and minimises the rotational inertia torque. The total frame size amounts to 77x18x28mm and the flap shoulder is 1.5mm thick (a flap shoulder of just 1mm thickness does not reveal a sufficient durability in preliminary test). The even more important scales of the flap are the distance from the flap tip to the centre of rotation (65mm) and the distance from the armature to the centre of rotation (9mm). The bearing axis is similar to the rotation axis here. The amplitude of the oscillations is enlarged by means of the ratio of these two geometric lengths. This leads to an amplitude gain of 7.2. The flap is mounted via press fit by two miniature ball bearings (company: *SKF*, type: *MR 105 2Z*) with an outer diameter of 6mm, an inner diameter of 5mm and a width of 4mm. The weight of each bearing is around 1.3g. The permanent magnet (around 4g) glues itself directly on the flap. If a simple one-mass oscillator is assumed, the total mass of 16.6g and the stiffness of 2.21N/mm leads to an eigen frequency of 58.1Hz.

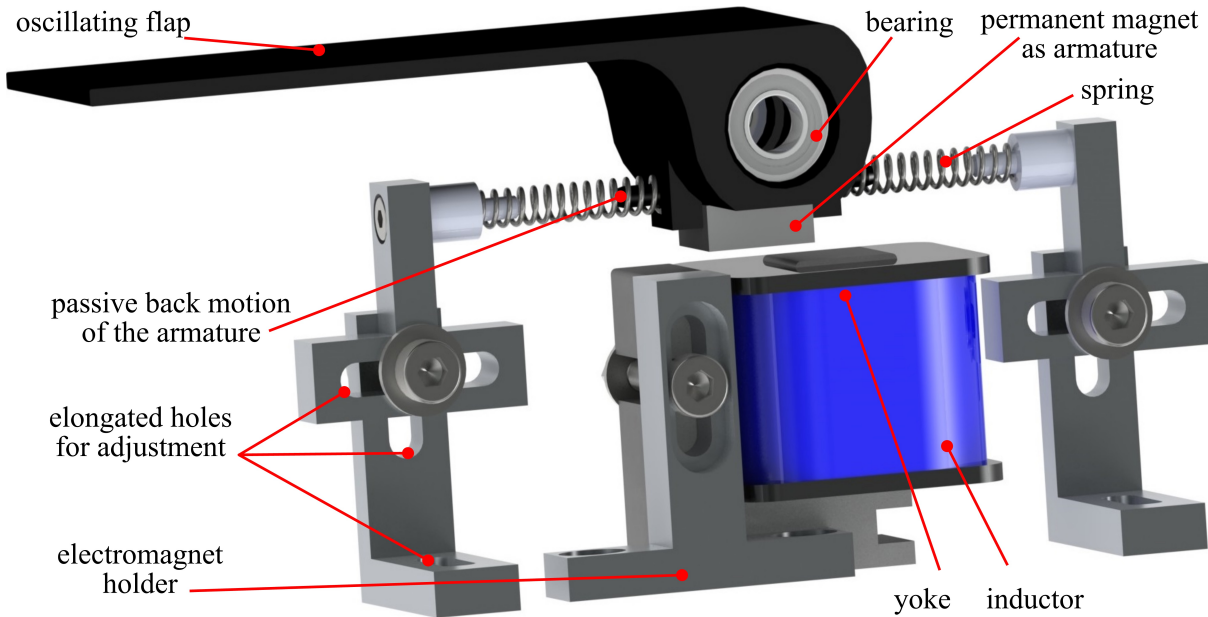


Figure 3.6.: Construction of one single oscillating flap with a total frame size of 114x48x32mm

The total size of one oscillating flap actuator is 114x48x28mm. The width of the flap is mainly determined by the width of the electromagnet (26mm). For a filigree adjustment, the preload of the springs, the azimuthal offset and the air gap are individually adjustable for each single flap. One noticeable observation during the preliminary tests is that for small amplitudes, the magnetic field is strong enough to perform actively the back motion and no passive system via springs is necessary.

3.2.2. Development of the flap array

The construction of the single oscillating flap enables a modular assembly of the desired amount of flaps along one shaft. The shared use of one single shaft positions all flaps at a similar height. Thus the arrangement of a flap array is achieved without further modifications. The more challenging element is the design of the electrical control system for 16 flaps. The available number of output channels at the HFI limits the amount of flaps to 16. Figure 3.7 represents the electrical circuit by means of the flap amplitude, frequency, and phase is controlled. The supply voltage is the common commercial 230V alternating current voltage at 50Hz. The operational amplifier requires a direct current reference potential. Therefore, the 230V voltage is transformed into two 115V AC voltages via two transformers in a first step. Four bridge rectifiers transform each 115V AC voltage into a 115V DC voltage. These two 115V DC voltages are connected to each other to ascertain that both exhibit the same reference potential at any time. Two capacitors (200 μ F) smooth the voltage to a constant reference potential for the operational amplifier. The maximum peak-to-peak input voltage range of $\pm 10V_{pp}$ of the 16 simultaneous analogue-output channels (company: *National Instruments*, type: *NI9264*) is amplified by an inverted [Brechmann et al., 2000]

high voltage power operational amplifier (company: *APEX*, type: *PA340*). The amplification factor is determined by the ratio of the two resistors, which amounts to $R_1/R_2 = 200k\Omega/10k\Omega = 20$. The OPA represents the main control unit and only a few types are able to handle such a high electrical potential of ± 115 DC voltage. The chosen OPA costs around €18 each. The amplified input voltage is the output signal in figure 3.7 and represents the supply voltage for the oscillating armature drives. Further details to electrical control circuits are given by Weißgerber [2008].

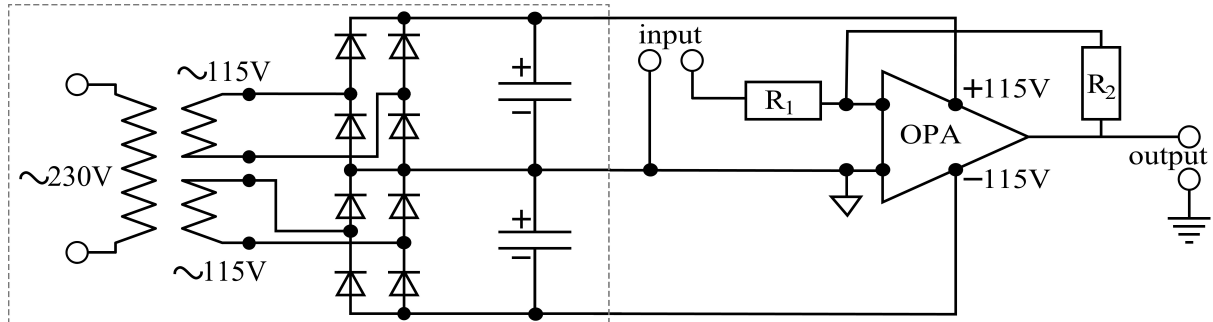


Figure 3.7.: Circuit layout of the supply voltage (grey dashed box) and the amplified control voltage

The frequency of the flaps is identical to the frequency of the AC part of the input signal which is generated in *LabVIEW*. The phase lag of each flap is software-controlled as well. The amplitude of a flap is governed by the RMS value of the AC voltage part. For instance, a sinusoidal $1V_{pp}$ AC voltage is similar to a $0.71V$ voltage and amplified by a factor of 20. This results in a supply voltage for the flaps of $\pm 14.1V$. However, the electrical potential of $115V$ DC allows only a maximum input of $\pm 8.13V_{pp}$. Higher input voltages are not amplified properly anymore and this leads theoretically to a sinusoidal supply voltage with cut off peaks. Furthermore, the azimuthal offset of each flap is adjustable by superimposing a DC voltage on the AC signal. This permits a fine calibration of the height of each flap tip.

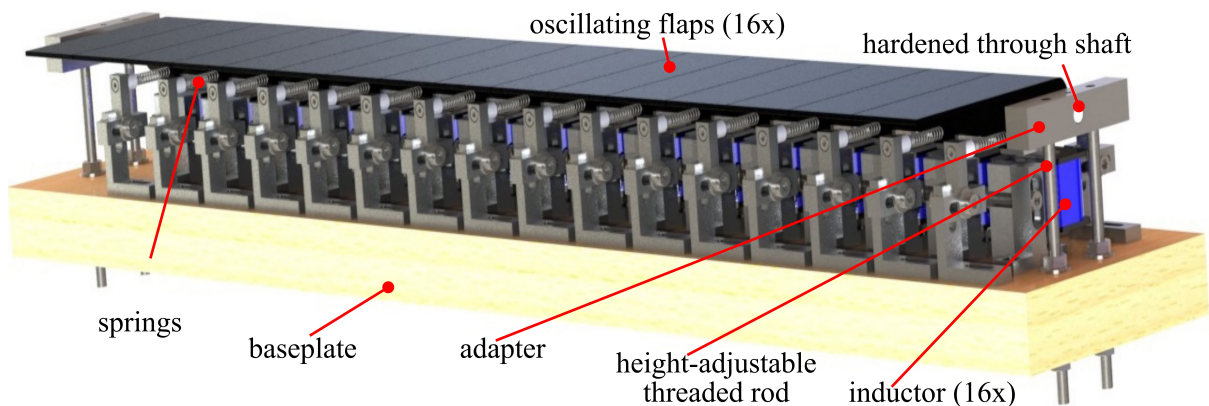


Figure 3.8.: Construction of the array including 16 oscillating flaps; the frequency and the phase are software-controlled, the amplitude is proportional to the RMS value of the AC supply voltage

The big advantage of this presented control circuit is that the supply and the control voltage circuit are two independent sub-systems. The supply voltage circuit is outlined with a grey dashed box in figure 3.7. This single supply circuit provides all 16 flaps and more if necessary. This reduces the costs significantly and the only remaining cost-pusher is the OPAs. Detailed circuit diagrams, printed circuit board layouts, more details to the electrical components and descriptions of the operating control software are given by Scheibel [2014]. A photo of the real electrical circuit for comparison is presented in appendix A (figure A.1).

Figure 3.8 shows the flap array of 16 flaps. The total length covered by flaps is $448mm$ and this corresponds to 41% of the 25° trailing edge. All flaps are mounted on a single hardened high-precision shaft and are at the same height. The spacer between the bearings are manually adjusted to minimise the gaps between

3. Experimental setup and validation

the flaps to $\leq 0.5\text{mm}$. The "floating mounting" concept avoids mechanical or thermal stress [Grote and Feldhusen, 2011]. The two shaft ends are positioned by two adapters. These adapters are connected via threaded rods to adjust the air gap between the flaps and the drivetrain. All items are fixed on a wooden baseplate. Thus, the array of 16 flaps is mounted and removed as one unit and hence easy to handle. Preliminary calibrations, optimisations and maintenance may be conducted outside the step and the wind tunnel.

Figure 3.9 illustrates a photo of the array in the laboratory. The two metal brackets on the sides of the baseplate are the connectors to the swept, backward facing step. The 16 cables on the left hand side belong to the control circuit. Furthermore, white rectangular profiles clue on the flap tip. This modified setup is discussed later.



Figure 3.9.: Photo of the flap array; cables on the left hand side deliver the supply voltage

3.2.3. Assessment of the flap motion

After the design, the construction and the assembly are elaborated, the motion of the oscillating flaps is assessed. The behaviour of each flap is measured by means of a laser Doppler vibrometer (company: *Polytec*, type: *OFV-5000*) [Hering and Martin, 2006]. This measurement technique is based on the Doppler effect [Doppler, 1842]. The LDV quantifies the velocity of moving objects and, through integration, the corresponding motion distance [Hering and Martin, 2006]. The sampling time for each measurement point is 2s and the sample rate is 1024Hz. Each flap possesses its own nonlinear behaviour and the amplitude is very sensitive to small changes in the setup. Hence, theoretical approaches for calibration are rendered impossible. Thus, all 16 flaps are calibrated individually in-situ (directly installed in the swept, backward facing step inside the wind tunnel) and the LDV is mounted on a two-axis traverse. The calibration process and the applied *LabVIEW*-software are discussed in more detail by Scheibel [2014].

The first verified parameter is the frequency. Only a stable, and reliable frequency control permits a sufficient phase control. The motion curves and the corresponding parameters of flap 10 are discussed here to give an impression of the quality of the actuation. Flap 10 is chosen because it is an unsuspecting flap with medium energy demand and average amplitudes. Figure 3.10 presents the flap motion amplitude for three arbitrary periods at 10, 25 and 60Hz. An ideal sine function with the same amplitude is added to the plot for comparison. At 10Hz, the measured motion is very similar to the ideal sine. Around the lower peaks, the flap motion differs slightly. Furthermore, a low variation of the amplitude of the minima and maxima are evident. This effect probably results from the LDV itself. It measures all vibrations between the oscillating flap and the measurement optic, thus disturbances like building vibrations overlap the effects and cause a moving offset. This effect is already compensated by means of a piecewise least-square-fit which subtract the time dependent offset (*detrend*-function in *MATLAB*). However, fragments of this distortion still persist. Thus, the amplitude is evaluated for each single period and then averaged and amounts to 1.46mm peak-to-peak at an input voltage of $\pm 6V_{pp}$ for this flap. At 25Hz, the agreement

between measured and ideal motion is very good. For the same input voltage as before, the peak-to-peak motion amplitude amounts to more than 3mm and the standard deviation is 0.016mm. At 60Hz, the maximum input voltage of $\pm 10V_{pp}$ leads to a peak-to-peak amplitude of 0.82mm. No peak cut-off effect is visible, and hence negligible, although this input voltage exceeds the maximum electrical reference potential of the OPA. Quite a high agreement is also evident for this case. In summary, these measurements demonstrate an accurate sinusoidal motion of the three frequencies.

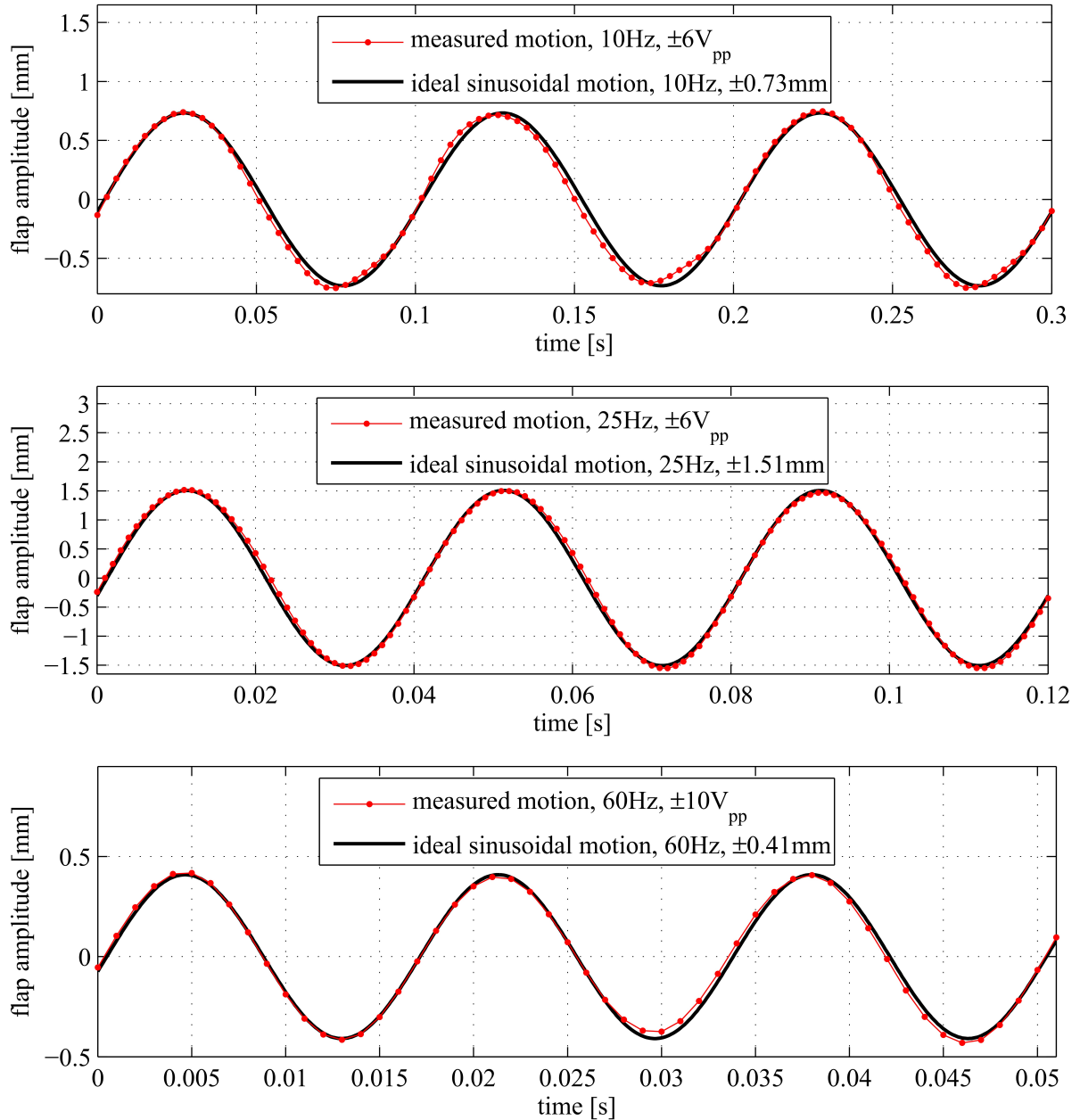


Figure 3.10.: Presentation of the measured amplitude of flap 10 for 10, 25 and 60Hz (via LDV). At each frequency, three arbitrary periods are depicted with the corresponding ideal sinusoidal motion curve. At 10Hz, only every third measurement sample is marked by a red point.

Figure 3.11 represents the linear scaled amplitude spectrum of a fast Fourier transformation [National Instruments, 2011] of the measurement in figure 3.10 at 60Hz and an input voltage of $10V_{pp}$. A clear and straight peak is obvious at the desired frequency of 60Hz. Although some low energy is presented at the neighbouring frequencies, this peak resembles a theoretical unitary step function. Thus, the oscillating flap acts almost like an undisturbed, perfect oscillator. For completeness, figure 3.12 shows the power spectral

3. Experimental setup and validation

density [Cerna and Harvey, 2000] of the same measured signal. The 60Hz peak dominates the spectrum at -25dB_V and is consistent with the amplitude spectrum. The highest noise amplitude of -75dB_V exists at 40Hz. Furthermore, no distinct subharmonics or higher harmonics are present. All the presented motion curves, and the associated parameters clarify the accurate and stable reproduction of the control signal as a sinusoidal oscillator at the desired frequency. Frequencies from 5 to 150Hz are measured and proven during the calibration process. The highly accurate reproduction of the control signal in the motion path raises the question whether other function types may be performed by these actuators. Additional tests including trigonometrical, serrated, or smooth step function as control signals will reveal further insight into the motion behaviour of these oscillating flaps in the future.

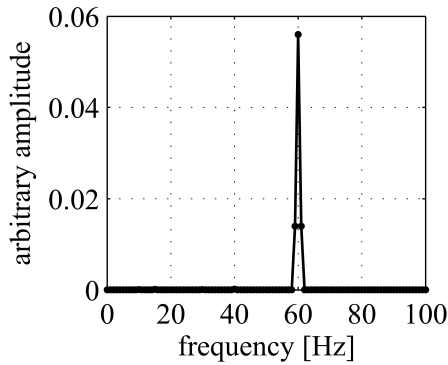


Figure 3.11.: Amplitude spectrum of flap 10 at 60Hz and $10V_{pp}$

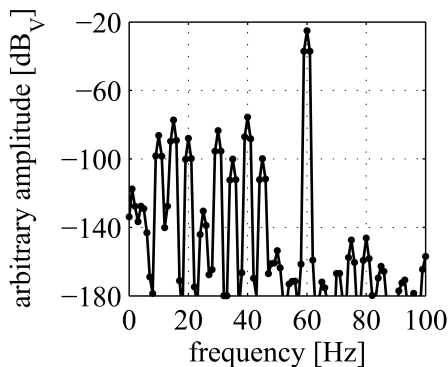


Figure 3.12.: Power spectral density of flap 10 at 60Hz and $10V_{pp}$

The second parameter verified in detail is the oscillating amplitude. It is very sensitive to small constructional variations. Thus, the amplitude depends on the input voltage and the desired frequency. Both parameters are discussed in the following text. Each flap is calibrated individually and the amplitude calibration is clarified for flap 10 again. Figure 3.13 depicts the peak-to-peak motion amplitude for constant frequencies at variable control voltages from 1 to $10V_{pp}$. All lines monotonically increase or in other words, a higher voltage always yields a higher amplitude as expected. This behaviour persists for all shown frequencies of 5 to 60Hz. At the maximum AC voltage of $10V_{pp}$ all amplitudes are more than 1mm. Between 5 and 35Hz the amplitude increases. Beyond this frequency, the amplitude decreases. This observation suggests an eigen frequency in the vicinity of 35Hz. Moreover, the slope at 35Hz (blue dashed line) is very high. At a control voltage of $2.5V_{pp}$ an amplitude of almost 5mm is reached. A further enhancement to 3V only slightly increases the amplitude. This is not a saturation effect, rather caused by the geometrical setup. The air gap between flap tips and the back panel of the step is around 2.5mm. Thus, at 3V the flap already hits the step and a further increased control voltage will damage the flap. However, without geometrical limits, the amplitude would further increase because the oscillating armature drive is insensitive to blockage. As mentioned before, the reference potential of the OPA ($\pm 115V$ AC) theoretically allows a maximum supply voltage of $8.13V_{pp}$. Above $8V_{pp}$, the measured amplitude

still increases which shows the system possesses considerable inertia. If, for instance, 10V instead of 8V are modulated, the magnetic flux is higher at any time as long as the maximum electrical potential is reached. A stronger magnetic field generates larger forces and accelerations and hence increases the amplitude although the supply voltage amplification stops at $8.13V_{pp}$. Furthermore, above $8V_{pp}$, a kink in the slope is visible, elucidated by the red and green dashed lines in figure 3.13. This is the consequence of reaching the maximum electrical potential. Now, a control voltage of 8 or $10V_{pp}$ does not yield a higher magnetic flux although the magnetic flux was higher before. In summary, the flaps depict a docile behavior for control voltages of 9 and $10V_{pp}$ proven by figures 3.10 to 3.13.

Figure 3.14 illustrates the peak-to-peak motion amplitude of flap 10 for four constant control voltage and variable frequencies. At each measured frequency, a higher voltage always promotes higher amplitudes. This is expected and consistent with figure 3.13. Up to a frequency of 20Hz, the flaps show a linear trend for all voltages. Above 20Hz, a nonlinear increase is evident until a global maximum in the range of 35Hz is reached. For frequencies higher than 35Hz, an amplitude decrease is present. The global trend from 40 up to 150Hz may be fitted by a logarithmic curve which tends to zero for infinite high frequencies. At 150Hz, a clear sinusoidal flap motion is observed although the small amplitude amounts to 0.09mm.

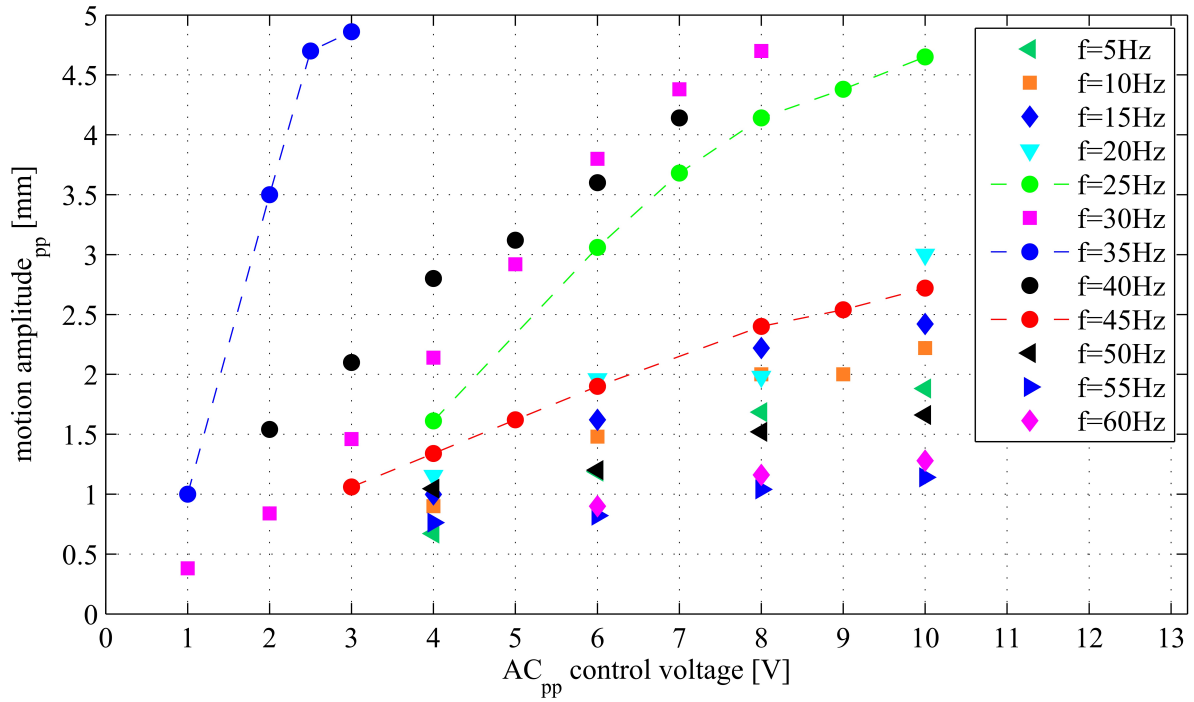


Figure 3.13.: Peak-to-peak motion amplitude of flap 10 at 5 to 60Hz and variable control voltages from 1 to 10V_{pp}

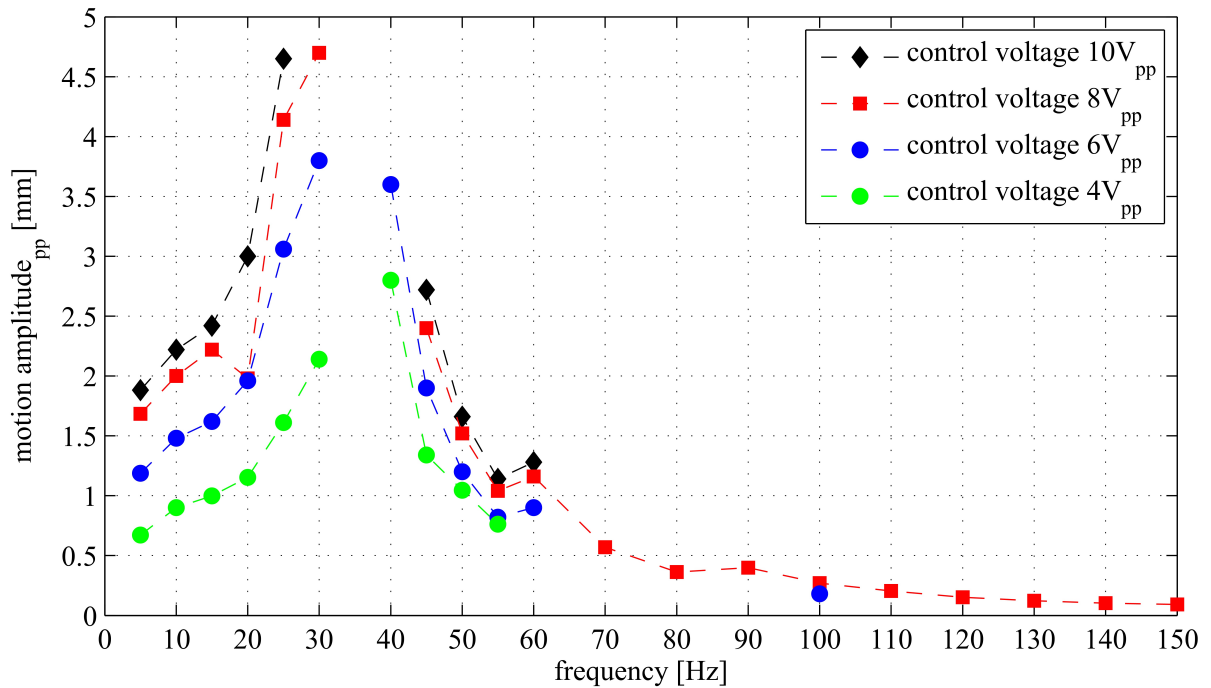


Figure 3.14.: Peak-to-peak motion amplitude of flap 10 at 4, 6, 8, and 10V_{pp} and variable frequencies from 5 to 150Hz

All voltages yield an amplitude spike at 60Hz and at 8V_{pp} another spike at 90Hz. This local enhancement is caused by the higher harmonics of the eigen frequency which seems to be closer to 30Hz than to 35Hz. A fourth harmonic at 120Hz is not observed due to too small amplitudes. Another observation is clearly depicted in the linear region. The amplitude gain from 4 to 6V_{pp} or from 6 to 8V_{pp} is approximately of the same magnitude. The gain from 8 to 10V_{pp} is much smaller, in the linear as well as in the nonlinear

3. Experimental setup and validation

region. This corresponds to the limited amplification (max $8.13V_{pp}$) of the electrical potential of the OPA as discussed before. Furthermore, the gain of an increased control voltage is fairly visible until frequencies $\leq 45\text{Hz}$. Beyond this distinct frequency, the amplitude gain is reduced significantly. If a linear trend is assumed between 0 and $8V_{pp}$ in figure 3.13, the estimated offset at $0V_{pp}$ is almost zero for all frequencies except 50, 55, and 60Hz. Considering these three cases, the predicted amplitude offset is around 0.5mm. This offset does not reveal any physical relevance but it indicates a modified behaviour. This is consistent with the reduced amplitude gain in figure 3.14 although a physical explanation requires more tests. A detailed amplitude description of flap 2 and further details regarding the calibration setup are specified by Scheibel [2014].

3.2.4. Calibration of the flap array

The discussed calibration procedure is performed for all 16 flaps. Once all amplitudes are known, the desired amplitude and frequency is selected (depending on the weakest flap). Table 3.15 determines the required control voltages at 30Hz and a peak-to-peak amplitude of 4mm for each flap. Flap 12 involves the lowest voltage with $4.2V_{pp}$ and flap 3 the highest with $9.8V_{pp}$. Flap 10 consumes an average voltage of $7V_{pp}$. This table emphasizes the fairly large amplitude variations between the flaps. Some reasons are the different eigen frequency of each flap, different air gaps between the yoke and the armature, varying prestresses of the springs, different assembly accuracies, etc.

flap	output voltage [V]
1	6.1
2	6.2
3	9.8
4	7.8
5	8.7
6	5.1
7	6
8	6.3
9	8.9
10	7
11	5.1
12	4.2
13	8
14	7.5
15	8.3
16	8.8

The third parameter, the phase lag, is directly controlled via the software generated output signals. A scope verifies the output signal phase lag between several control channels. No undesired distortions are observable. Furthermore, the software control voltage and the measured flap motion are recorded and evaluated. A phase rotation of 180° appears between the control signal and the oscillation for all flaps due to the amplification of the signal. A direct measurement of the flap motion phase lag is not realised because only one LDV is available. A visual check at lower frequencies for several phase shifts reveals the impression of a reliable and highly accurate phase control of all flaps.

During the calibration of one single flap, the other flaps are switched off and during the experiments, all flaps oscillate. At frequencies of 30 and 35Hz, small interactions between the flaps were recognised. The amplitude varies slightly although the flaps are calibrated for a constant value. These effects are compensated by an additional calibration where all flaps are moving in-phase. At 40Hz and higher oscillation frequencies, strong interactions occur. In the worst case, some flaps do not move at all although the input voltage is $10V_{pp}$. Other flaps already reach the maximum amplitude and hit the back panel although the input voltage is less than 2_{pp} . The interaction

Figure 3.15.: Analogue output voltage determined by the in-situ calibration at a frequency of 30Hz and at a desired peak-to-peak amplitude of 4mm

totally changes for different phase angles. The eigen frequency of the flaps is close to 30Hz, but the strong interactions occur above 40Hz. This behaviour suggests the assumption that the eigen frequency of the flaps do not cause these distortions. Rather, the eigen frequency of the entire system with one single shaft may be the cause. The shaft starts to vibrate above 40Hz and thus transports vibrations to other flaps through the bearings. A segmented shaft for each flap will avoid this problem. However, reliable in-phase measurements are taken at frequencies from 5 to 35Hz and measurements including arbitrary phase angles from 5 to 20Hz.

3.3. Numerical implementation of the Orr-Sommerfeld equation

Intermediate conclusion: No analytical solution for the Orr-Sommerfeld equation exists. Thus, a numerical solution method is required. The spectral method including Chebyshev polynomials and Gauss-Lobatto sampling points is used. Then, a discussion of the transformation function and the formulation of the derivations follows. Finally, the numerical formulation of the Orr-Sommerfeld equation is depicted.

Several methods exist to solve the partial differential equations such as the Orr-Sommerfeld equation [Dziuk, 2010]. In this presented work, the spectral method is chosen. This method transforms the problem from a physical domain into a spectral domain by means of globally defined ansatz functions. In this new domain, the Hilbert space, the equations reduce to an algebraic problem with an orthogonal basis and only the coefficients of the ansatz functions have to be determined. Commonly used ansatz functions are, for instance, Fourier series. The discussed physical problem considers a semi-infinity shear layer (boundary layer) or a free infinity shear layer. In both cases, strong velocity gradients are expected and steady conditions confine this problem. Thus, Chebyshev (Tschebyschow, Tschebyscheff) polynomials of the first kind T_n are practical for this problem. They are based on a weighted norm in a complete orthogonal system. These polynomials are able to capture high gradients of the disturbance amplitude \tilde{w} at solid walls [Canuto et al., 1988]. For an exact numerical integration, the ansatz functions are evaluated at the Gauss-Lobatto points which are formally defined as $\eta_{u,j} = \cos(\frac{\pi j}{N})$. By means of these sampling points, the integration is formally exact, numerically stable and hence minimises the numerical error [Canuto et al., 1988].

The disturbance amplitude in equation 3.3 at the Gauss-Lobatto sampling points η_j is the Chebyshev polynomial T_n multiplied with the amplitude function C_n [Schwarz and K ockler, 2004].

$$\tilde{w}(\eta_{u,j}) \approx \sum_{n=0}^N C_n T_n(\eta_{u,j}) \quad (3.3)$$

The Chebyshev polynomials are only defined on the unit interval $[-1,1]$ which is expressed by η_u . Thus, only a Hagen-Poiseuille or a Couette stream is computed directly on this grid. In the case of shear layers, the unit interval is theoretically transformed into a semi-infinite $[0,+\infty)$ or an infinite interval $[-\infty,+\infty)$. For a numerically manageable transformation, these intervals are cut off to a "sensible" physical space with the following margins $(-\infty < a < b < +\infty)$. A linear transformation is not suitable for the Orr-Sommerfeld equation because the second and fourth derivation become zero [Schwarz and K ockler, 2004]. A commonly used bijective mapping $S(\eta_u) = z \in [a, b]$ for shear layers is $z = c_s \tanh(\eta_u)$. The polynomials may be derived directly at the sampling points $(\frac{dT_n}{d\eta_{u,n}})$ to yield the derivations. This approach is formally correct. From a numerical point of view the use of a derivation matrix is more convenient. This matrix D depends only on the total number of the predetermined sampling points N and is calculated just one time at the beginning of the entire computation. The detailed derivation of D is given by Oertel [1996]. Equation 3.4 yield the derivation of the disturbance amplitude on the unit interval.

$$\frac{d\tilde{w}}{d\eta_u}(\eta_j) \approx \sum_{k=0}^N C_n \frac{dT_n}{d\eta_{u,j}} = \sum_{k=0}^N D_{jk} \tilde{w}(z_k) \quad (3.4)$$

Derivations of a higher degree are correctly calculated by multiplication of the derivation matrix $(\frac{d^n \tilde{w}}{d\eta^n} \approx D^n \tilde{w})$ [Oertel, 1996]. This approach may provoke numerical inaccuracies. The use of the chain rule is more stable and yields a higher precision [Don and Solomonoff, 1995]. Furthermore, the use of trigonometric identities avoids the computation of differences like $x(k) - x(j)$. This approach is suggested by Don and Solomonoff [1995] and harvests an enhanced accuracy. Further on, for small arguments $\sin(t)$ is computed by means of the "flipping trick" which yields a higher precision. The implementation is described in detail by Weideman and Reddy [2000]. Baltensperger and Trummer [2003] claimed that further accuracy due to roundoff errors is reached by implementing the "negative sum trick".

However, the derivations are known on the unit interval. For a transformation into the physical domain,

3. Experimental setup and validation

the derivations of the mapping function S are required as well. A detailed calculation of these derivations $\frac{dS^{-1}}{dz}$ is given by Doppel [2014]. The final expressions are given in equations 3.5 to 3.8.

$$\frac{d}{dz} \approx \Delta_1 D^1 =: D_1 \quad (3.5)$$

$$\frac{d^2}{dz^2} \approx \Delta_2 D^1 + \Delta_1^2 \Delta_2 =: D_2 \quad (3.6)$$

$$\frac{d^4}{dz^4} \approx \Delta_4 D^1 + (4\Delta_3 \Delta_1 + 3\Delta_2^2) D^1 + 6\Delta_2 \Delta_1^2 D^3 + \Delta_1^4 D^4 =: D_4 \quad (3.7)$$

$$\Delta_n := \begin{pmatrix} \frac{d^n S^{-1}}{dz^n}(z_0) & \cdots & 0 \\ \vdots & \ddots & \vdots \\ 0 & \cdots & \frac{d^n S^{-1}}{dz^n}(z_N) \end{pmatrix}, \quad D^n := \begin{pmatrix} D_{00} & \cdots & D_{0N} \\ \vdots & \ddots & \vdots \\ D_{N0} & \cdots & D_{NN} \end{pmatrix}^n \quad (3.8)$$

The derivations of the disturbance amplitude in the physical domain $\tilde{w}(z)$ are now the derivations of the Chebyshev polynomials at the Gauss-Lobatto sampling points on the unit interval. These are the general derivations for arbitrary coordinate range defined by the mapping function S [Schwarz and Köckler, 2004]. Hence, the numerical formulation of the Orr-Sommerfeld equation yields equation 3.9.

$$\left\{ (aU_s + bV_s) [D_2 - (a^2 + b^2)] - \left(a \frac{d^2 U_s}{dz^2} + b \frac{d^2 V_s}{dz^2} \right) + \frac{i}{Re} [D_2 - (a^2 + b^2)]^2 - \omega [D_2 - (a^2 + b^2)] \right\} \tilde{w} = 0 \quad (3.9)$$

The matrices U_s and V_s are diagonal matrices. The trace represents the basic flow at the transformed Gauss-Lobatto sampling points or their second derivation. Thus, by means of a given basic velocity field, given number of sampling points and the desired coordinate transformation S , the Orr-Sommerfeld equation 2.32 reduces to an ordinary linear eigenvalue problem of the kind $(C_0 + \omega C_1)\tilde{w} = 0$. The implementation of the boundary conditions is required to yield a distinct solution. Several options exist to consider them. Today, memory and storage are no longer a problem in modern computers. Hence, the boundary conditions are implemented in a simple way. The amplitude of the disturbances becomes zero at the fringes of the domain. Thus, these conditions in equation 2.33 are considered implicit by deleting the first and the last column and row in the eigenvalue matrix. The stability problem is just solved on the inner domain [Trefethen, 2000], [Boyd, 2001]. For large Reynolds numbers ($Re \rightarrow \infty$), the entire term involving $1/Re$ becomes zero. Hence, only the second derivations persist and the Orr-Sommerfeld equation is reduced to the Rayleigh equation.

In the case of a temporal stability analysis, the two wave numbers a_r and b_r are predetermined and the eigen-frequency ω is wanted. Only real wave numbers are physically reasonable. The frequency with the largest positive imaginary part $\omega_i > 0$ experiences the most amplification, see equation 2.27. This is the dominate frequency. If a one-dimensional shear is considered, b is zero due to the Squire-theorem. Thus, only one positive eigenvalue is determined via the stability analysis [Oertel, 1996]. A spatial stability analysis yields the spatial direction of amplification at a given ω and global coordinate system.

For the sake of completeness, there is one typo in Oertel [1996]. They claim on page 206 in their sample calculation of a boundary layer that the boundary conditions have to be implemented in all \hat{U}_j . However, the wave number a is independent of the boundary conditions, hence their implementation is required only in \hat{U}_0 .

3.4. Derivation of the unsteady bound circulation and vorticity sheet

Intermediate conclusion: The previous theories discussed only predict global parameters like the lift and the pitching moment. Thus, the existing theory is extended to predict the unsteady pressure distribution

along the chord. As a first step, based on the general formulations of van der Wall, the unsteady shed wake vorticity has to be determined. The circulation is the integral of the bound vorticity sheet. During the integration, most Fourier coefficients become zero. In the current case, all coefficients have to be calculated to predict the unsteady bound vorticity sheet. Under the assumption of harmonic fluctuation in time, the problem is transformed into an infinite summation including two integrals with infinity as the upper margin. A closed solution of these expressions is found by means of a linear combination of confluent hypergeometric Kummer functions which enables the prediction of the unsteady pressure distribution along the chord.

¹ Although the spanwise and the streamwise circulation distribution is the important link to predict the interaction by means of Betz's theory, the local pressure distribution remains unknown. Nevertheless, the pressure field is highly requested as well to get a better understanding of the vortex structure interactions close to the wing tip. This approach allows a coupling of spanwise pressure on an infinite wing and the experimentally measured pressures produced by the streamwise vortex. Furthermore, the pressure field is essential for all acoustic predictions and thus crucial for the purpose of broadband noise reduction. In section 2.5, the time varying lift including the lift overshoot due to unsteady flow is calculated. Nevertheless, the lift is an integral force and does not disclose local flow structures along the wing's chord. Thus, a new expression for the unsteady bound vorticity sheet $\gamma_b(x, t)$ of a flat plate is derived here. The first step for this purpose is the calculation of the time varying shed wake vorticity strength. Equation 3.10 expresses the approach for the normal velocity distribution along the chord motivated by van der Wall [1992]. The first term describes an unsteady angle of attack as well as an unsteady free stream velocity. The second term enables an arbitrary positioning of the pitching axis relative to the mid-chord. The third term defines a time varying plunge motion and the last term depicts the contribution of the shed vorticity in the wake. All following equations are based on the small disturbance assumption ($\alpha \equiv \sin(\alpha)$).

$$v_{n,b}(x, t) = \alpha(t)u(t) + (x - 0.5ac)\dot{\alpha}(t) + \dot{h}(t) + v_{n,w}(x, t) \quad (3.10)$$

The shed vorticity is generated continuously at the trailing edge and convects downstream. Thereby, the shed wake vorticity strength is the time derivation of the unsteady bound circulation $\dot{\Gamma}(\tau)$. These shed vortices in the wake induce velocity components normal to the chord as described by Biot-Savart's law [Schade et al., 2007]. Thus, at each instant of time τ , the entire unsteady wake needs to be taken into account to determine valid unsteady effects. Equation 3.11 shows the wake induced normal velocities $v_{n,w}$, whereby $W(t)$ is the distance travelled by the airfoil (the coordinate transformation is $x = 0.5c \cos(\Theta)$) [van der Wall, 1992].

$$v_{n,w}(\Theta, t) = -\frac{1}{2\pi} \int_{-\infty}^t \frac{\dot{\Gamma}(\tau)}{1 + \frac{W(t)-W(\tau)}{0.5c} - \cos(\Theta)} d\tau \quad (3.11)$$

Normalisation by the half-chord $c/2$ and transformation into a Fourier series yield equation 3.12.

$$v_{n,w}(\Theta, t) = \frac{b_0(t)}{2} + \sum_{n=1}^{\infty} b_n(t) \cos(n\Theta) \quad (3.12)$$

Furthermore, the self-induced normal velocities $v_{n,b}$ caused by the bound vorticity sheet γ_b are given in equation 3.13.

$$v_{n,b}(\Theta, t) = \frac{1}{2\pi} \int_0^{\pi} \frac{\gamma_b(\theta, t) \sin \theta}{\cos(\Theta) - \cos(\theta)} d\theta \quad (3.13)$$

¹The work presented in this section is partly based on Strangfeld et al. [2014]. Hans Müller-Vahl prepared the experimental setup at the Technion, Haifa, Israel. Christian Navid Nayeri and Christian Oliver Paschereit were responsible for the administrative frame work during this international cooperation. David Greenblatt mainly contributed to the idea to validate Isaacs' and Greenberg's theory based on the performed unsteady measurements. He also had the idea to predict the unsteady pressure distribution. However, all excerpts are written by myself.

3. Experimental setup and validation

Transformation of $v_{n,b}$ into a Fourier series gives equation 3.14.

$$v_{n,b}(\Theta, t) = \frac{d_0(t)}{2} + \sum_{n=1}^{\infty} d_n(t) \cos(n\Theta) \quad (3.14)$$

Now, all quantities in equation 3.10 are known except the vorticity sheet γ_b which gives the circulation by integration along the chord $\Gamma(t) = \int_{-c/2}^{c/2} \gamma_b(x, t) dx$. Flow tangency is required to solve this problem. A comparison of the Fourier series coefficients yields the following identities for the Fourier coefficients in equations 3.15 to 3.18 [Isaacs, 1945].

$$c_0(t) = 2\alpha(t)u(t) + c(0.5 - a)\dot{\alpha}(t) + 2\dot{h}(t) + b_1(t) + b_0(t) \quad (3.15)$$

$$c_1(t) = -2\alpha(t)u(t) + ac\dot{\alpha}(t) - 2\dot{h}(t) + b_2(t) - b_0(t) \quad (3.16)$$

$$c_2(t) = -0.5c\dot{\alpha}(t) + b_3(t) - b_1(t) \quad (3.17)$$

$$c_n(t) = b_{n+1}(t) - b_{n-1}(t) \quad n \geq 3 \quad (3.18)$$

Furthermore, the Kutta condition requires a stagnation point at the wing's trailing edge [Amiet, 1990]. $c_0(t)$ in equation 3.19 invokes this condition, because b_n converges to zero for $n \rightarrow \infty$.

$$c_0(t) = -\sum_{n=1}^{\infty} c_n(t) \quad (3.19)$$

Finally, the circulation is depicted in cylinder coordinates in equation 3.20 [Isaacs, 1945].

$$\begin{aligned} \Gamma(t) &= \frac{c}{2} \int_0^{\pi} \gamma_b(\Theta, t) \sin(\Theta) d\Theta \\ &= \frac{c}{2} \int_0^{\pi} \left[c_0(t) + \sum_{n=1}^{\infty} c_n(t) \cos(n\Theta) \right] d\Theta = \frac{\pi c}{2} c_0(t) \end{aligned} \quad (3.20)$$

Equation 3.20 is an elegant and simple interim result for the time varying circulation. Via the calculation of the last remaining coefficient $c_0(t)$, the problem may be solved. Furthermore, all $c_n(t)$ are functions of $b_n(t)$ which themselves vary only in time. Thus, the spatial variable x or Θ is eliminated. The formulation in equation 3.20 leads to an integro-differential equation of $\Gamma(t)$. In 1945, Isaacs publishes a solution for an unsteady free stream [Isaacs, 1945]. In 1992, van der Wall extends Isaacs' theory to unsteady plunge and pitching motion [van der Wall, 1992]. Both state the following expression for $b_n(t)$ with $\Lambda = W(t) - W(\tau)$ and $\dot{Q}(W(t) - \Lambda) = \dot{\Gamma}(t - T) = \dot{\Gamma}(\tau)$

$$b_n(t) = -\frac{2}{\pi c} \int_0^{\infty} \dot{Q}(W(t) - \Lambda) \frac{\left[1 + 2\Lambda/c - \sqrt{(1 + 2\Lambda/c)^2 - 1}\right]^n}{\sqrt{(1 + 2\Lambda/c)^2 - 1}} d\Lambda \quad (3.21)$$

Under the assumption that all explicit variables, for example, $u(t)$, $\alpha(t)$, $h(t)$, are periodic in time with the angular frequency ω and the starting process is negligible, the resulting circulation $\Gamma(t)$ is periodic in time as well. Thus, the time derivation of the circulation, which is equivalent to the shed wake vorticity strength, is given in equation 3.22.

$$\dot{Q}(W(t) - \Lambda) = \sum_{m=-\infty}^{\infty} a_m i m \frac{\omega}{u_s} e^{i m \frac{\omega}{u_s} (W(t) - \Lambda)} \quad (3.22)$$

$W(t)$ describes the distance travelled by the airfoil through the unsteady inflow. Hence, $W(t)$ is the time integral of the free stream velocity $u(t)$. The most general formulation of the coefficients a_m is given by van der Wall [1992].

The equations 2.67 to 2.73 represent a closed solution of the unsteady wake. An unsteady free stream, unsteady pitching motion, and unsteady plunge motion are obviously included in the presented coefficients.

3.4. Derivation of the unsteady bound circulation and vorticity sheet

Thereby, the terms J describe Bessel-functions of the first kind. For clarity, the argument $m\sigma$ of the functions J, H has been omitted in the equations 2.67 and 2.68. k is the reduced frequency introduced in equation 2.50. By means of the known shed vorticity, the circulation of the wing section is now determined in equation 3.20. This enables the computation of the "Joukowsky" lift and the "impulsive pressure" lift. For this purpose, only the two coefficients $c_0(t)$ and $c_1(t)$ need to be evaluated for the desired unsteady motion as Isaacs and van der Wall already did.

As already mentioned, the unsteady vorticity sheet provides deeper insight into the flow structures compared to integral values such as the lift. The integration of the vorticity sheet along the chord in equation 3.20 avoids the calculation of the coefficients $c_n \geq 2$. Nevertheless, this is the starting point for the new derivation of the unsteady bound vorticity sheet γ_b in equation 3.23, which directly follows from equation 3.20.

$$\gamma_b(\Theta, t) = \frac{c_0(t) + \sum_{n=1}^{\infty} c_n(t) \cos(n\Theta)}{\sin(\Theta)} \quad (3.23)$$

As a first step, the limit values at the boundaries of the codomain are investigated. At the leading edge ($\Theta = \pi$) and at the trailing edge ($\Theta = 0$), the denominator becomes zero in the equation 3.24 and 3.25.

$$\lim_{\Theta \rightarrow \pi}(\gamma) = \frac{c_0(t) + \sum_{n=1}^{\infty} (-1)^n c_n(t)}{"0"} \rightarrow \infty \quad (3.24)$$

$$\lim_{\Theta \rightarrow 0}(\gamma) = \frac{c_0(t) + \sum_{n=1}^{\infty} c_n(t)}{"0"} = \frac{-\sum_{n=1}^{\infty} c_n(t) + \sum_{n=1}^{\infty} c_n(t)}{"0"} = \frac{"0"}{"0"} \quad (3.25)$$

By means of the Kutta condition in equation 3.19, equation 3.25 does not give a definite result. Thus, a re-evaluation using the rule of Bernoulli-L'Hopital is required.

$$\lim_{\Theta \rightarrow 0}(\gamma) \Rightarrow = \frac{-\sum_{n=1}^{\infty} \sin(n\Theta)}{\cos(\Theta)} = \frac{"0"}{1} = 0 \quad (3.26)$$

Equation 3.26 depicts that the vorticity sheet strength becomes zero at the trailing edge. This is a direct consequence of the Kutta condition which requires a stagnation point at the trailing edge. Thus, the unsteady vorticity sheet derived here and the well known steady vorticity sheet [Anderson, 2011] possess the same marginal limits. Furthermore, in steady conditions all coefficients b_n in equation 3.21 are identical to zero and combining equation 3.23 with the equations 3.15 to 3.19 gives the well known equation for the steady vorticity sheet (compare with equation 4.23 in [Anderson, 2011]).

Although the limits of the unsteady bound vorticity sheet are consistent with the steady case, the time varying coefficients c_n are still unknown in equation 3.23. Unfortunately, here all coefficients have to be calculated in contrast to equation 3.20 where the integration along the chord eliminates all coefficients except c_0 . However, equation 3.21 combined with the periodic formulation of the unsteadily shed vorticity in equation 3.22 leads to equation 3.27.

$$b_n(t) = -\frac{2}{\pi c} \int_0^{\infty} \sum_{m=-\infty}^{\infty} a_m i m \frac{\omega}{u_s} e^{i m \frac{\omega}{u_s} (W(t) - \Lambda)} \frac{[1 + 2\Lambda/c - \sqrt{(1 + 2\Lambda/c)^2 - 1}]^n}{\sqrt{(1 + 2\Lambda/c)^2 - 1}} d\Lambda \quad (3.27)$$

A rearrangement of equation 3.27 is expressed in equation 3.28.

$$b_n(t) = -\frac{2}{\pi c} \sum_{m=-\infty}^{\infty} a_m i m \frac{\omega}{u_s} e^{i m \frac{\omega}{u_s} W(t)} \int_0^{\infty} e^{-i m \frac{\omega}{u_s} \Lambda} \frac{[1 + 2\Lambda/c - \sqrt{(1 + 2\Lambda/c)^2 - 1}]^n}{\sqrt{(1 + 2\Lambda/c)^2 - 1}} d\Lambda \quad (3.28)$$

3. Experimental setup and validation

The distance travelled by the airfoil $W(t)$ is still undetermined. Now, the sinusoidal velocity profile from equation 2.51 will be assumed. The starting process is not considered, thus the time integration yields the distance travelled with $W(t) = \int u(t)dt = u_s(t - \frac{\sigma}{\omega} \cos(\omega t))$. Furthermore, the definition of the reduced frequency k from equation 2.50 is used in equation 3.29.

$$b_n(t) = -\frac{2}{\pi c} \sum_{m=-\infty}^{\infty} a_m im \frac{2k}{c} e^{im(\omega t - \sigma \cos(\omega t))} \int_0^{\infty} e^{-im \frac{2k}{c} \Lambda} \frac{\left[1 + 2\Lambda/c - \sqrt{(1 + 2\Lambda/c)^2 - 1}\right]^n}{\sqrt{(1 + 2\Lambda/c)^2 - 1}} d\Lambda \quad (3.29)$$

The coefficient $a_m = \frac{A_m}{R_m}$ is already determined in general in the equations 2.69 to 2.73. For clarity, the coefficient A_m is $\frac{im}{2m} \pi c \alpha_s u_s \sigma (J_{m+1} - J_{m-1})$ for the explicitly given sinusoidal free stream velocity profile. The already derived expression for $R_m = 1 + imk \frac{2}{c} \int_0^{\infty} e^{-im \frac{\omega \Lambda}{u_s}} (\sqrt{\frac{c}{\Lambda} + 1} - 1) d\Lambda$ [van der Wall, 1992] represents the denominator in equation 3.30. The phase angle $\phi = \omega t$ is introduced for simplification without loss of generality.

$$b_n(\phi) = -\frac{2}{\pi c} \sum_{m=-\infty}^{\infty} A_m im \frac{2k}{c} e^{im(\phi - \sigma \cos(\phi))} \frac{\int_0^{\infty} e^{-imk \frac{2\Lambda}{c}} \frac{\left[1 + 2\Lambda/c - \sqrt{(1 + 2\Lambda/c)^2 - 1}\right]^n}{\sqrt{(1 + 2\Lambda/c)^2 - 1}} d\Lambda}{1 + imk \frac{2}{c} \int_0^{\infty} e^{-imk \frac{2\Lambda}{c}} (\sqrt{\frac{c}{\Lambda} + 1} - 1) d\Lambda} \quad (3.30)$$

$S_m = im \frac{2k}{c} e^{im(\phi - \sigma \cos(\phi))}$ is introduced and the substitution $\Lambda = c\tilde{\Lambda}$ with $d\Lambda = c d\tilde{\Lambda}$ simplifies the final equation of $b_n(\phi)$.

$$b_n(\phi) = -\frac{2}{\pi} \sum_{m=-\infty}^{\infty} A_m S_m \frac{\int_0^{\infty} e^{-imk 2\tilde{\Lambda}} \frac{\left[1 + 2\tilde{\Lambda} - 2\sqrt{\tilde{\Lambda}^2 + \tilde{\Lambda}}\right]^n}{2\sqrt{\tilde{\Lambda}^2 + \tilde{\Lambda}}} d\tilde{\Lambda}}{1 + 2imk \int_0^{\infty} e^{-imk 2\tilde{\Lambda}} \left(\sqrt{\frac{1}{\tilde{\Lambda}} + 1} - 1\right) d\tilde{\Lambda}} \quad (3.31)$$

Now, the problem of the unsteady bound vorticity sheet $\gamma_b(\Theta, t)$ is completely solved. By means of the known coefficients b_n , $\gamma_b(\Theta, t)$ is determined for all arbitrary amplitudes σ and reduced frequencies k . Although A_m , S_m , and the denominator in equation 3.31 are independent of n , the integral in the numerator possesses n as an exponent. Thus, for all desired wave numbers m and coefficients b_n , this equation has to be solved separately. This results in an excessive processing time because several hyperbolic Bessel functions K and confluent hypergeometric Kummer functions M are part of the solution. Exact solutions of the integrals, named $\kappa(n)$, are given in the appendix for arbitrary σ and k . The numerical values of b_n and c_n are given for $\sigma = 0.5$ and $k = 0.074$ by Strangfeld et al. [2014].

3.5. Experimental setup for validation of Isaacs' and van der Wall's theories at high inflow velocity ratios

Intermediate conclusion: A validation of Isaacs' and van der Wall's theories at moderate and high velocity amplitudes is, at yet, missing. Thus, the experimental setup with the unsteady wind tunnel and the NACA 0018 airfoil is presented. The installed louver mechanism generates strong free stream velocity amplitudes of 50%. The expected dynamic effects lie in the range of 10 to 25%. Thus, the unsteady free stream velocity profile is measured and analysed intensively to ensure a reliable and repeatable gust generation. The maximum deviation amounts to 3% compared to an ideal sine, thus this innovative setup allows an experimental validation of the mentioned theories. This validation is the basis for Betz's theory under unsteady conditions. Only with an exact prediction of the bound circulation, the interaction of spanwise and streamwise circulation and the long-wavelength actuation of the wing tip vortex are accurately predicted.

¹ Besides an extension of the existing theory, the experimental validation especially for high velocity amplitudes is of high interest. This validation is the key to theoretically link the spanwise and the streamwise circulation. Thus, Betz's theory under unsteady conditions is based on this validation. In this section, the wind tunnel designed for unsteady measurements is described first. Then, the NACA 0018 airfoil, including the opportunities of AFC, is presented. At the end, the louver mechanism to control the unsteady free stream velocity is shown and the velocity profile is quantified.

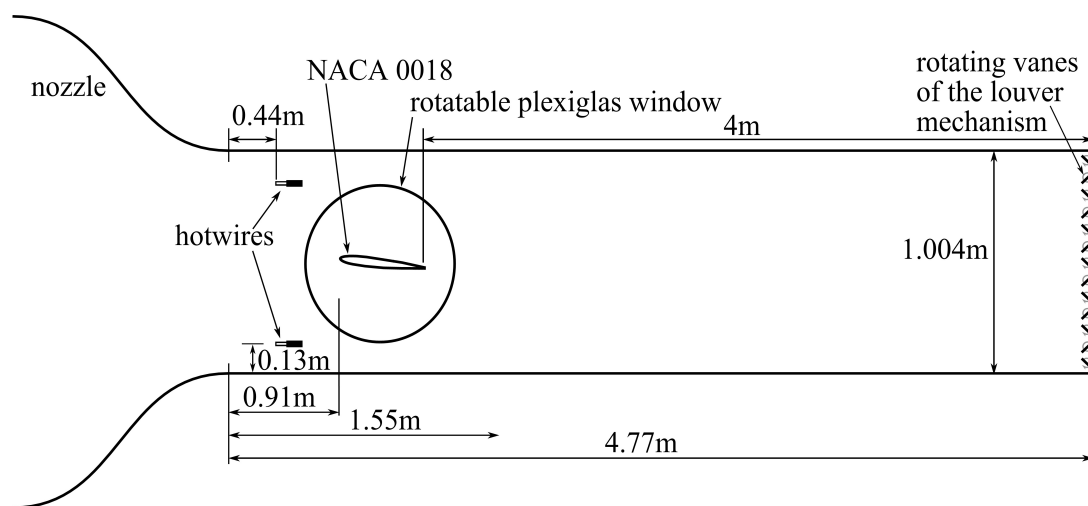


Figure 3.16.: Sketch of the wind tunnel setup: The louver mechanism is placed at the end of the wind tunnel. The wing is rotatable and the unsteady free stream velocity is recorded upstream of the wing via two hotwires.

Figure 3.16 depicts a sketch of the entire wind tunnel setup. The blow down wind tunnel possesses a cross-section of 0.61m by 1.004m and a 8:1 contraction ratio. The maximum free stream velocity is 55m/s with a turbulence level of less than 0.3%. The wind tunnel is powered by a revolutions per minute regulated 75kW radial blower. The blower is specifically designed to operate smoothly under stalled conditions, allowing for a dynamic variation of the wind tunnel speed by adjusting the cross-sectional area of the wind tunnel exit. The ceiling, floor, and side walls of the test section incorporating the airfoil are equipped with Plexiglas to ensure optimal optical access for PIV measurements. At the end of the 4.77m long test track louvers control the free stream velocity dynamically. The distance from the louvers to the trailing edge of the wing is 3.5m, which may prevent any inhomogeneities propagating upstream to the

¹The work presented in this section is partly based on Strangfeld et al. [2014]. Hans Müller-Vahl prepared the experimental setup at the Technion, Haifa, Israel. He conducted most of the experiments. Christian Navid Nayeri and Christian Oliver Paschereit were responsible for the administrative frame work during this international cooperation. David Greenblatt hosts and supervises the wind tunnel. He designed the wind tunnel and initiated the unsteady NACA 0018 measurements.

3. Experimental setup and validation

wing. The louver mechanism consists of 13 fully rotatable vanes driven by a 0.75kW servo motor. The maximum blockage amounts to 95%. A detailed description and reference measurements are published by Furman et al. [2013]. The phase lag of the pressure wave which travels upstream as a result of a change in the louver position was determined to be below 1deg for all free stream velocities considered at 1Hz. Thus, all conceivable phase lags along the chord are negligible.

Figure 3.16 shows a schematic of the experimental setup. The two-dimensional NACA 0018 airfoil profile is placed at the vertical centre of the test section. The leading edge is positioned 0.825m downstream of the nozzle. Three-dimensional effects such as wing tip vortices are avoided by the stiff mounting of the NACA 0018 directly on the wind tunnel walls. The side walls are made of two rotatable Plexiglas windows with a diameter of 0.93m. Both windows are synchronously driven by a 1.5kW servo motor placed above the test section. This permits any arbitrary pitching motion including complete 360° loops. In all configurations, the pitching axis is located at the quarter-chord point. The unsteady free stream velocity in the test section is measured by two hotwires. The data acquisition of the surface pressures and the wind tunnel speed were synchronized, both were recorded at a frequency of 497Hz. Thus for each unsteady pressure measurement the associated free stream velocity is recorded. The data are recorded via an anemometry system (company: *A.A. Lab Systems*, type: *AN-1003 Test Module*). The hotwires are calibrated every day before the measurements start by means of a Pitot tube above the wing. The Pitot tube measures the steady free stream velocity, which is recorded by a Dwyer Manganese pressure transducer. The hotwire technique prevents any phase lag due to long tubes which render the usage of the Pitot tube impossible for the unsteady oscillating free stream.

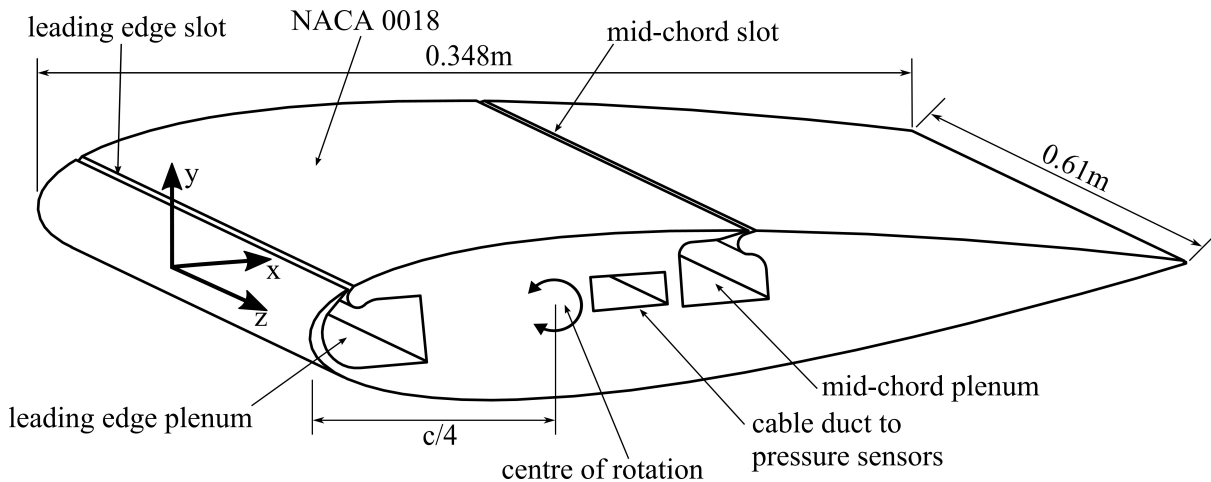


Figure 3.17.: Schematic sketch of the used NACA 0018 airfoil including the two AFC slots

Figure 3.17 illustrates the used NACA 0018 airfoil in detail. The chord is $c = 0.348\text{m}$ and the span is $s = 0.61\text{m}$, resulting in an aspect ratio of 1.75. The wing is equipped with two slots on one wing side for optional active flow control methods such as steady blowing or zero mass flux excitation. The slot positions are 5% and 50% of the chord. The slots along the entire span are 1.2mm wide and a cavity is located below. The slots are sealed to disable any undesired mass flow through the slots. The wing profile centre line is equipped with 40 pressure taps with a diameter of 0.8mm to measure the static pressure at the wing surface, see figure 3.18. The pressure taps of the pressure and suction side are symmetrically distributed, the corresponding positions are documented in table 3.19. This is an important detail because the vorticity sheet strength is proportional to the pressure difference at a certain chordwise position. The static pressure is recorded synchronised by means of two piezoresistive pressure scanners (company: *Chell Instruments*, type: *ESP-32HD*) up to a sample rate of 500Hz. These two pressure scanners are placed inside the wing and each pressure port is connected to the pressure tap by a 44cm long tube. The uniform tube length may provoke a constant phase lag of the dynamic pressure measurements for all taps [Greenblatt et al., 2001]. However, the lag was found to be negligible for the oscillation frequencies considered here.

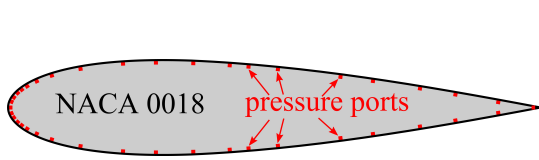


Figure 3.18.: Illustration of the symmetrically distributed pressure taps

no.	x/c	no.	x/c	no.	x/c	no.	x/c
1	0	6	.025	11	.276	16	.626
2	.002	7	.05	12	.345	17	.695
3	.005	8	.085	13	.434	18	.776
4	.01	9	.14	14	.463	19	.922
5	.015	10	.216	15	.514	20	1

Figure 3.19.: Chordwise position of the 40 pressure sensors

All presented quantities are normalised by means of the dynamic pressure of the free stream. Two hotwires are used to record the instantaneous free stream velocity in the test section. The assumed actual free stream velocity is the average of both hotwires. As discussed before, any phase lags between the leading edge and the trailing edge are negligible. The lift is calculated by means of the 40 pressure taps. The measured static pressure, which acts normal to the surface, is weighted by the half distance to the neighbouring pressure taps and transformed in the coordinate system of the wing chord. The summation yields the lift and the pressure drag (drag due to friction is not quantified). The cross product of the static pressure at each pressure tap and the distance to the $c/4$ -line gives the pitching moment. The phase reconstruction is based on the averaged free stream velocity of the two hotwires. Taking into account that the amplitude of the free stream oscillation varies slightly, each single period was fitted by an ideal sine to avoid any unphysical scatter in the data. Each measurement consists of at least 150 periods. The data are averaged at each $\alpha = 0.5^\circ$ step with a window size of $\pm 0.3^\circ$ and at each $\phi = 2^\circ$ step with a window size of $\pm 1^\circ$.



Figure 3.20.: Photograph of the 13 louver vanes at the end of the test section in open and closed position

The presented theoretical models are able to handle simple sinusoidal oscillating inflow. Thus, the fundamental basis for experimentally measured dynamic effects is a precise and accurate adjustment of the time varying free stream velocity $u(\phi) = u_s(1 + \sigma \sin(\phi))$. A deviation of u_s mainly causes an offset of the measured forces. Even more important is the amplitude of the velocity variation σ . It has a direct impact on the dynamic effects. Figure 3.21 shows a representative comparison of the measured phase averaged free stream velocity and the sinusoidal free stream velocity profile, which is assumed in Isaacs' theory. The corresponding time averaged Reynolds number is $\overline{Re} = 300000$ and the oscillation frequency is $f = 1.2\text{Hz}$. As already mentioned, the free stream velocity in the test section is controlled by the louver mechanism at the end of the test

track. It is obvious that the two velocity profiles are very similar to each other. The ideal time averaged free stream velocity is $\bar{u}_{s,ideal} = 13.32\text{m/s}$ and the measured time averaged one is $\bar{u}_{s,measured} = 13.3\text{m/s}$, resulting in a deviation of around 0.15%. The desired amplitude is $\sigma = 0.5$ and the measured one is $\sigma_m = 0.5061$. The resulting difference is approximately 1.2%. Thus, both parameters are considered to be experimentally reproduced with sufficient accuracy. Furthermore, figure 3.21 depicts the relative divergence for one complete cycle. In the range of $\phi = 250^\circ$ an overshoot of almost 3% is evident although for the other ϕ , a slight undershoot exists. The current data set does not admit a quantification of possible errors caused by the deviations of approximately $\pm 3\%$. For lower frequencies of 0.75Hz, the deviation reduces to 2% [Strangfeld et al., 2014]. Furthermore, the maximum and minimum peak possess

3. Experimental setup and validation

a phase lag of around 180° . This may be caused by the dynamic stall of the rotating louver vanes. This strong phenomenon immediately affects the blockage of the vanes and may lead to nonlinear blockage and pressure losses. However, in summary, due to the low differences between measured and desired parameters, these deviations are assumed to be negligible. Hence, the entire free stream velocity profile is expected to be sufficient for dynamic measurements.

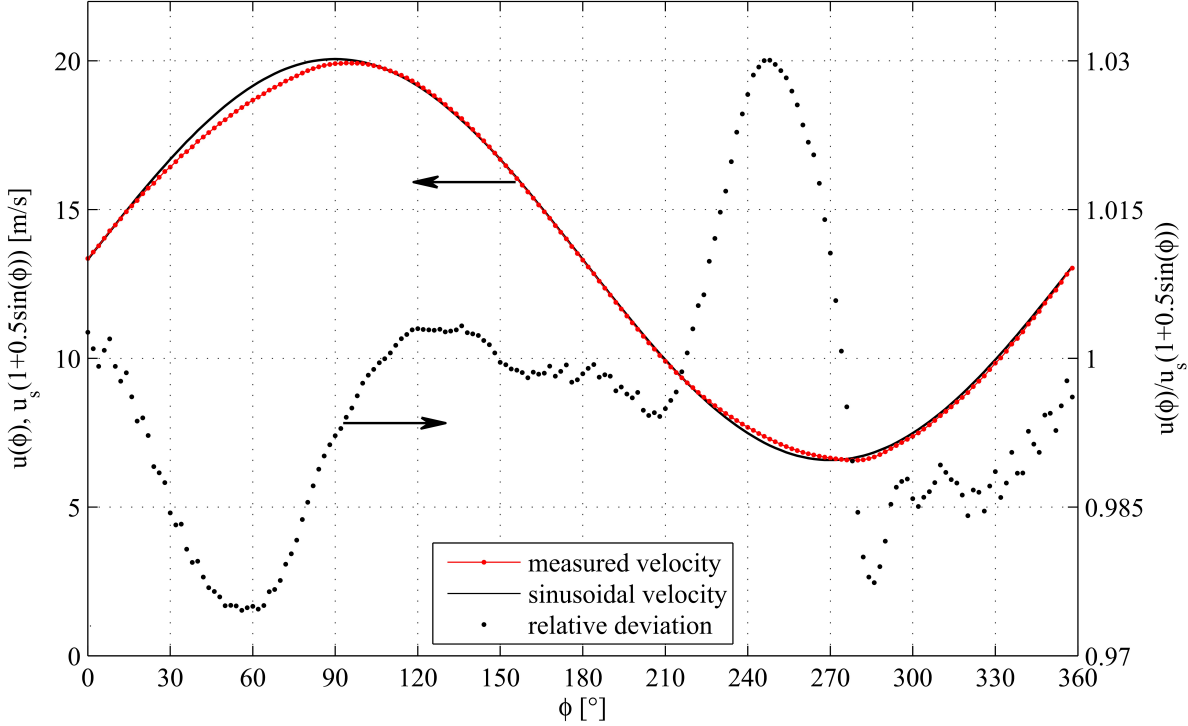


Figure 3.21.: Comparison of the measured free stream velocity $u(\phi)$ and the ideal sinusoidal free stream velocity $u_s(1 + 0.5 \sin(\phi))$ at a frequency of $f = 1.2 \text{ Hz}$ and $\overline{Re} = 300000$; the relative deviation of the experimental data from the ideal profile is shown on the ordinate on the right hand side

Although the presented precision of the adapted oscillating velocity profiles is high, one systematic disparity between the experiments and the theory exists. Figure 3.22 (a) shows the experimental setup. The steady wing is facing an oscillating free stream. The wavelength of the oscillating flow is much longer than the wing chord ($\lambda_{osc} \gg c$). Figure 3.22 (b) depicts the case propagated by, for example, Isaacs's theory (fore-aft wing motion). The free stream velocity remains constant the entire time whereas the wing is moving up- and downstream with $\pm u_w$. This assumption implies that the normal velocity component v_n is constant in space, more precisely along the chord, whilst changing in time. In the current study, the unsteady free stream hits the trailing edge first and convects towards the leading edge. Consequently, a gradient of the induced normal velocity exists along the chord $v_c(x, t)$. This methodical disparity is inherent in this presented experimental setup. The gradient of $v_c(x, t)$ may be reduced by increasing the wavelength of the oscillating free stream relative to the free stream velocity itself. However, this implies a reduced frequency k as well. Hence, dynamic effects are distinctly mitigated. However, van der Wall [1992] already discussed this issue. He states, at large reduced frequencies $k \rightarrow \infty$, the noncirculatory lift will be zero for a static wing facing unsteady free stream as it is the case in a vertical gust field. In the opposite case, a fore-aft moving wing in steady flow, the noncirculatory lift becomes infinite. As far as is known by the author, it is unknown so far beyond which k the dynamic effects are reduced significantly.

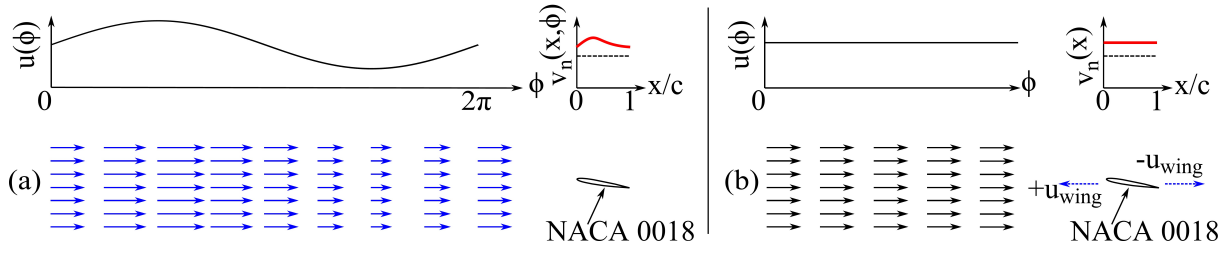


Figure 3.22.: (a): a static wing encounters an oscillating free stream (blue arrows); (b) a fore-aft moving wing (blue arrows) in a constant free stream; the diagrams show the free stream velocity profile $u(\phi)$ and the induced normal velocity along the chord v_n (red line)

3.6. Determination of the streamwise and spanwise vorticity interaction

Intermediate conclusion: The theory from Betz and the inverse Betz method are briefly summarised. The existing equations are extended to take the unsteady conditions into account. With this ansatz, the unsteady circulation strength and the centroid meandering are determined.

Betz's theory is considered to be the most accurate way of calculating the wake vortex characteristics. Furthermore, it is an inviscid theory and the implementation is relatively easy compared to viscous models or CFD simulations. Thus, the governing equations of Betz's theory are briefly repeated in the form published by Donaldson [1971]. The assumption of Betz is that the circulation is constant in the entire system. Hence, the generated circulation along the span Γ_{sp} has to be equal to the circulation of the streamwise vortex Γ_{st} in the wake which is expressed in equation 3.32 [Betz, 1932].

$$\int_{r_1}^{r_2} \frac{\partial \Gamma_{st}(r)}{\partial r} dr = - \int_{y_1}^{y_2} \frac{\partial \Gamma_{sp}(y)}{\partial y} dy = const \quad (3.32)$$

This general formulation is adapted to the considered case of a simple, finite wing. Thus, the boundaries of integration are the wing mid-span at $y = 0$ and the wing tip at $y = s/2$. This implies that the upper margin of this integral becomes zero because the circulation production is zero at the wing tip at all times. Furthermore, the time dependent behaviour of the circulation due to the unsteady environmental conditions is taken into account.

$$\int_0^R \frac{\partial \Gamma_{st}(r, t)}{\partial r} dr = - \int_{y=0}^{y=s/2} \frac{\partial \Gamma_{sp}(y, t)}{\partial y} dy = \Gamma_{sp}(y, t)|_{y=s/2}^{y=0} = \Gamma_{sp}(y = 0, t) \quad (3.33)$$

Equation 3.33 is an interesting result. The strength of the streamwise vortex depends only on the amount of circulation at mid-span. Under unsteady conditions, a lift overshoot or deficit is generated which may be predicted by the discussed theories of Theodorsen, Isaacs, and van der Wall. The consequence is that only the dynamic response of the lift or the circulation at mid-span influences the vortex strength of the streamwise vortex. The second parameter of interest of the streamwise vortex is its centre position. Equation 3.34 recapitulates the determination of the centroid position y_c proposed by Donaldson [1971].

$$y_c = \frac{1}{\Gamma_{sp}(y_1)} \int_{y_1}^{y_2} y \frac{\partial \Gamma_{sp}(y)}{\partial y} dy \quad (3.34)$$

The margins of this formulation are adapted to the simple finite wing and the time-dependency of the spanwise circulation is implemented.

$$y_c(t) = \frac{1}{\Gamma_{sp}(y = 0, t)} \int_{y=0}^{y=s/2} y \frac{\partial \Gamma_{sp}(y, t)}{\partial y} dy \quad (3.35)$$

To solve equation 3.35, the entire unsteady spanwise circulation distribution is required. Furthermore, the

3. Experimental setup and validation

amount of circulation at mid-span in the denominator has a direct impact on the centroid position as well. This proposed approach in equations 3.33 and 3.35 enables the prediction of the unsteady circulation strength of the streamwise vortex under unsteady conditions. This emphasises the need of an accurate prediction of unsteady lift at each spanwise position with the corresponding reduced frequency via the theories of Theodorsen, Isaacs, or van der Wall.

The third axiom of Betz's theory is that the second moment of vorticity has to be constant. The maximum radius and the circulation distribution of the emitted trailing vortex are determined based on this approach. Equation 3.36 shows the conservation of the second moment of vorticity, whereby the time dependency is already implemented.

$$\int_{y=s/2}^{y_1} (y_c(y_1, t) - y)^2 \frac{\partial \Gamma_{sp}(y, t)}{\partial y} dy = \int_0^{r_1} r(t)^2 \frac{\partial \Gamma_{st}(r, t)}{\partial r} dr \quad (3.36)$$

The roll up process starts at the wing tip by assumption, hence equation 3.36 can be applied piecewise. This ansatz yields directly a mathematical relation between the spanwise position y_1 and the corresponding radius position r_1 . The vortex centre of this emitted trailing vortex is located at the centroid position of the spanwise circulation. This relation is presented in equation 3.37 [Rossow, 1973].

$$r_1(t) = \frac{1}{\Gamma_{sp}(y_1, t)} \int_{y=s/2}^{y_1} \Gamma_{sp}(y, t) dy \quad (3.37)$$

The inverse Betz method submits the calculation of the spanwise circulation based on the streamwise vortex quantities. Here, the formulation of Rossow is used in equation 3.38 [Rossow, 1975, 1999]. The time dependency is already implemented.

$$\frac{b}{2} - y_1(t) = r(t) + \int_0^{r_1} \frac{r(t)}{\Gamma_{st}(t)} \frac{d\Gamma_{st}(t)}{dr} dr \quad (3.38)$$

The transversal actuation of the streamwise vortex by means of the segmented flaps modifies the vortex strength at its origin. With the inverse Betz method, the impact on the spanwise circulation distribution is determined and load control may be performed via AFC.

4. Results

Firstly, the control authority of streamwise vortices by means of short-wavelength actuation is quantified. Thus, baseline measurements of the swept, semi-span, backward facing step by means of smoke and surface oil flow visualisation as well as surface pressure measurements are considered. The influence of the active flow control is quantified for several frequencies, amplitude, and phase velocities. The boundary layer on the step top, which represents the main initial condition for AFC, is measured and the form parameter is determined. The three velocity components directly downstream of the trailing edge are depicted and a temporal stability analysis based on an ideal, two-dimensional shear layer is performed. Secondly, the pitching NACA 0018 airfoil in unsteady inflow is presented. Baselines, a pure pitching motion, a pure unsteady inflow, a simple superposition of these two effects, and a simultaneous occurrence of these two effects are discussed theoretically and experimentally. These theories and their validation deliver the required theoretical basis to predict the spanwise circulation distribution along a finite wing under unsteady conditions. As a final step, Betz's theory is used to quantify the time depended interaction between the spanwise and streamwise circulations. The computations of the vortex strength and the centroid position meandering depict the opportunities of the long-wavelength actuation of the trailing vortex.

4.1. Flow visualisation of the baseline flow at the swept, semi-span, backward facing step

Intermediate conclusion: The swept, semi-span, backward facing step is a newly developed geometry to generate streamwise vortices. The baseline measurements via smoke and surface oil flow visualisation yield a strong and stable streamwise vortex downstream of the swept trailing edge of the step. The three-dimensional smoke flow structures reveal vortical structures. The rolling up shear layer is similar to wing tip vortices and to primary vortices on delta wings. The surface oil discloses the existence of a secondary vortex between the primary vortex and the trailing edge. Furthermore, a spanwise oriented separation bubble originating from the side wall is identified. These flow characteristics are equal to the flow structures on the slanted back of an Ahmed body. Finally, an analogy from the swept, semi-span, backward facing step to trailing vortices, delta wings and the wake of an Ahmed body is shown.

Although three swept angles are available for step, only the $\theta_{step} = 25^\circ$ case is discussed here in detail. In the case of higher swept angles, the step acts more like a bluff body without the generation of a streamwise vortex. This is validated by means of preliminary surface pressure, and stereo-PIV measurements [Dash, 2012]. This behaviour is consistent with, for example, the CFD simulation of Fares [2006] at an Ahmed body with a 35° swept angle and with the measurements of Hucho [2005].

4.1.1. Smoke visualisation of the streamwise vortex

Flow visualisations occupy a long tradition in the field of fluid dynamics [Prandtl, 1904] and still remain a powerful tool for several types of flow [Samimy et al., 2003]. Smoke is injected at the trailing edge of the swept, semi-span, backward facing step to visualise the baseline flow and the steady three-dimensional streamwise vortex generated by the rolling up shear layer. Figure 4.1 and 4.2 depict the flow structures at a swept angle of 25° . The smoke is injected on the top surface of the step through holes with a diameter of 4mm. The distance to the trailing edge is 1cm and the gap between two holes amounts to 4cm. The smoke machine (company: *Stairville*, type: *SF-80*) is placed directly inside the step's body. The low pressure at the trailing edge is strong enough to suck out the smoke inside the step. Hence, no blowing and tubing is

4. Results

required. Thus, any disturbances regarding the mass or energy balance are neglected [Lachmann, 1961]. The influence of the momentum is hard to quantify [Merzkirch, 1987]. As mentioned, no blowing is required and hence the additional momentum is reduced to its minimum. Thus, the disturbances of the momentum balance are neglected in this setup as well. The size of the particles is a trade-off between high reflections and the ability to follow the stream [Nitsche and Brunn, 2006]. A water-glycol mixture with a mean particle size of approximately $0.5\mu\text{m}$ is used [Eckelmann, 1997]. The photos are taken via a *Nikon D80* with a fixed-focus lens of 30mm and a maximum aperture of 1.8.

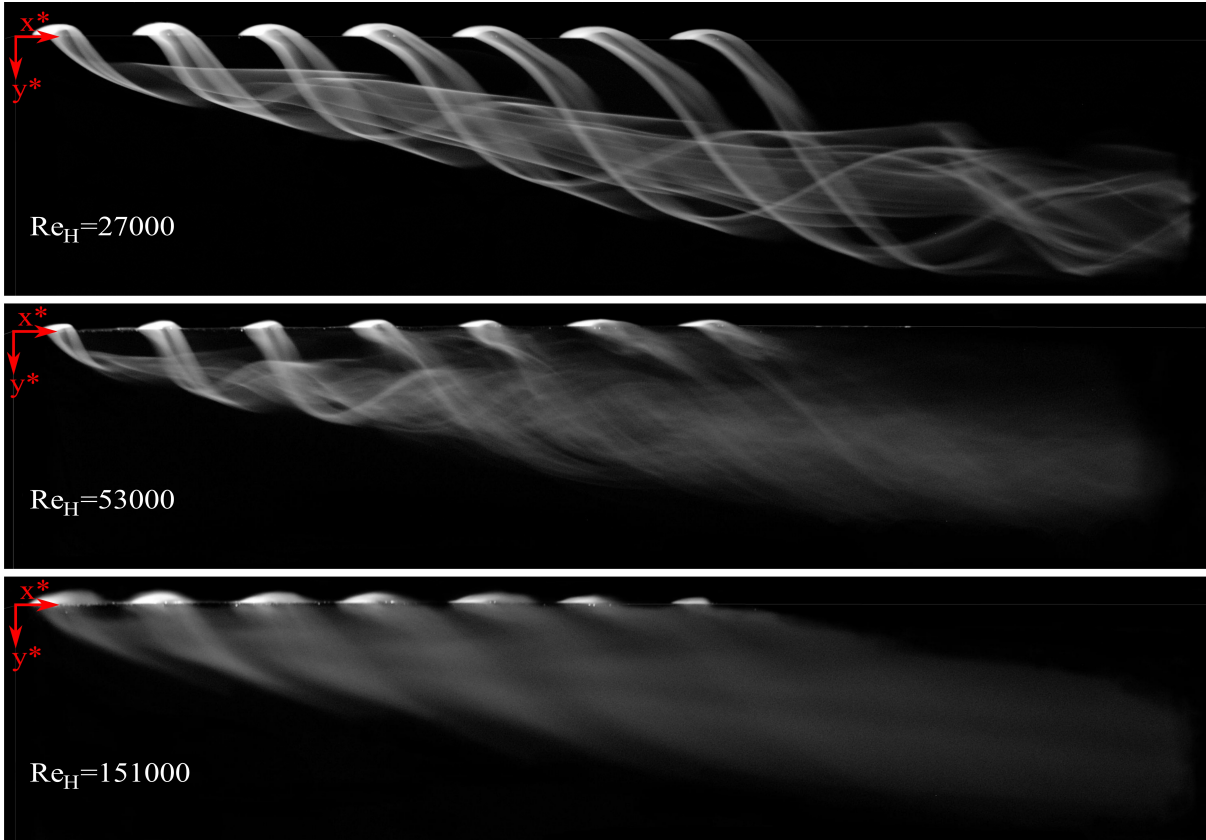


Figure 4.1.: Photographs perpendicular to the back panel of the rolling up shear layer downstream of the swept, semi-span, backward facing step at three different Reynolds numbers; settings: ISO 640, aperture 2.2, exposure time = 1/50s

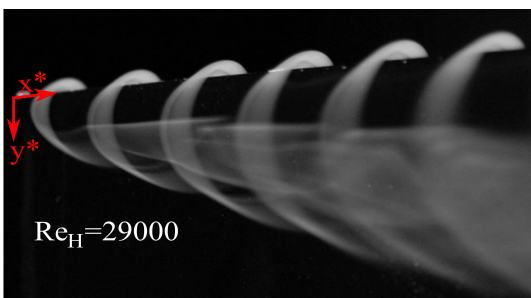


Figure 4.2.: Photographs perpendicular to the inflow of the rolling up shear layer downstream of the swept, semi-span, backward facing step at $Re_H = 29000$; settings: ISO 250, aperture 3.2, exposure time = 1/8s

regarded as laminar. At the medium Reynolds number, the smoke comes out straight and ordered through the holes as well. Until the third hole, distinct and undisturbed lines are visible. Downstream of the

Figure 4.1 shows the streamwise vortex downstream of the trailing edge for three different Reynolds numbers of $Re_H = 27000, 53000, 151000$ which corresponds to a free stream velocity of 0.8, 1.58, 4.5 m/s. The camera is positioned normal to the back panel of the step. Hence, the free stream comes out of the image plain and is tilted by the step angle of 25° . At the lowest Reynolds number, the laminar manner of the flow is clearly visible. The sucked out smoke escapes through the holes in straight lines. No disturbances are detectable although the shear layer rolls up on highly curved trajectories. All seven smoke trails roll into the vortex and clearly visualise the conical, helical shape around the vortex tube. As far as the end of the photo, the flow structures continue to be sharp and well organised. Thus, the entire vortex is

fourth hole, the lines in the vortex tube become blurred although the rolling up shear layer and the helical shape are still visible. A more diffuse cloud starts to emerge. Around the sixth hole, the rolling up shear layer is already blurred as well. The vortex tube is just a completely diffuse cloud. Therefore, this case is regarded as transitional flow. The flow structures appear laminar around the first three holes. Then, transition occurs and the vortex tube becomes more blurred although some distinct trajectories are still identifiable. Downstream of the sixth hole, the emitted rolling up shear is already turbulent. Furthermore, the diffuse vortex tube does not show distinct structures anymore. Hence, the transition finished and the entire flow is turbulent. At the highest Reynolds number, no fine structures exist. The smoke trails are already blurred directly above the holes suggesting a turbulent boundary layer on the step's top panel. The free shear layer emitted is entirely turbulent and rolls up into the streamwise vortex. In the middle of the vortex, a darker straight tube is slightly visible. This is probably the vortex core.

A direct comparison to other studies is not possible, because no flow visualisation downstream of a swept, semi-span, backward facing step exists. Hence, a comparison to finite wings, delta wings, and to the Ahmed body is drawn. Dacles-Mariani et al. [1995] investigate a finite NACA 0012 airfoil experimentally and numerically. Their simulations and smoke visualisations show clearly a rolling up shear layer and the onset of a streamwise vortex along the wing tip. Birch et al. [2004] use a bubble rake for visualising the tip vortex on a finite wing. The photographs depict clearly the rolling up process and the conical shape of the wing tip. Freymuth et al. investigate a rectangular NACA 0015 airfoil. The smoke visualises the wing tip vortex and, in the case of leading edge stall, a spanwise recirculation region. The size, the conical shape, and the rolling up process remain almost unaffected by the leading edge stall. This result further confirms the promoted analogy between the streamwise vortex downstream of a swept, semi-span, backward facing step and the wing tip vortex of a finite wing [Freymuth et al., 1986], [Freymuth et al., 1987], [Williamson et al., 1998]. Lambourne and Bryer [1962] use smoke on a delta wing and visualise the rolling up shear layer by means of smoke. The onset of the secondary vortex is visible as well. The conical shape of the primary vortex agrees to the presented ones. The flow visualisation of Délery [2001] on a delta wing with a 75° sweep coincides. The visualisations made by Lawson [1991] agree as well. Further, in a crosswise plane he shows clearly K-H instabilities in the rolling up shear layer. Beaudoin et al. [2004] visualise the vortex core of the streamwise vortex via cavitation and the vortex tube orientation is similar. Vio et al. [2005] combine smoke visualisations and PIV velocity measurements. Both measurement techniques reveal the rolling up shear layer and the conical shape of the streamwise vortex at the C-pillar. The entire wake of the Ahmed body is visualised, based on the LES simulations of Wassen and Thiele [2007]. The rolling up shear layer and the conical streamwise vortex coincide well with the presented flow structures. Heft et al. [2011] show the same flow structures at an Ahmed body for different turbulence models.

Figure 4.2 is taken parallel to the side wall of the step. Hence, the flow comes out perpendicular to the photo plain. In this perspective view, the rolling up shear layer downstream of the first two holes clearly outlines the conical, helical shape of the vortex comparable to a spiral. The structures on the right hand side of this photo appear blurred. In this region, the smoke is out of the focus plain and causes the blur (and not transition). At this Reynolds number, the entire flow field is laminar. Further photographs and detailed case studies are documented by [Düwel, 2012], [Strangfeld et al., 2013a].

Gilliéron and Spohn [2002] show flow visualisation of the streamwise vortex in a perspective view on the slant of the Ahmed body. The flow structures agree well. In summary, the smoke visualisations yield a high agreement of the swept, semi-span, backward facing step with wing tip vortices, delta wings, and furthermore with the Ahmed body and confirm the motivated analogy.

4.1.2. Surface oil flow visualisation on the slanted back panel

Figure 4.3 depicts the oil structures on the surface of the back panel due to the surrounding flow. The photograph is oriented perpendicular to the slanted back. Hence, the inflow comes out of the photo plain and is tilted by the slant angle of 25° . The flow separates at both edges of the step top and the side wall. On the left hand side, a region of reverse flow is visible. A line of diverse pattern of the tracer lines represents the reattachment line and is marked by the dashed red line. The reattachment line surrounds the spanwise orientated recirculation vortex downstream of the side wall. In the upper range of the photograph, a straight white line is clearly apparent. This is the separation line of the primary vortex. At a certain

4. Results

point, the rotational flow lifts from the surface. Below this white line, tilted lines are present. This is the footprint of the primary vortex due to the high axial and tangential velocities. These twisted tracer lines yield a smooth "S"-shape. The inflation point of the "S"-form corresponds to the highest slope of the tracer to the step top. This indicates the highest tangential velocities which probably occur beneath the vortex centre. In this region, the lowest surface pressure is detectable as well. Below the area with twisted lines, the orientation becomes more and more aligned with the free stream direction. This is the merging area of the streamwise vortex and the spanwise recirculation vortex and its reattached wake. Otherwise, above the primary vortex a region including tracer lines in the form of a mirrored "S" indicates a secondary vortex. Furthermore, a second thin straight line appears which is probably its separation line. This flow visualisation depicts that the spatial dimensions of the primary vortex are remarkably large compared to the secondary one.

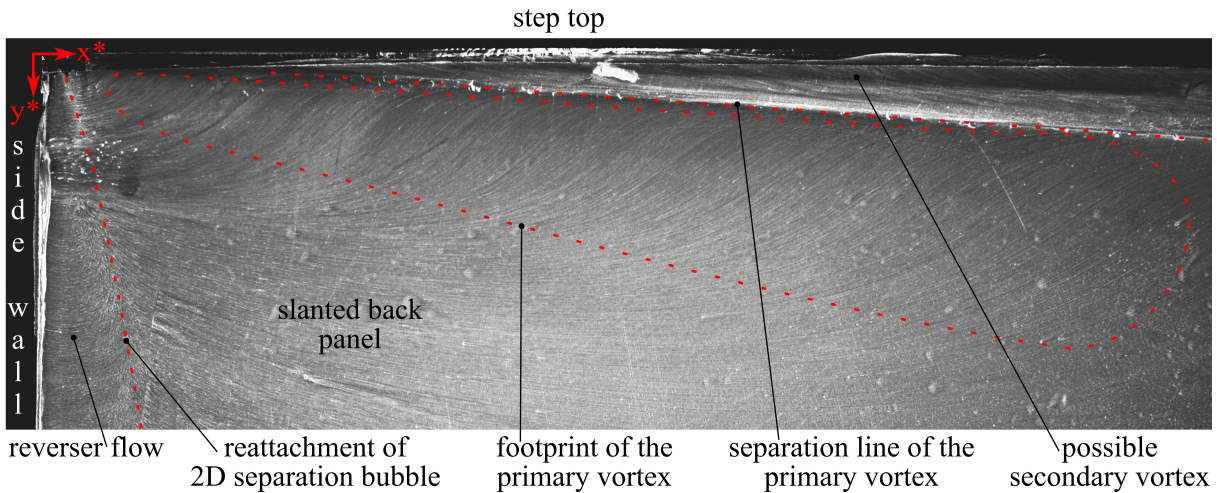


Figure 4.3.: Photograph of the surface oil flow visualisation perpendicular to the slanted back panel

This described tracer line pattern is in strong agreement with several Ahmed body investigations. The surface oil visualisations of Lienhart et al. [2002] have a poor quality but resemble the described effects globally. Sims-Williams [2001] conducts surface flow visualisations on an Ahmed body which coincide with the results. The china clay images of Vino et al. [2004] yield a high quality and agree well with the observations presented. In their images, a horse-shoe vortex inside the 2D separation bubble is present as well. The flow structure is suppressed here because the splitter plate prohibits such an interaction. Krajnović and Davidson [2005a] deliver a highly resolved tracer line pattern around the entire back of the Ahmed body based on their LES simulations. They investigate the difference between a static floor and a moving belt. Although the entire wake changes significantly, the flow structures at the C-pillar and on the slanted back vary only slightly. Hummel and Redeker [2003] investigate a delta wing. His experiments demonstrate the same pattern including a primary and a secondary vortex.

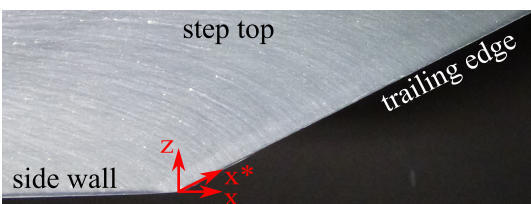


Figure 4.4.: Photograph of the surface oil flow visualisation of the step top

The photograph in figure 4.4 depicts the step top. The inflow comes from the left and separates at the trailing edge. The closer the tracer lines are to the trailing edge, the more they are tilted towards the edge. The trace lines are almost perpendicular in the vicinity of the trailing edge where the streamwise vortex originates. More downstream, along x^* , the twist is reduced. Upstream of the trailing edge, the flow is already tilted towards the side wall. The flow partly convects towards the side wall.

Thus, there is already an interaction between the side and the top flow. This phenomenon is known for the Ahmed body and for realistic vehicle models as well [Strangfeld et al., 2013b], [Wieser et al., 2014]. Krajnovic and Davidson [2004] show tracer lines on the side wall of an Ahmed body as well, based on a LES simulation. The entire behaviour with the strong tilted lines close to the trailing edge is confirmed. Especially at the origin of the streamwise vortex the lines are almost perpendicular to the edge.

4.2. Pressure measurements of the baseline and forced flow

Intermediate conclusion: Time resolved surface pressure measurements are used to quantify the short-wavelength actuation effects. Nevertheless, baseline measurements reveal a high Reynolds number dependency. Furthermore, the pressure field reacts sensitively to geometrical changes in the setup like the angle of the splitter plate diffusor. Thus, the effects of the Reynolds number and of the active flow control have to be separated carefully. With an optimised setup, the control effect amounts to 8% at a Reynolds number of 153000. At the end, the influence of the phase angle is investigated. Although the pressure field does not yield any significant effect for different phase angles, the frequency spectra of the pressure sensors along the vortex axis show that the desired actuation frequency is the dominant one. Furthermore, an almost linear trend of the phase velocity along the vortex axis is measured between an in-phase and a phase shifted actuation. In this section, the streamwise vortex is quantified via pressure measurements on the back panel. At first, the baseline and its dependency on variations in the setup is discussed. Then, the effects of the short-wavelength AFC is quantified. At the end of this section, the control of the phase angle of the AFC and the corresponding phase angle in the flow field are discussed in detail.

4.2.1. Pressure measurements of the baseline flow

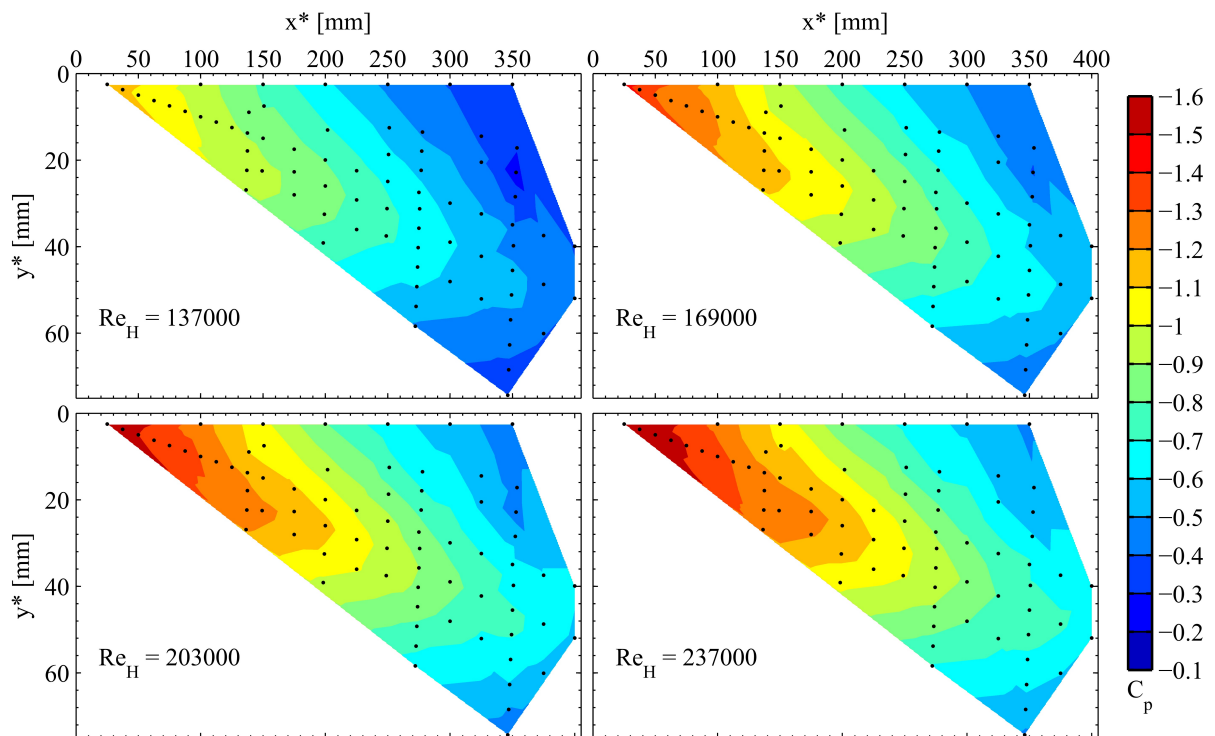


Figure 4.5.: Contour plot of the pressure coefficient C_p for four different Reynolds numbers; black dots mark the pressure taps

Figure 4.5 depicts the measured pressure field for four different Reynolds numbers. To yield a first impression and an orientation, a contour plot illustrates the pressure coefficient C_p . The 72 pressure taps equipped with pressure sensors are marked by means of black dots (compare to figure 3.4). The sensors possess a measurement range of 1000Pa (company: *Sensortech*, type: *HDOM010DE8P*) and each sensor is connected via an 8cm long tube. The entire setup is calibrated in situ by means of a reference pressure device (company: *Halstrup Walcher GmbH*, type: *KAL84*). Thus, the theoretical measurement uncertainty is approximately 0.25%. The reference pressure during the measurements is the static pressure of the free stream drawn off the Prandtl tube. The lowest Reynolds number of $Re_H = 137000$ corresponds to a free stream velocity of 4m/s. At this speed, the dynamic pressure amounts to approximately 9.6Pa. The tube length from the Prandtl tube to the pressure sensors is around 3m. This long tubing generates a

4. Results

time lag, if the ambient pressure changes due to a wind gust hitting the wind tunnel or the HFI-building. Pressure variations of around 1Pa are observable in the worst case scenario. To reduce this uncertainty, 32768 samples at a sample rate of 2048Hz are recorded. Furthermore, each measurement is repeated seven times to minimise the variance.

Nevertheless, these time averaged pressure measurements illustrate the footprint of a streamwise vortex. The lowest pressure is located at the $x^* = <50\text{mm}$. At this position, the vortex is small and the vorticity is concentrated in the vortex centre [Strangfeld et al., 2011]. Furthermore, the vortex is very close to the surface and thus generates the highest impact. Further downstream, the pressure increases. These findings are consistent with, for example, pressure measurements of streamwise vortices on delta wings [Guy et al., 1999a] and simulations at the Ahmed body [Wassen and Thiele, 2007]. The locally lowest pressure in crosswise direction is detectable close to the second streamwise oriented pressure tap line at 7.4° . Assuming the lowest pressure beneath the vortex axis, these pressure measurements reveal a vortex axis angle of around 7.4° . These observations hold for all Reynolds numbers although a high Reynolds number dependency is obvious. The higher the Reynolds number is, the lower the pressure coefficient becomes.

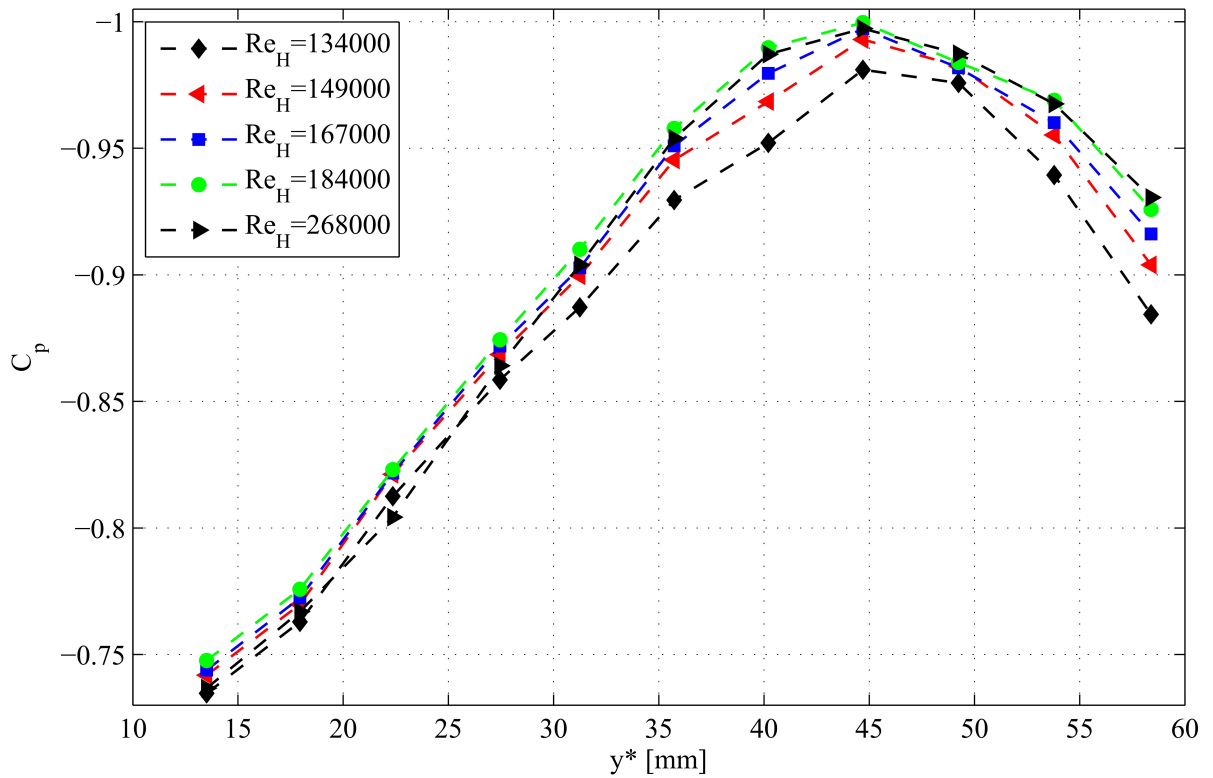
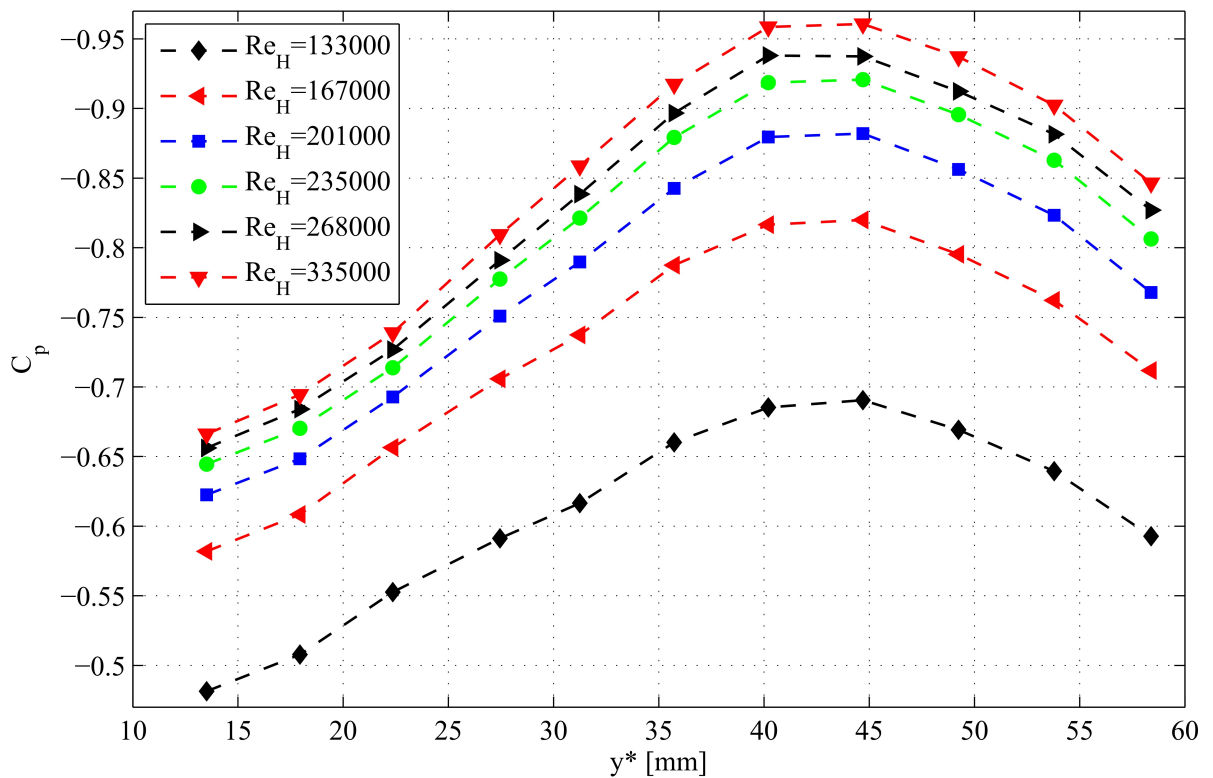
Although this contour plot is an intuitive presentation of the measurements, a direct quantification of the effects is complex. Thus, a representative section of the vortex is required for further quantification. Later discussed measurements with AFC do not show clear trends in the region from $x^* = 25\text{mm}$ to $x^* = 137.5\text{mm}$. Pressure measurements downstream of $x^* = 350\text{mm}$ become more blurred. The vortex is probably too far away from the surface and ambient noise has more influence. Crosswise measurements at a $x^* = 275\text{mm}$ with eleven pressure sensors yield a high spatial resolution. The pressure field is dominated by the vortex and ambient noise is negligible. This crosswise section at $x^* = 275\text{mm}$ is used in the following discussion to quantify the effects of the Reynolds number and the AFC system.

4.2.2. Baseline flow dependency due to geometrical changes

As discussed in chapter 3.1, preliminary tests and measurements are performed before the wind tunnel is reconstructed. In this old setup, pressure variations of 8% due to short-wavelength AFC are measured [Scheibel, 2014]. After the reconstruction, the same setup yields totally different baselines. This high dependency of the baseline due to geometrical changes of the wind tunnel and the setup is discussed here briefly.

Figure 4.6 shows the crosswise measured pressure profiles at $x^* = 275\text{mm}$ for five Reynolds numbers. The step is installed in the initial setup, which corresponds to the preliminary measurements before the wind tunnel reconstruction. In this initial setup, the downstream diffuser possesses an angle to the splitter plate of 14° . The lowest pressure is reached at $y^* = 45\text{mm}$ which indicates the vortex centre location. Above a Reynolds number of $Re_H = 167000$, no Reynolds number effects are detectable any more. In this configuration, seven Reynolds numbers between $Re_H = 134000$ and $Re_H = 332000$, and at each Reynolds number four frequencies between 5Hz to 20Hz at different amplitudes are investigated. During all measurements, the AFC system does not yield a significant influence. This stands in contrast to the preliminary tests where effects of 8% are measured. It is noticeable that the new baseline yields Reynolds number effects of $\Delta C_p = 0.03$ whereas the old baseline before the reconstruction shows effects of $\Delta C_p = 0.6$ [Scheibel, 2014]. Several attempts are conducted to generate a baseline which is comparable to the old one. For instance, tripping 10cm downstream of the leading edge and the installation of a slanted ceiling in the measurement box do not reveal any improvement.

Another attempt is to adjust the downstream diffuser angle. Figure 4.7 depicts the baseline for a diffuser angle of 6° . The baseline changes significantly and the Reynolds number effects amount to $\Delta C_p = 0.3$. At the highest Reynolds number of $Re_H = 335000$, independency is still not reached. One explanation may be that at an angle of 14° , the diffuser already stalls and no manipulation of the pressure ratio is gained. At 6° , the flow probably stays attached and the pressure ratio above and beneath the splitter plate is affected. This may lead to a higher mass flow through the bypass and less ram air exists upstream of the inlet. This may prevent flow separations at the step top as well. The modified pressure ratio also affects the static pressure around the step model and influences the boundary layer transition and the separation process. All these explanations are speculative and require further investigations. The conclusion of the

Figure 4.6.: Crosswise pressure coefficients at $x^* = 275$ mm with a downstream diffuser angle of 14° Figure 4.7.: Crosswise pressure coefficients at $x^* = 275$ mm with a downstream diffuser angle of 6°

discussion is the fact that allegedly small geometrical changes alter the entire flow field. In the scope of the fundamental changes in the wind tunnel during the reconstruction, an inaccurate reproduction of the

4. Results

baseline seems reasonable. Thus, the final wind tunnel measurement campaign has to be regarded as a stand alone measurement and cross-checks to other baselines in the past are highly questionable.

4.2.3. Effects of oscillating flaps

Based on the baseline measurements in figure 4.7, short-wavelength AFC is used to manipulate the flow. At a Reynolds number of $Re_H = 133000$, four different frequencies, 5, 10, 15, and 20Hz, are generated. Figure 4.8 represents the results. The black line with the diamond symbol depicts the baseline. The minimum pressure lies at $y^* = 45\text{mm}$. The most significant variations due to AFC occur between $y^* = 40\text{mm}$ and $y^* = 55\text{mm}$. All cases with an excited shear layer display an increased pressure in this area. The maximum deviation is $\Delta C_p = 0.05$. The highest control effects are evident for the lowest amplitude of $MA_{pp} = 0.5\text{mm}$ at 10, 15 and 20Hz. This result is unexpected because a higher amplification of instabilities due to a higher amplitude causes, in general, stronger effects until saturation is reached. All these observations lead to the assumption that the control authority is based only on Reynolds number effects. Although the flap array is leveled installed below the step top, a small gap between the flap array and the surface exists due to the concave shape of the flap's bearing housing. Also, small gaps between the flaps exist and induce further roughness. Hence, the disturbances generated by the flaps already influence the flow upstream of the trailing edge. This may explain the high Reynolds number sensitivity of the baseline and the AFC effects. However, the roughness influence and the Reynolds effects have to be reduced to yield a discrete net-effect of the AFC system. This leads to a third setup described in the next section.

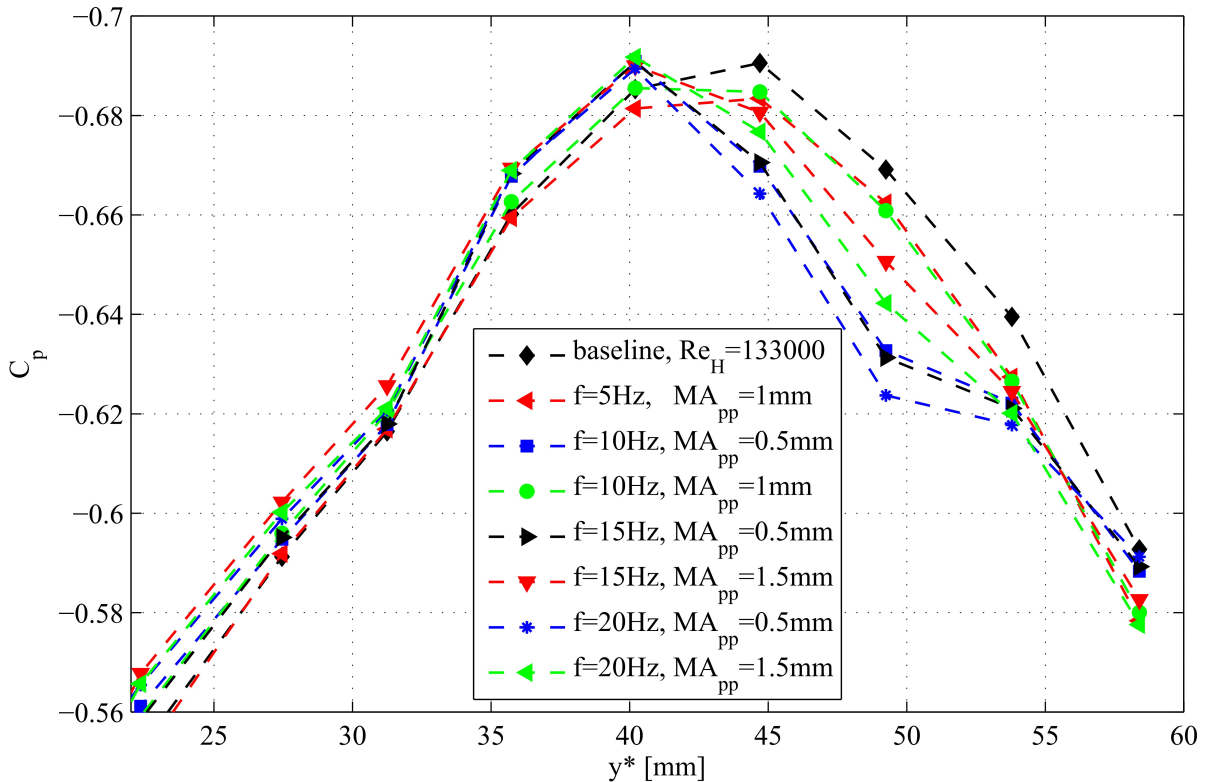


Figure 4.8.: Crosswise AFC measurements at $x^* = 275\text{mm}$ and at $Re_H = 133000$ with various frequencies and amplitudes

4.2.4. Effects of oscillating tabs

The final setup is photographed in the appendix A and documents the optimum setup in the large field of geometrical parameters. The step top is covered by a polyethylene plate of 1mm thickness. This very

smooth layer covers the entire step top and ends approximately 5mm upstream of the trailing edge. The flap array is positioned approximately 3mm under the step top. Hence, the entire array lies beneath the polyethylene plate. Small rectangular profiles clue on the flap tip. These profiles are 3.25mm broad and several heights are available. By means of this setup, any upstream roughness effects due to the flaps vanish. The rectangular profiles are driven by the flaps, although the flow only recognises the small structure at the trailing edge. Hence, this setup is more consistent with tabs instead of flaps. Figure 4.9 shows the baseline measurements with a profile height of 6.4mm which withstands approximately 2.8mm above the layer. The high Reynolds number dependency still exists and at a Reynolds number of $Re_H = 270000$, no independency is reached. The pressure minimum is shifted to $y^* = 35$ mm, which means the vortex centre moves upwards. This is consistent with the geometrical changes. The layer and the rectangular profile increase the distance from the point of flow separation to the pressure taps by approximately 4mm.

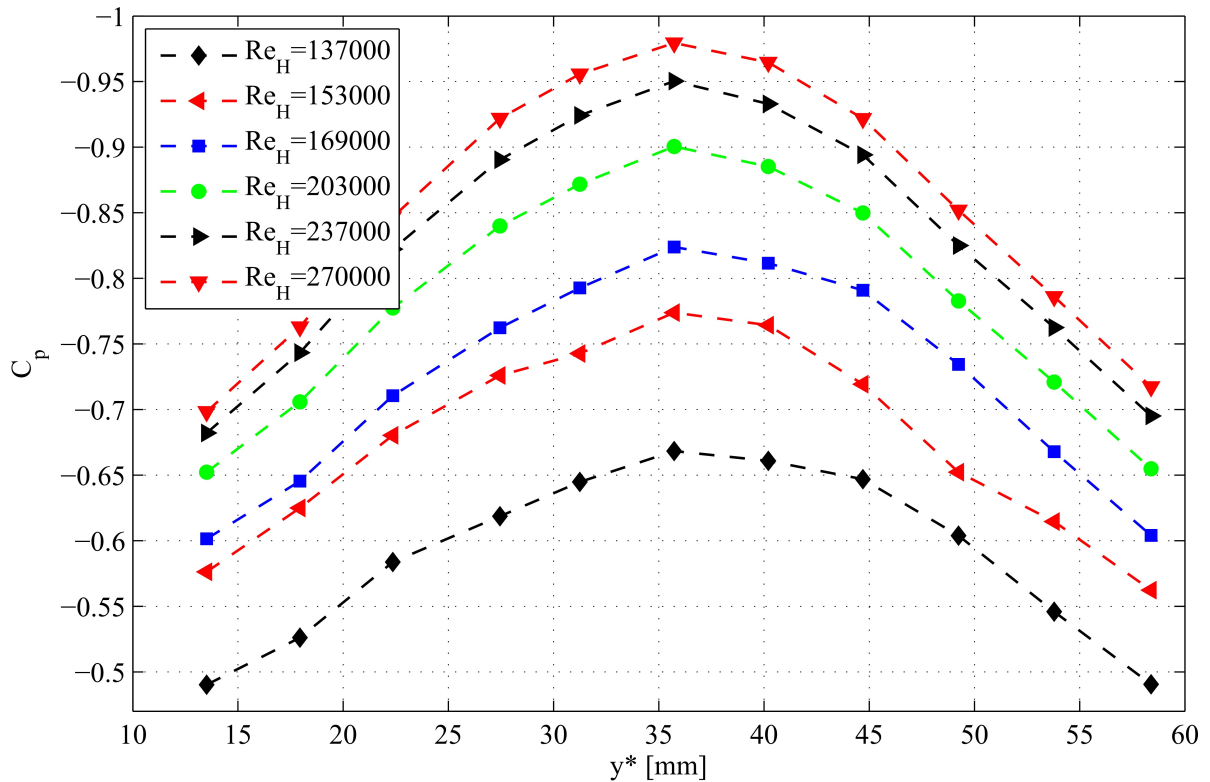


Figure 4.9.: Crosswise pressure coefficients at $x^* = 275$ mm with a downstream diffuser angle of 6° and a polyethylene layer on the step top; the rectangular profiles on the flap tips overhang 2.8mm

Figure 4.10 depicts the influence of the AFC system. The maximum pressure deviation to the baseline (black diamond symbols) amounts to $\Delta C_p = 0.035$ which corresponds to a relative change of 4.4%. Furthermore, actuation with higher amplitudes generates higher control effects, which is consistent with the theory. Moreover, the trend clearly depends on the actuation frequency. At 5Hz, the pressure decreases and at 20Hz the pressure increases. The highest effects exist between $y^* = 14$ mm and $y^* = 44$ mm. These findings are in contrast to figure 4.8. Hence, the smooth polyethylene layer changes the characteristics of the AFC. Other rectangular profiles are also tested with different heights at the same AFC amplitudes and frequencies. A height of 8mm, which corresponds to an overhang of approximately 5.3mm, generates a maximum variance of $\Delta C_p = 0.015$. This effect is only slightly above the measurement accuracy. Another profile with a height of 3.1mm is almost leveled to the layer on the step top. No significant effects are observed although this setup is close to the other setup with uncovered flaps. This finding constitutes two suggestions. The observed AFC effects in figure 4.8 are probably just a manipulation of the boundary layer on the step top upstream of the trailing edge. Furthermore, the leveled profile does not produce any significant effects and probably operates in the viscous dominated sublayer of the boundary layer. All

4. Results

the described settings are tested at a Reynolds number of $Re_H = 273000$ as well and all control effects become insignificant. However, these parameter studies yield an optimum overhang of the profiles above the layer of 2.8mm.

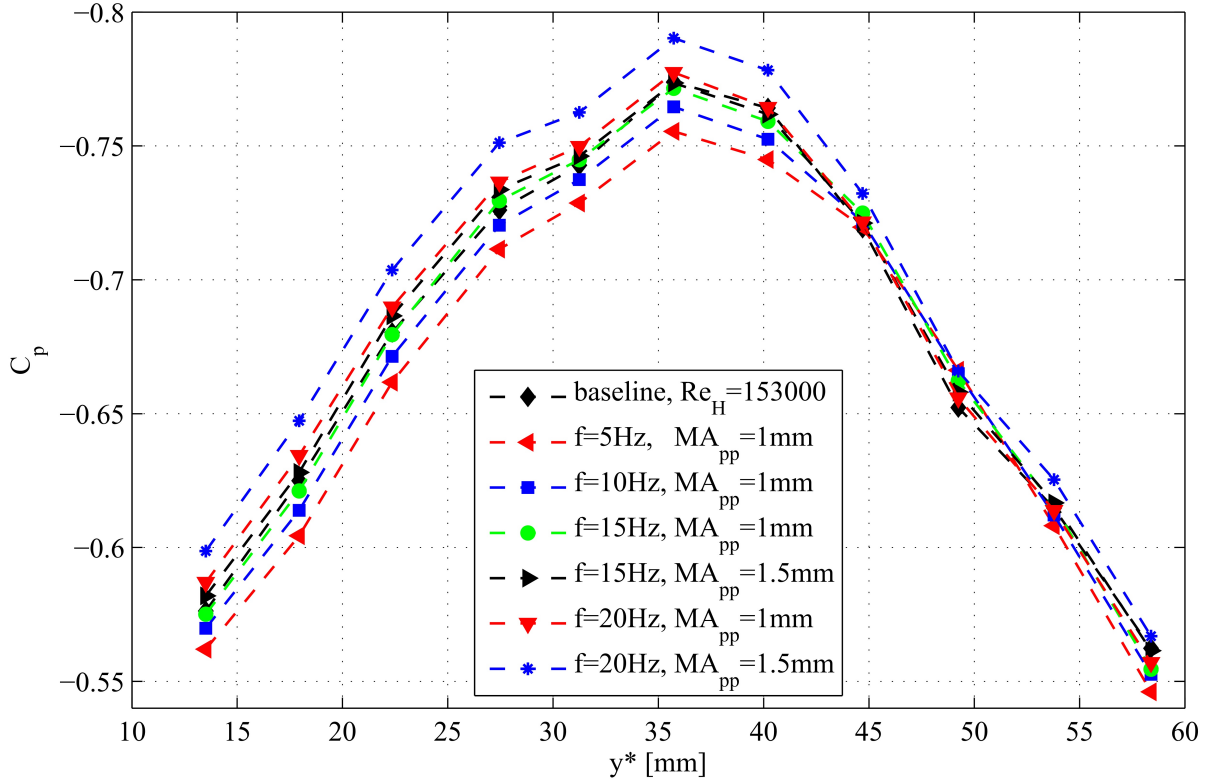


Figure 4.10.: Crosswise AFC measurements at $x^* = 275\text{mm}$ and at $Re_H = 153000$ with various frequencies and amplitudes; the flaps are covered by a polyethylene layer and act more like tabs

The control authority of 4.4% has to be further clarified because at these low Reynolds numbers, the control effects may be affected by noise. As described above, each measurement is repeated seven times for a better validation and to reduce the influence of outliers. Figure 4.11 illustrates each single measurement for the baseline and the two cases with the highest control effects in figure 4.10. The red symbols represent an actuation frequency of 5Hz and a $MA_{pp} = 1\text{mm}$ and the blue ones a frequency of 20Hz and a $MA_{pp} = 1.5\text{mm}$. The averaged influence of 4.4% is in general reproduced by each single measurement. Between $y^* = 14\text{mm}$ and $y^* = 23\text{mm}$ a clear and ordered trend is visible. At 5Hz the pressure decreases and at 20Hz the pressure increases. Between $y^* = 30\text{mm}$ and $y^* = 40\text{mm}$, the influence weakens and the effects get more scattered. At $y^* \geq 45\text{mm}$, no significant effects exist. Nevertheless, this is a very promising result. Each single measurement confirms the global trend. The baseline pressure field is controlled in both directions to higher or lower values depending on the frequency. This opens a broad field of technical applications. However, one open question remains why the observed effects are not stronger. On the one hand, the AFC may be too weak to influence the flow field strongly enough. On the other hand, the inflow conditions may be too inhomogeneous and turbulent, which reduces the AFC effects.

The frequency spectrum of the two pressure sensors at $y^* = 14\text{mm}$ and $y^* = 58\text{mm}$ in figure 4.11 are investigated in detail. This approach discloses the effectiveness of the short-wavelength AFC system and quantifies the impact on the flow field. Figure 4.12 illustrates the frequency spectrum of a FFT analysis at 20Hz and a $MA_{pp} = 1.5\text{mm}$ and averaged over all seven measurements. This corresponds to the blue points in figure 4.11 at $y^* = 14\text{mm}$. Although at 20Hz no strong vibrations of the model are observable, small vibrations, electromagnetic noise, or acoustic waves may exist. These noise sources may overlie the frequency spectrum because the pressure sensors are positioned close to the AFC system ($< 5\text{cm}$). Thus, the net-effect of the AFC has to be determined. The black line in figure 4.12 shows the spectrum of the

forced flow at a Reynolds number of $Re_H = 153000$. The logarithmic scaled amplitude demonstrates a dominant peak at 20Hz which is almost two magnitudes higher than the rest of the spectrum. A peak of the higher harmonic at 40Hz is present as well. The blue line depicts the spectrum with only flow passing the step without AFC. The AFC system is switched off and no electrical current influences the piezo-electric membrane of the pressure sensors. This spectrum is calculated based on the baseline curve in figure 4.11. The blue and black lines possess a high accordance except at 20 and 40Hz. Thus, the AFC system does not amplify other frequencies beyond the desired one. The red line represents the measured spectrum at an actuation frequency of 20Hz with the same amplitude and without any flow. In general, the amplitude is two magnitudes lower compared to the noise level of the natural flow. At 20Hz, the amplitude increases drastically and reaches the noise level of the natural flow. Thus, the AFC produces a considerably high noise level. Whether vibrations or electromagnetic noise are the reason is not yet identified. Furthermore, the higher harmonic at 40Hz and a possible sub-harmonic around 10Hz exist. Nevertheless, to yield the net-effect of the AFC, the noise level of the flow (blue line) and the noise level of the AFC (red line) are subtracted from the measured control case (black line). This calculation is performed in the linear space and the result is transformed in the semi-logarithmic scale. At all frequencies, the net-effect (green line) is smaller than the amplitude of the uncorrected AFC measurement. This is expected because the noise of

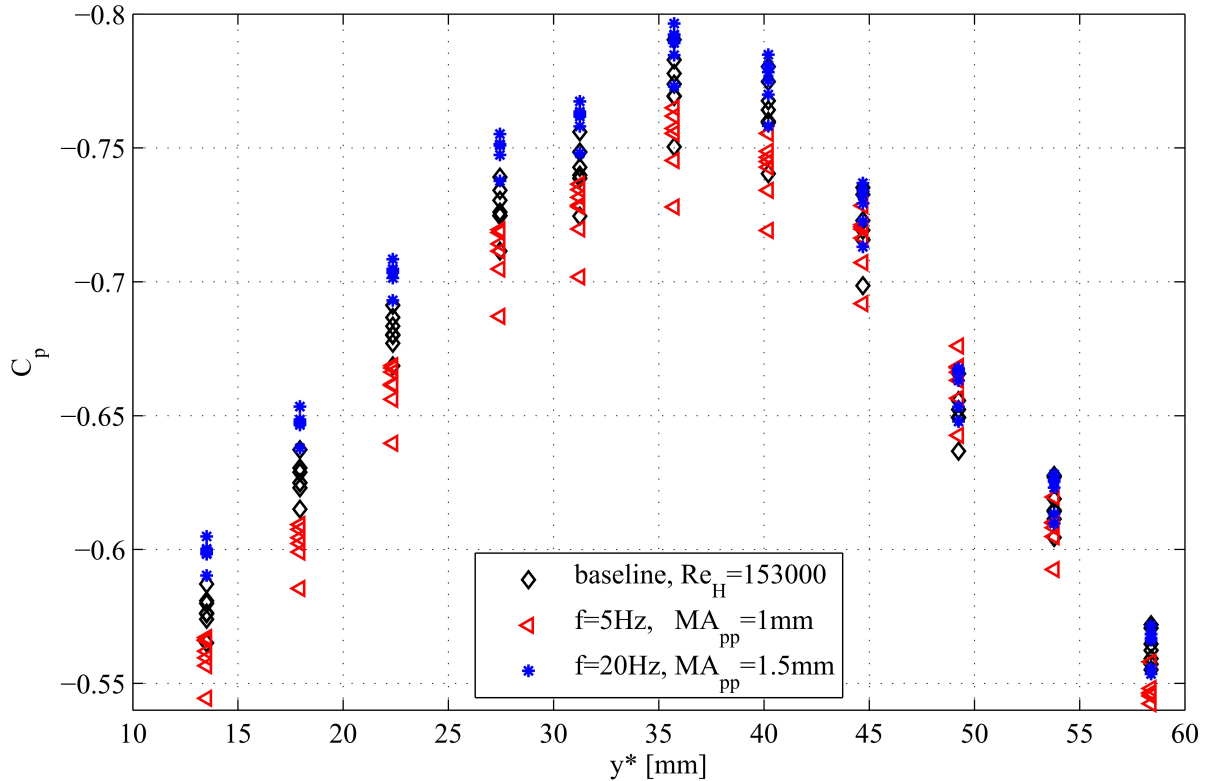


Figure 4.11.: Crosswise AFC measurements at $x^* = 275\text{mm}$ and at $Re_H = 153000$ for the baseline and for 5Hz and 20Hz; the flaps are covered by a polyethylene layer and act more like tabs

the natural flow and the AFC are positive at all frequencies. For most frequencies, the net-effect is below 10^{-3} and also achieves negative values. At 20Hz, the net-effect becomes 10^{-1} and exceeds the natural noise level of the unexcited flow by more than one magnitude. This implies that the flow field is highly penetrated by the short-wavelength AFC and the actuation frequency determines the dominant frequency in the flow at this pressure tap position. As proven, the flow is highly affected by the AFC at $y^* = 14\text{mm}$ in figure 4.11. In this region, the AFC also manipulates the pressure field. Thus, the interesting question is whether the flow field also shows this dominant frequency although the pressure field is not affected. On the right hand side of figure 4.11, at $y^* = 58\text{mm}$, there is no significant difference between baseline and excitation. Figure 4.13 illustrates the spectrum at 20Hz and $MA_{pp} = 1.5\text{mm}$ at this position. The forcing frequency clearly dominates the spectrum and the flow field. The net-effect of the actuation is

4. Results

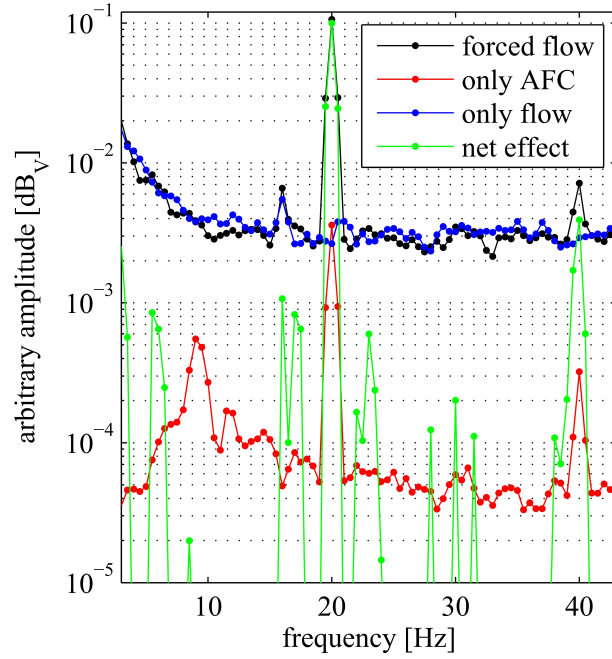


Figure 4.12.: Frequency spectrum of the pressure tap position $x^* = 275\text{mm}$, $y^* = 14\text{mm}$ at $Re_H = 153000$, $f = 20\text{Hz}$, $MA_{pp} = 1.5\text{mm}$

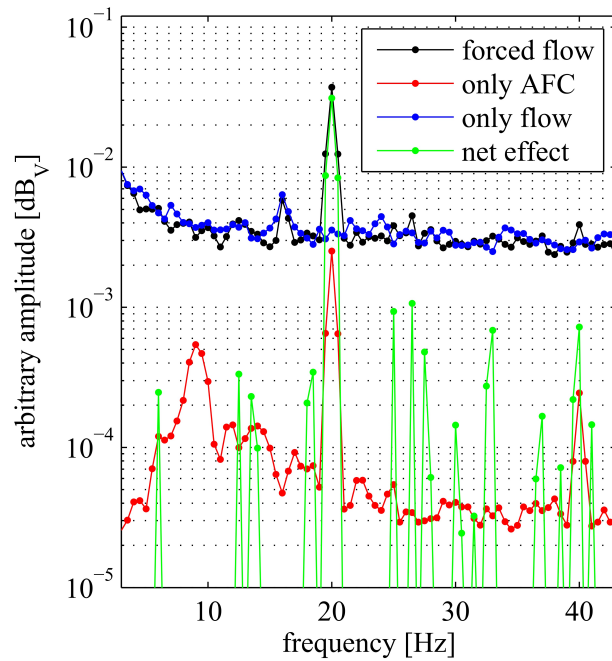


Figure 4.13.: Frequency spectrum of the pressure tap position $x^* = 275\text{mm}$, $y^* = 58\text{mm}$ at $Re_H = 153000$, $f = 20\text{Hz}$, $MA_{pp} = 1.5\text{mm}$

approximately one magnitude higher than the noise of the natural flow. The noise level of the natural flow possesses the same amplitude in the two figures 4.12 and 4.13. At $y^* = 14\text{mm}$ the net-effect yields a much higher amplitude compared to $y^* = 58\text{mm}$. This reduced amplitude of the forced flow may be an explanation for the uninfluenced pressure. In general, the existence of the dominant frequency holds for all pressure taps up to $x^* = 350\text{mm}$ and all excitation frequencies. Downstream of this line, the peak is still dominant for some pressure taps. This reduced effect far downstream is expected because the distance from the emitted shear layer and the vortex axis to the pressure taps increases and the ambient

noise plays a more important role. However, for $y^* \leq 350\text{mm}$, the noise influence is negligible and the AFC is powerful enough to penetrate the entire streamwise vortex.

The spectrum of the baseline flow (blue line) in figures 4.12 and 4.13 yields another small peak at 16Hz. This corresponds to a Strouhal number of $St = 1.77$ at the given free stream velocity of 4.5m/s [Tropea et al., 2007]. This peak is found for other velocities as well (e.g., 14.5Hz at 4m/s, 17.5Hz at 5m/s, 24Hz at 7m/s, 27.5Hz at 8m/s). Thus, the resulting Strouhal number is approximately 1.75. This number does not coincide with the Kelvin-Helmholtz instability frequency from other experimental investigations. Moreover, this peak appears only at some pressure sensors and at a free stream velocity of 6m/s, no peak is found. The forced flow in the two figures (black line) still represents this peak. No lock-in effect is observed although the actuation frequency is close to the peak of the unexcited flow. Although this Strouhal number is inherent in the flow, the source is not determined. It may be a phenomenon related to the step or a feature of the wind tunnel itself. Further investigations at this point are required.

4.2.5. Phase angle validation of the short-wavelength actuation

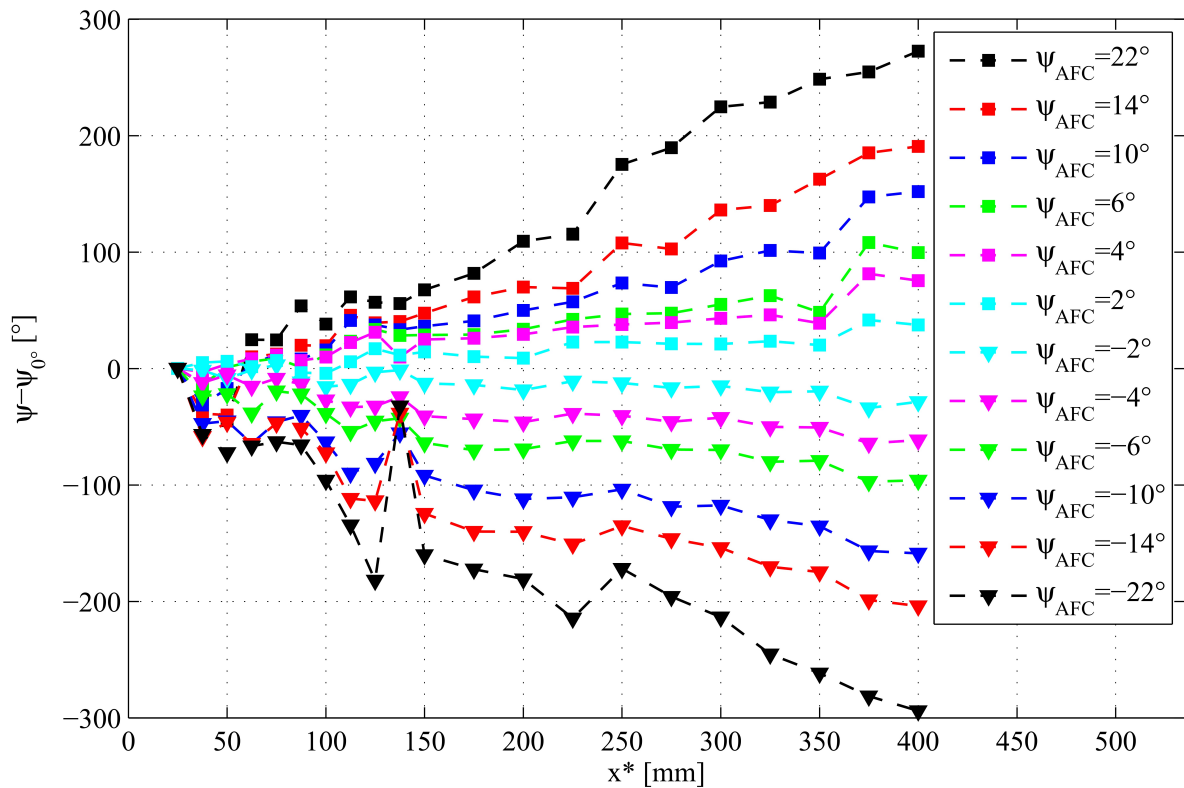


Figure 4.14.: Measured net phase angle at $Re = 151000$, $f = 15\text{Hz}$, and $MA_{pp} = 1.5\text{mm}$ as a function of the controlled flap phase angle

As shown before, the actuation frequency is clearly the dominant frequency in the flow field. The numerous measurements with AFC and varying phase angles do not show any significant effects in the flow field. Nevertheless, the synchronised, time resolved pressure measurements allow the calculation of the phase velocity of the dominant frequency by means of an FFT analysis [Bachmann, 1992]. Figure 4.14 presents the phase angle at 15Hz and $MA_{pp} = 1.5\text{mm}$. The corresponding baseline measurements are already depicted in figures 4.9 and 4.10. In this setup, the step top does not possess a polyethylene layer. However, the phase angle difference ($\psi - \psi_{0^\circ}$) is calculated along the streamwise oriented pressure taps at 5.7° (compare to figure 3.4). In a first step, the phase angle between an arbitrary pressure tap on this line and the first pressure tap at $y^* = 25\text{mm}$ is computed for the in-phase case (ψ_{0°). This procedure is repeated for other measurements with varying phase angles (ψ). The resulting phase angle is subtracted by the in-phase phase angle. Thus, the abscissa in figure 4.14 represents the baseline and the other lines

4. Results

the variations relative to the in-phase case. In this context, a phase angle of, for example, $\psi_{AFC} = 6^\circ$, describes the phase shift between two adjacent flaps. Hence, the phase angle between the first and the last flap amounts to 90° in this case.

In figure 4.14, phase angles with the same absolute value are depicted in the same colour, whereas squares represent positive angles and triangles negative ones. The phase angle of the first pressure tap at $y^* = 25\text{mm}$ is zero for all cases. It is the reference sensor and does not possess a phase angle to itself. All other sensors show clearly the trends for $y^* \geq 50\text{mm}$. Negative phase angles of the AFC result in a negative phase angle in the flow and vice versa for positive angles. Furthermore, large AFC angles in absolute values yield large phase angles in the flow. The trends in the range of $y^* = 50\text{mm}$ to $y^* = 137.5\text{mm}$ are inhomogenous and partly a little bit chaotic. Downstream of $y^* = 150\text{mm}$, the trends become much more uniform and an almost linear trend is evident. A symmetry is evident with almost similar absolute values for positive and negative AFC phase angles. Additionally, if the AFC angle is doubled up, the slope of the phase lag doubles up as well. Hence, the entire system behaves linear with some scatter. If a linear function between $y^* = 25\text{mm}$ and $y^* = 400\text{mm}$ is assumed for all phase angles, the averaged slope over all 12 lines is $0.0411^\circ/\text{mm}$. This estimation and the linear trends hold also for higher AFC angles up to 180° . Other measurements with installed polyethylene layer and rectangular profiles show clearly the same behaviour and linear trends. This means, in fact, that the chosen approach of phase control is proven by these promising experimental results.

All the actuator testing in chapter 3.2.4 and the results depicted in this section demonstrate clearly that the frequency, the amplitude, and the phase are adjustable. Furthermore, the entire flow field is dominated by the AFC frequency and phase angle. Hence, any kind of wave package is emitted in arbitrary downstream direction by means of these powerful actuators. This advanced short-wavelength AFC system fulfils all the desired requirements and is highly reliable.

4.3. Investigation of the twisted boundary layer upstream of the trailing edge

Intermediate conclusion: The boundary layer upstream of the trailing edge of the swept step represents the main initial conditions. Thus, the form parameters of the arriving boundary layers are measured. At all investigated upstream positions above the top plate, the form parameter of the boundary layers is similar to that of an ideal turbulent boundary layer. In particular, at the lowest free stream velocity, a sub-critical Reynolds number is expected. However, the measured boundary layers are turbulent and therefore, the assumption of a laminar boundary layer has to be rejected. This probably explains the weak effect of the AFC because a distinct actuation of the K-H instabilities is not possible in a fully turbulent boundary layer. Furthermore, the yaw angle directly upstream of the trailing edge is quantified. It is around 17° and smaller than expected during the surface oil visualisation.

The AFC system dominates the flow field at arbitrary frequencies and phase angles in a highly reliable way, as demonstrated by means of the frequency spectrum and the almost linear behaviour of the phase angle in the flow. Hence, the AFC system is considered to be sufficient to amplify K-H instabilities in the emitted shear layer. Due to this modified vorticity distribution and entrainment, the circulation of the streamwise vortex is controlled at its origin. However, the impact of the AFC on the pressure field is minor. Hence, the inflow conditions upstream of the trailing edge have to be investigated in more details. In particular, the type of approaching boundary layer, laminar or turbulent, has a strong influence on the AFC system as discussed in chapter 2.1. Thus, the boundary layer thickness is investigated in this section. In the case of a two-dimensional boundary layer, a hotwire, LDV, or Pitot tube are able to record the velocity profile. On the step top, the boundary layer is twisted towards the trailing edge (see figure 4.3). In this case, single point measurements are only projections of the twisted boundary layer on the chosen coordinate system. Therefore, a three-hole pressure probe is manufactured in the workshop of the HFI to determine the dynamic pressure and the angle of the current flow. The newly manufactured probe is used for the first time and is calibrated before the experiments. Just for completeness, the construction and the calibration functions for the dynamic pressure of the probe are shown in appendix A.

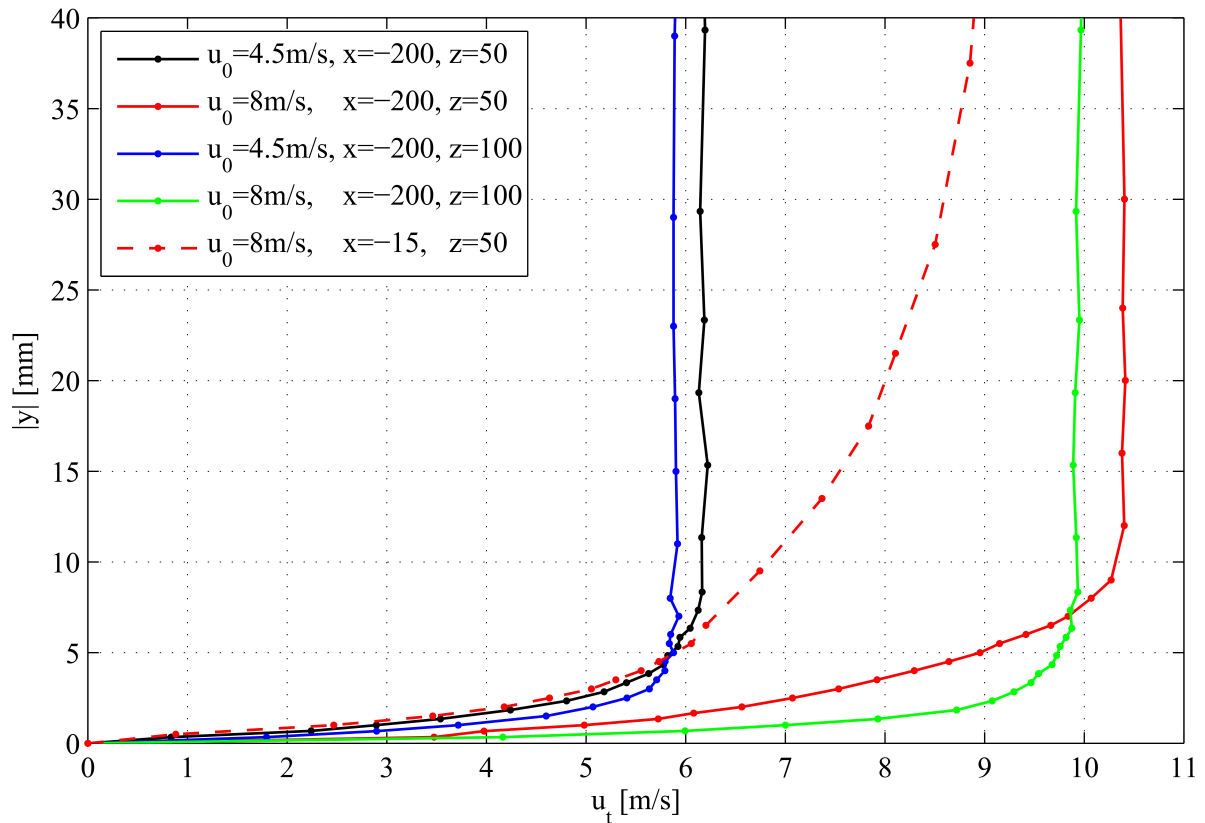


Figure 4.15.: Boundary layer velocity profiles at different streamwise and spanwise positions on the step top; coordinates in mm

In the investigated configuration, the polyethylene layer is installed and the overhang of the leveled rectangular profile on the flap tip is approximately zero. Figure 4.15 depicts five boundary layer profiles measured by means of the three-hole probe. The measurement starts on the surface ($y = 0\text{mm}$) and ranges to $y = -120\text{mm}$. First of all, an overshoot of the velocities of around 30% is noticeable. This high amount may result partly from the displacement effect of the step model. But this effect is estimated to be at maximum 10% and is experimentally confirmed [Ruwisch, 2013]. The remaining gap of around 20% is unexplained. An inaccurate calibration curve or a biased reference pressure may cause the deviation. However, the absolute values are of minor interest here. The four solid lines are measured 200mm upstream of the trailing edge in two different spanwise positions. At $z = 50\text{mm}$, the velocity is increased compared to $z = 100\text{mm}$ and the gradient to the wall seems slightly reduced. Nevertheless, the streamwise position is the same, the presented differences display an inhomogeneous boundary layer in spanwise direction. Varying boundary layer shapes require different appropriate actuation frequencies and phase angles. This may reduce the efficiency of the AFC at the trailing edge. Furthermore, spanwise inhomogeneities may cause three-dimensional flow structures in the boundary layer. In the laminar case, transition is accelerated [Schlichting and Gersten, 2006]. In a turbulent boundary layer, these structures may be insensitive to the actuation at the trailing edge. However, an experimental assessment of all turbulence scales in a twisted boundary layer is challenging and out of the framework of this thesis. The red dashed line in figure 4.15 illustrates the boundary layer 15mm upstream of the trailing edge. The velocity is significantly reduced to $x^* = -200\text{mm}$. Moreover, the shape is highly convex and a sensible estimation of the boundary layer height is not possible up to $|y| = 40\text{mm}$. This dramatic shape change from $x = -200\text{mm}$ to $x = -15\text{mm}$ remains unexplained. This phenomenon suggests that other strong influence factors around the step model exist. A non-uniform static pressure inside the wind tunnel track or large scale turbulence from the inflow may affect the boundary layer significantly. Secondary flow phenomena in the free stream [Institutsbericht HFI, 2008] may also cause boundary

4. Results

layer inhomogeneities in spanwise direction.

Although the boundary layer variations in spanwise and streamwise direction are unsatisfying, the kind of boundary layer is quantified by means of the form parameter H_{12} . The form parameter is the ratio of the boundary layer displacement thickness δ_1 and the boundary layer momentum thickness δ_2 . Equations 4.1 to 4.3 quantify the corresponding relations for a two-dimensional boundary layer [Schlichting and Gersten, 2006].

$$\delta_1(x) = \int_0^{\delta(x)} \left(1 - \frac{u(x, y)}{u_\delta(x)}\right) dy \quad (4.1)$$

$$\delta_2(x) = \int_0^{\delta(x)} \frac{u(x, y)}{u_\delta(x)} \left(1 - \frac{u(x, y)}{u_\delta(x)}\right) dy \quad (4.2)$$

$$H_{12}(x) = \frac{\delta_1(x)}{\delta_2(x)} \quad (4.3)$$

Some further necessary assumptions are required to solve these equations based on the velocity measurements. In the presented study, a twisted boundary layer is investigated. Hence, the total velocity $u_t(y)$ has to be considered instead of an unidirectional velocity $u(y)$. Furthermore, the boundary layer height $\delta(x)$ has to be defined. Jürgens and Kaltenbach [2012] show a velocity overshoot above the boundary layer of approximately 5%. They state that the maximum velocity of the velocity profiles represents the boundary layer height. Due to measurement noise in the present study, the boundary layer height is set to the location of 98% of the maximum velocity $u_\delta = 0.98u_{t,max}$. Now, all factors are defined and the form parameter is determined via numerical integration. A two-dimensional laminar boundary layer yields a form parameter of $H_{12} = 2.6$ [Schade et al., 2007] and a turbulent one $H_{12} \approx 1.4$ [Schlichting and Gersten, 2006].

u_0 [m/s]	x [mm]	z [mm]	δ_1 [mm]	δ_2 [mm]	H_{12}	$\theta_{yaw}(y=0)$
4.5	-200	50	5.97	4.16	1.44	-1.67°
8	-200	50	11.7	8.5	1.38	3.95
4.5	-200	100	3.4	2.51	1.35	7.18
8	-200	100	9.35	8.44	1.11	7.19
4.5	-15	50	52.9	38.78	1.36	18.18
8	-15	50	46.66	33.75	1.38	17.07
4.5	-15	100	37.86	31.13	1.22	17.71
8	-15	100	41.32	32.88	1.26	17.07
12	-15	100	34.94	27.53	1.27	15.62

Table 4.1.: Overview of the measurement positions and the corresponding boundary layer parameters

Table 4.1 illustrates the considered parameters for all investigated boundary layers on the step top. The free stream velocity u_0 and the different streamwise and spanwise locations are the exogenous parameters. The computed boundary layer displacement thickness δ_1 and the boundary layer momentum thickness δ_2 do not show distinct trends. This is probably caused by the measurement noise and the boundary layer twist. Nevertheless, the form parameter H_{12} remains in the range of 1.1 to 1.45. Although the transmission of the form parameter of two-dimensional boundary layer to twisted boundary layers is debatable, the resulting numbers clearly reveal a fully turbulent boundary layer. At $x^* = -200$ mm, the current length of the step top is 600mm. Together with the lowest free stream velocity of 4.5m/s, the current Reynolds number is $1.8 \cdot 10^5$ and more than two times lower than the critical Reynolds number Re_{crit} . This result proves that the inflow conditions affect the boundary layer and accelerate transition. This uncertainty is somewhat caused by the incomplete wind tunnel reconstruction as described in chapter 3.1.

The turbulent boundary layer is probably the main reason for the low level of control authority. Lehmann [2014] investigates the shear layer downstream of a straight backward facing step. The used plasma actuators show only low control authority and the boundary layer is turbulent. With the same setup,

Correale et al. [2014] excite a laminar boundary layer by means of plasma actuators. The control effects are more than one magnitude higher comparing to the turbulent boundary layer cast. This strong influence of the boundary layer type on a swept, semi-span, backward facing step is analogous to a straight backward facing step.

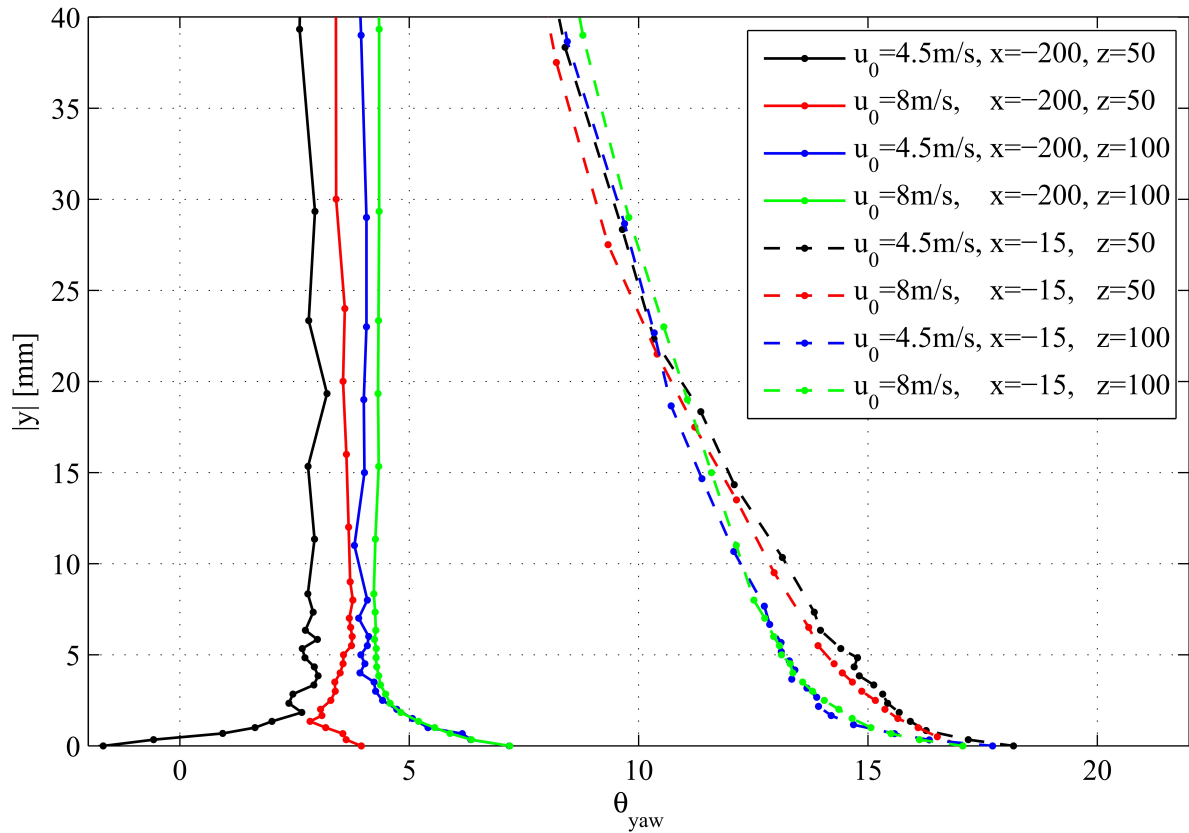


Figure 4.16.: Boundary layer yaw angle θ_{yaw} at different streamwise and spanwise positions on the step top

The three-hole probe also allows the quantification of the actual yaw angle θ_{yaw} of the boundary layer. Figure 4.16 illustrates the variations of θ_{yaw} for eight different boundary layers. At $x^* = -200$ mm, the skewness is in the range of -3° to 7° . Close to the trailing edge at $x^* = -15$ mm, the twist increases significantly. Close to the surface, a maximum skewness angle of 18.2° is recorded (see table 4.1). Furthermore, this tilt is not limited to the first millimeters at the surface. It is detectable in the entire boundary layer. These observations are expected and consistent with the flow visualisation in figure 4.3, although the china clay may predict even higher angles.

4.4. Shear layer velocity profiles and their instabilities

Intermediate conclusion: The three velocity components are measured directly downstream of the trailing edge at different spanwise and vertical positions. The global flow field is in good agreement to the baseline flow visualisations and the surface pressure measurements. In the region of the shear layer, the velocity gradients are very large. Furthermore, a direct isolation of the shear layer is not possible because the criteria to determine the local shear layer thickness fail due to the high tilt and twist of the shear layer. Thus, a stability analysis based on the measured velocities is excluded. Comparisons of the proposed stability analysis approach with simple one-dimensional shear layers yield a good agreement. Velocity profiles for 2.5-dimensional shear layers to compare with the results of the stability computations do not exist. However, a viscous temporal stability analysis is performed for a theoretical shear layer which possesses two mean flow velocity components.

In a first step, the global flow structure and measured shear layer velocity profiles are presented and discussed. Then, the linear stability analysis is validated by means of inviscid and viscous one-dimensional boundary and shear layers. An attempt of validating a two-dimensional shear layer according to Kelch [2003] is discussed before a viscous, two-dimensional, linear stability analysis based on discrete velocity profiles is presented.

4.4.1. Shear layer velocity profiles

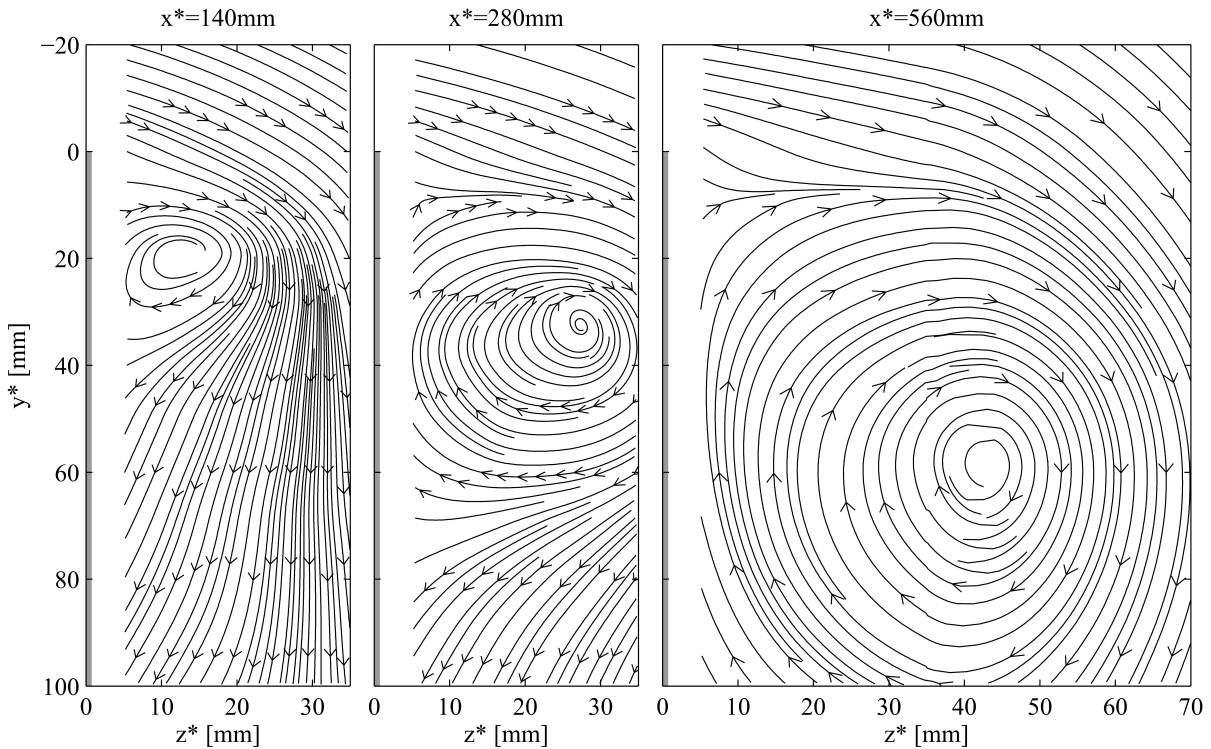


Figure 4.17.: Qualitative illustrations as streamlines of the v^* , w^* velocity component at $Re_H = 176000$ ($u_0 = 5\text{m/s}$)

Figure 4.17 depicts the projected streamlines of the v^* , w^* velocity component in the step coordinate system at $Re_H = 176000$. All three velocity components are measured with a 12-hole probe (company: *Aeroprobe Corporation*, type: *Omniprobe*), hence the projection is based on the complete three-dimensional velocity field. The qualitative velocity field is presented at three different positions along the trailing edge, $x^* = 140, 280, \text{ and } 560\text{mm}$. The grey line at $z^* = 0\text{mm}$ indicates the step's back panel. The measurements are interpolated and based on 84 measurements points at $x^* = 140$ and 280mm and on 105

points at $x^* = 560\text{mm}$. At all three x^* positions one sees clearly the global flow structure of a streamwise vortex in cross-sectional view. The estimated vortex centre (the centre of the concentric streamlines) moves away from the back panel and from the step top in downstream direction. Meanwhile, the vortex structure itself is increasing in size. At approximately $y^* = 7\text{mm}$, the streamlines of the free stream and of the streamwise vortex merge together. The shear layer is probably located at this position. In the vortex centre, high axial velocities u^* are measured but not drawn here for clarity. The current velocity field is similar to cross-sectional PIV measurements on a delta wing measured by Strangfeld et al. [2011]. Nevertheless, the measurement accuracy of the 12-hole probe is sufficient to capture the global velocity field. However, a much higher spatial resolution is required, especially in the region of the shear layer where the highest velocity gradients are expected for an accurate stability analysis.

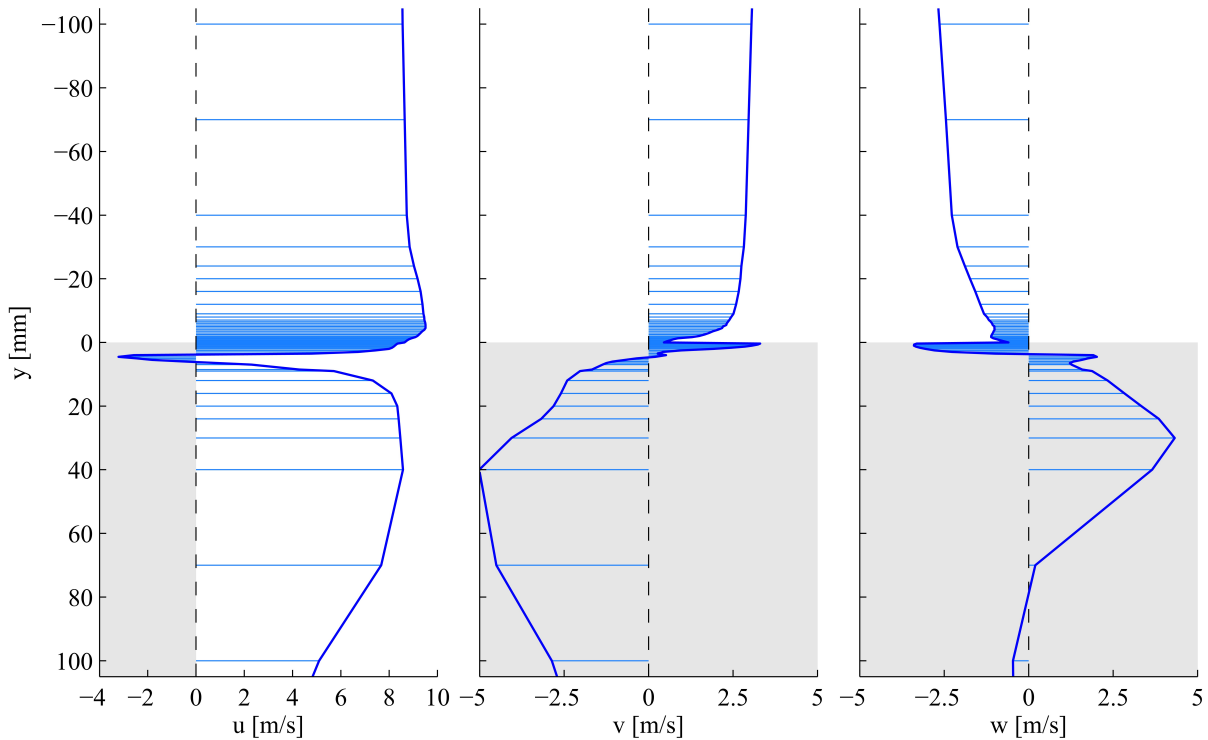


Figure 4.18.: Velocity components of the free rolling up shear layer at $x = 11\text{mm}$, $z = 100\text{mm}$, and $Re_H = 269000$ ($u_0 = 8\text{m/s}$); bold blue line: velocity amplitude; thin blue vertical lines: measurement positions; grey surface: step's back panel

Figure 4.18 illustrates the three-velocity components of the shear layer at $z = 100\text{mm}$ in the free stream coordinate system at $Re_H = 269000$. The probe head is placed downstream of the trailing edge at $x = 11\text{mm}$. Due to the slanted back and the probe head diameter of 10mm , the minimum normal distance of the probe is approximately 3mm . The bold blue lines represent the amplitude of the velocity components u , v , and w . The thin vertical blue lines imply the measurement positions which are adapted to the expected velocity gradient. From $y = 7\text{mm}$ to $y = -7\text{mm}$, the spatial resolution is at least 0.5mm . The grey surfaces represent the step's back panel in the corresponding view. The black dash lines at zero velocity are included for a better orientation. The three velocity components show clearly, that the u velocity possesses the largest velocity amplitude and is regarded as the main stream direction as required by stability analyses. Furthermore, in the far field at $y = 100\text{mm}$, the velocity amounts to $u = 8.56\text{m/s}$. The two other velocity components at this position amount to $v = 3.05\text{m/s}$ and $w = -2.64\text{m/s}$ and leads to a total velocity of $\sqrt{v^2 + w^2} = 9.46\text{m/s}$. This total velocity magnitude is in agreement with the hotwire measurements. However, significantly smaller v and w velocities are expected in the far field. This observation suggests that remarkable unintended cross-flows exist.

In the region of the estimated shear layer, the axial velocity decreases between $y = -2\text{mm}$ to $y = 12\text{mm}$. This is a kind of wake velocity caused by the boundary layer with zero velocity on the step top. At

4. Results

$y = -5\text{mm}$, the streamwise velocity reaches its maximum speed of 9.09m/s and is significantly larger than the free stream velocity in the far field. This observation is in agreement with the DNS simulation of Jürgens and Kaltenbach [2012]. The negative u velocities at $y = 4\text{mm}$ may be generated by the secondary vortex which is already observed in figure 4.3. This interpretation is supported by the w velocity peak at this position. The secondary vortex achieves high axial velocities as well. By means of the w velocity, the streamwise vortex is estimated between $y = 7\text{mm}$ to $y = 70\text{mm}$. This is in agreement with the several presented pressure measurement and the global velocity field measurements in figure 4.17. At $y = 100\text{mm}$, the w velocity becomes negative. This is reasonable because in this area the spanwise recirculation bubble and its wake influence the flow (compare figure 3.2). The diameter of the spherical probe head is 10mm , and the shear layer thickness is of the same magnitude. Hence, the probe head is probably too large because the high gradients in the region of the shear layer cause a gradient along the probe head. This is not considered during the calibration process and disturbs and distorts the measurement results. Thus, the observed negative velocities may be a measurement error. Furthermore, a probe head size comparable to the flow structure size itself will definitely affect its shape and flow physics. However, both effects are hard to quantify in terms of measurement accuracy.

4.4.2. Validation of the stability analysis and predictions for the three-dimensional case

The chosen disturbance-ansatz in equation 2.27 and the numerical implementation of the Orr-Sommerfeld equation on discrete, non-equidistant grid points has to be validated. First of all, an expression for the velocity profiles $u_0(z)$ and $v_0(z)$ in equation 2.22 are required. The common test case is a two-dimensional shear layer, hence the $v_0(z)$ velocity component is zero. For the axial velocity, a tanh-function is used to approximate the real velocity profile. The parametric expression is $u_0(z) = e_1(e_2 s + \tanh(z))$ whereas e_1, e_2 are free constants. A superposition of several parametric velocity profiles may represent more complex and realistic shear layers in technical applications. Furthermore, a transformation from the Gauss-Lobatto sampling points to the physical domain is required. In the literature, the function $z = c_s \tanh(z)$ is commonly used [Laurien, 1985]. This function transforms a physical domain for $\pm\infty$ to ± 1 . This transformation function does not have to be a tanh function. The coincidence of the velocity profile function and the transformation function at this point is actually random. However, the free constant c is a transformation constant and has to be adjusted individually for each single case and is performed manually.

Several test cases are considered to validate the stability analysis. In all the following discussed cases, the stability analysis is computed on the inner domain. Thus, the boundary conditions of equation 2.33 are implicitly fulfilled in the viscous and inviscid case. The first validation velocity profile is a two-dimensional shear layer in inviscid flow. In this case, the Orr-Sommerfeld-equation reduces to the Rayleigh-equation. Hence, only second derivations exist and only two boundary conditions are implemented. For a compact comparison, the complex phase velocity c is considered and defined in equation 4.4 [Oertel, 1996]. a and b are the wave numbers of the considered wave and ω its angular frequency.

$$c = c_r + ic_i = \frac{\omega}{a_\phi} \quad (4.4)$$

$$a_\phi = \sqrt{(a^2 + b^2)} \quad (4.5)$$

wave number a	reference	computation
	$c_i, c_r = 0.5$	$c_i, c_r = 0.5$
0.1	0.4184	0.4181
0.2	0.3487	0.3487
0.4	0.2352	0.2352
0.8	0.0674	0.0673

Table 4.2.: Comparison of the computed phase velocity c with the reference values from Michalke [1964]

The velocity profile is $u_0(z) = 0.5(1 + \tanh(z))$ and depicted in figure 4.19. The chosen transformation constant is $c_s = 5$ and 300 sampling points are used for the computation. Due to the Squire theorem, the wave number b is zero for all two-dimensional simulations. The velocity profile is antisymmetric with respect to its inflection point with $(u_0(-y) = -u_0(y))$, hence it follows for this distinct velocity profile a real phase velocity of $c_r = 0.5(u_0(\infty) + u_0(-\infty)) = 0.5$ [Tatsumi and Gotoh, 1960]. Thus, the real phase velocity is independent of the wave number. Table 4.2 compares the computed phase velocity of the temporal, inviscid linear stability analysis with the reference values given by Michalke [1964]. An agreement to the third decimal place is observable. A more detailed comparison and a second inviscid velocity profile according to the work of Betchov and Szewczyk [1963] is given in Doppel [2014].

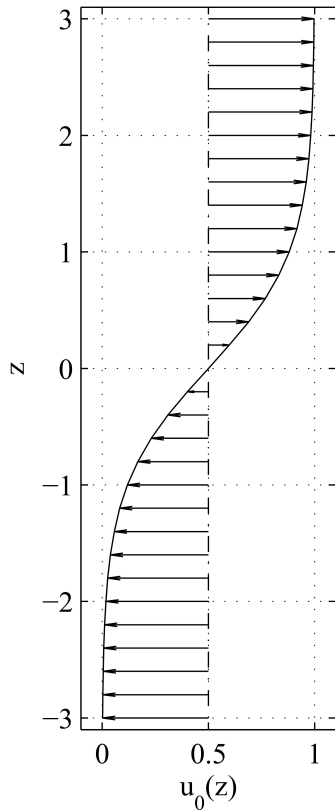


Figure 4.19.: u z Plot of the computed shear layer velocity profile $u_0(z) = 0.5(1 + \tanh(z))$

A more complex analysis is a viscous analysis. In this case, the fourth derivation is taken into account as well. Figure 4.20 illustrates the discrete eigenvalue spectrum of the velocity profile $u_0(z) = 0.5(1 + \tanh(z))$. The transformation constant is $c_s = 10$ and 300 sampling points are computed. The shape of the eigenvalue spectrum at ± 1 shows the onset of the characteristic funnel form. Only one eigenvalue achieves a positive image part of $c_i = 0.386$. c_r is zero due to the symmetric inflection point of this considered velocity profile. The eigenvalue of this viscous, temporal, linear stability analysis coincides up to the third decimal place to the results of Betchov and Szewczyk [1963]. A more detailed discussion of this viscous shear layer and a further computation of a viscous Blasius boundary layer is given in Doppel [2014]. Furthermore, a spatial, linear stability analysis of a viscous Blasius boundary layer achieves an agreement to the fourth decimal place to the results of Danabasoglu and Biringen [1990]. In summary, all the performed comparisons to the literature of temporal and spatial, linear stability analysis for inviscid and viscous flow yield a sufficient agreement. Numerical noise or amplification do not influence noticeably the computation. Hence, the numerical implementation is considered as valid and accurate.

As discussed in chapter 2.3.2, Kelch [2003] computes a linear, stability analysis of a skewed mixing layer with the Chebyshev collocation method. He uses a superposition of continuous analytical functions and their analytical derivations as input velocity profiles. For a comparison, an exact definition of the approximation of the two velocity profiles u_0 and v_0 is required for a computation. Plots of the two velocity components are given in Jürgens and Kaltenbach [2003], [Kelch, 2003], [Jürgens, 2006]. However, only Kelch gives an exact, parametric description of the velocity functions. He chooses an approximation consisting of a superposition of several hyperbolic tangent and hyperbolic cosine

functions. The u_0 velocity contains 24 parameters and the v_0 velocity 25. Although a recalculation of the u_0 velocity achieves the globally expected behaviour (as plotted), the v_0 velocity yields unphysical values. The normalised velocity at the surface is -0.4 instead of zero and 1.3 in the far field, although the maximum has to be 1. It is not clear which of the 25 coefficients is incorrect. Hence, unfortunately, a comparison is rendered impossible. To the best knowledge of the author, other stability analyses considering skewed shear layers have not yet been published.

Besides the missing validation of the two-dimensional analysis, the measurements reveal further difficulties. In the disturbance ansatz in equation 2.22, the w_0 velocity component is neglected. One argues that this velocity component is small compared to the other. Looking at the measured velocity profiles in figure 4.18, it is not clear which velocity is small compared to the others. Hence, the chosen two-dimensional disturbance ansatz will lead to significant inaccuracies. Furthermore, the stability analysis assumes a main stream direction. This is the u component with the highest velocity. In the far field, only this velocity should be present and the others should become zero. Nevertheless, the two other measured velocities still show a strong amplitude at $y = -100\text{mm}$. Hence, it is difficult to argue which is the main

4. Results

flow direction. Using the x direction appears insufficient and arbitrary in the presented case. Although a computation in this coordinate system is possible, a comparison to other investigations in the future will be difficult and questionable. The potentially greatest difficulty is the definition of the region of interest. The stability of the shear layer is of interest, hence only the region should be analysed. Thus, a precise definition of the shear layer thickness and its position is required. If the computational range is too broad, additional inflation points and curvatures influence the stability analysis. This causes more eigenvalues with a positive imaginary part and the requested distinction between desired physical and undesired numerical instabilities (due to noise) is becoming more complex. However, Jürgens [2006] states the highest velocity above the step is the upper limit of the shear layer. In the presented measurements, this point is at $y = -5\text{mm}$. In the case of a 2.5-dimensional step, the lower limit is the floor downstream of the step. In this experimental study, this lower limit does not exist.

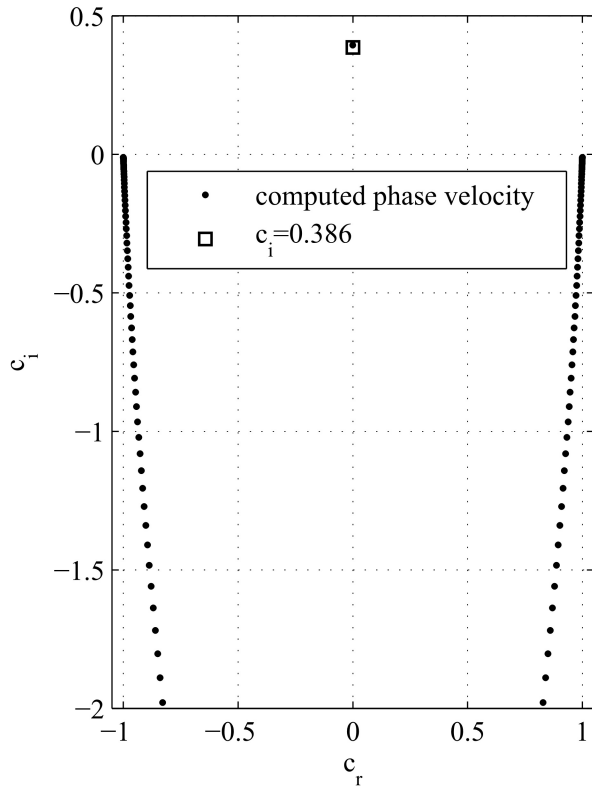


Figure 4.20.: Eigenvalue spectrum of the velocity function $u_0(z) = 0.5 * (1 + \tanh(z))$ at $Re = 40$ and $a = 0.4$; comparison to Betchov and Szewczyk [1963]

based on the existing experimental data. Due to the several difficulties regarding the stability analysis and the high uncertainties during the measurements, an analysis based on the experiments is not sensible. However, to demonstrate that the code computes reasonable results and to give a benchmark for comparison, a theoretical two-dimensional shear layer is assumed. The velocity functions are defined in the two equations 4.6 and 4.7.

$$u_0 = 0.5(1 + \tanh(z)) \quad (4.6)$$

$$v_0 = 0.5e^{-(z-0.1)^2} \quad (4.7)$$

The physical domain ranges from $z = \pm 20$ with a step width of 0.25. 100 sampling points are used to transform this velocity profile on the Gauss-Lobatto points. The transformation function is $z = c \tanh(z)$ with $c_s = 4.8269$ and the Reynolds number is 100. Figure 4.21 illustrates the amplitude to the largest imaginary eigenvalue for the corresponding wave numbers a and b (the step size is 0.2). The maximum eigenvalue is $\omega_{i,max}$ is 0.0913 at $a = 0.44$ and $b = 0.34$. A similar but inviscid test case is presented in

The shear layer and the streamwise vortex are more or less the same flow structure. It is hard to distinguish which part of generated vorticity comes from the shear layer and from the rotation of the vortex. A cut off between the primary vortex and the shear layer is probably the most convincing attempt. However, this approach does not work close to the trailing edge where the free rolling up shear layer is emitted. In this region, the occurrence of the secondary vortex further complicates the definition of a lower limit and makes the flow in this region completely three-dimensional. This requires a three-dimensional stability analysis which goes beyond the scope of this thesis. A last unresolved issue is the normalisation of the velocity profiles which is of high importance for the stability analysis [Jürgens, 2006]. He suggests using the maximum velocity directly upstream of the trailing edge. Although this overspeed at the boundary layer fringe at the step top is observed in the experiments as well, see figure 4.15, close to the trailing edge at $x = -15\text{mm}$, the shape of the boundary layer changes completely. A distinct overspeed or even a boundary layer thickness is not observable anymore. Thus, an appropriate normalisation is difficult

Doppel [2014]. The eigenvalue spectrum of certain wave numbers show more than one positive imaginary eigenvalue, in general two or three. This is consistent with the used velocity functions. In general, u_0 possesses one inflation point and v_0 two. Hence, at maximum three positive eigenvalues are expected. Thus, the developed stability ansatz in this thesis yields consistent and physically sensible results.

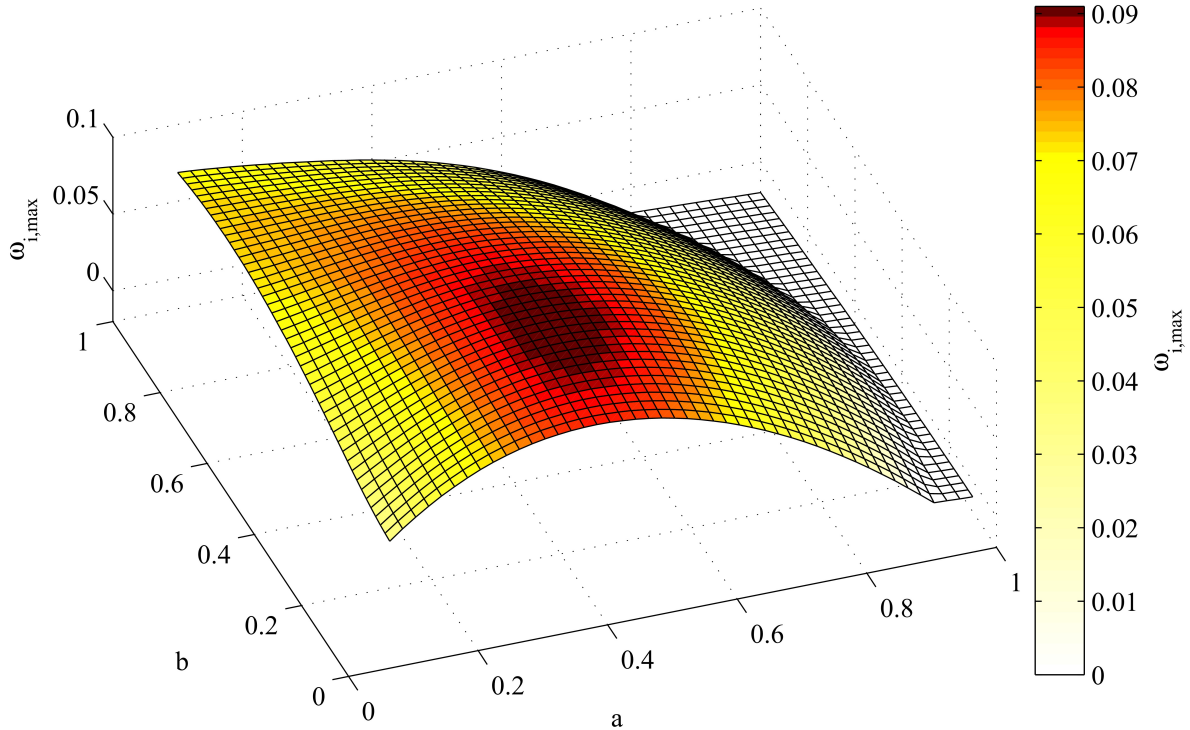


Figure 4.21.: Maximum imaginary eigenvalue for the two wave numbers a and b at $Re = 100$; $\omega_{i,max} = 0.0913$ at $a = 0.44$ and $b = 0.34$

4.5. Validation and results of the unsteady bound circulation

Intermediate conclusion: The determination of the unsteady bound circulation is crucial for the desired long-wavelength trailing vortex excitation. As a first step, the baselines of the lift and moment coefficients are discussed in detail because a clear and accurate separation of the Reynolds number effects is required especially for the unsteady free stream oscillations. In a second step, the pure pitching motion is taken into account. Between the reduced frequencies of 0.068 and 0.263, a switch of the rotational sense of the hysteresis loop is observed in Theodorsen's theory and confirmed by experiments. Based on this validation, a parameter study for high k -values is performed and a strong nonlinear behaviour is visualised. In a third step, the pure free stream oscillation at high amplitudes of 50% is discussed. A good agreement between the measurements and Isaacs' theory is achieved. The amplitude and the phase of the predicted lift overshoot of 26% are confirmed by the measurements. Based on these strong unsteady lift effects, the measured pressure distribution at three different phase angles is presented. Then, the theoretical pressure distribution of the extended unsteady theory proposed in this thesis is computed. The magnitude and the difference to the quasi steady baseline coincide with the measurements. Hence, the extended theory is validated. In the final step, the combined effect of a simultaneous free stream oscillation and a pitching motion is depicted. The measured unsteady lift is almost identical to the predictions of van der Wall. Furthermore, both effects are measured and predicted individually and then superimposed. The nonlinear interaction of the two unsteady varying degrees of freedom is proven by the experiments. In summary, the bound circulation prediction is validated under all unsteady conditions and provides the basis for the

4. Results

long-wavelength trailing vortex excitation.

The prediction of the bound vorticity and the experimental validation are discussed in this section. First, the baseline measurements regarding the lift and moment coefficient are considered. Then, a pure pitching motion is compared to Theodorsen's theory. This is followed by a comparison of Isaacs' theory and experiments of an airfoil facing an unsteady free stream. In this context, the extended theory from chapter 3.4 is experimentally validated and confirmed. At the end of this section, the combined in-phase cases of a synchronised and simultaneous pitching motion and free stream velocity oscillation are experimentally and theoretically discussed. The findings validate van der Wall's theory.

4.5.1. Baseline measurements

The expected net dynamic effects of unsteadiness are between 10% to 30%. Reynolds number effects may disturb or overlay these effects. Thus, detailed baselines are carefully recorded and discussed here.

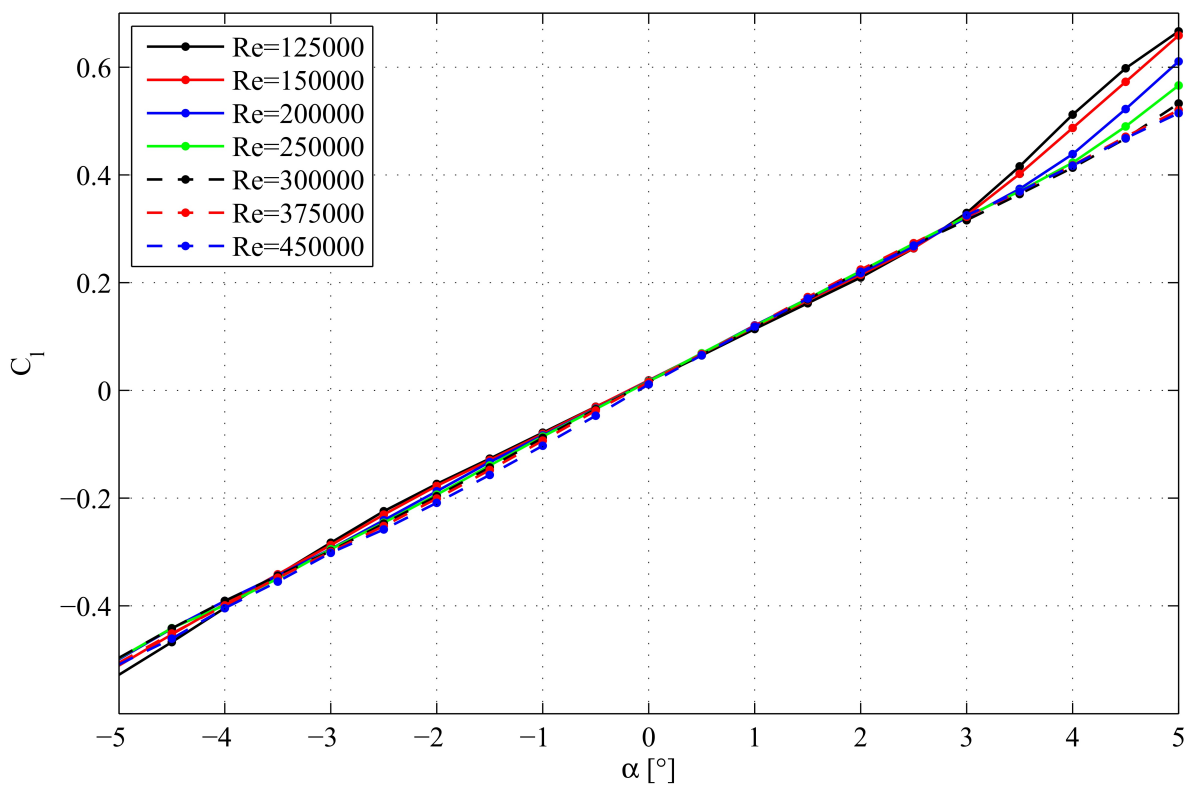


Figure 4.22.: Static lift coefficient C_l of the NACA 0018 airfoil at different Reynolds numbers

Figure 4.22 illustrates the lift coefficient C_l versus the angle of attack α for different Reynolds numbers. Between $0^\circ \leq \alpha \leq 3^\circ$, the lift coefficient for all Reynolds numbers is similar and close to the potential flow slope of 2π . The variation is between 2-3%, which is in the range of the overall measurement accuracy. For $\alpha > 3^\circ$, a clear Reynolds number dependency appears. At $\alpha = 4^\circ$, the Reynolds number effect amounts to 18.5%. For Reynolds numbers higher than 250000, no significant deviation is measured. The trend changes at negative angles of attack. Between $-3^\circ \leq \alpha \leq 0^\circ$, a Reynolds dependency is visible for all Reynolds numbers. At $\alpha = -2^\circ$, the effect amounts to 17%. The different behaviours for positive and negative angles of attack are explained by the unsymmetrical airfoil geometry. At positive angles of attack, the surface including the two slots for active flow control is the suction side (compare figure 3.17). These slots act as tripping and the boundary layer becomes turbulent. At negative angles of attack, the smooth surface is the suction side. The boundary layer probably persists laminar more downstream due to the negative pressure gradient. Thus, the expected Reynolds number effects caused by transition are larger or arise at lower angles of attack. However, for Reynolds numbers larger than 200000, almost no effect

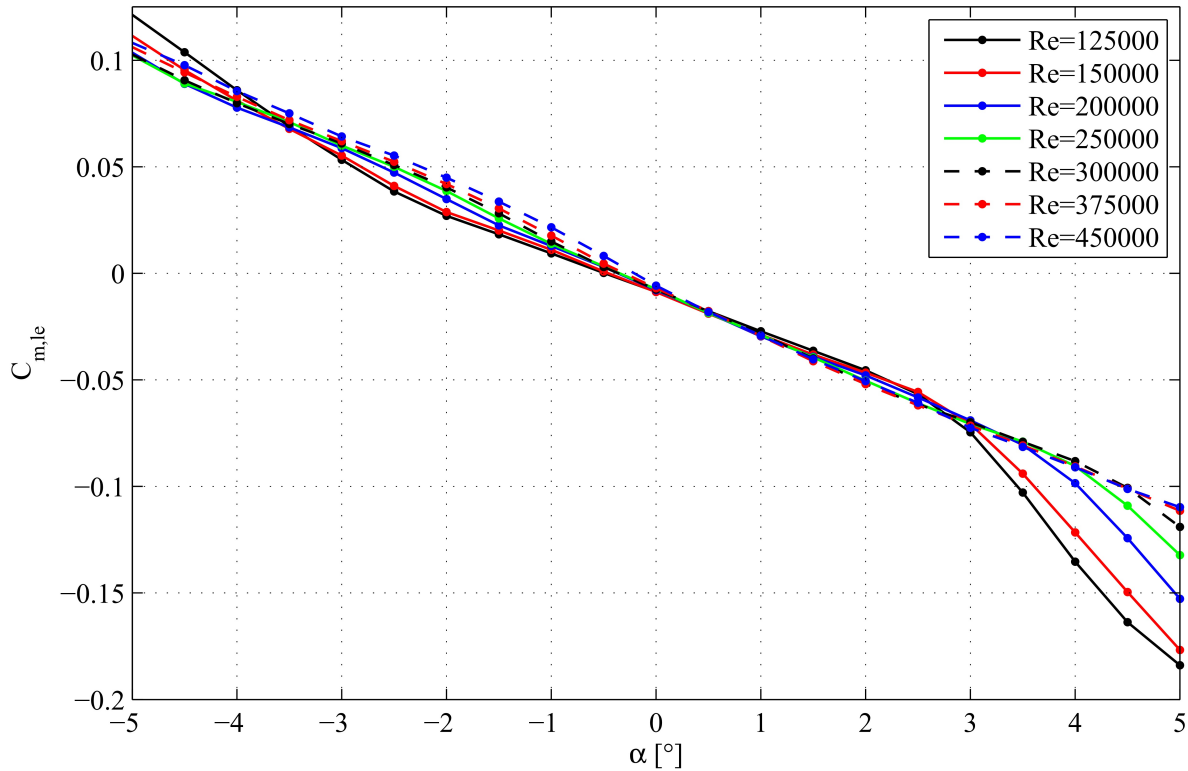


Figure 4.23.: Static moment coefficient C_m of the NACA 0018 airfoil at different Reynolds numbers

exists for positive angles of attack and it is less than 10% at negative ones. Nevertheless, a quantification of dynamic effects requires a Reynolds number compensation based on these baselines. Moreover, at angles of attack larger than $\pm 8^\circ$, the lift coefficient differs significantly from the 2π slope, which indicates the onset of trailing edge stall [Strangfeld et al., 2014].

Figure 4.23 depicts the baseline curves for the leading edge pitching moment. The leading edge moment is considered instead of the quarter-chord moment because the latter one is zero for symmetrical airfoil at all angles of attack [Katz and Plotkin, 2001]. However, a strong Reynolds number dependency exists. Only in the range of $0^\circ \leq \alpha \leq 3^\circ$ is a fairly independent behaviour evident. Due to the strong Reynolds number dependency, and the corresponding limited range of angles of attack, the moment coefficient is just tangentially discussed during the unsteady measurements.

4.5.2. Pure pitching motion

The pitching motion of the airfoil is one of the two sources of unsteadiness in this specific setup. The pitching axis is the quarter chord. In the following, only the lift coefficient is considered due to the high Reynolds number dependency of the leading edge pitching moment. Furthermore, the Reynolds numbers are between 300000 and 500000 in order to reduce the undesired effects of transition. The pitching motion discussed here follows the function $\alpha(t) = 2^\circ + 2^\circ \sin(\phi)$. Another pitching motion with $\alpha(t) = 0^\circ + 4^\circ \sin(\phi)$ is recorded as well. The latter one is not presented here because at negative angles of attack, the effects are blurred due to the Reynolds number effects. However, the governing parameter to quantify the influence of the unsteady effects is the reduced frequency. Figure 4.24 shows the resulting unsteady lift coefficient at $Re = 350000$ and a pitching frequency of 0.97Hz. This results in a low reduced frequency of $k = 0.068$. The beginning of the loop is located at the mean angle of attack at two degrees. Then, a pitch up motion is performed to the maximum angle of attack, followed by a pitch down. The loop ends with a pitch up from zero degree to 1.85 degrees. The theoretical prediction (green line in figure 4.24) is based on the theory of Theodorsen [1935]. The black line illustrates the measured values and the grey line the quasi steady slope of $2\pi\alpha$. The dynamic effects and the amplitude of the hysteresis

4. Results

are small in both cases. In particular in the range of $\alpha(t) \leq 2^\circ$, the theory and the prediction agree well. Furthermore, both loops are slightly tilted into the horizontal direction compared to the quasi steady line. The rotational direction is oriented counter-clockwise for both loops. Figure 4.25 illustrates the same

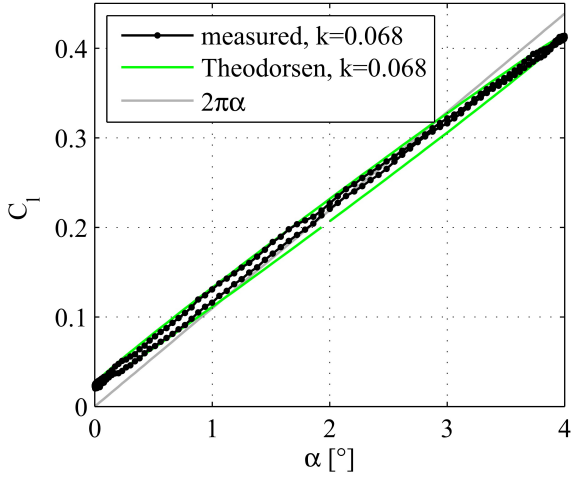


Figure 4.24.: Pure pitching motion at $Re = 350000$ and $k = 0.068$, $\alpha(t) = 2^\circ + 2^\circ \sin(\phi)$

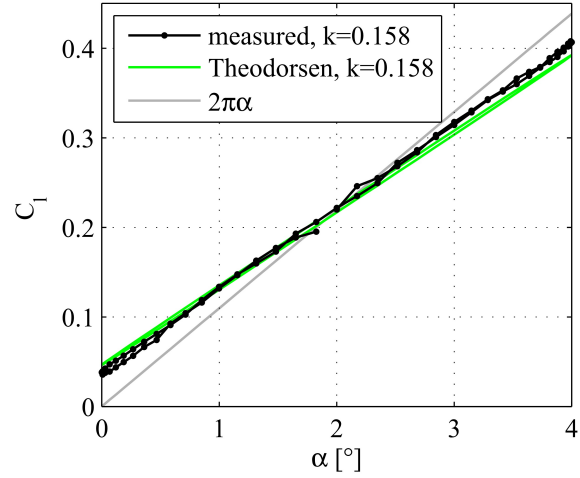


Figure 4.25.: Pure pitching motion at $Re = 500000$ and $k = 0.158$, $\alpha(t) = 2^\circ + 2^\circ \sin(\phi)$

pitching motion at $Re = 500000$ and a frequency of 3.2Hz. This yields a reduced frequency of $k = 0.158$. In this case, no hysteresis is visible. The predicted unsteady lift coefficient loop (green line in figure 4.25) reduces to an almost straight line. The measurements (black line in figure 4.25) show the same behaviour. The small fluctuations lie in the range of the measurement accuracy and do not yield any reliable trend. The slope of the unsteady lines is further tilted horizontally compared to the quasi steady case (grey line). The maximum lift at the maximum angle of attack is reduced by approximately 8%. At the minimum angle of attack, the lift coefficient does not become zero anymore and amounts to $C_l = 0.035$.

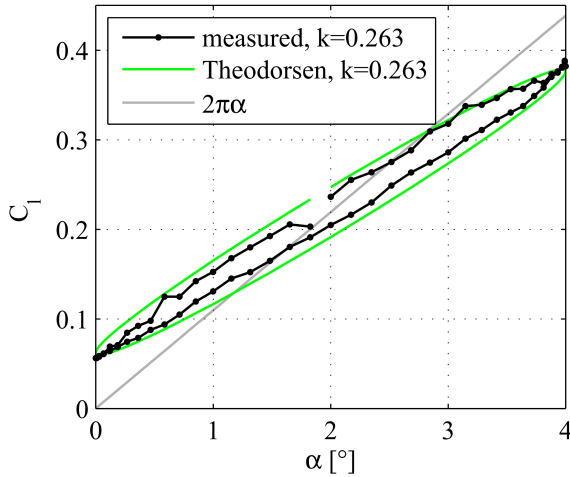


Figure 4.26.: Pure pitching motion at $Re = 350000$ and $k = 0.263$, $\alpha(t) = 2^\circ + 2^\circ \sin(\phi_\alpha)$

Figure 4.26 depicts the lift coefficient for the highest measured reduced frequency of $k = 0.263$ at a Reynolds number of $Re = 350000$. Here, hysteresis effects become stronger. The amplitude of the loop between pitch up and down is increased. The overall slope of the loop tends further horizontally compared to the quasi steady case. The main difference is that the rotational direction of the loop is now oriented clockwise. Thus, the behaviour at this moderate reduced frequency is inverted to the low reduced frequency case in figure 4.24. This finding is already theoretically predicted by, for example, McCroskey [1982] and van der Wall [1992]. An experimental validation is partly performed by Favier et al. [1988] at higher angles of attack, which may include trailing edge stall. However, the current study focuses on fully attached flow and the considered low angles of attack avoid the onset of trailing edge stall. Thus, these experiments constitute an ideal validation of Theodorsen's theory. Besides, the increased noise level is probably caused by the electrical motor. At such high frequencies of 3.2Hz, the motor requires strong electrical current to accelerate and decelerate the airfoil. This may disturb the pressure sensors. However, the measurements globally reproduce the amplitude and the rotational direction of the theoretical prediction well.

Based on the high agreement between the measurements and the prediction, Theodorsen's theory regarding pitching airfoils in constant free stream is further validated and considered as valid. Thus, these promising results allow the prediction of the lift coefficient at higher reduced frequencies.

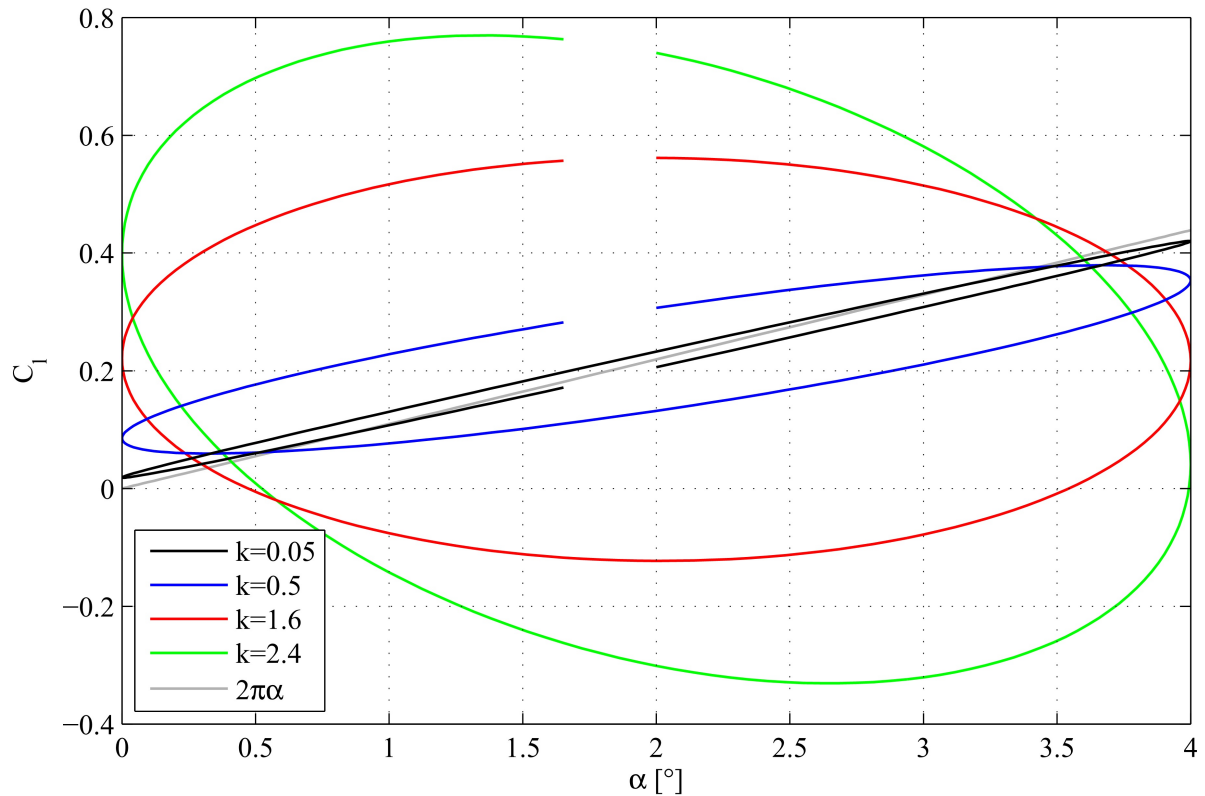


Figure 4.27.: Prediction of the unsteady lift coefficient at low, moderate, and high reduced frequencies

Figure 4.27 shows the theoretical results for different reduced frequencies based on Theodorsen's theory [Theodorsen, 1935]. The black line illustrates a low reduced frequency with $k = 0.05$. The rotational direction is oriented counter-clockwise and the amplitude of the hysteresis is small. At $k = 0.5$ (blue line in figure 4.27), a clockwise rotational direction is clearly visible. The amplitude of the loop becomes larger and the averaged slope becomes more horizontal. At higher reduced frequencies like $k = 1.6$, the hysteresis loop and its amplitude increase significantly. Moreover, the entire loop is oriented horizontally and symmetrically to the mean lift at the mean angle of attack which is the steady case (grey line). During the pitch down from $\alpha = 3.5^\circ$ to $\alpha = 0.5^\circ$, the lift coefficient becomes negative, although the angle of attack is still positive. At a high reduced frequency of $k = 2.4$, the overall slope of the hysteresis loop becomes negative. The lift response is somehow counter-intuitive. On the one hand, during a pitch up starting at two degrees, the lift is decreasing although the angle of attack is increasing. On the other hand, during a pitch down from $\alpha = 2.5^\circ$ to $\alpha = 0^\circ$, the lift increases continuously. Thus, the global behaviour is completely inverted to the quasi steady case. At an angle of attack of $\alpha = 0.5^\circ$ during the pitch up, the current lift coefficient is approximately ten times higher compared to the quasi steady value. On the other hand, during the pitch down, a long period of negative lift coefficients is achieved with noticeably negative values. The minimum amounts to $C_l = -0.33$.

Figure 4.28 depicts the normalised lift coefficient plotted over the phase angle. This is an unusual presentation but is required later for a comparison of the combined effects. A depiction over the angle of attack is more common than seen before. However, at a phase angle of $\phi = 0^\circ$, the current angle of attack corresponds to the mean angle of $\alpha = 2^\circ$ (same at $\phi = 180^\circ$). The maximum angle of attack is reached at $\phi = 90^\circ$ and the minimum at $\phi = 270^\circ$. The unsteady lift is normalised with the quasi steady lift at the mean angle of $\alpha = 2^\circ$. The measured unsteady lift is normalised with the measured quasi steady lift of $C_{l,qs} = 0.22$ and the theoretical curves are normalised with the theoretical quasi steady lift of

4. Results

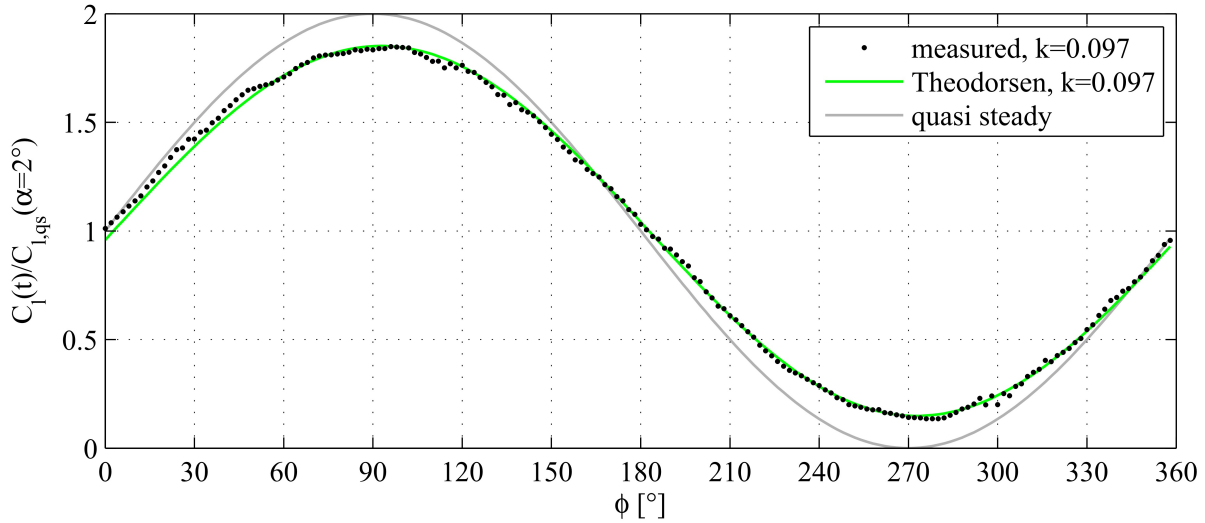


Figure 4.28.: Comparison of the measured and theoretical lift ratio over the phase angle, $Re = 300000$, $k = 0.097$, $\alpha(t) = 2^\circ + 2^\circ \sin(\phi_\alpha)$

$C_{l,qs} = 0.219$. The considered reduced frequency is $k = 0.097$ at a Reynolds number of $Re = 300000$. The comparison of experiment and Theodorsen's theory achieves a good agreement. The small deviations of the two curves are in the range of the measurement accuracy. The maximum quasi steady lift is reached at $\phi = 90^\circ$ and the current angle of attack amounts to $\alpha = 4^\circ$. Hence, the actual angle of attack is two times higher than the mean angle, thus the lift ratio is exactly two at this point. The unsteady lift achieves a lower lift ratio in this range. At a phase angle of $\phi = 270^\circ$, the quasi steady lift coefficient is zero because the current angle of attack is zero. Nevertheless, the unsteady lift coefficient ratio is clearly above zero and amounts to $C_l(\phi = 270^\circ)/C_{l,qs} = 0.14$. In conclusion, Theodorsen's theory and the corresponding measurements are considered to be reliable and are able to reproduce all unsteady effects. This is the basis to predict the effects of a long-wavelength trailing vortex excitation by means of pitching oscillations.

4.5.3. Pure unsteady free stream

Figure 4.29 shows the lift coefficient ratio for an unsteady free stream at a constant angle of attack of $\alpha = 2^\circ$. Although the wing is at a constant angle of attack, the unsteady inflow generates dynamic effects which affect the pressure distribution and loads. In all cases presented here, the wing is facing a sinusoidal velocity profile of $u(\phi) = u_0 (1 + 0.5 \sin(\phi))$. Figure 4.29 illustrates the dynamic lift effects as a function of the phase angle at $Re = 300000$, $k = 0.099$, and $\alpha = 2^\circ$. The time varying lift coefficient $C_l(t)$ is normalised with the quasi steady lift coefficient $C_{l,qs}$ of the corresponding Reynolds number. However, the grey dots in figure 4.29 depict the phase averaged measurement at the corresponding phase angle with a window size of $\phi = \pm 1^\circ$. For $0^\circ < \phi < 180^\circ$, the current free stream velocity $u(\phi)$ is larger than u_0 . In this range, the dynamic effects reduce the lift coefficient ratio to a minimum of $C_l(\phi = 45^\circ)/C_{l,qs} = 0.93$. At $\phi > 180^\circ$, $u(\phi)$ is below u_0 . Furthermore, the slope increases until a maximum lift overshoot of around 27% is reached at $\phi = 280^\circ$. In the range of $250^\circ < \phi < 320^\circ$, the variance of the measured lift overshoot is notably high. On the one hand, figure 3.21 already illustrates that in this phase angle range the deviation of the velocity profile from a perfect sinusoidal one attains the maximum. On the other hand, at $\phi = 270^\circ$ the free stream velocity reaches its minimum value of $u(t) = 0.5u_0$. The combination of the slow inflow and the low angle of attack of $\alpha = 2^\circ$ produces only small differential pressures. Thus, the measurement uncertainty of the pressure transducers reaches its maximum. Another approach is to explain the measured deviations by means of variations of unsteady free stream. At a phase-angle of $\phi = 250^\circ$, the instantaneous free stream is 3% higher compared to an ideal one. At $\phi = 280^\circ$, the unsteady free stream is almost 3% lower compared to an ideal one (see figure 3.21). This rapid deviation of the unsteady free stream reveals further unsteady lift effects. A computation with an assumed velocity amplitude of

$\sigma = 3\%$ and $k = 1$ reveals an additional lift overshoot of less than 2%. Hence, this phenomenon is unable to explain the lift overshoot observed. However, beyond the lift overshoot, the normalised lift coefficient $C_l(\phi)/C_{l,qs}$ tends to one at $\phi = 360^\circ$. For a better comparison of the measured dynamic effects with the theory and also for data smoothing, the measured coefficients are fitted by means of the Fourier series with the first two harmonics (solid black line in figure 4.29). Furthermore, Isaacs' as well as Greenberg's theory are included for the same input parameters ($\sigma = 0.5$ and $k = 0.099$). A good qualitative agreement between the measurements and the theory is observed. The measurements show a slight phase lag of around $\phi = +20^\circ$ at the global minimum and maximum. The maximum amplitude is equal to the prediction from Isaacs. Greenberg's theory underpredicts the dynamic effects significantly at $\sigma = 0.5$. Thus, this result confirms the statement of van der Wall [1992] that Greenberg's theory holds only for moderate velocity amplitudes up to $\sigma = 0.4$. The red dashed line in figure 4.29 illustrates the measured lift coefficient at the corresponding free stream velocity under steady conditions. The linear interpolation of 11 baseline measurements at different free stream velocities yields low Reynolds number effects of around 2% which is in the range of the measurement accuracy. Thus, Reynolds number effects are neglected in the following discussion. However, the amplitude and the phase presented here show a good agreement with Isaacs' theory. Thus, for the first time, Isaacs' approach is experimentally validated for such large velocity amplitudes and higher reduced frequencies.

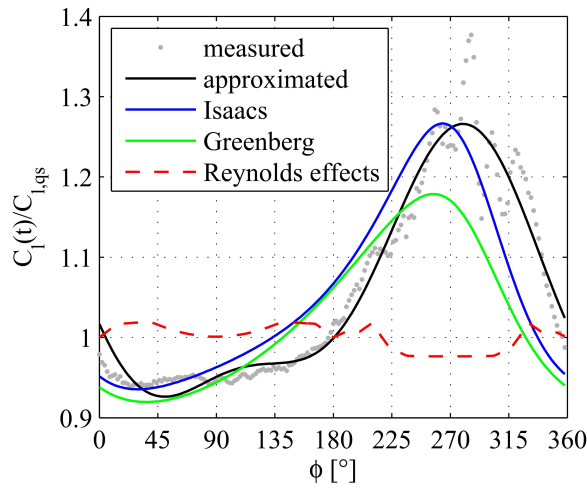


Figure 4.29.: Unsteady lift coefficient at a free stream velocity oscillation and at a constant angle of attack, $\alpha = 2^\circ$, $\overline{Re} = 300000$, $k = 0.099$, and $\sigma = 0.5$

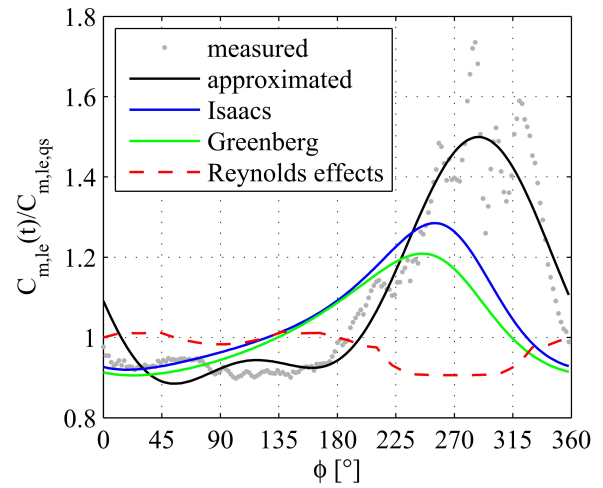


Figure 4.30.: Unsteady leading edge moment coefficient at a free stream velocity oscillation and at a constant angle of attack, $\alpha = 2^\circ$, $\overline{Re} = 300000$, $k = 0.099$, and $\sigma = 0.5$

Figure 4.30 illustrates the dynamic behaviour of the leading edge moment coefficient $C_{m,le}$. Theoretically, $C_{m,le}$ is a linear transformation of the lift coefficient C_l . Thus, the scatter of the measurements is caused by the same uncertainties as discussed for the lift. However, the global minimum and maximum of the Fourier series in figure 4.30 show a phase lag of around $\phi = +30^\circ$ according to Isaacs' and Greenberg's theory ($\sigma = 0.5$ and $k = 0.099$). Although the measured minimum of $C_{m,le}(t)/C_{m,le,qs} = 0.89$ is close to the theories, the theoretical overshoot of $C_{m,le}(t)/C_{m,le,qs} = 1.3$ is clearly exceeded by the experiments. The maximum of the measured leading edge moment overshoot amounts to $C_{m,le}(t)/C_{m,le,qs} = 1.5$. This is a significant deviation between theory and measurements. Probably the nose radius of the fairly thick airfoil leads to a different pressure distribution in the region of the leading edge compared to a flat plate in potential flow. Furthermore, the calculated Reynolds number effects are around 10%, which is consistent with the baselines in figure 4.23. In summary, the measurements qualitatively capture the leading edge moment fluctuations caused by the unsteady inflow although the phase and the amplitude show distinct deviations from the theory. Thus, only the lift coefficient is further discussed.

Figure 4.31 shows the measured phase averaged pressure coefficient distributions C_p at $\alpha = 2^\circ$ and at the time averaged Reynolds number of $\overline{Re} = 300000$. The steady case corresponds to $Re = 300000$ without

4. Results

any dynamic effects. The wind speed variation factor is $\sigma = 0.5$ and the reduced frequency amounts to $k = 0.099$ for the unsteady measurements. Furthermore, C_p is presented for three different phase angles during unsteady inflow. Considering the first case at $\phi = 0^\circ$, the pressure is decreased on the suction and the pressure side. The current free stream velocity is identical to the steady case and the pressure difference is similar to the steady case, thus the lift ratio is close to one which is consistent with figure 4.29. The pressure at the trailing edge is lower due to a reduced pressure recovery. This results in a higher pressure drag of $C_{pd}(\phi = 0^\circ) = 0.051$. The $\phi = 120^\circ$ line lies close to the steady baseline. In this case, it matches almost the baseline even though the instantaneous velocity is $u(\phi = 120^\circ) = 1.43u_0$. The lift overshoot is close to zero as well. The current pressure drag is $C_{pd}(\phi = 120^\circ) = 0.007$. The third case with $\phi = 240^\circ$ illustrates the opposite effect. The pressure is increased on the pressure and suction side. Furthermore, the pressure difference is increased as well, which leads to an increase in lift. The trailing edge pressure is higher compared to the steady case, which results in a reduced pressure drag of ($C_{pd}(\phi = 240^\circ) = 0.07$). The illustration of the three different phase angles clearly demonstrates that the free stream velocity is not the only influence on the lift at constant angle of attack as is the case under quasi steady conditions. In contrast, the oscillating wake vorticity due to the fast free stream variations provokes a phase lag of the lift response. Furthermore, strong pressure drag variations of the factor of 32 occur from $C_{pd}(\phi = 144^\circ) = 0.005$ to $C_{pd}(\phi = 288^\circ) = 0.161$. In figure 4.31, the measured unsteady pressure

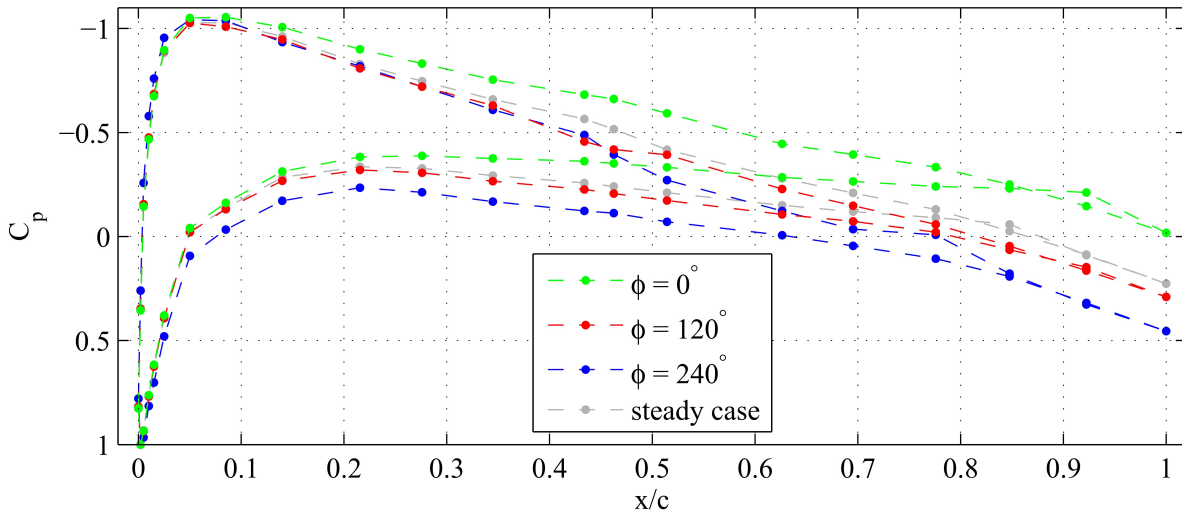


Figure 4.31.: Measured unsteady pressure distribution at three different phase angles, $\overline{Re} = 300000$, $\sigma = 0.5$, $k = 0.099$, $\alpha = 2^\circ$

distribution is discussed. Furthermore, the theory of van der Wall is extended in this thesis to predict the unsteady vorticity sheet along the chord facing unsteady free stream. By means of the difference in the static pressure on the suction and pressure side of the airfoil at the same chordwise position, the unsteady vorticity sheet is calculated via $\gamma_b = \Delta p / (\rho u_\infty)$. This quantity is compared with the theoretical prediction developed in equation 3.31.

Figure 4.32 illustrates this comparison. The black solid line yields the unsteady vorticity sheet at a phase angle of $\phi = 250^\circ$ and a reduced frequency of $k = 0.099$. The black dashed line depicts the quasi steady vorticity sheet distribution. The black solid line clearly achieves a larger amplitude along the entire chord compared to the quasi steady case. Hence, the increased vorticity sheet indicates a higher lift because the integral of the vorticity sheet is equal to the current lift. This is consistent with figure 4.29 because the actual lift overshoot amounts to $C_l(\phi = 250^\circ) / C_{l,qs} = 1.25$. Thus, the extended theory is consistent to Isaacs' theory. On the other hand, measurements at the same reduced frequencies are available and already discussed in figure 4.31. Now, a conversion of the measured unsteady pressure distribution yields the solid red line. For comparison, the quasi steady case is included as the red dashed line. On the first half of the airfoil, the measured unsteady vorticity sheet possesses a significant larger amplitude than the quasi steady one. This is consistent with the measured lift overshoot. Moreover, the measured unsteady

vorticity sheet is almost perfectly aligned with theoretical prediction in the range of $0.08 \leq x/c \leq 0.45$. In this region, the amplitude differences between unsteady and quasi steady conditions are equal in both cases. In the rear part of the wing, the measurements no longer show such a smooth trend. This is caused by the small angle of attack combined with the low free stream velocity at this phase angle and the small differential pressures at this chordwise position. However, the agreement between the unsteady measured and the theoretical predicted vorticity sheet is convincing. Thus, this comparison is a further experimental validation of Isaacs' theory of unsteady free stream at high velocity ratios.

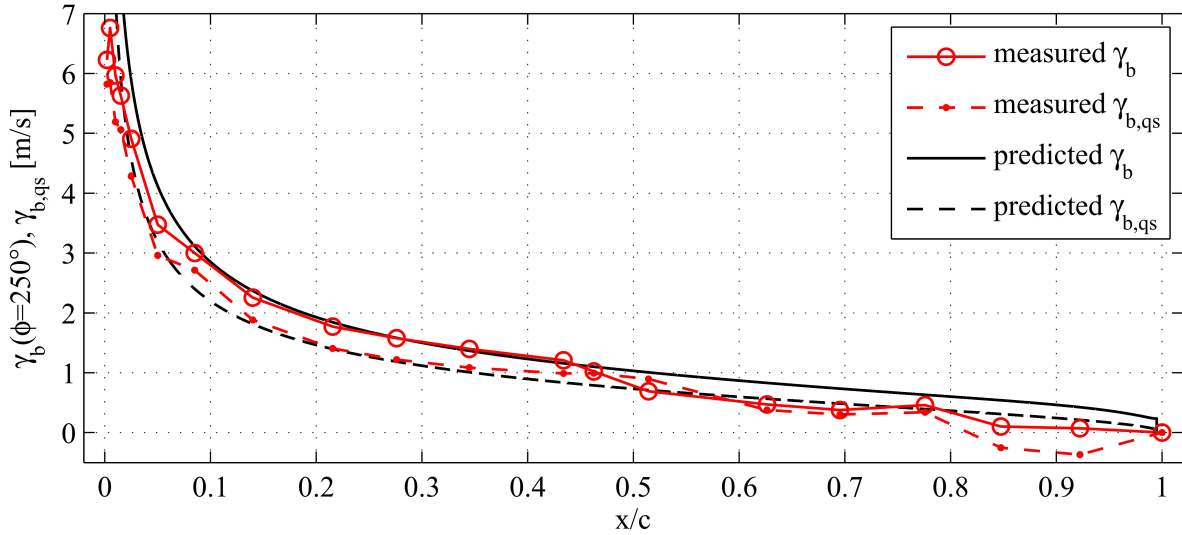


Figure 4.32.: Comparison of the measured and theoretical bound vorticity sheet at $\phi = 250^\circ$, $\overline{Re} = 300000$, $\sigma = 0.5$, $k = 0.099$, $\alpha = 2^\circ$

Based on the unsteady vorticity sheet, an integration yields the unsteady lift. For a further validation of the extended theory, the vorticity sheet is integrated along the chord for each phase angle. The maximum deviation between Isaacs' theory and the extended theory in equation 3.31 amounts to 4% [Strangfeld et al., 2014]. Hence, the proposed analytical extension is considered to be correct.

In summary, the validation of Isaacs' theory and the accurate determination of the bound circulation enable the prediction of long-wavelength trailing vortex excitation due to an unsteady inflow. Furthermore, the theory extension to compute the unsteady pressure distribution is the basis for calculating the acoustic noise emission and the interaction with the rolling up shear layer at the wing tip.

4.5.4. Combined effects

In the last two sections, the unsteady pitching airfoil at a steady free stream is compared to Theodorsen's theory and the airfoil at constant angle of attack facing an unsteady free stream is compared to Isaacs' theory. The discussed results agree well and are promising for a further investigation of both effects occurring simultaneously in-phase.

Figure 4.33 shows the unsteady lift ratio at an averaged Reynolds number of $\overline{Re} = 300000$. The unsteady free stream follows the function $u(t) = u_0(1 + 0.5 \sin(\phi))$ and the angle of attack profile is $\alpha(t) = 2^\circ + 2^\circ \sin(\phi)$. Both motions are in-phase and synchronised at a frequency of $f = 1.18\text{Hz}$, which leads to a reduced frequency of $k = 0.097$. Thus, the maximum angle of attack and the maximum free stream velocity are reached at $\phi = 90^\circ$ and their minima at $\phi = 270^\circ$. The unsteady lift coefficient is normalised by the quasi steady lift coefficient at the mean Reynolds number and the mean angle of attack. The black solid line in figure 4.33 represents the theoretical predictions of Isaacs' generalised theory, which is developed by van der Wall. This generalised theory includes an arbitrary pitching axis and the integration of arbitrary harmonic pitching and plunge motions [van der Wall, 1992]. On the one hand, van der Wall's theory predicts a lift deficit during the pitch up motion at an increasing free stream velocity compared to the quasi steady case (grey line in figure 4.33). The maximum is $C_l(\phi = 98^\circ)/C_{l,qs}(\alpha = 2^\circ) = 1.87$. On

4. Results

the other hand, a significant lift overshoot is predicted in the range of the minimum angle of attack and free stream velocity. The minimum lift ratio is $C_l(\phi = 282^\circ)/C_{l,qs}(\alpha = 2^\circ) = 0.536$, although the quasi steady lift is close to zero. Furthermore, a phase lag of around 15° is observable. The black dots yield the measured unsteady effects at the same reduced frequency. The phase averaged values are smoothed by means of a Fourier-series incorporating only the first two harmonics. However, the amplitude and the phase agree well with van der Wall's theory. The maximum is $C_l(\phi = 98^\circ)/C_{l,qs}(\alpha = 2^\circ) = 1.85$ and the minimum is $C_l(\phi = 284^\circ)/C_{l,qs}(\alpha = 2^\circ) = 0.492$. The phase is reproduced with a maximum deviation of no more than $\Delta\phi = 2^\circ$. Thus, these measurements at large velocity amplitudes combined with pitching motion represent a high quality validation of van der Wall's theory.

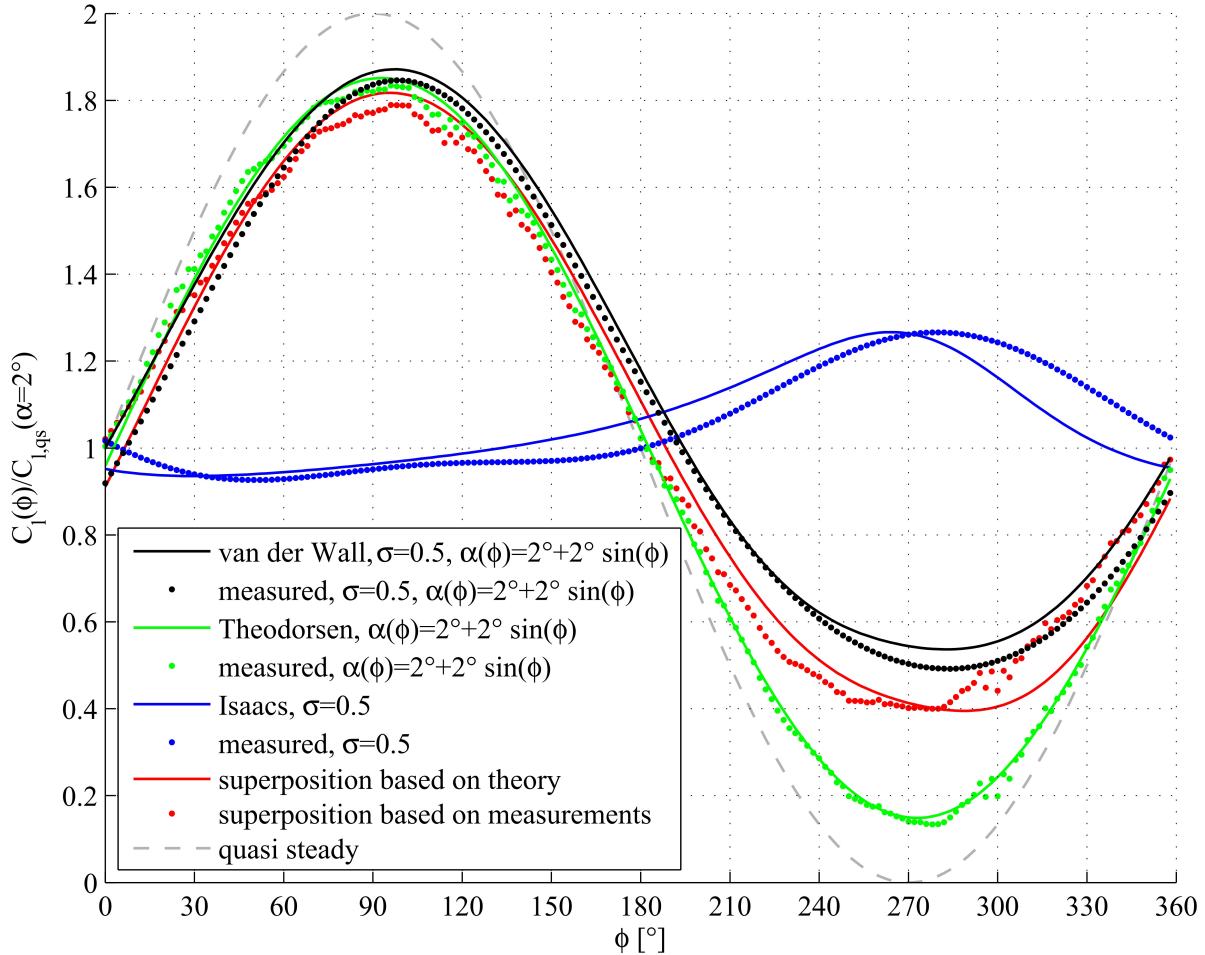


Figure 4.33.: Depiction of the unsteady lift ratio during synchronized, simultaneous pitching $\alpha(t) = 2^\circ + 2^\circ \sin(\phi)$ and oscillating free stream $u(t) = u_0(1 + 0.5 \sin(\phi))$, $Re = 300000$, $k = 0.097$

The corresponding baseline measurements allow a separated evaluation of the two unsteady effects. On the one hand, the blue solid line and the markers in figure 4.33 yield Isaacs' unsteady lift prediction and the measurements at a constant angle of attack of $\alpha = 2^\circ$. These curves are already discussed in figure 4.29. During the first half of the oscillation, the unsteady effects are weak and the ratio is around one. During the second half, a significant lift overshoot, due to a pure unsteady free stream, is observable. On the other hand, the green solid line and the markers yield Theodorsen's theory and the corresponding measurements. Both curves are already presented in figure 4.28. Here, in the first half, the pure pitching motion is close to the combined case. In the second half, the predicted lift coefficients are smaller and deviate from the combined cases distinctly. However, the differential equations from van der Wall yield a nonlinear behaviour of the unsteady free stream and the pitching motion. A superposition of the pure free stream oscillation and the pure pitching motion quantifies the nonlinearity for this certain case. The solid red line illustrates the theoretical superposition. In the first half, no large differences emerge because the

pure pitching motion is close to the combined case and the pure free stream oscillation does not contribute strong unsteady effects. During the second half of this oscillation, the superposition clearly deviates from the combined case. As expected, the nonlinear system reveals another amplitude as the superposition of the single effects. This comes from the emitted wake vorticity. The induced normal velocities on the airfoil chord possess different strengths and phase lags. Thus, nonlinearities arise. Nevertheless, experimental validation at high velocity ratios is still lacking today. The red markers reveal the superposition of the measured effects. It agrees well with the predicted values in phase and amplitude. The superposition yields almost the same effects and the same differences compared to the combined case. Thus, the nonlinear system response is reproduced well by the experiments and the observed deviations are comfortably in the range of the measurement accuracy. Thus, based on this validation, van der Wall's theory is experimentally confirmed for the first time and considered to be able to recapture the unsteady behaviour with the required reliability.

This validation of the combined effects enables the prediction of the long-wavelength trailing vortex excitation due to the combined occurrence of a pitching oscillation and an unsteady free stream. For these mentioned unsteadiness, the nonlinear evolution of the bound circulation is the required input for Betz's theory. In summary, all prerequisites are now calculated to quantify the trailing vortex strength and position under unsteady conditions.

4.6. Interaction between streamwise and spanwise vortices

Intermediate conclusion: The developed extension of Betz's theory is used to determine the wing tip vortex strength and position under unsteady conditions. The unsteady response due to a sinusoidal pitching is considered for an elliptical wing. On the one hand, the unsteady lift overshoot is dominated by the quasi steady variations and thus has only a weak effect. On the other hand, the centroid position is significantly influenced. Hence, it is shown that the vortex tube has clearly a spiral form instead of a straight line. Thus, all investigations considering wing tip vortices under unsteady conditions have to incorporate the centroid meandering.

According to Holzäpfel [2014], the control of the spanwise loading is the only remaining approach for wake and trailing vortex control. The experimental validation of Theodorsen's, Isaacs', and van der Wall's theories for an infinite airfoil enables the prediction of the wing tip vortex on a finite wing under unsteady conditions. At each spanwise position, the unsteady lift overshoot with the corresponding reduced frequency is calculated. By means of Betz's theory, the integration of the spanwise loading reveals the streamwise wing tip vortex strength and its position. In chapter 3.6, Betz's theory is extended to handle unsteady effects like pitching motion, unsteady free stream, plunge motion, or the combination of these. Equation 4.8 predicts the circulation of the streamwise vortex Γ_{st} and equation 4.9 the centroid position y_c . Both quantities vary in time due to the unsteady conditions.

$$\Gamma_{st}(t) = \Gamma_{sp}(y = 0, t) = |\Gamma_{sp}(y = s/2, t) - \Gamma_{sp}(y = 0, t)| = \int_{y=0}^{y=s/2} \frac{\partial \Gamma_{sp}(y, t)}{\partial y} dy \quad (4.8)$$

$$y_c(t) = \frac{1}{\Gamma_{sp}(y = 0, t)} \int_{y=0}^{y=s/2} y \frac{\partial \Gamma_{sp}(y, t)}{\partial y} dy \quad (4.9)$$

Equation 4.8 states that the unsteady circulation of the wing tip vortex is equal to the variation of the spanwise circulation at mid-span. The behaviour of the centroid position in equation 4.9 does not scale linearly to the circulation at mid-span. In this case, each spanwise position is leveraged with the distance to the mid-span y . Thus, the entire spanwise circulation has to be determined to predict the centroid position in unsteady flow regimes.

Equation 3.37 is used to determine the circulation distribution of the trailing vortex. Thereby, in the case on an elliptical lift distribution, the maximum radius is identical to the centroid position in steady situations. With the know relation between the spanwise position y_1 and the radius r_1 , the circulation

4. Results

distribution is predicted via equation 3.32.

$$\Gamma_{st}(r_1) = \int_0^{r_1} \frac{\partial \Gamma_{st}(r)}{\partial r} dr = - \int_{y=s/2}^{y_1} \frac{\partial \Gamma_{sp}(y)}{\partial y} dy = \Gamma_{sp}(y_1) \quad (4.10)$$

The integrals are solved piecewise, beginning at the wing tip. Hence, equation 4.10 yields the circulation distribution of the trailing vortex in a simple form. The spanwise circulation is zero all the time $\Gamma_{sp}(y = s/2, t) = 0$. This argument leads directly to a circulation in the vortex centre of zero $\Gamma_{st}(r = 0, t) = 0$ by means of equation 4.10. Therefore, no singularities exist in the flow field and the kinetic energy remains finite. The tangential velocities are determined by $2\pi r_1(t)v_\theta = \Gamma_{st}(r_1, t)$ for an axially symmetric vortex. By means of the know tangential velocity field, the axial velocity of the trailing vortex u_{axial} can be computed via equation 4.11 under the assumption of neglecting the viscous head drop in the vortex core [Batchelor, 1964].

$$\frac{u_{axial}(t)}{u_0} = \sqrt{1 + \frac{\rho}{q} \int_{r=0}^{r=r_{max}} \frac{v_\theta(t)^2}{r(t)} dr} \quad (4.11)$$

To demonstrate the capability and importance of the developed extension of Betz's theory, an example of a harmonic pitching DeHavilland Beaver DHC-2 is given. This airplane is used during the free field flight tests of Chevalier [1973]. It possesses a rectangular wing. The wingspan is $s = 14.63\text{m}$ and the wing area is 23.2m^2 [Rossiter, 1999] which leads to a chord length of $c_0 = 1.59\text{m}$. The spanwise loading is not known precisely and the steady centroid position is not documented in the literature. Thus an elliptical loading is assumed as a first approach and determined in equation 4.12. The steady circulation at mid-span is $\Gamma(y = 0) = \pi^2 \alpha(t) c_0 u_0$. This kind of loading is produced only by an elliptical wing geometry and the chord length along the span $c(y)$ is given in equation 4.13.

$$\Gamma_{sp}(y, t) = \Gamma(y = 0, t) \sqrt{1 - \left(\frac{2y}{s}\right)^2} \quad (4.12)$$

$$c(y) = c_0 \sqrt{1 - \left(\frac{2y}{s}\right)^2} \quad (4.13)$$

Figure 4.34 shows the distribution of the spanwise circulation Γ_{sp} , the streamwise circulation $\Gamma_{st}(z = 0)$ and the tangential velocities $v_\theta(z = 0)$ after the roll up process in the wake is completed for the assumed lift and wing geometry in equations 4.12 and 4.13. The black line illustrates the steady results. The spanwise circulation is zero at the wing tip and increase to its maximum towards mid span. In the case of a periodic pitch motion, the lift distribution varies due to the change of the angle of attack $\alpha(\phi) = 6^\circ + 2^\circ \sin(\phi)$ and the unsteady lift response. The pitch frequency is 0.5Hz which corresponds to a maximum reduced frequency at mid span of $k_{max} = 0.0624$. Due to the nonlinear lift overshoot, the lift distributions are not elliptical anymore which shifts the centroid position. This is documented by the streamwise circulation distribution $\Gamma(\phi, z = 0)$ of the trailing vortex. In the steady case, the centroid position is $2\pi/8$ which coincide with the maximum radius of the trailing vortex. The centroid in the unsteady cases is shifted in spanwise direction, inboard for $\phi = 90^\circ$ and outboard for $\phi = 270^\circ$. The maximum streamwise circulation is reached at the maximum radius and coincides with the maximum spanwise circulation at mid span due to equation 4.10. Beyond the maximum radius, the circulation is zero. The streamwise circulation becomes zero at the vortex centre in all cases. This prohibits a singularity in the vortex centre and leads to a finite tangential v_θ velocity in the vortex centre of the fully developed trailing vortex. The entire tangential velocity is shown in figure 4.34 as well. Stronger spanwise circulation distributions lead to higher tangential velocities. The three presented quantities in the steady case in this figure coincide with the results of Rossow [1973].

The integration of the tangential velocity from the vortex centre to the vortex fringe yields the pressure in the vortex centre. Hence, an equilibrium between centrifugal and centripetal forces is achieved. By means of the mass balance, a relation between the tangential velocity profile and the axial velocity of the

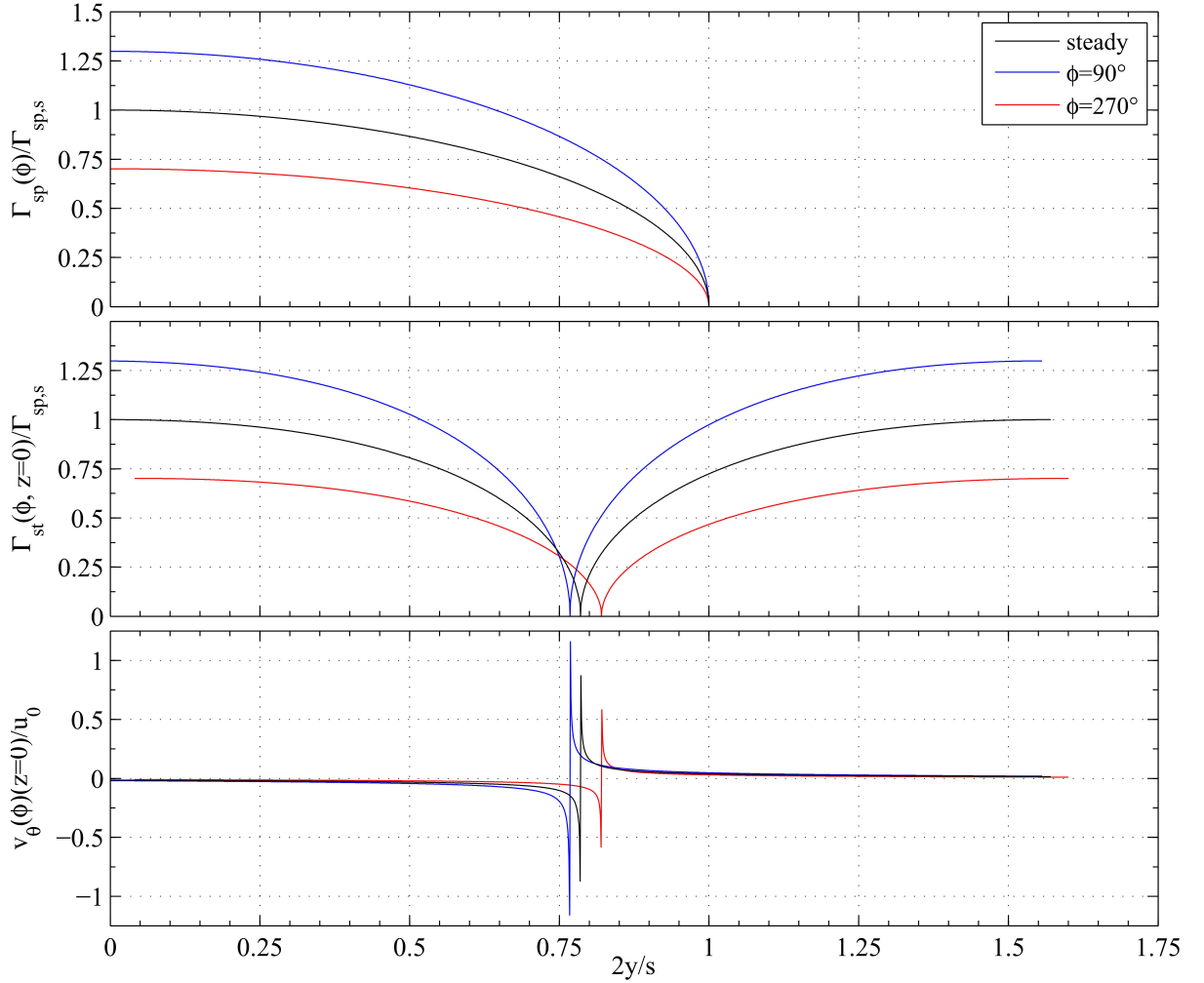


Figure 4.34.: Distribution of the spanwise circulation Γ_{sp} , the streamwise circulation $\Gamma_{st}(z = 0)$ and the tangential velocities $v_{\theta}(z = 0)$ of the fully developed trailing vortex for a periodic pitch motion at $\alpha(\phi) = 6^{\circ} + 2^{\circ} \sin(\phi)$, $u_0 = 40\text{m/s}$ and $f = 0.5\text{Hz}$

vortex centre is derived by Batchelor [1964], see equation 4.11. Figure 4.35 shows the velocity ratio for the pitch motion at $\alpha(\phi) = 6^{\circ} + 2^{\circ} \sin(\phi)$, $u_0 = 40\text{m/s}$ and $f = 0.5\text{Hz}$. In the steady case, this ratio is $u_{axial}/u_0 = 1.273$. Furthermore, the quasi steady and the unsteady cases are presented as well. Both lines are similar to another, hence the global effect is dominated by the quasi steady angle of attack variation and the unsteady effects are tiny. However, the ratio of the maximum axial velocity at $\phi = 90^{\circ}$ and the minimum axial velocity at $\phi = 270^{\circ}$ is 1.97 for the given angle of attack profile. This ratio would lead theoretically to an identical streamwise position of the lowest and the highest axial velocity after almost a half period. It is still an open question if this flow topology promotes vortex bursting, because this velocity ratio is independent of the pitch frequency, it only depends on the mean angle of attack and the pitch amplitude. Following this idea, vortex bursting would be only just a "catch-up" mechanism. Considering the steady case, the Crow instability is only required to start this mechanism via induced velocities. This would agree with Chevalier's second speculative explanation of his flight test results [Chevalier, 1973]. However, as seen in figure 4.34, the spanwise centroid position is affected by the unsteady pitch motion. In contrast to the axial velocity ratio, the centroid meandering is highly affected by the reduced frequency. Figure 4.36 depicts a small parameter study regarding the centroid position. The green and the blue line resemble the flight tests of Chevalier [1973] with a mean angle of attack of $\alpha_0 = 6^{\circ}$ and a pitching frequency of $f = 0.25$ or $f = 0.5\text{Hz}$. The latter corresponds to a maximum reduced frequency of $k = 0.0624$ at mid-span and reduces to zero at the wing tip. The amplitude of the sinusoidal pitching motion is $\pm 2^{\circ}$. In this case, the maximum unsteady lift overshoot determined by means of Theodorsen's

4. Results

theory is 5.7%. The ratio between the lowest angle of attack of 4° and the highest of 8° leads to doubling of the spanwise circulation. Thus, the unsteady overshoot is dominated by the quasi steady lift variation due to the pitching. Based on this estimation, the unsteadiness may have only a weak influence on the vortex strength. However, under steady conditions, the centroid position normalised by the wing span is $\pi/8$ for an elliptical loading [Donaldson, 1971]. This result is reproduced by the numerical integration of equation 4.9 in the developed code based on 733 sampling points along the span. Furthermore, although equation 4.8 is trivial, this expression is re-evaluated numerically to validate the code. This validation reveals that the deviations between analytical and numerical results are negligible. However, under unsteady conditions, the reduced frequency varies at each spanwise position due to the elliptical shape. Thus, the unsteady lift overshoot varies as well along the span and this has a direct nonlinear influence on the centroid position because the lift distribution is not elliptical anymore. The result would be a spiral vortex centre meandering and the geometrical shape is very similar to the natural flow pattern of a Crow instability. Following this idea, vortex bursting is promoted by the Crow instability and hence, the wavelength of the pitch motion should be adjusted to the natural wavelength of the Crow instability which is 8.6 times $s\pi/4$ for an elliptical lift distribution [Crow, 1970]. In the case of the discussed flight tests, the optimal actuation frequency would be approximately between 0.25 and 0.5Hz. This would agree with Chevalier's first speculative explanation of his flight test results [Chevalier, 1973]. A case study for different angle of attack motions at various reduced frequencies may disclose the governing parameter for vortex bursting.

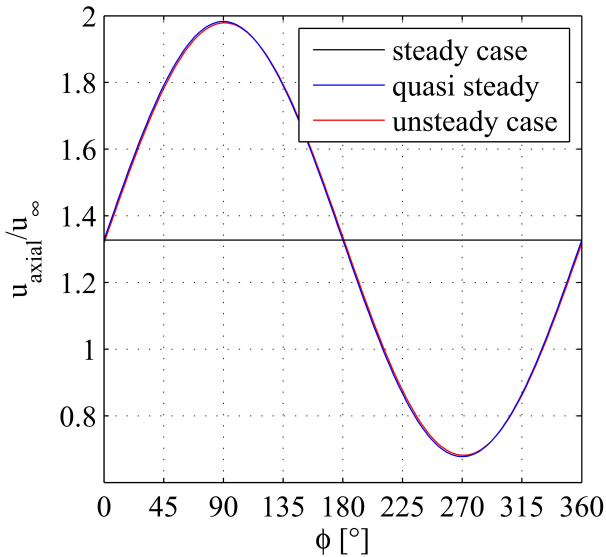


Figure 4.35.: Normalised axial velocity in the trailing vortex centre for a periodic pitch motion at $\alpha(\phi) = 6^\circ + 2^\circ \sin(\phi)$, $u_0 = 40\text{m/s}$ and $f = 0.5\text{Hz}$

Chevalier observes that the initial burst coincides with the minimum angle of attack position. The unsteady centroid meandering is a possible explanation of this phenomenon. In figure 4.36, the grey dashed line represents the steady case at the normalised centroid position of $\pi/8$. In the case of a pitching frequency of $f = 0.5\text{Hz}$ and a mean angle of attack of $\alpha_0 = 6^\circ$, the minimum normalised centroid position of $y_c = 0.3816$ is reached at a phase angle of $\phi = 45^\circ$. The maximum of $y_c = 0.4125$ occurs at $\phi = 247^\circ$. This corresponds to a change of approximately 8% or in real units to a vortex centre meandering of 0.45m. Hence, although the unsteady pitching has only a minor effect on the vortex strength, the vortex centre position is already significantly influenced. At lower mean angle of attack and the same pitching amplitude of $\pm 2^\circ$, the effects become stronger and exceed a variation of 25%. This proposed approach is a conservative estimation of the expected unsteady effects. The original wing is rectangular and thus, more span-

wise circulation is generated in the region of the wing tip compared to an elliptical wing. This leads in general to strong wing tip vortices [Brown, 1973], [Mason and Marchman, 1973].

The observations of Chevalier [1973] are not completely understood and the existing fluid dynamic theory fails to explain this phenomenon. Chevalier [1973] speculates that an increase of the streamwise circulation is required to amplify instabilities. This interpretation might be wrong because at the phase angle of a circulation increase, approximately at $\phi = 270^\circ$, the centroid deflection also reaches its maximum. The presented approach in this thesis does not explain the entire phenomenon but it clearly shows that the variation of the centroid position is significant and much higher than the unsteady lift overshoot. Thus, the centroid meandering has to be taken into account in all analyses considering vortex bursting. Especially in the case of stability analysis, the assumption of a straight vortex tube is not convincing anymore. It is believed by the author, that the spiral vortex tube plays a crucial role in enhanced wing tip vortex bursting if these are linked to the Crow instability.

The inverse Betz's method is not considered here because the effects of the AFC via segmented flaps yield only weak effects. These effects are unfortunately too weak to generate significant influence on a spanwise loading.

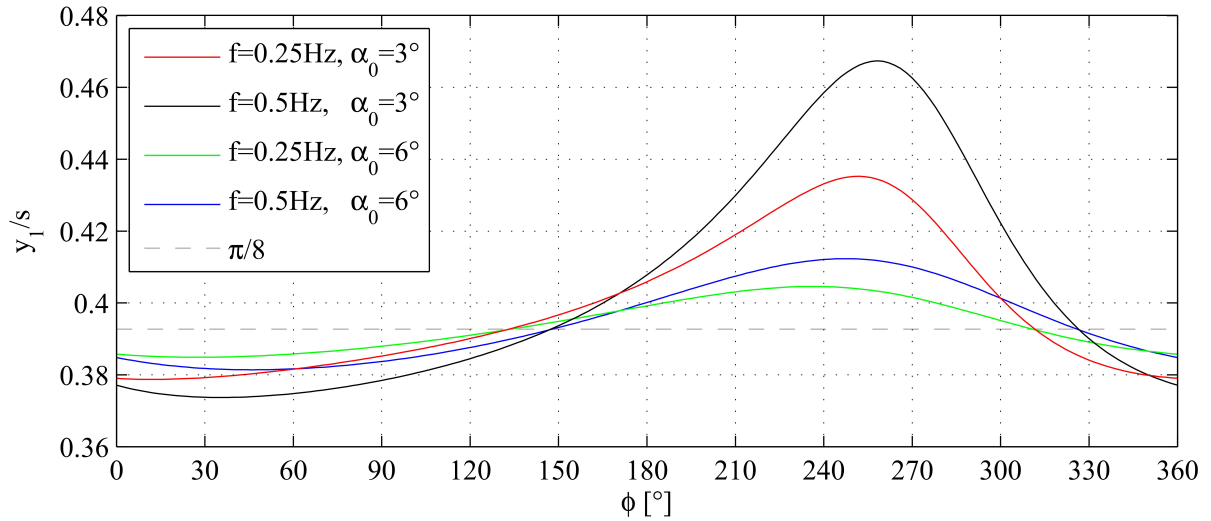


Figure 4.36.: Normalised centroid meandering of the wing tip vortex due to sinusoidal pitching

4.7. Improvement and future work

First, improvements of the experimental setup and the short-wavelength AFC system to control streamwise vortex at its origin are summarised. Then, the experimental validations and further extensions of the mentioned theories for long-wavelength excitation are discussed.

4.7.1. Short-wavelength actuation

The main problems during the measurements using the swept, semi-span, backward facing step are the unknown inflow conditions and a possible flow separation at the leading edge. As long as the inflow conditions are unknown, a valid and reliable statement regarding the short-wavelength AFC is not possible. As already discussed in chapter 3.1, the inflow characteristics of the wind tunnel are sparsely documented. During the preliminary tests, the test track and the nozzle possess a misalignment of almost one degree. During the final measurements, a large gap of approximately 10cm in the settling chamber probably distorts the inflow. Furthermore, a secondary stream exists in this wind tunnel. In conclusion, this wind tunnel is considered to be insufficient for such high precision measurements. Hence, a repetition of these measurements in the laminar wind tunnel of the HFI institute is recommended. The wind tunnel has a very low inflow turbulence level and the flow is regarded as laminar. Intensive quantification of the inflow is required to determine exactly the turbulence level and the main stream direction. The model has to be aligned with the inflow to avoid any kind of separation or static pressure variations in front of or along the step model. In this new setup, the boundary layers on the step top and on the side wall have to be laminar until the critical Reynolds number is reached. Kaltenbach [2004] already states that the independence principle in its strong form does not hold for turbulent boundary layers.

Another challenge is the closed test section. The developed bypass system including two diffusers is partly able to control the mass flow above and below the splitter plate. However, this also involves a large parameter space. Furthermore, the boundary layer of the wind tunnel wall at one side of the model may also disturb the flow and pressure field on the step top. The occurrence of three-dimensional structures at the step inlet or on the step top are possible. An open test section is favourable to avoid these problems mentioned. The laminar wind tunnel at the HFI also allows operation with an open test section. In this setup, the constant static pressure in the potential core will reduce these adverse effects. No wind tunnel

4. Results

boundary layer affects the step's top flow. Even more important is the absence of a complex bypass regulation system. Any overflow convects to the side or beneath the model, into the ambient air. No diffusors are required anymore and no static pressure gradient is generated upstream of the splitter plate trailing edge. A further reduction of the step length reduces the influence of the emitted boundary layers as well. If the entire step model generates laminar boundary layers, tripping will easily provoke turbulent conditions. The chosen approach of covering the flaps upstream of the trailing edge by an additional thin layer on the step top is promising and may be integrated in all future measurements.

The measurement range with 1000Pa of the *HDO*-pressure sensors is too large for these low free stream velocities. Pressure sensors with a maximum range of approximately 60Pa are sufficient. Good experience is made with other pressure sensors (company: *Sensortech*, type: *LBA*, type: *LDE*). The long connection of more than 3m between the Pitot tube and the pressure sensors is too long. The corresponding time lag is the main error source of the pressure measurement. Thus, a short connection between the static reference pressure and the sensors is highly recommended. A 12-hole probe with a smaller head will reduce the adverse effects and may yield a higher spatial resolution of the rolling up shear layer. One way is a smaller probe (company: *Omniprobe*) with a head diameter of approximately 4mm. Another solution is high resolution Stereo-PIV measurements downstream of the trailing edge. The recommended minimum spatial resolution is 0.2mm. In these small dimensions, it is complex to capture the velocity gradients correctly via PIV. Another general improvement is a more extensive electromagnetic shielding of the oscillating armature drives to reduce the noise emission.



Figure 4.37.: Construction of a new actuator with a separated shaft

very time consuming. On the other hand, a linear amplitude response for frequencies up to 20Hz is documented in this thesis. Beyond this frequency, the nonlinear behaviour due to the eigen frequency at around 35Hz arises. Thus, the use of stiffer springs is one attempt to shift the eigen frequency to higher frequencies and hence widen the range of linear amplitude response. Moreover, single bearing on a stiff ground plate may allow a pre-calibration instead of an in-situ calibration. The documented time resolved flap motion paths of high precision yield that inertia does not dampen or distort the movement. This gratifying behaviour allows a higher motion leverage to enlarge the motion amplitude. Figure 4.37 illustrates such a new actuator. The separated shaft and the adjusted flap geometry are the main improvements of this prototype. Furthermore, only sinusoidal motion functions are tested right now. Other functions like trigonometrical, serrated, or smoothed step functions may be tested as well. More general improvements are a higher number of flaps to perform smoother transversal waves and a higher manufacturing accuracy, which in combination with support from the work shop will probably increase the overall performance.

Future work with these powerful, highly reliable, and accurate oscillating flaps is very promising. Besides small improvements of the AFC, a new optimised model in an appropriate wind tunnel has to be investigated. The initial flow has to be laminar to study all three flow types by means of tripping. In an open test section, the swept, backward facing step model should be long enough to cover the entire potential core downstream of the nozzle. Hence, a two or 2.5-dimensional step is realised. This unique and reliable setup allows a direct validation of the theoretical work of Jürgens [2006]. In the

In general, the newly developed AFC system with 16 segmented flaps performs excellently, especially for frequencies below 25Hz. The precise control of the amplitude, frequency, and phase is implemented and only 75% of the financial budget is required. The AFC system works most accurately and reliably for frequencies between 1 and 25Hz. Above 35Hz, strong vibrations of the single shaft lead to an unintended interaction of the flaps. Hence, each flap requires its own single shaft to avoid interactions. The use of elastic bearing will further reduce the mechanical vibrations. On the one hand, the process of the amplitude calibration of each flap for several frequencies is

next step, the entire model is partly pulled out to modify the 2.5-dimensional step to a semi-span model with completely three-dimensional flow structures. This setup covers a broad span of experiments. In particular, a comparison of the 2.5 and three-dimensional cases will give a much deeper insight into the flow physics. This will establish a valuable data base for validation of CFD codes and stability analysis in highly three-dimensional flow. Analyses of curved and tilted self-preserving shear layers and the sweep independence principle at different geometries including the three flow states (laminar, transitional, turbulent) will give a huge contribution to fundamental research in the field of fluid dynamics.

4.7.2. Long-wavelength actuation

The entire setup of the unsteady wind tunnel at the Technion, Haifa, Israel, is actually close to perfection. Some tiny improvements are the use of servomotors with encoder instead of stepper motors to control the angle of attack and the louvers. Hence, a more direct and user-friendly implementation of arbitrary motions is possible. The electromagnetic shielding could be improved in the entire lab although a lot of effort has already been made. In particular, the motors of the pitching and louver mechanism and the sensitive measurement techniques still show some unwanted electromagnetic interactions. The louver mechanism varies the free stream velocity as desired. Hence, the static pressure in the test section varies significantly as well. A direct time resolved record of the static pressure via pressure taps in the wind tunnel wall upstream and downstream of the airfoil will improve the pressure data correction. More general improvements are a higher aspect ratio of the airfoil and a larger wind tunnel height to reduce the blockage effects at high angles of attack including deep stall. Higher reduced frequencies and a higher Reynolds number are favourable as well. However, these parameters cause aversion to each other. A higher Reynolds number decreases the reduced frequencies, a higher aspect ratio at constant span decreases the Reynolds number but increases the reduced frequency. Hence, an appropriate balance between these parameters has to be found. This ideally balanced setup is probably close to the existing one. For the purpose of a pure validation of Theodorsen's, Isaacs', and Greenberg's theory, a NACA 0018 airfoil profile is inferior to a NACA 0012. Already the baseline characteristic of a NACA 0012 is closer to the predictions of a flat plate in potential flow. Thus, the unsteady effects are probably captured in a better way as well.

This unique and progressive wind tunnel enables a broad span of unsteady investigations. A pitching airfoil including a flap will further validate Theodorsen's theory. Additional unsteady inflow has never been examined, thus an extension of the theory is required to capture all unsteady effects. Another approach is the simulation of realistic inflow conditions at horizontal axis wind turbines. Actually, all theories assume a sinusoidal inflow velocity profile. Wind turbines especially are facing more complex inflow velocities. Thus, the inclusion of a Fourier approximation of an arbitrary inflow function extends the theory significantly and avoids the assumption of simple sinusoidal inflow. Furthermore, a comprehensive approach including unsteady inflow, pitching, vertical wing tip motion, and yaw misalignment with the corresponding phase lags will give a much deeper insight in the unsteady loads. This is considered only by ordinary safety factors during the designing and certification. However, today no one is taking into account the real unsteady loads due to the huge lack of unsteady experiments and analytical approaches. Furthermore, these load predictions will be the input for aeroelastic calculations to predict the damping of the blades. Due to the unsteady lift variations, the damping may be already significantly reduced in fully attached flow. Hence, this is not only a lifetime cycle issue, it directly affects the safety of rotational systems. This issue is very important for wind turbines and helicopters and requires a better understanding of the unsteady loads and the flow physics causing the phase lag. For helicopters in particular, the extension of the theories to describe compressible effects as well will be an additional feature of high interest.

The prediction of the long-wavelength actuation determines the unsteady trailing vortex strength and position. These promising results are based on the assumption of an elliptical loading along the span. With more precise loading distributions as input parameters, a more realistic computation is possible. Furthermore, the unsteady free stream is crucial for the unsteady lift in the field of wind turbines and helicopters. Thus, by means of a realistic blade geometry including the corresponding spanwise loadings, the long-wavelength excitation due to a combined occurrence of an unsteady free stream and a pitching

4. Results

motion reveals the unsteady behaviour of the trailing vortex. Such a comprehensive case study predicts the trailing vortex strength and the vortex centre meandering. A deeper insight into the flow physics is important for a better understanding of vortex-blade interactions, acoustic broadband noise emission, load control, and interaction with the subsequent wing.

Another approach is the control of the spanwise loads by means of short-wavelength actuation at the wing tip. The modified wing tip vortex generates a different downwash and, consequently, changes the entire trailing vortex. This effect may be quantified by the inverse Betz's method. If the velocity distribution of the streamwise vortex is known, for example, obtained by means of PIV measurements, the spanwise bound circulation distribution can be calculated. Hence, a strong short-wavelength actuation possesses the capability to control the spanwise loadings and the trailing vortex. However, due to the low control authority of the short-wavelength actuation, this approach is not experimentally validated.

5. Conclusion

The thesis quantifies the effects of long- and short-wavelength actuation on finite wings. Both approaches are investigated experimentally and theoretically and, finally, are linked by means of the Betz's theory under unsteady conditions.

To investigate the concept of short-wavelength control of streamwise vortices, a generic model is developed in this thesis: the swept, semi-span, backward facing step. This new geometry is designed, constructed, and tested in the large wind tunnel GroWiKa at the HFI. Smoke and surface oil flow visualisations confirm the generation of a stable streamwise vortex downstream of the trailing edge. The rolling up shear layer and the emitted streamwise vortex are similar to the flow structures of trailing vortices on finite wings. The surface pressure measurements show clearly the footprint of a streamwise vortex and further verify the similarity. Hence, the baseline measurements confirm the appearance of a streamwise vortex based on this newly developed geometry and prove the propagated analogy to trailing vortices, delta wings, and the Ahmed body.

A new experimental concept of flow control is developed for an effective actuation of the emitted shear layer. The actuator design is motivated and its optimisation is discussed in detail. These segmented actuators yield an excitation in transversal direction. An AFC system is successfully constructed, implemented, and calibrated in the swept, semi-span, backward facing step. It consists of 16 segmented flaps and the entire system fulfils the desired requirements to control the amplitude, frequency, and phase velocity. This developed setup enables an actuation in all arbitrary downstream directions of the trailing edge. Intensive tests of the actuators reveal a high accuracy, reliability, and repeatability in controlling the frequency, amplitude, and phase velocity up to 30Hz.

At a moderate Reynolds number of 150000, control effects up to 8% of the generated static pressure on the back panel are reached. A pressure reduction or enhancement is performed by varying the actuation frequency. The frequency spectra of the pressure sensors along the vortex axis yield an almost linear phase shift of the dominant frequency, depending on the desired phase lag of the AFC. This validates the ambitious ability of the developed actuation system to excite the flow in all arbitrary transversal directions. Boundary layer investigations upstream of the trailing edge yield a form parameter which is representative for turbulent boundary layers. This shows the existence of a fully turbulent boundary layer, although the predicted and favoured flow state is significantly sub-critical, which renders any investigation with laminar inflow impossible. This is probably the main reason of the weak AFC effects and can only be compensated by using another, more sufficient wind tunnel for this kind of experiment.

The stability analysis is formulated for two-dimensional shear layers and successfully implemented with a numerically more stable formulation of the spatial derivations. By means of this proposed approach, analytical functions to determine the derivations are not requested anymore. Hence, this ansatz is highly convincing to perform linear stability analysis for skewed mixing layers based on discrete, non-equidistant distributed sampling points of the velocity profile. Validations of different inviscid and viscous reference cases prove the high accuracy of this approach. A temporal, linear stability analysis is computed based on an ideal shear layer which possesses two velocity components in the mean field. Thus, the existing theory is extended to further fulfil the requirements based on experimental data.

The theories of Theodorsen, Greenberg, Isaacs, and van der Wall are used to predict the unsteady circulation of bound vortices to quantify the effect of long-wavelength actuation. The experimental setup at the Technion, Haifa, Israel permits the, as yet, missing validations of the mentioned theories at medium and high free stream velocity ratios. The installed NACA 0018 airfoil performs sinusoidal pitching oscillations up to 3.2Hz. The louver mechanism generates sinusoidal free stream velocity oscillations with amplitudes up to 50% and frequencies up to 1.2Hz. Baseline measurements reveal a maximum difference of 3% between the measured velocity profile and an ideal sinusoidal profile. The lift coefficient of the airfoil has a slope of 2π which is consistent with the theory of potential flow. Thus, the suitability of this setup to

5. Conclusion

validate the unsteady lift theories is confirmed.

Furthermore, the existing theory of van der Wall is extended to predict the pressure distribution under unsteady conditions. This approach gives a more comprehensive understanding of the flow structures and the dynamic behaviours of an airfoil facing unsteady inflow. The proposed, closed analytical solution predicts the unsteady pressure distribution for all arbitrary reduced frequencies and arbitrary velocity fluctuation amplitudes. On a finite wing, these results will be linked with the generated pressure field due to the wing tip vortex in the future. The combination of the time-varying pressure fields will enable a deeper insight into the flow induced acoustic field and broadband noise generation on the outer part of the wing.

The experimental investigation of a pure pitching motion at reduced frequencies between 0.05 and 0.263 yields a switch in the rotational sense of the hysteresis loop. This behaviour is consistent with Theodorsen's theory. At a reduced frequency of around 0.16, the predicted and measured hysteresis loop becomes insignificant and only the slope of the lift coefficient is reduced. Hence, Theodorsen's theory and the experiments show a high degree of agreement with each other.

The pure unsteady free stream oscillations at velocity amplitudes of 33% and 50% and at reduced frequencies up to 0.1 validate the unsteady lift behaviour of Isaacs' and van der Wall's theory. The predicted and measured lift overshoots amount to approximately 26% in both cases, within the range of the lowest temporary free stream velocity. The maximum Reynolds number effect is less than 3% during these experiments. The high agreement of the amplitude and the phase of the lift overshoot validates Isaacs' theory at medium and high inflow velocity amplitudes. Furthermore, the unsteady pressure distribution is predicted by means of the extension of the theory. The agreement between predictions and experiments is highly promising for the quasi steady and unsteady pressure distribution at all phase angles and validates the extended theory proposed in this thesis.

Besides a pure pitching oscillation and a pure unsteady free stream, both unsteady effects are performed in-phase simultaneously to validate van der Wall's theory. The agreement between the experiments and the theory is high. This validates van der Wall's theory experimentally for the first time. Furthermore, each single unsteady degree of freedom is measured and predicted individually and then superimposed. The superposition deviates significantly from the simultaneous oscillation in both cases. Hence, the experiments confirm the nonlinear interaction of these two unsteady oscillations.

The comprehensive validation of the mentioned theories and their reliable prediction of the bound circulation under unsteady conditions is the basis for quantifying the long-wavelength actuation effects. Betz's theory is extended in order to take the unsteady spanwise circulation into account. This enables the computation of the trailing vortex strength and its position during pitching oscillations, unsteady free stream, or vertical airfoil motion. A finite wing at a mean angle of attack of 6° and a pitching amplitude of $\pm 2^\circ$ is simulated. This setup is comparable to the free field experiments of Chevalier. On the one hand, it is shown that the trailing vortex strength is dominated by the quasi steady state changes and the unsteady lift overshoot is negligible at these low reduced frequencies. On the other hand, the conservative simulations yield a centroid position variation of the wake up to 8% of the span at a reduced frequency of 0.031. At a mean angle of attack of 3° , this centroid meandering of the wake already amounts to 25% at the same reduced frequency. This significant effect at these low reduce frequencies is probably the reason for the accelerated trailing vortex bursting.

The investigated ansatz of short- and long-wavelength actuations and the disclosed interaction between the time varying spanwise and streamwise circulations give a much deeper insight into the flow physics of finite wings. The presented fundamental research reveals several approaches for practical applications. Wind turbine, helicopter and airplane aerodynamics and the adverse effects of hazardous vortices, broadband noise, flow induced vibrations, etc., repose on the same phenomena which are intensively discussed in this thesis.

Bibliography

- E. W. Adams. *Experiments on the structure of turbulent reattaching flow*. PhD thesis, Stanford University, 1984.
- S. Ahmed, G. Ramm, and G. Faltin. Some salient features of the time-averaged ground vehicle wake. *SAE Technical Paper 840300*, 1984.
- AIRBUS. Global market forecast, 2014.
- R. Amiet. Gust response for flat-plate airfoils and the kutta condition. *AIAA Journal*, 28(10):1718–1727, 1990.
- J. D. Anderson. *A History of Aerodynamics: And Its Impact on Flying Machines*, volume 8. Cambridge University Press, 1998.
- J. D. Anderson. *Fundamentals of Aerodynamics*. McGraw-Hill Education, Singapore, 2011. ISBN 9780071289085.
- B. F. Armaly, F. Durst, J. Pereira, and B. Schönung. Experimental and theoretical investigation of backward-facing step flow. *Journal of Fluid Mechanics*, 127:473–496, 1983.
- W. Bachmann. *Signalanalyse*. Vieweg Verlag Braunschweig, 1992.
- R. Baltensperger and M. R. Trummer. Spectral differencing with a twist. *SIAM Journal on Scientific Computing*, 24(5):1465–1487, 2003.
- T. Barlas and G. Van Kuik. Review of state of the art in smart rotor control research for wind turbines. *Progress in Aerospace Sciences*, 46(1):1–27, 2010.
- G. K. Batchelor. Axial flow in trailing line vortices. *Journal of Fluid Mechanics*, 20(4):645–658, 1964.
- R. G. Batt. Layer some measurements on the effect of tripping the two-dimensional shear. *AIAA Journal*, 13(2):245–247, 1975.
- J. Beaudoin, O. Cadot, J. Aider, K. Gosse, P. Paranthoën, B. Hamelin, M. Tissier, D. Allano, I. Mutabazi, M. Gonzales, et al. Cavitation as a complementary tool for automotive aerodynamics. *Experiments in Fluids*, 37(5):763–768, 2004.
- D. W. Bechert. A model of the excitation of large scale fluctuations in a shear layer. *AIAA Aeroacoustics Conference, Atlanta, Georgia*, 8(83-0724):1–9, 1983.
- D. W. Bechert. Excitation of instability waves in free shear layers. Part 1. Theory. *Journal of Fluid Mechanics*, 186:47–62, 1988.
- D. W. Bechert and B. Stahl. Excitation of instability waves in free shear layers Part 2. Experiments. *Journal of Fluid Mechanics*, 186:63–84, 1988.
- L. Bernal and A. Roshko. Streamwise vortex structure in plane mixing layers. *Journal of Fluid Mechanics*, 170:499–525, 1986.
- R. Betchov and A. Szewczyk. Stability of a shear layer between parallel streams. *Physics of Fluids*, 6(10):1391–1396, 1963.

Bibliography

- A. Betz. Verhalten von wirbelsystemen. *Zeitschrift für Angewandte Mathematik und Mechanik*, 12(3): 164–174, 1932.
- A. J. Bilanin, M. E. Teske, and G. G. Williamson. Vortex interactions and decay in aircraft wakes. *AIAA Journal*, 15(2):250–260, 1977.
- P. Billant, J.-M. Chomaz, and P. Huerre. Experimental study of vortex breakdown in swirling jets. *Journal of Fluid Mechanics*, 376:183–219, Dec. 1998.
- J. M. Birch, W. B. Dickson, and M. H. Dickinson. Force production and flow structure of the leading edge vortex on flapping wings at high and low reynolds numbers. *Journal of Experimental Biology*, 207(7):1063–1072, 2004.
- G. Biswas, M. Breuer, and F. Durst. Backward-facing step flows for various expansion ratios at low and moderate Reynolds numbers. *Journal of fluids engineering*, 126(3):362–374, 2004.
- J. P. Boyd. *Chebyshev and Fourier Spectral Methods*. Dover Publications, Mineola, New York, 2001.
- P. Bradshaw and F. Wong. The reattachment and relaxation of a turbulent shear layer. *Journal of Fluid Mechanics*, 52(01):113–135, 1972.
- G. Brechmann, W. Dzieia, E. Hörnemann, H. Hübscher, D. Jagla, and J. Klaue. *Elektrotechnik, Tabellen Kommunikationselektronik; 3. Auflage*. Westermann Schulbuchverlag, Braunschweig, 2000.
- C. Breitsamter. Wake vortex characteristics of transport aircraft. *Progress in Aerospace Sciences*, 47(2): 89–134, 2011.
- C. Breitsamter and A. Allen. Transport aircraft wake influenced by oscillating winglet flaps. *Journal of Aircraft*, 46(1):175–188, 2009.
- F. K. Browand. An experimental investigation of the instability of an incompressible, separated shear layer. *Journal of Fluid Mechanics*, 26(02):281–307, 1966.
- C. E. Brown. Aerodynamics of wake vortices. *AIAA Journal*, 11(4):531–536, 1973.
- G. L. Brown and A. Roshko. On density effects and large structure in turbulent mixing layers. *Journal of Fluid Mechanics*, 64(04):775–816, 1974.
- A. Brunn, E. Wassen, D. Sperber, W. Nitsche, and F. Thiele. Active drag control for a generic car model. In *Active Flow Control*, pages 247–259. Springer-Verlag, Berlin, 2007.
- J. W. Butler and E. Edwards. Number 2115. *Majesty's Patent Office, London, England*, 1867.
- C. Canuto, M. Y. Hussaini, A. Quarteroni, and T. A. Zang. *Spectral methods in fluid dynamics*. Springer-Verlage, Berlin, Heidelberg, 1988.
- I. P. Castro. Turbulence in incompressible separated flows. In *Separated flows and jets*, pages 191–205. Springer-Verlag Berlin, 1991.
- I. P. Castro and P. Bradshaw. The turbulence structure of a highly curved mixing layer. *Journal of Fluid Mechanics*, 73(02):265–304, 1976.
- L. Cattafesta, D. Williams, C. Rowley, and F. Alvi. Review of active control of flow-induced cavity resonance. In *33rd AIAA Fluid Dynamics Conference and Exhibit, Orlando, Florida*, 2003.
- L. N. Cattafesta and M. Sheplak. Actuators for active flow control. *Annual Review of Fluid Mechanics*, 43:247–272, 2011.
- M. Cerna and A. F. Harvey. The fundamentals of FFT-based signal analysis and measurements. Technical Report 041, National Instruments, 2000.

- C. Chandrsuda and P. Bradshaw. Turbulence structure of a reattaching mixing layer. *Journal of Fluid Mechanics*, 110:171–194, 1981.
- D. R. Chapman, D. M. Kuehn, and H. K. Larson. *Investigation of separated flows in supersonic and subsonic streams with emphasis on the effect of transition*. NACA-Report, 1958.
- S. Cheng, M. Tsubokura, T. Nakashima, Y. Okada, and T. Nouzawa. Numerical quantification of aerodynamic damping on pitching of vehicle-inspired bluff body. *Journal of Fluids and Structures*, 30: 188–204, 2012.
- S. Y. Cheng, M. Tsubokura, T. Nakashima, T. Nouzawa, and Y. Okada. A numerical analysis of transient flow past road vehicles subjected to pitching oscillation. *Journal of Wind Engineering and Industrial Aerodynamics*, 99(5):511–522, 2011.
- H. Chevalier. Flight test studies of the formation and dissipation of trailing vortices. *Journal of Aircraft*, 10(1):14–18, 1973.
- K. Chun and H. Sung. Visualization of a locally-forced separated flow over a backward-facing step. *Experiments in Fluids*, 25(2):133–142, 1998.
- K.-B. Chun and H. J. Sung. Control of turbulent separated flow over a backward-facing step by local forcing. *Experiments in Fluids*, 21(6):417–426, 1996.
- N. J. Cook. *The designer's guide to wind loading of building structures*. Butterworth-Heinemann Ltd, 1985.
- G. Correale, T. Michelis, and M. Kotsonis. NS-DBD plasma actuation on a backward facing step. In *52nd AIAA Aerospace Sciences Meeting, National Harbor, Maryland*, 2014.
- S. Corrsin. Statistical behavior of a reacting mixture in isotropic turbulence. *Physics of Fluids*, 1(1): 42–47, 1958.
- E. Creusé, A. Giovannini, and I. Mortazavi. Vortex simulation of active control strategies for transitional backward-facing step flows. *Computers & Fluids*, 38(7):1348–1360, 2009.
- S. C. Crow. Stability theory for a pair of trailing vortices. *AIAA Journal*, 8(12):2172–2179, 1970.
- J. Dacles-Mariani, G. G. Zilliac, J. S. Chow, and P. Bradshaw. Numerical/experimental study of a wingtip vortex in the near field. *AIAA Journal*, 33(9):1561–1568, 1995.
- G. Danabasoglu and S. Biringen. A Chebyshev matrix method for the spatial modes of the Orr-Sommerfeld equation. *International Journal for Numerical Methods in Fluids*, 11:1033–1037, 1990.
- J. Dandois, E. Garnier, and P. Sagaut. Numerical simulation of active separation control by a synthetic jet. *Journal of Fluid Mechanics*, 574:25–58, 2007.
- G. Dash. Investigation of the trailing edge vortex behind a swept semi-span backward-facing step. Master's thesis, University of Bath, 2012.
- I. De Visscher, T. Lonfils, and G. Winckelmans. Fast-time modeling of ground effects on wake vortex transport and decay. *Journal of Aircraft*, 50(5):1514–1525, 2013.
- M. De Zhou and I. Wygnanski. The response of a mixing layer formed between parallel streams to a concomitant excitation at two frequencies. *Journal of Fluid Mechanics*, 441:139–168, 2001.
- J. M. Déleroy. Robert Legendre and Henri Werlé: toward the elucidation of three-dimensional separation. *Annual Review of Fluid Mechanics*, 33(1):129–154, 2001.

Bibliography

- Deutscher Bund, Bundesministerium für Wirtschaft und Technologie, and Bundesministerium für Umwelt, Naturschutz und Reaktorsicherheit. *Erster Monitoring-Bericht "Energie der Zukunft"*. Bonifatius GmbH, Paderborn, 2012.
- P. E. Dimotakis. Two-dimensional shear-layer entrainment. *AIAA Journal*, 24(11):1791–1796, 1986.
- P. E. Dimotakis and G. L. Brown. The mixing layer at high Reynolds number: large-structure dynamics and entrainment. *Journal of Fluid Mechanics*, 78(03):535–560, 1976.
- W. S. Don and A. Solomonoff. Accuracy and speed in computing the Chebyshev collocation derivative. *SIAM Journal on Scientific Computing*, 16(6):1253–1268, 1995.
- C. d. Donaldson. A brief review of the aircraft trailing vortex problem. Technical report, TR-71-1910, Air force office of scientific research, Wright-Patterson air force base, Ohio, 1971.
- S. Doppel. Stabilitätsanalyse einer nicht-parallelen Scherschicht basierend auf diskreten, nicht-äquidistanten Stützstellen. Master's thesis, Technische Universität Berlin, 2014.
- C. Doppler. *Ueber das farbige Licht der Doppelsterne und einiger anderer Gestirne des Himmels*. Borrosch & André, 1842.
- A. V. Dovgal, V. V. Kozlov, and A. Michalke. Contribution to the instability of laminar separating flows along axisymmetric bodies. II: Experiment and comparison with theory. *European Journal of Mechanics. B, Fluids*, 14(3):351–365, 1995.
- A. D'Ovidio and C. Coats. Organized large structure in the post-transition mixing layer. Part 1. Experimental evidence. *Journal of Fluid Mechanics*, 737:466–498, 2013.
- D. M. Driver and H. L. Seegmiller. Features of a reattaching turbulent shear layer in divergent channel flow. *AIAA Journal*, 23(2):163–171, 1985.
- F. Durst and C. Tropea. Turbulent, backward-facing step flows in two-dimensional ducts and channels. In *Proc. 3rd Int. Symp. on Turbulent Shear Flows*, 1981.
- K. Düwel. Strömungssichtbarmachung von Längswirbeln an einer schrägen, halbspannweitigen, rückwärtigen Stufe. Master's thesis, Technische Universität Berlin, 2012.
- G. Dziuk. *Theorie und Numerik partieller Differentialgleichungen*. de Gruyter Studium, 2010.
- J. K. Eaton and J. P. Johnston. A review of research on subsonic turbulent flow reattachment. *AIAA Journal*, 19(9):1093–1100, 1981.
- H. Eckelmann. *Einführung in die Strömungsmesstechnik*. B. G. Teubner, Stuttgart, 1997.
- EN 14067-6. Railway applications-aerodynamics-part 6: Requirements and test procedures for cross wind assessment. *CEN Brüssel*, 2010.
- E. Erturk. Numerical solutions of 2-D steady incompressible flow over a backward-facing step, Part I: High Reynolds number solutions. *Computers & Fluids*, 37(6):633–655, 2008.
- M. Escudier. Vortex breakdown: observation and explanations. *Progress in Aerospace Science*, 25: 180–229, 1988.
- S. Eskinazi and J. Yeh. An investigation on fully developed turbulent flows in a curved channel. *Journal of the Aeronautical Sciences*, 23(1):23–34, 1956.
- E. Fares. Unsteady flow simulation of the Ahmed reference body using a lattice Boltzmann approach. *Computers & Fluids*, 35(8):940–950, 2006.

- D. Favier, J. Rebont, and C. Maresca. Large-amplitude fluctuations of velocity and incidence of an oscillating airfoil. *AIAA Journal*, 17(11):1265–1267, 1979.
- D. Favier, A. Agnes, C. Barbi, and C. Maresca. Combined translation/pitch motion-a new airfoil dynamic stall simulation. *Journal of Aircraft*, 25(9):805–814, 1988.
- H. H. Fernholz. Near-wall phenomena in turbulent separated flows. In *Fluid-and Gasdynamics*, pages 57–67. Springer-Verlag, Berlin, 1994.
- Feuerwehr-Schweiz. Nachtrag Kyrill: Bahnkomposition wegen Sturm entgleist. Technical report, <http://www.feuerwehr-schweiz.ch/index.php?module=News&func=display&sid=484>; last view: 09.10.2014, 2007.01.25.
- H. E. Fiedler. Coherent structures in turbulent flows. *Progress in Aerospace Sciences*, 25(3):231–269, 1988.
- H. E. Fiedler and H. H. Fernholz. On management and control of turbulent shear flows. *Progress in Aerospace Sciences*, 27(4):305–387, 1990.
- H. E. Fiedler and P. Mensing. The plane turbulent shear layer with periodic excitation. *Journal of Fluid Mechanics*, 150(1):281–309, 1985.
- H. E. Fiedler, H. Gründel, and R. Spieweg. Observations in three-dimensional mixing layers. In *Proceedings*. Indian Institute of Science, Bangalore, India, 1995.
- H. E. Fiedler, C. N. Nayeri, R. Spieweg, and C. O. Paschereit. Three-dimensional mixing layers and their relatives. *Experimental Thermal and Fluid Sciences*, 16:3–16, 1998.
- D. G. Fink and D. Christiansen. *Electronic Engineers' Handbook*. McGraw-Hill, San Francisco, 1989.
- O. Fleig and C. Arakawa. Numerical simulation of wind turbine tip noise. In *42nd AIAA Aerospace Sciences Meeting and Exhibit*, 2004.
- Frankfurter Allgemeine Tageszeitung. Der Wettlauf der Boten-Drohnen hat begonnen. *Frankfurter Allgemeine*, 2014.08.29.
- P. Freymuth. On transition in a separated laminar boundary layer. *Journal of Fluid Mechanics*, 25: 683–704, 1966.
- P. Freymuth, W. Bank, and F. Finaish. Visualization of wing tip vortices in accelerating and steady flow. *Journal of Aircraft*, 23(9):730–733, 1986.
- P. Freymuth, W. Bank, and F. Finaish. Further visualization of combined wing tip and starting vortex systems. *AIAA journal*, 25(9):1153–1159, 1987.
- Y. Furman, H. Müller-Vahl, and D. Greenblatt. Development of a low-speed oscillatory-flow wind tunnel. In *51st AIAA Aerospace Sciences Meeting, Grapevine, Texas*, 2013.
- J. Gabrysch. Containerverluste auf See - Eine statistische Analyse der Jahre 1990 bis 2005. Master's thesis, Hochschule Bremen, 2006.
- M. Gad-el Hak and R. F. Blackwelder. The discrete vortices from a delta wing. *AIAA Journal*, 23(6): 961–962, 1985.
- M. Gad-el Hak and R. F. Blackwelder. Control of the discrete vortices from a delta wing. *AIAA Journal*, 25(8):1042–1049, August 1987.
- M. Gad-el Hak, A. Pollard, and J.-P. Bonnet. *Flow control: fundamentals and practices*, volume 23. Springer-Verlag, Berlin, 1998.

Bibliography

- Q. Gallas, R. Holman, T. Nishida, B. Carroll, M. Sheplak, and L. Cattafesta. Lumped element modeling of piezoelectric-driven synthetic jet actuators. *AIAA Journal*, 41(2):240–247, 2003.
- M. Gaster, E. Kit, and I. Wygnanski. Large-scale structures in a forced turbulent mixing layer. *Journal of Fluid Mechanics*, 150:23–39, 1985.
- M. Gaunaa. Unsteady 2D potential-flow forces on a thin variable geometry airfoil undergoing arbitrary motion. Technical report, Technical University of Denmark, 2006.
- A. Gaylard. Improving aerodynamic characteristics: Challenges and opportunities. In *International Forum, Future Automotive Aerodynamics, Berlin, Germany*, 2012.
- M. M. Gibson and W. Rodi. A Reynolds-stress closure model of turbulence applied to the calculation of a highly curved mixing layer. *Journal of Fluid Mechanics*, 103:161–182, 1981.
- M. M. Gibson and B. A. Younis. Turbulence measurements in a developing mixing layer with mild destabilising curvature. *Experiments in Fluids*, 1(1):23–30, 1983.
- P. Gilliéron and A. Spohn. Flow separations generated by a simplified geometry of an automotive vehicle, IUTAM Symp. *Unsteady Separated Flows*, 2002.
- H. Glauert. The force and moment on an oscillating aerofoil. In A. Gilles, L. Hopf, and T. Kármán, editors, *Vorträge aus dem Gebiete der Aerodynamik und verwandter Gebiete*, pages 88–95. Springer-Verlag, Berlin, Heidelberg, 1930. ISBN 978-3-662-33394-5. doi: 10.1007/978-3-662-33791-2_16.
- K. Gompertz, C. Jensen, P. Kumar, D. Peng, J. W. Gregory, and J. P. Bons. Modification of transonic blowdown wind tunnel to produce oscillating freestream mach number. *AIAA Journal*, 49(11):2555–2563, 2011.
- M. Goodrich and J. Gorham. Wind tunnels of the western hemisphere. In *Federal Research Division Library of Congress, Washington, DC*, pages 81–82, 2008.
- R. E. Gordnier and M. R. Visbal. Unsteady vortex structure over a delta wing. *Journal of Aircraft*, 31(1): 243–248, 1994.
- K. Granlund, B. Monnier, M. Ol, and D. Williams. Airfoil longitudinal gust response in separated vs. attached flows. *Physics of Fluids*, 26(2):027103, 2014. doi: <http://dx.doi.org/10.1063/1.4864338>.
- J. M. Greenberg. Airfoil in sinusoidal motion in a pulsating stream. Technical report, NACA TN1326, 1947.
- D. Greenblatt. Managing flap vortices via separation control. *AIAA Journal*, 44(11):2755–2764, 2006.
- D. Greenblatt. Dual location separation control on a semispan wing. *AIAA Journal*, 45(8):1848–1860, 2007.
- D. Greenblatt and I. J. Wygnanski. The control of flow separation by periodic excitation. *Progress in Aerospace Sciences*, 36(7):487–545, 2000.
- D. Greenblatt, J. Kiedaisch, and H. Nagib. Unsteady-pressure corrections in highly attenuated measurements at moderate mach numbers. In *31st AIAA Fluid Dynamics Conference & Exhibit, Anaheim, California*, 2001.
- D. Greenblatt, S. Vey, O. C. Paschereit, and R. Meyer. Flap vortex management using active gurney flaps. *AIAA Journal*, 47(12):2845–2856, 2009.
- K.-H. Grote and J. Feldhusen. *DUBBEL Taschenbuch für den Maschinenbau*. Springer-Verlag, Berlin, 2011.

- H. Gründel and H. E. Fiedler. The mixing layer between non-parallel streams. In *Advances in Turbulence IV*, pages 167–171. Springer-Verlag, Berlin, 1993.
- H. Gründel, R. Spieweg, and H. Fiedler. The mixing layer behind a slanted trailing edge. In *Advances in Turbulence V*, pages 171–178. Springer-Verlag, Berlin, 1995.
- I. Gursul. Recent developments in delta wing aerodynamics. *The Aeronautical Journal*, 108:437–452, September 2004.
- I. Gursul and W. Xie. Origin of vortex wandering over delta wings. *Journal of Aircraft*, 37(2):348–350, 2000.
- Y. Guy, J. A. Morrow, and T. E. McLaughlin. Pressure measurements and flow field visualization on a delta wing with periodic blowing and suction. In *AIAA Atmospheric Flight Mechanics Conference and Exhibit, Portland, Oregon*, 1999a.
- Y. Guy, J. A. Morrow, and T. E. McLaughlin. Control of vortex breakdown on a delta wing by periodic blowing and suction. In *37th AIAA Aerospace Sciences Meeting and Exhibit, Reno, Nevada*, 1999b.
- Y. Guy, J. A. Morrow, T. E. McLaughlin, and I. J. Wygnanski. Velocity measurements on a delta wing with periodic blowing and suction. In *38th AIAA Aerospace Sciences Meeting and Exhibit, Reno, Nevada*, 2000.
- G. D. Häberle and H. O. Häberle. *Transformatoren und Elektrische Maschinen in Anlagen der Energietechnik; 2. Auflage*. Haan-Gruiten: Verl. Europa-Lehrmittel Nourney, Vollmer, 1990.
- J. E. Hackett and D. K. Cox. The three-dimensional mixing layer between two grazing perpendicular streams. *Journal of Fluid Mechanics*, 43:77–96, 8 1970. doi: 10.1017/S0022112070002240.
- N. Ham, P. Bauer, and T. Lawrence. Wind tunnel generation of sinusoidal lateral and longitudinal gusts by circulation of twin parallel airfoils. *NASA STI/Recon Technical Report N*, 75:29–51, 1974.
- M. Hammas, J. Johansson, and H. Skärnell. Large eddy simulations of the flow around an Ahmed body with active flow control. Master's thesis, Chalmers University of Technology, Gothenburg, Sweden, 2010.
- M. A. Z. Hasan. The flow over a backward-facing step under controlled perturbation: laminar separation. *Journal of Fluid Mechanics*, 238:73–96, 1992.
- M. A. Z. Hasan and A. S. Khan. On the stability characteristics of a reattaching shear layer with nonlaminar separation. *International Journal of Heat and Fluid Flow*, 13, 1992.
- A. I. Heft, T. Indinger, and N. A. Adams. Investigation of unsteady flow structures in the wake of a realistic generic car model. In *29th AIAA Applied Aerodynamics Conference, Honolulu, Hawaii*, 2011.
- W. Heisenberg. *Über Stabilität und Turbulenz von Flüssigkeitsströmen*. Springer-Verlag, Berlin, 1924.
- E. Hering and R. Martin. *Photonik Grundlagen, Technologie und Anwendungen*. Springer, 2006.
- J. C. Hill. Homogeneous turbulent mixing with chemical reaction. *Annual Review of Fluid Mechanics*, 8 (1):135–161, 1976.
- C.-M. Ho and L.-S. Huang. Subharmonics and vortex merging in mixing layers. *Journal of Fluid Mechanics*, 119:443–473, 1982.
- A. G. L. Holloway and S. Tavoularis. The effects of curvature on sheared turbulence. *Journal of Fluid Mechanics*, 237:569–603, 1992.
- R. Holman, Y. Utturkar, R. Mittal, B. L. Smith, and L. Cattafesta. Formation criterion for synthetic jets. *AIAA Journal*, 43(10):2110–2116, 2005.

Bibliography

- F. Holzäpfel. Probabilistic two-phase aircraft wake-vortex model: further development and assessment. *Journal of Aircraft*, 43(3):700–708, 2006.
- F. Holzäpfel. Effects of environmental and aircraft parameters on wake vortex behavior. *Journal of Aircraft*, pages 1–11, 2014.
- F. Holzäpfel and M. Steen. Aircraft wake-vortex evolution in ground proximity: analysis and parameterization. *AIAA Journal*, 45(1):218–227, 2007.
- W.-H. Hucho. *Aerodynamik des Automobils*. Vieweg + Teubner, 2005.
- P. Huerre and P. A. Monkewitz. Local and global instabilities in spatially developing flows. *Annual Review of Fluid Mechanics*, 22:473–537, 1990. doi: 10.1146/annurev.fl.22.010190.002353.
- D. Hummel and G. Redeker. A new vortex flow experiment for computer code validation. Technical report, DTIC Document, 2003.
- A. Huppertz. Beeinflussung der Strömung hinter einer rückwärtsgewandten Stufe durch dreidimensionale Anregung. Master's thesis, Technische Universität Berlin, 1994.
- A. Huppertz. *Aktive Beeinflussung der Strömung stromab einer rückwärtigen Stufe*. PhD thesis, Technische Universität Berlin, 2001.
- A. Huppertz and G. Janke. Preliminary experiments on the control of three-dimensional modes in the flow over a backward-facing step. In *Advances in Turbulence VI*, pages 461–464. Springer-Verlag, Berlin, 1996.
- A. K. M. F. Hussain and W. C. Reynolds. The mechanics of an organized wave in turbulent shear flow. *Journal of Fluid Mechanics*, 41(02):241–258, 1970.
- M. Iida, O. Fleig, C. Arakawa, and M. Shimooka. Wind turbine flow and noise prediction by large eddy simulation. In *43rd AIAA Aerospace Sciences Meeting and Exhibit*, 2005.
- Institutsbericht HFI. Einfluss von Filtermatten auf die Querkomponente am Beginn der Messstrecke des GroWiKas. Technical report, Hermann-Föttinger Institut, Technische Universität Berlin, 2008.
- R. Isaacs. Airfoil theory for flows of variable velocity. *Journal of the Aeronautical Sciences*, 12(1): 113–117, 1945.
- R. Isaacs. Airfoil theory for rotary wing aircraft. *Journal of the Aeronautical Sciences*, 13(4):218–220, 1946.
- D. Ivanov. Analyse und aktive Beeinflussung des Strömungsfeldes eines generischen Fahrzeuges. Master's thesis, Technische Universität Berlin, 2011.
- H. Janocha. *Aktoren Grundlagen und Anwendungen*. Springer-Verlag, Berlin, 1992.
- J. Jimenez. The role of coherent structures in modelling turbulence and mixing. In *Proceedings of the International Conference, Madrid, Spain, June 25-27, 1980*, volume 136, 1981.
- L. Jisheng and H. E. Fiedler. On the evolution of large scale structures in three-dimensional mixing layers. *Acta Mechanica Sinica*, 17(1):10–23, 2001.
- R. T. Jones. The unsteady lift of a wing of finite aspect ratio. *NACA Rep. No. 681*, 1940.
- N. Joukowski. On adjoint vortices. *Izviestia*, 13:12–25, 1906.
- W. Jürgens. *Untersuchung der beeinflussten Strömung über eine gepfeilte, rückspringende Stufe mittels Stabilitätsanalyse und numerischer Simulation*. PhD thesis, Technische Universität Berlin, 2006.

- W. Jürgens and H. J. Kaltenbach. Eigenmode decomposition of turbulent velocity fields behind a swept, backward-facing step. *Journal of Turbulence*, 4(018):1–21, 2003.
- W. Jürgens and H.-J. Kaltenbach. The effect of sweep on the forced transitional flow over a backward-facing step. *Computers & Fluids*, 59:1–10, 2012.
- M. Kallenbach, R. Eick, P. Quendt, T. Ströhla, and K. Feindt. *Elektromagnete: Grundlagen, Berechnung, Entwurf und Anwendung; 3. Auflage*. Vieweg+Teubner, 2008.
- H. Kaltenbach. Turbulent flow over a swept backward facing step. *European Journal of Mechanics*, 23: 501–518, 2004.
- H. Kaltenbach and G. Janke. Direct numerical simulation of flow separation behind a swept, rearward-facing step at $Re_H=3000$. *Physics of Fluids*, 12(9):2320–2337, 2000.
- P. G. Kapiris and D. S. Mathioulakis. Experimental study of vortical structures in a periodically perturbed flow over a backward-facing step. *International Journal of Heat and Fluid Flow*, 47:101–112, 2014.
- J. Katz and A. Plotkin. *Low-speed aerodynamics*, volume 13. Cambridge University Press, 2001.
- A. Kelch. Dreidimensionale Stabilitätsuntersuchung einer Scherschicht hinter einer sträg angeströmten Stufe. Master's thesis, Technische Universität Berlin, 2003.
- L. Kelvin. Hydrokinetic solutions and observations. *Philosophica Magazine*, 42:362–377, 1871.
- F. Kost. The behaviour of probes in transonic flow fields of turbomachinery. In *8th European Conference on Turbomachinery - Fluid Dynamics and Thermodynamics, Graz, Austria, 2009*.
- S. B. R. Kottapalli. Unsteady aerodynamics of oscillating airfoils with inplane motions. *American Helicopter Society*, 30:62–63, 1985.
- V. Kottke. Wärme-, Stoff- und Impulsübertragung in abgelösten Strömungen. *Chemie Ingenieur Technik*, 54(2):86–94, 1982.
- A. Kourta and P. Gilliéron. Impact of the automotive aerodynamic control on the economic issues. *Journal of Applied Fluid Mechanics*, 2(2), 2009.
- S. Krajnović. Shape optimization of high-speed trains for improved aerodynamic performance. *Proceedings of the Institution of Mechanical Engineers, Part F: Journal of Rail and Rapid Transit*, 223(5): 439–452, 2009.
- S. Krajnovic and L. Davidson. Large-eddy simulation of the flow around simplified car model. *SAE Technical Paper 2004-01-0227*, 2004.
- S. Krajnović and L. Davidson. Influence of floor motions in wind tunnels on the aerodynamics of road vehicles. *Journal of Wind Engineering and Industrial Aerodynamics*, 93(9):677–696, 2005a.
- S. Krajnović and L. Davidson. Flow around a simplified car, part 2: Understanding the flow. *Journal of Fluids Engineering*, 127(5):919–928, 2005b.
- A. Kremser. *Elektrische Maschinen und Antriebe: Grundlagen, Motoren und Anwendungen*. Vieweg+Teubner Verlag, 2007.
- J. Kruscha and H. E. Fiedler. Untersuchung zur Stabilität eines nicht-parallelen Scherschicht. Master's thesis, Technische Universität Berlin, 1994.
- D. A. D. Kuehn. Effects of adverse pressure gradient on the incompressible reattaching flow over a rearward-facing step. *AIAA journal*, 18(3):343–344, 1980.
- K. Küpfmüller, W. Mathis, and A. Reibiger. *Theoretische Elektrotechnik*. Springer-Verlag, Berlin, 2008.

Bibliography

- W. Kutta. Auftriebskräfte in strömenden Flüssigkeiten. *Illustrierte Aeronautische Mitteilungen*, 6:133–135, 1902.
- G. V. Lachmann. *Boundary layer and flow control: its principles and application*, volume 2. Pergamon Press, Oxford, New York, 1961.
- N. C. Lambourne and D. W. Bryer. *The bursting of leading-edge vortices: some observations and discussion of the phenomenon*. HM Stationery Office, 1962.
- J. C. Lasheras and H. Choi. Three-dimensional instability of a plane free shear layer: an experimental study of the formation and evolution of streamwise vortices. *Journal of Fluid Mechanics*, 189:53–86, 1988.
- E. Laurien. Lösung der Orr-Sommerfeld-Gleichung für die Balsius'sche Grenzschichtströmung mittels Chebyshev-Kollokation. Internal report: IB 221-85 A 02, Deutsches Zentrum für Luft- und Raumfahrt, 1985.
- H. Le, P. Moin, and J. Kim. Direct numerical simulation of turbulent flow over a backward-facing step. *Journal of Fluid Mechanics*, 330:349–374, 1997.
- J. Leconte. On the influence of musical sounds on the flame of a jet of coal-gas. *Philosophical Magazine*, 4, 1858.
- R. Lehmann. Effects of Ns-DBD plasma actuators on turbulent shear layers. Master's thesis, Technische Universität Berlin, 2014.
- B. Lehugeur. *Caractérisation et contrôle des structures tourbillonnaires longitudinales en aérodynamique automobile*. PhD thesis, Paris 6, 2007.
- B. Lehugeur and P. Gilliéron. Active control of vortex breakdown phenomenon in the wake of a simplified car geometry. In *ASME 2006 2nd Joint US-European Fluids Engineering Summer Meeting Collocated With the 14th International Conference on Nuclear Engineering*, pages 709–714. American Society of Mechanical Engineers, 2006.
- S. Leibovich. Structure of vortex breakdown. *Annual Review of Fluid Mechanics*, 10:221–246, 1978.
- J. G. Leishman. *Principles of helicopter aerodynamics*. Cambridge University Press, 2000.
- J. G. Leishman. Challenges in modelling the unsteady aerodynamics of wind turbines. In *21st ASME Wind Energy Symposium and the 40th AIAA Aerospace Sciences Meeting, Reno, Nevada*, 2002.
- J. G. Leishman and A. Bagai. Challenges in understanding the vortex dynamics of helicopter rotor wakes. *AIAA Journal*, 36(7):1130–1140, 1998.
- E. Lenz. Über die Bestimmung der Richtung der durch elektrodynamische Vertheilung erregten galvanischen Ströme. *Annalen der Physik*, 107(31):483–494, 1834.
- S. Leyh. Experimentelle Untersuchung des Nachlaufs einer rückwärtigen Stufe bei verschiedenen Neigungswinkeln. Master's thesis, Technische Universität Berlin, 2014.
- H. Lienhart, C. Stoots, and S. Becker. Flow and turbulence structures in the wake of a simplified car model (Ahmed model). In *New Results in Numerical and Experimental Fluid Mechanics III*, pages 323–330. Springer-Verlag, Berlin, 2002.
- H. W. Liepmann and J. Laufer. Investigations of free turbulent mixing. *NACA Technical Note*, 1257, 1947.
- H. J. Lim, M. K. Chung, and H. J. Sung. The evolution of initially uniform shear flow through a nearly two-dimensional 90° curved duct. *Experiments in Fluids*, 19(3):173–187, 1995.
- M. V. Lowson. Visualization measurements of vortex flows. *Journal of Aircraft*, 28(5):320–327, 1991.

- G. Lu and S. K. Lele. Inviscid instability of a skewed compressible mixing layer. *Journal of Fluid Mechanics*, 249:441–463, 1993.
- S. Margalit, D. Greenblatt, A. Seifert, and I. J. Wygnanski. Active flow control of a delta wing at high incidence using segmented piezoelectric actuators. In *1st AIAA Flow Control Conference, Saint Louis, Missouri*, 2002.
- S. Margalit, D. Greenblatt, A. Seifert, and I. J. Wygnanski. Delta wing stall and roll control using segmented piezoelectric fluidic actuators. *Journal of Aircraft*, 42(3):698–709, 2005.
- D. Margolis and J. Lumley. Curved turbulent mixing layer. *Physics of Fluids*, 8(10):1775–1784, 1965.
- J. M. Martin, R. W. Empey, W. J. McCroskey, and F. X. Caradonna. An experimental analysis of dynamic stall on an oscillating airfoil. *Journal of the American Helicopter Society*, 19(1):26–32, 1974.
- W. H. Mason and J. F. Marchman. Far-field structure of aircraft wake turbulence. *Journal of Aircraft*, 10(2):86–92, 1973.
- W. J. McCroskey. Unsteady airfoils. *Annual Review of Fluid Mechanics*, 14(1):285–311, 1982.
- W. J. McCroskey and J. J. Philippe. Unsteady viscous flow on oscillating airfoils. *AIAA Journal*, 13(1):71–79, 1975.
- W. J. McCroskey, L. W. Carr, and K. W. McAlister. Dynamic stall experiments on oscillating airfoils. *AIAA Journal*, 14(1):57–63, 1976.
- M. Menke, H. Yang, and I. Gursul. Experiments on the unsteady nature of vortex breakdown over delta wings. *Experiments in Fluids*, 27(3):262–272, 1999.
- W. Merzkirch. *Flow visualization*. Academic Press, Orlando, 1987.
- A. Michalke. On the inviscid instability of the hyperbolic-tangent velocity profile. *Journal of Fluid Mechanics*, 19:543–556, 1964.
- A. Michalke. On spatially growing disturbances in an inviscid shear layer. *Journal of Fluid Mechanics*, 23:521–544, 1965. doi: 10.1017/S0022112065001520.
- A. Michalke, V. V. Kozlov, and A. V. Dovgal. Contribution to the instability of laminar separating flows along axisymmetric bodies. I: Theory. *European Journal of Mechanics. B, Fluids*, 14(3):333–350, 1995.
- R. W. Miksad. Experiments on the nonlinear stages of free-shear-layer transition. *Journal of Fluid Mechanics*, 56(04):695–719, 1972.
- A. Mitchell and J. Délery. Research into vortex breakdown control. *Progress in Aerospace Sciences*, 37:385–418, 2001.
- P. A. Monkewitz and P. Huerre. Influence of the velocity ratio on the spatial instability of mixing layers. *Physics of Fluids*, 25(7):1137–1143, 1982.
- S. A. Morton, Y. Guy, J. A. Morrow, and D. C. Blake. Numerical simulation of periodic suction and blowing control of vortex breakdown on a delta wing. In *17th Applied Aerodynamics Conference, AIAA Conference, Norfolk, Virginia*, 1999.
- R. D. Moser and M. M. Rogers. The three-dimensional evolution of a plane mixing layer: pairing and transition to turbulence. *Journal of Fluid Mechanics*, 247:275–320, 1993.
- T. J. Mueller. *Introduction to the design of fixed-wing micro air vehicles*. American Institute of Aeronautics and Astronautics, 2007.

Bibliography

- H. Müller-Vahl, C. N. Nayeri, C. O. Paschereit, and D. Greenblatt. Control of unsteady aerodynamic loads using adaptive blowing. In *32nd AIAA Applied Aerodynamics Conference, AIAA Aviation, Atlanta, Georgia*, 2014a.
- H. Müller-Vahl, C. Strangfeld, C. Nayeri, C. Paschereit, and D. Greenblatt. Thick airfoil deep dynamic stall. In M. Hölling, J. Peinke, and S. Ivanell, editors, *Wind Energy- Impact of Turbulence*, pages 35–40, 2014b.
- H. Müller-Vahl, C. Strangfeld, C. N. Nayeri, C. O. Paschereit, and D. Greenblatt. Control of thick airfoil, deep dynamic stall using steady blowing. *AIAA Journal*, 53(2):277–295, 2015. doi: 10.2514/6.2013-854.
- M. Münk. General theory of thin wing sections. *NACA Report*, 142:243, 1922.
- H. Nagib, P. Reisenthel, and D. Koga. On the dynamical scaling of forced unsteady separated flows. In *AIAA Shear Flow Control Conference: AIAA-85-0553*, 1985.
- A. Nassoufis and A. Rabenstein. Einstürzende Neubauten. *Stern, Germany*, 2007.01.19.
- National Instruments. FFT-Praxis in NI DIAdem. Technical report, National Instruments, www.ni.com, 2011.
- C. N. Nayeri. *Investigation of the three-dimensional shear layer between confined coaxial jets with swirl*. PhD thesis, Technische Universität Berlin, 2000.
- A. H. Nayfeh and W. S. Saric. Non-linear Kelvin-Helmholtz instability. *Journal of Fluid Mechanics*, 46(02):209–231, 1971.
- A. H. Nayfeh and W. S. Saric. Nonlinear waves in a Kelvin-Helmholtz flow. *Journal of Fluid Mechanics*, 55(02):311–327, 1972.
- U. Neumann. Experimentelle Untersuchung zur Beeinflussung des leeseitigen Wirbels bei Seitenwind am ICE3 Zugmodell. Master's thesis, Technische Universität Berlin, 2014.
- B. Nishri and I. J. Wygnanski. Effects of periodic excitation on turbulent flow separation from a flap. *AIAA Journal*, 36(4):547–556, 1998.
- W. Nitsche and A. Brunn. *Strömungsmesstechnik, 2. aktualisierte und bearbeitete Auflage*. Springer-Verlag, Berlin, Heidelberg, 2006.
- K. Oberleithner, M. Sieber, C. N. Nayeri, C. O. Paschereit, C. Petz, H. C. Hege, B. R. Noack, and I. J. Wygnanski. Three-dimensional coherent structures in a swirling jet undergoing vortex breakdown: stability analysis and empirical mode construction. *Journal of Fluid Mechanics*, 679:383–414, 2011.
- H. Oertel. *Strömungsmechanische Instabilitäten*. Springer-Verlage, Berlin, 1996.
- Y. Okada, T. Nouzawa, T. Nakamura, and S. Okamoto. Flow structures above the trunk deck of sedan-type vehicles and their influence on high-speed vehicle stability 1st report: On-road and wind-tunnel studies on unsteady flow characteristics that stabilize vehicle behavior. Technical report, SAE Technical Paper, 2009.
- W. M. Orr. The stability or instability of the steady motions of a liquid. Part 1. In *Proceedings of the Royal Irish Academy*, volume 27, 1907a.
- W. M. Orr. The stability or instability of the steady motions of a liquid. Part 2. In *Proceedings of the Royal Irish Academy*, volume 27, 1907b.
- J. M. Ortega, R. L. Bristol, and Ö. Savas. Experimental study of the instability of unequal-strength counter-rotating vortex pairs. *Journal of Fluid Mechanics*, 474:35–84, 2003.

- D. Oster and I. J. Wygnanski. The forced mixing layer between parallel streams. *Journal of Fluid Mechanics*, 123:91–130, 1982.
- D. Oster, I. J. Wygnanski, B. Dziomba, and H. E. Fiedler. On the effect of initial conditions on the two dimensional turbulent mixing layer. In *Structure and Mechanisms of Turbulence I*, pages 48–64. Springer, 1978.
- M. V. Ötügen. Expansion ratio effects on the separated shear layer and reattachment downstream of a backward-facing step. *Experiments in Fluids*, 10(5):273–280, 1991.
- C. O. Paschereit, S. Terhaar, B. Čosić, and K. Oberleithner. Application of linear hydrodynamic stability analysis to reacting swirling combustor flows. *Journal of Fluid Science and Technology*, 9(3), 2014.
- F. M. Payne. *The structure of leading edge vortex flows including vortex breakdown*. PhD thesis, University of Notre Dame, 1987.
- G. Pechlivanoglou. *Passive and active flow control solutions for wind turbine blades*. PhD thesis, Technische Universität Berlin, 2013.
- G. Pechlivanoglou, C. N. Nayeri, and C. O. Paschereit. Performance optimization of wind turbine rotors with active flow control. In *ASME 2011 Turbo Expo: Turbine Technical Conference and Exposition*, pages 763–775. American Society of Mechanical Engineers, 2011.
- S. Pfaffel, V. Berkhout, S. Faulstich, P. Kühn, K. Linke, P. Lyding, and R. Rothkegel. *Windenergie Report Deutschland 2011*. Fraunhofer IWES, 2012.
- G. A. Pierce, D. L. Kunz, and J. B. Malone. The effect of varying freestream velocity on airfoil dynamic stall characteristics. *Journal of the American Helicopter Society*, 23(2):27–33, 1978.
- R. T. Pierrehumbert and S. E. Widnall. The two- and three-dimensional instabilities of a spatially periodic shear layer. *Journal of Fluid Mechanics*, 114:59–82, 1982.
- L. Prandtl. Über Flüssigkeitsbewegung bei sehr kleiner Reibung. In *Verhandlungen des III. Internationaler Mathematiker-Kongresses, Heidelberg*, pages 484–491. Teubner, Leipzig, 1904.
- L. Prandtl. Tragflügeltheorie. i. mitteilung. *Nachrichten von der Gesellschaft der Wissenschaften zu Göttingen, Mathematisch-Physikalische Klasse*, 1918:451–477, 1918.
- L. Prandtl. Tragflügeltheorie. ii. mitteilung. *Nachrichten von der Gesellschaft der Wissenschaften zu Göttingen, Mathematisch-Physikalische Klasse*, 1919:107–137, 1919.
- L. Prandtl. Bemerkungen über die Entstehung der Turbulenz. *Zeitschrift für Angewandte Mathematik und Mechanik*, 1(6):431–436, 1921.
- L. Rayleigh. On the stability, or instability, of certain fluid motions. *Proceedings of the London Mathematical Society*, 1(1):57–72, 1879.
- J. P. Retelle, J. M. McMichael, and D. A. Kennedy. Harmonic optimization of a periodic flow wind tunnel. *Journal of Aircraft*, 18(8):618–623, 1981.
- B. Robins, C. Hutton, and J. Wilson. *New Principles of Gunnery (reprint)*. F. Wingrave, in the Strand, 1805.
- F. W. Roos and J. T. Kegelmann. Control of coherent structures in reattaching laminar and turbulent shear layers. *AIAA Journal*, 24(12):1956–1963, 1986.
- A. Roshko. Structure of turbulent shear flows: a new look. *AIAA Journal*, 14(10):1349–1357, 1976.
- S. Rossiter. *The Immortal Beaver: The World's Greatest Bush Plane*. Douglas & McIntyre, Vancouver, 1999.

Bibliography

- V. J. Rossow. On the inviscid rolled-up structure of lift-generated vortices. *Journal of Aircraft*, 10(11): 647–650, 1973.
- V. J. Rossow. Prediction of span loading from measured wake-vortex structure-an inverse betz method. *Journal of Aircraft*, 12(7):626–628, 1975.
- V. J. Rossow. Extended-betz methods for roll-up of vortex sheets. *Journal of Aircraft*, 34(5):592–599, 1997.
- V. J. Rossow. Lift-generated vortex wakes of subsonic transport aircraft. *Progress in Aerospace Sciences*, 35(6):507–660, 1999.
- M. Rütten. Global field invariants and local vortex axis invariants analysis for flow prediction. In *37th AIAA Fluid Dynamics Conference and Exhibit, Miami, Florida, 2007*.
- C. Ruwisch. Experimentelle Untersuchung der freien Scherschicht an einer halbspannweitigen, rückwärtigen, schrägen Stufe. Master's thesis, Technische Universität Berlin, 2013.
- P. G. Saffman and G. R. Baker. Vortex interactions. *Annual Review of Fluid Mechanics*, 11(1):95–121, 1979.
- M. Samimy, K. S. Breuer, L. G. Leal, and P. H. Steen. *A gallery of Fluid Motion*. Cambridge University Press, 2003.
- S. Šarić, S. Jakirlić, and C. Tropea. A periodically perturbed backward-facing step flow by means of LES, DES and T-RANS: an example of flow separation control. *Journal of Fluids Engineering*, 127(5): 879–887, 2005.
- T. Sarpkaya. Turbulent vortex breakdown. *Physics of Fluids*, 7(10):2301–2303, 1995.
- H. Schade, E. Kunz, F. Kameier, and C. O. Paschereit. *Strömungslehre*. de Gruyter, Berlin, 2007.
- M. Scheibel. Entwicklung von segmentierten Klappenaktuatoren zur aktiven Strömungsbeeinflussung von Längswirbeln. Master's thesis, Technische Universität Berlin, 2014.
- H. Schlichting. Zur Entstehung der Turbulenz bei der Plattenströmung. *Nachrichten von der Gesellschaft der Wissenschaften zu Göttingen*, 42:181–208, 1933.
- H. Schlichting and K. Gersten. *Grenzschichttheorie*. Springer Press, 2006.
- G. B. Schubauer and P. S. Klebanoff. Contributions on the mechanics of boundary-layer transition. *NACA-TN-Report 3489 and NACA-TN-Report 1289 (1956)*, 1955.
- G. B. Schubauer and H. K. Skramstad. Laminar boundary-layer oscillations and transition on a flat plate. Technical report, Journal of Research of the National Bureau of Standards. 38: 251-92. Reprint of NACA Adv. Conf. Rep. (1943), 1947.
- G. B. Schubauer and H. K. Skramstad. Laminar-boundary-layer oscillations and transition on a flat plate. *NACA Report No. 909*, 1948.
- H. R. Schwarz and N. Köckler. *Numerische Mathematik; 5. überarbeitete Auflage*. Vieweg+Teubner Verlag, 2004.
- V. S. Selby. *Phenomenological study of subsonic turbulent flow over a swept rearward-facing step*. PhD thesis, University of Delaware, 1982.
- J. Serrin. On the stability of viscous fluid motions. *Archive for Rational Mechanics and Analysis*, 3(1): 1–13, 1959.

- H. Shan, L. Jiang, and C. Liu. Direct numerical simulation of three-dimensional flow around a delta wing. In *38th AIAA Aerospace Sciences Meeting & Exhibit, Ruston, Louisiana*, 2000.
- R. D. Shell. *Shell Energy Scenarios to 2050: An Era of Revolutionary Transitions*. Shell, 2008.
- Shell Deutschland Oil GmbH. Shell PKW-Szenarien bis 2030; Fakten, Trends und Handlungsoptionen für nachhaltige Auto-Mobilität. *Shell Deutschland, Hamburg*, 2009.
- S. Siegel, T. E. McLaughlin, and J. A. Albertson. Partial leading edge forcing of a delta wing at high angles of attack. In *1st AIAA Flow Control Conference, St. Louis, Missouri*, 2002.
- E. Simiu and R. H. Scanlan. *Wind effects on structures*. Wiley, 1996.
- D. Sims-Williams. *Self-excited aerodynamic unsteadiness associated with passenger cars*. PhD thesis, Durham University, 2001.
- A. Sommerfeld. Ein Beitrag zur hydrodynamischen Erklärung der turbulenten Flüssigkeitsbewegungen. In *Proceedings of the 4th International Congress of Mathematicians 3*, 1908.
- P. R. Spalart. Airplane trailing vortices. *Annual Review of Fluid Mechanics*, 30(1):107–138, 1998.
- R. Spieweg and H. Gründel. Die Scherschicht hinter einer schrägen Abströmkante. In *Institutsbericht 1993-1994*. Hermann-Föttinger-Institut für Strömungsmechanik, Technische Universität Berlin, 1995.
- J. R. Spreiter and A. H. Sacks. The rolling up of the trailing vortex sheet and its effect on the downwash behind wings. *Journal of the Aeronautical Sciences*, 18(1):21–32, 1951.
- G. Springer, P. Bastian, and A. Valny. *Fachkunde Elektrotechnik*. Verlag Europa-Lehrmittel, 1997.
- Statistisches Bundesamt. *Unfälle von Güterkraftfahrzeugen im Straßenverkehr*. Statistisches Bundesamt, Wiesbaden, 2013.
- H.-D. Stölting. *Handbuch Elektrische Kleinantriebe*. Hanser Verlag, 2006.
- C. Strangfeld, C. N. Nayeri, L. Taubert, and C. O. Paschereit. Parametric investigations of the leading edge vortex on a delta wing. In *20th AIAA Computational Fluid Dynamics Conference, 2011, Honolulu, Hawaii*, 2011.
- C. Strangfeld, K. Düwel, C. N. Nayeri, and C. O. Paschereit. Rolling up shear layer. Poster, 2013a. American Physical Society, 66th Annual Meeting, Division of Fluid Dynamics.
- C. Strangfeld, D. Wieser, H.-J. Schmidt, R. Woszidlo, C. Nayeri, and C. Paschereit. Experimental study of baseline flow characteristics for the realistic car model driver. Technical report, SAE Technical Paper, 2013b.
- C. Strangfeld, H. Müller-Vahl, C. N. Nayeri, C. O. Paschereit, and D. Greenblatt. Unsteady aerodynamics of an airfoil in an oscillating free stream. In *7th AIAA Theoretical Fluid Mechanics Conference, AIAA Aviation, Atlanta, Georgia*, 2014.
- J. W. Strutt and J. W. S. Rayleigh. On the instability of jets. *Proceedings of the London Mathematical Society*, 10:4–13, 1878.
- A. Szumowski and G. Meier. Forced oscillations of airfoil flows. *Experiments in Fluids*, 21(6):457–464, 1996.
- K. Taira and T. Colonius. Three-dimensional flows around low-aspect-ratio flat-plate wings at low Reynolds numbers. *Journal of Fluid Mechanics*, 623:187–207, 2009a.

Bibliography

- K. Taira and T. Colonius. Effect of tip vortices in low-Reynolds-number poststall flow control. *AIAA Journal*, 47(3):749–756, 2009b.
- D. M. Tang, P. G. A. Cizmas, and E. H. Dowell. Experiments and analysis for a gust generator in a wind tunnel. *Journal of Aircraft*, 33(1):139–148, 1996.
- T. Tanneberger. Optimization of a double decker train regarding crosswind stability. Master’s thesis, Technische Universität Berlin, 2012.
- T. Tatsumi and K. Gotoh. The stability of free boundary layers between two uniform streams. *Journal of Fluid Mechanics*, 7(03):433–441, 1960.
- T. Theodorsen. General theory of aerodynamic instability and the mechanism of flutter. *NACA rep., No. 496*, pages 413–433, 1935.
- J. Tihon, V. Pěnkavová, and M. Pantzali. The effect of inlet pulsations on the backward-facing step flow. *European Journal of Mechanics-B/Fluids*, 29(3):224–235, 2010.
- W. Tollmien. Über die Entstehung der Turbulenz. 1. Mitteilung. *Nachrichten von der Gesellschaft der Wissenschaften zu Göttingen, Mathematisch-Physikalische Klasse*, 1929:21–44, 1928.
- W. Tollmien. Calculation of turbulent expansion processes. Technical report, DTIC Document, 1945.
- L. N. Trefethen. *Spectral Methods in Matlab*. Society for Industrial and Applied Mathematics, 2000.
- C. Tropea, A. L. Yarin, and J. F. Foss. *Handbook of Experimental Fluid Mechanics*, volume 1. Springer-Verlag, Berlin, Heidelberg, 2007.
- TSI HS RST. Commission decision of 21st. february 2008 concerning a technical specification for interoperability relating to the ‘rolling stock’ sub-system of the trans-european high-speed rail system. *Official Journal of the European Union L847132*, 2008.
- M. Tsubokura, R. Kobayashi, Y. Ikawa, T. Nakashima, Y. Okada, T. Kamioka, and T. Nouzawa. Unsteady aerodynamics of road vehicle in dynamic maneuvering. In *30th AIAA Applied Aerodynamics Conference, New Orleans, Louisiana*, 2012.
- J. Tyndall. On sounding and sensitive flames. *The London, Edinburgh, and Dublin Philosophical Magazine and Journal of Science*, 33(221):92–99, 1867.
- B. G. van der Wall. The influence of variable flow velocity on unsteady airfoil behavior. M.s. thesis, University of Maryland, College Park, USA, 1991. UM-AERO 91-46.
- B. G. van der Wall. The influence of variable flow velocity on unsteady airfoil behavior. Technical report, DLR-FB 92-22, Braunschweig, Germany, 1992.
- B. G. van der Wall and J. G. Leishman. The influence of variable flow velocity on unsteady airfoil behavior. In *18th European Rotorcraft Forum, Avignon, France*, 1992.
- B. G. van der Wall and J. G. Leishman. On the influence of time-varying flow velocity on unsteady aerodynamics. *Journal of the American Helicopter Society*, 39(4):25–36, 1994.
- S. Vey. Flap vortex management by active Gurney flaps. Master’s thesis, Technische Universität Berlin, 2007.
- S. Vey. *Low Aspect Ratio Wing Flow Control at Low Reynolds Numbers*. PhD thesis, Technische Universität Berlin, 2014.
- S. Vey, C. N. Nayeri, C. O. Paschereit, and D. Greenblatt. Plasma flow control on low aspect ratio wings at low reynolds numbers. In *48th AIAA Aerospace Sciences Meeting Including the New Horizons Forum and Aerospace Exposition, Orlando, Florida*, 2010.

- G. V. V. S. Watkins, P. Mousley, J. Watmuff, and S. Prasad. The unsteady near-wake of a simplified passenger car. In *15th Australasian Fluid Mechanics Conference, Sydney, Australia*, pages 13–17, 2004.
- G. V. V. S. Watkins, P. Mousley, J. Watmuff, and S. Prasad. Flow structures in the near-wake of the Ahmed model. *Journal of Fluids and Structures*, 20(5):673–695, 2005.
- M. R. Visbal and R. E. Gordnier. Origin of computed unsteadiness in the shear layer of delta wings. *Journal of Aircraft*, 32(5):1146–1148, 1995.
- M. R. Visbal and R. E. Gordnier. On the structure of the shear layer emanating from a swept leading edge at angle of attack. In *33rd AIAA Fluid Dynamics Conference and Exhibit, Orlando, Florida*, June 2003.
- K. Visser, R. Nelson, and T. Ng. A flow visualization and aerodynamic force data evaluation of spanwise blowing on full and half span delta wings. In *27th AIAA Aerospace Sciences Meeting, Reno, Nevada*, 1989.
- H. von Helmholtz. Über discontinuirliche Flüssigkeits-Bewegungen. In *Monatsberichte der Königlich Preussische Akademie der Wissenschaften zu Berlin*, volume 23, pages 215–228, 1868.
- H. Wagner. Über die Entstehung des dynamischen Auftriebes von Tragflügeln. *Zeitschrift für Angewandte Mathematik und Mechanik*, 5(1):17–35, 1925.
- S. Wagner, R. Bareiss, and G. Guidati. *Wind turbine noise*. Springer-Verlag, Berlin, 1996.
- E. Wassen and F. Thiele. LES of wake control for a generic fastback vehicle. In *37th AIAA Fluid Dynamics Conference and Exhibit, Miami, Florida*, 2007.
- E. Wassen and F. Thiele. Drag reduction for a generic car model using steady blowing. *4th AIAA Flow Control Conference, Seattle, Washington*, 2008.
- E. Wassen and F. Thiele. Road vehicle drag reduction by combined steady blowing and suction. In *39th AIAA Fluid Dynamics Conference, San Antonio, Texas*, 2009.
- D. Wee, T. Yi, A. Annaswamy, and A. F. Ghoniem. Self-sustained oscillations and vortex shedding in backward-facing step flows: Simulation and linear instability analysis. *Physics of Fluids*, 16(9):3361–3373, 2004.
- J. A. Weideman and S. C. Reddy. A matlab differentiation matrix suite. *ACM Transactions on Mathematical Software (TOMS)*, 26(4):465–519, 2000.
- T. Weinkauff, H.-C. Hege, B. Noack, M. Schlegel, and A. Dillmann. Coherent structures in a transitional flow around a backward-facing step. *Physics of Fluids*, 15(9):S3, 2003.
- I. Weisbrot and I. J. Wygnanski. On coherent structures in a highly excited mixing layer. *Journal of Fluid Mechanics*, 195:137–159, Apr. 1988. doi: 10.1017/S0022112088002356.
- I. Weisbrot, S. Einav, and I. J. Wygnanski. The nonunique rate of spread of the twodimensional mixing layer. *Physics of Fluids*, 25:1691–1693, 1982.
- W. Weißgerber. *Elektrotechnik für Ingenieure 1: Gleichstromtechnik und Elektromagnetisches Feld. Ein Lehr- und Arbeitsbuch für das Grundstudium*. Springer-Verlag, Berlin, 2008.
- H. Wengle, A. Huppertz, G. Bärwolff, and G. Janke. The manipulated transitional backward-facing step flow: an experimental and direct numerical simulation investigation. *European Journal of Mechanics-B/Fluids*, 20(1):25–46, 2001.
- H. Werlé. Sur l'éclatement des tourbillons d'apex d'une aile delta aux faibles vitesse. *La Recherche Aéronautique*, 74, 1960.
- F. M. White and I. Corfield. *Viscous fluid flow*, volume 3. McGraw-Hill New York, 1991.

Bibliography

- D. Wieser, H.-J. Schmidt, S. Müller, C. Strangfeld, C. N. Nayeri, and C. O. Paschereit. Experimental comparison of the aerodynamic behavior of fastback and notchback driver models. Technical report, SAE Technical Paper, 2014.
- C. H. K. Williamson, T. Leweke, and G. D. Miller. Fundamental instabilities in spatially-developing wing wakes and temporally-developing vortex pairs. In *Proceedings of FEDSM 98, 1998 ASME Fluids Engineering Division Summer Meeting, Washington DC*, 1998.
- C. D. Winant and F. K. Browand. Vortex pairing: the mechanism of turbulent mixing-layer growth at moderate Reynolds number. *Journal of Fluid Mechanics*, 63(02):237–255, 1974.
- J. Wojciak, N. Adams, T. Indinger, P. Theissen, and R. Demuth. Investigation of unsteady vehicle aerodynamics under time-dependent flow conditions. In *29th AIAA Applied Aerodynamics Conference, Honolulu, Hawaii*, 2011.
- S.-H. Wong, M. Papadakis, L. S. Nizampatham, and R. K. Hoffmann, Klaus A. and Agarwal. Computational investigation of blade vortex interaction noise. In *38th AIAA Aerospace Sciences Meeting and Exhibit, Reno, Nevada*, 2000.
- I. Wygnanski and I. J. Weisbrot. On the pairing process in an excited plane turbulent mixing layer. *Journal of Fluid Mechanics*, 195:161–173, 1988.
- I. J. Wygnanski and H. E. Fiedler. The two-dimensional mixing region. *Journal of Fluid Mechanics*, 41(02):327–361, 1970.
- I. J. Wygnanski and R. A. Petersen. Coherent motion in excited free shear flows. *AIAA Journal*, 25(2): 201–213, February 1987.
- I. J. Wygnanski, D. Oster, H. E. Fiedler, and B. Dziomba. On the perseverance of a quasi-two-dimensional eddy-structure in a turbulent mixing layer. *Journal of Fluid Mechanics*, 93(02):325–335, 1979.
- I. J. Wygnanski, P. Tewes, H. Kurz, L. Taubert, and C. Chen. The application of boundary layer independence principle to three-dimensional turbulent mixing layers. *Journal of Fluid Mechanics*, 675: 336–346, 2011.
- I. J. Wygnanski, P. Tewes, and L. Taubert. Applying the boundary-layer independence principle to turbulent flows. *Journal of Aircraft*, 51(1):175–182, 2014.
- J. Wyngaard, H. Tennekes, J. Lumley, and D. Margolis. Structure of turbulence in a curved mixing layer. *Physics of Fluids (1958-1988)*, 11(6):1251–1253, 1968.
- S. Yoshioka, S. Obi, and S. Masuda. Organized vortex motion in periodically perturbed turbulent separated flow over a backward-facing step. *International Journal of Heat and Fluid Flow*, 22(3):301–307, 2001a.
- S. Yoshioka, S. Obi, and S. Masuda. Turbulence statistics of periodically perturbed separated flow over backward-facing step. *International Journal of Heat and Fluid Flow*, 22(4):393–401, 2001b.
- C. Zellmann. Reduktion der Reynoldsabhängigkeit aerodynamischer Beiwerte von Schnellzügen im Windkanal durch Turbulenzgitter. Master's thesis, Technische Universität Berlin, 2011.
- Q. Zhou, F. He, and M. Shen. Direct numerical simulation of a spatially developing compressible plane mixing layer: flow structures and mean flow properties. *Journal of Fluid Mechanics*, 711:437, 2012.

A. Appendix

Appendix I

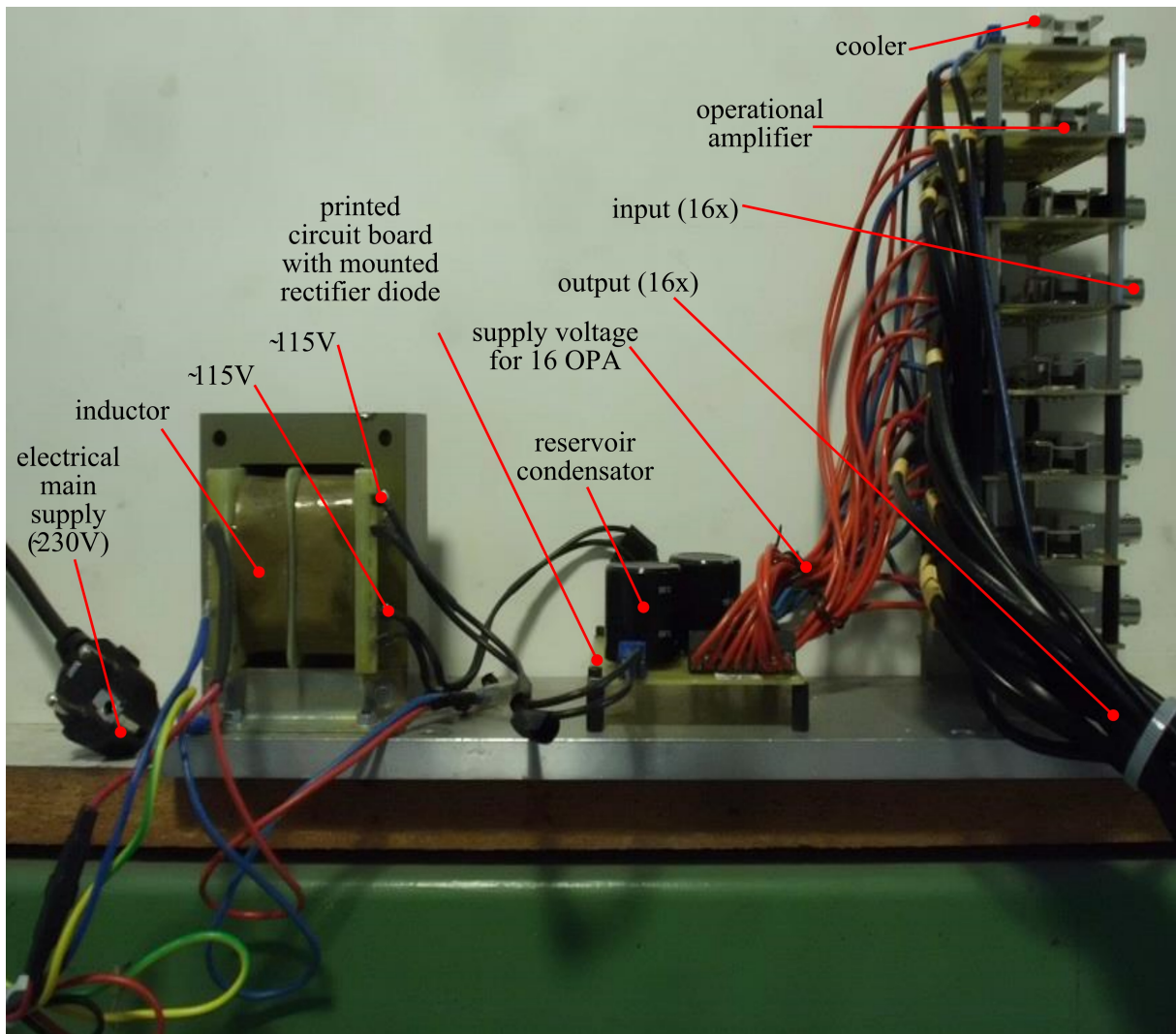


Figure A.1.: Photo of the electrical supply and control circuit

Appendix II

$$C_{\alpha} = \frac{p_{sl} - p_{sr}}{p_{0s} - p_{sm}}$$

$$p_{sm} = \frac{p_{sl} + p_{sr}}{2}$$

Equation according to [Kost, 2009]

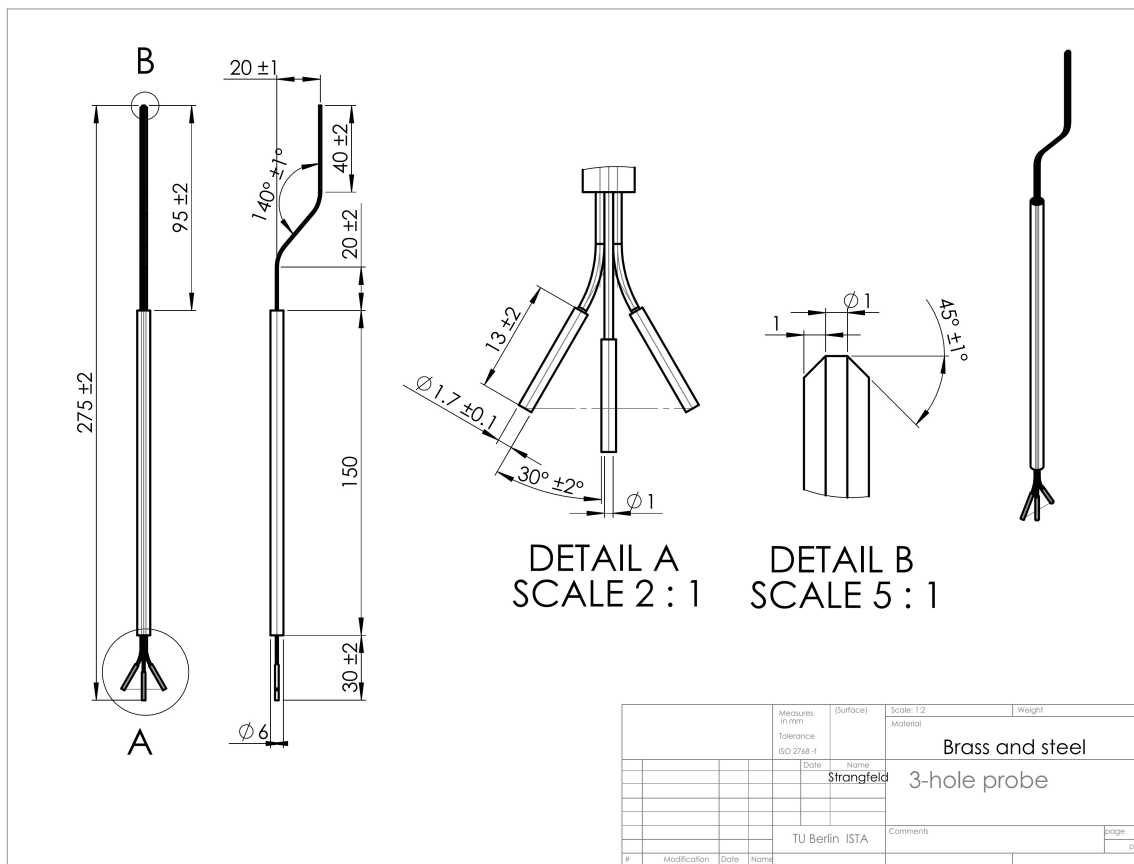


Figure A.2.: General assembly drawing of the three-hole probe

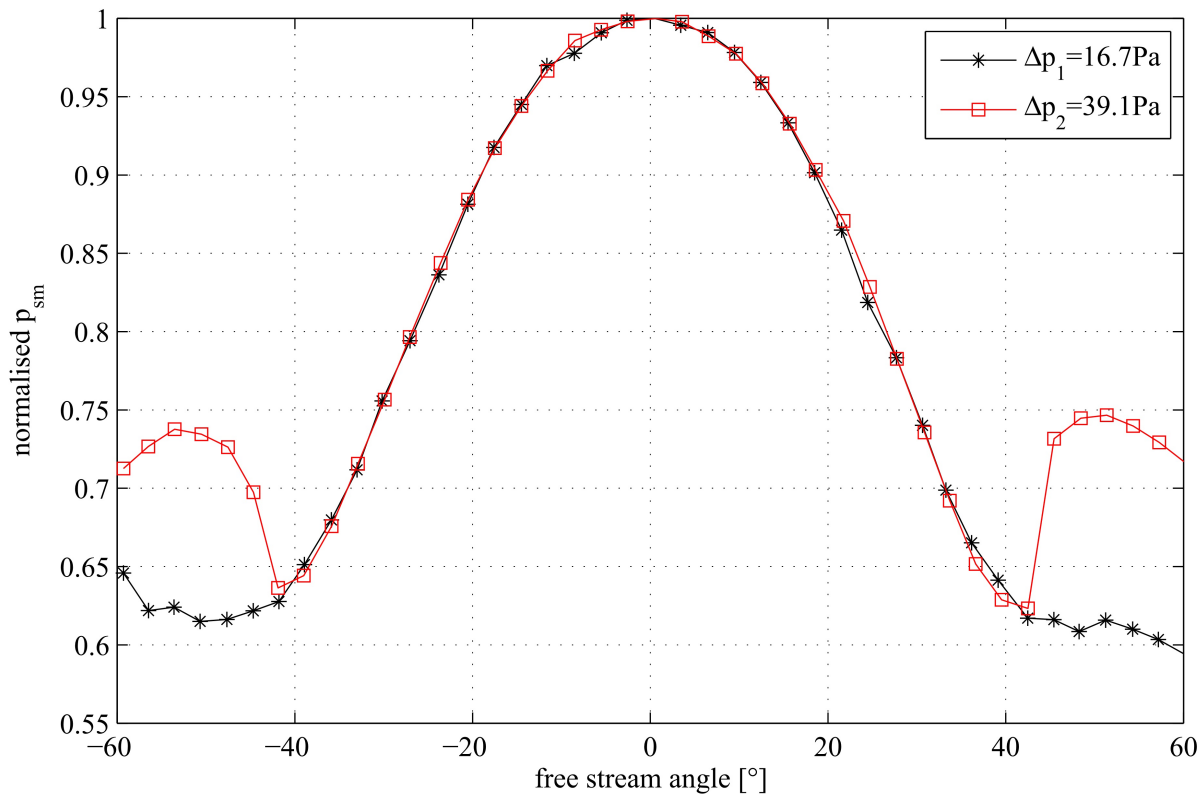


Figure A.3.: Average probe pressure of the left and right tube; normalised by its maximum value

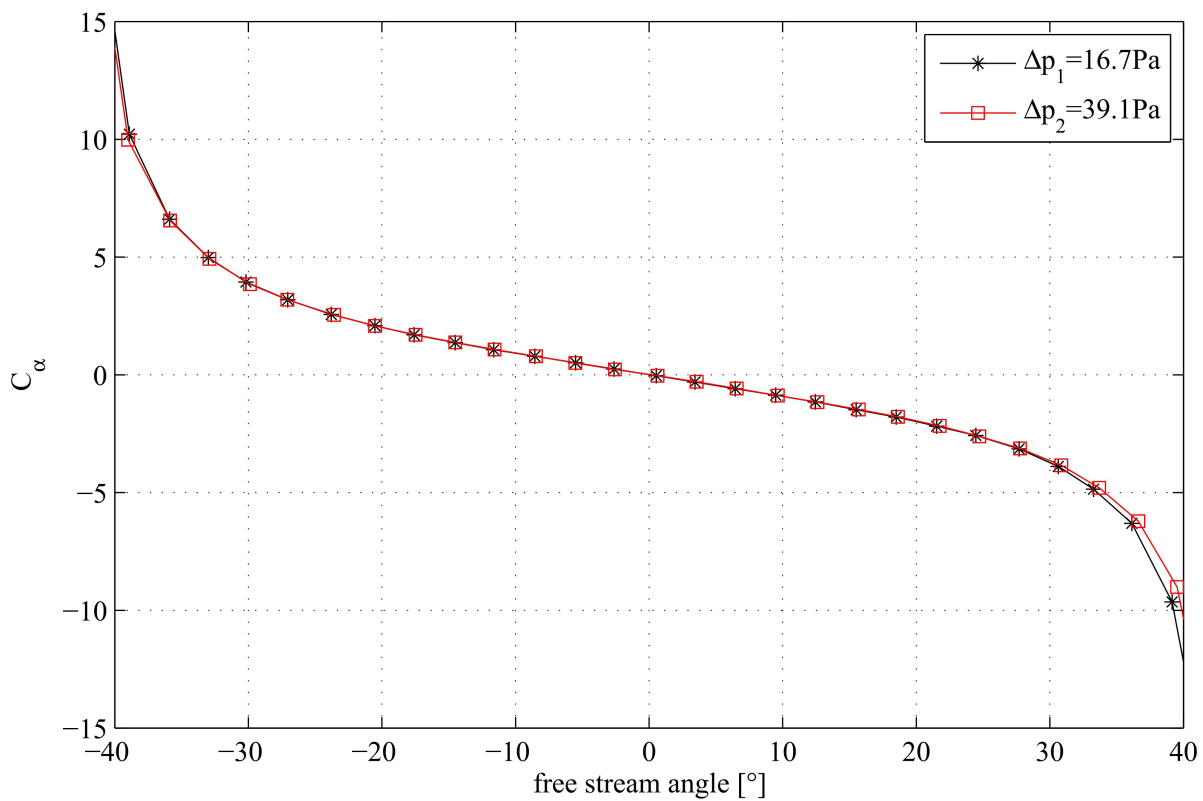


Figure A.4.: Calibrated angle coefficient

Appendix III

The unsteady vorticity sheet $\gamma_b(\phi)$ is computed via equation 3.31. This includes two integrals. The function κ represents the integral in the numerator in equation 3.31. The following equations depict their solutions for $0 \leq n \leq 7$ for arbitrary k and m .

$$\begin{aligned} \kappa(n) &= \int_0^\infty e^{-imk2\tilde{\Lambda}} \frac{[1 + 2\tilde{\Lambda} - 2\sqrt{\tilde{\Lambda}^2 + \tilde{\Lambda}}]^n}{2\sqrt{\tilde{\Lambda}^2 + \tilde{\Lambda}}} d\tilde{\Lambda} \\ \kappa(n=0) &\Rightarrow 0.5e^{ikm} K(0, ikm) \\ \kappa(n=1) &\Rightarrow 0.5e^{ikm} K(0, ikm) - i \frac{-2 + \sqrt{\pi} M(0.5, 0, 2ikm)}{4km} \\ \kappa(n=2) &\Rightarrow \frac{4 + 4ikm + e^{ikm} k^2 m^2 (\pi Y(2, km) + 2J(2, km) (\log(ikm) - \log(km)))}{4k^2 m^2} \\ \kappa(n=3) &\Rightarrow -0.5(-7e^{ikm} K(0, ikm) + \frac{6}{km} e^{ikm} (i + km) K(1, ikm) \\ &\quad + \frac{i}{8k^3 m^3} (64 + 64ikm - 24k^2 m^2 - 18\sqrt{\pi} M(-0.5, -2, 2ikm) \\ &\quad - 15\sqrt{\pi} K(0.5, -2, 2ikm) + 12k^2 m^2 \sqrt{\pi} M(0.5, 0, 2ikm))) \\ \kappa(n=4) &\Rightarrow \frac{1}{32k^4 m^4} (-768 - 768ikm + 320k^2 m^2 + 64ik^3 m^3 \\ &\quad + 16e^{ikm} k^2 m^2 (-21 + 14ikm + 13k^2 m^2) K(0, ikm) \\ &\quad - 32e^{ikm} km (-21i - 14km + 13ik^2 m^2 + 6k^3 m^3) K(1, ikm) \\ &\quad + 168ikm \sqrt{i} M(-0.5, -2, 2ikm) + 105\sqrt{\pi} M(0.5, -3, 2ikm) \\ &\quad + 120ikm \sqrt{\pi} M(0.5, -2, 2ikm) - 32ik^3 m^3 \sqrt{\pi} M(0.5, 0, 2ikm)) \\ \kappa(n=5) &\Rightarrow -0.5(-3k^{-2} m^{-2} e^{ikm} (-45 + 30ikm + 7k^2 m^2) K(0, ikm) \\ &\quad + k^{-3} m^{-3} 10e^{ikm} (-27i - 18km + 11ik^2 m^2 + 2k^3 m^3) K(1, ikm) \\ &\quad + \frac{i}{32k^5 m^5} (-12288 - 12288ikm + 5376k^2 m^2 + 1280ik^3 m^3 - 160k^4 m^4 \\ &\quad + 3150\sqrt{\pi} M(-0.5, -4, 2ikm) - 960k^2 m^2 \sqrt{\pi} M(-0.5, -2, 2ikm) \\ &\quad + 945\sqrt{\pi} M(0.5, -4, 2ikm) + 1050ikm \sqrt{\pi} M(0.5, -3, 2ikm) \\ &\quad - 600k^2 m^2 \sqrt{\pi} M(0.5, -2, 2ikm) + 80k^4 m^4 \sqrt{\pi} M(0.5, 0, 2ikm))) \\ \kappa(n=6) &\Rightarrow \frac{1}{128k^6 m^6} (245760 + 245760ikm - 110592k^2 m^2 - 28672ik^3 m^3 + 4480k^4 m^4 \\ &\quad + 384ik^5 m^5 + 64e^{ikm} k^4 m^4 (-507 + 338ikm + 31k^2 m^2) K(0, ikm) \\ &\quad - 128e^{ikm} k^3 m^3 (-507i - 338km + 184ik^2 m^2 + 15k^3 m^3) K(1, ikm) \\ &\quad - 58590\sqrt{\pi} M(-0.5, -5, 2ikm) - 52080ikm \sqrt{\pi} M(-0.5, -4, 2ikm) \\ &\quad + 4320ik^3 m^3 \sqrt{\pi} M(-0.5, -2, 2ikm) - 10395\sqrt{\pi} M(0.5, -5, 2ikm) \\ &\quad - 11340ikm \sqrt{\pi} M(0.5, -4, 2ikm) + 6300k^2 m^2 \sqrt{\pi} M(0.5, -3, 2ikm) \\ &\quad + 2400ik^3 m^3 \sqrt{\pi} M(0.5, -2, 2ikm) - 192ik^5 m^5 \sqrt{\pi} M(0.5, 0, 2ikm)) \end{aligned}$$

A. Appendix

$$\begin{aligned}
\kappa(n=7) \Rightarrow & -0.5(-e^{ikm}k^{-2}m^{-2}(-1449 + 966ikm + 43k^2m^2)K(0, ikm) \\
& + k^{-3}m^{-3}42e^{ikm}(-69i - 46km + 24ik^2m^2 + k^3m^3)K(1, ikm) \\
& + \frac{i}{128k^7m^7}(5898240 + 5898240ikm - 2703360k^2m^2 - 737280ik^3m^3 \\
& + 129024k^4m^4 + 14336ik^5m^5 \\
& - 896k^6m^6 - 1309770\sqrt{\pi}M(-0.5, -6, 2ikm) - 1190700ikm\sqrt{\pi}M(-0.5, -5, 2ikm) \\
& + 488040k^2m^2\sqrt{\pi}M(-0.5, -4, 2ikm) - 16800k^4m^4\sqrt{\pi}M(-0.5, -2, 2ikm) \\
& - 135135\sqrt{\pi}M(0.5, -6, 2ikm) - 145530ikm\sqrt{\pi}M(0.5, -5, 2ikm) \\
& + 79380k^2m^2\sqrt{\pi}M(0.5, -4, 2ikm) + 29400ik^3m^3\sqrt{\pi}M(0.5, -3, 2ikm) \\
& - 8400k^4m^4\sqrt{\pi}M(0.5, -2, 2ikm) + 448k^6m^6\sqrt{\pi}M(0.5, 0, 2ikm))
\end{aligned}$$

The integral of the denominator in equation 3.31 is independent of n , thus only one solution exists for arbitrary k and m .

$$\int_0^\infty e^{-ikm2\tilde{\Lambda}} \left(\sqrt{\frac{1}{\tilde{\Lambda}} + 1} - 1 \right) d\tilde{\Lambda} = \frac{1}{km} (0.5i - 0.886227iM(-0.5, 0, 2ikm))$$

Appendix IV



Figure A.5.: Photo of the swept, semi-span, backward facing step in the large wind tunnel at the HFI